Design of a Compact, Resource-Efficient and Charge-Resolving Spaceborne Plasma Mass Spectrometer

by

Tyler Eddy

A dissertation submitted in partial fulfillment
of the requirements for the degree of
Doctor of Philosophy
(Climate and Space Sciences and Engineering)
in The University of Michigan
2026

Doctoral Committee:

Professor Susan Lepri, Co-Chair
Associate Professor Jim Raines, Co-Chair
Research Professor Stefano Livi
Professor Emeritus David Wehe

Tyler J. A. Eddy

tjeddy@umich.edu

ORCID iD: 0000-0001-6054-442X

© Tyler J. A. Eddy 2026

Dedication

To my wife, Kaitlin Marie Eddy,

without whom none of it would be possible.

Acknowledgements

I am incredibly grateful for all the support and guidance I have received over the years while I worked on my dissertation. First, I would like to thank my advisors Susan Lepri and Jim Raines for the many great scientific discussions, but also for the mentorship and career advice I received concerning how to be a good physicist, lecturer, and member of a research group. You have been a model for the type of advisor I hope to be some day. In addition, I would like to thank Stefano Livi for all the excellent conversations in the laboratory and about instrumentation during which I felt I could ask any question and learned so much. Furthermore, I am thankful to David Wehe for being willing to be a part of my dissertation committee just after retirement and for taking his excellent course on radiation detectors that helped expand my awareness and understanding of particle detectors and my own field.

Secondly, I am thankful to my lab partners, office mates, and co-workers who helped me with everything throughout my dissertation. I would like to thank Christopher Bert for being my first lab partner at University of Michigan and helping get the laboratory set up in the beginning. In addition, I am grateful for all the guidance and support from Samantha Vaughn as the Helio Lab manager without whom many projects would have gotten lost or went unfinished. In addition, I would like to thank the many SPRL engineers but especially Fernando Saca and Louis Marr for always being willing to mentor a long-lost physics student in engineering and for their dedication to T-FIPS. Next, I would like to thank the lab crews that I worked with who ultimately completed most of the work for the T-FIPS development and to whom the work in this dissertation is eternally indebted: Karthik Kamaraj, Marcello Lara, Arjun Sharma, Gaston Wlodawer, Ben Miller, Isaac Fertig, Jayveer Phull, Jaccob Bell, and Sarah Feldman. Finally, I would like to thank my office mates Michael Hackett, Aidan Nakleh, and Katie Ballard and many friends in the department for all the amazing conversations, scientific and not, over the years – I am hopeful for many more to come.

Finally, I would like to thank my family for all the support I have received throughout my dissertation and along the path that brought me to where I am today. Thank you to my wife, Kaitlin (Watts) Eddy who has been by my side through everything. I would like to thank my parents Suzanne Chartrand, Donald J. Eddy, and Debra Eddy for always pushing me to be the best I can and for supporting my dreams. I am grateful to my grandparents for being my inspiration and driving me towards something bigger and more meaningful. Lastly, I am grateful for my children for always being there to remind me of what is most important; I hope you are always willing to chase your dreams.

Semper fidelis

Table of Contents

Dedication ..... **ii**

Acknowledgements ..... **iii**

List of Figures ..... **vii**

Abstract ..... **x**

Chapter 1 Introduction **1**

Section 1.1 Scientific Background 3

1.1.1 History of Space Instrumentation 3

1.1.2 Space Plasma Composition 19

Section 1.2 T-FIPS Instrument Concept 37

1.2.1 FIPS Heritage 38

1.2.2 Electrostatic Analyzer 40

1.2.3 Time-of-Flight Chamber 43

1.2.4 Energy Detector System 45

Chapter 2 Designing and Optimizing the T-FIPS Sensor **49**

Section 2.1 CAD Development 49

Section 2.2 Electrostatic and Ion Optical Simulations 51

2.2.1 Numerical Modeling Background 52

2.2.2 Fisheye Electrostatic Analyzer 58

2.2.3 3D Cam ESA Concentric Einzel Lens 61

2.2.4 T-FIPS Time-of-Flight Chamber 64
2.2.5 Electrostatic Mirrors 69
Section 2.3 Ancillary Developments 73
2.3.1 Electroformed Grids 73
2.3.2 MCP Crosstalk 76
2.3.3 Microchannel Plate Alignment 78
2.3.4 Photon Occulter 83
2.3.5 Energy Detector System 85

Chapter 3 Hardware Developments and Laboratory Testing 92

Section 3.1 Laboratory Improvements 93
Section 3.2 Experimental Tests 100
3.2.1 FIPS Time-of-Flight Chamber 100
3.2.2 T-FIPS Fisheye Electrostatic Analyzer 102
Section 3.3 Hardware Development 104
3.3.1 T-FIPS Start Detector 104
3.3.2 T-FIPS Time-of-Flight Prototype Chamber 105
3.3.3 Summary of Future Work 106

Overview: The Importance of In-Flight Calibrations and Observational Analyses 107

Chapter 4 EPEE Calibration and Measurements of Top-Side Ionosphere 111

Section 4.1 Earth's Ionosphere 111
Section 4.2 Description of the ÉPÉÉ Spectrometer 115
Section 4.3 Calibration of the ÉPÉÉ Data Products 116
Section 4.4 Analysis ÉPÉÉ Measurements and the Topside Ionosphere 122

Chapter 5 Heavy Ion Sensor Calibration and Observational Analysis 130

Section 5.1 Heavy Ions of the Solar Wind 130
Section 5.2 Description of the Heavy Ion Sensor 132
Section 5.3 Heavy Ion Sensor 3D VDF Calibration 135
Section 5.4 Heavy Ion Sensor Radial Differential Streaming 145

Chapter 6 Conclusion 163

References 168

List of Figures

Figure 1.1 Explorer I and Instrumentation 4
Figure 1.2 Explorer VI Scintillator Detector 7
Figure 1.3 Early Spaceborne Solid-State Detectors 8
Figure 1.4 Early Spaceborne Faraday Cups 9
Figure 1.5 Electrostatic Analyzers and Magnets 11
Figure 1.6 Advances in Spaceborne Electrostatic Analyzers 13
Figure 1.7 Foil Exposure to the Solar Wind 15
Figure 1.8 Space Plasma Composition Measurements 17
Figure 1.9 Ionization Potentials 20
Figure 1.10 Solar Wind Frozen Charge States 21
Figure 1.11 Wave-Particle Interactions 23
Figure 1.12 Solar Wind Heavy Ions 25
Figure 1.13 Solar Wind Speed and Charge Student Abundance 26
Figure 1.14 Interchange Reconnection 29
Figure 1.15 Alfvén Wave Heating of the Corona 30
Figure 1.16 Solar Wind Proton Velocity Distribution Functions 32
Figure 1.17 The Hermitian Magnetosphere and Plasma Sources 34
Figure 1.18 Measurements of Enceladus' Plume 35
Figure 1.19 The Fast Imaging Plasma Spectrometer (FIPS) 39
Figure 1.20 T-FIPS Principles of Operation 40
Figure 1.21 The 3D Cam Electrostatic Analyzer 42

Figure 1.22 Solid-State Detectors and Avalanche Photodiodes 46
Figure 2.1 The T-FIPS Computer-Aided Designs 50
Figure 2.2 Toy Ion Optical Geometries and Simulations 53
Figure 2.3 The COMSOL Simulation Process 56
Figure 2.4 Fisheye ESA Electrostatic Models 60
Figure 2.5 Fisheye ESA Electromechanical Study 61
Figure 2.6 3D Cam ESA Concentric Einzel Lens Geometry and Electrostatics 63
Figure 2.7 3D Cam ESA Concentric Einzel Lens Particle Ray Tracing 64
Figure 2.8 T-FIPS Time-of-Flight Chamber Configurations 65
Figure 2.9 Time-of-Flight Chamber Particle Distributions 66
Figure 2.10 T-FIPS Time-of-Flight Chamber Ion Optical Model 67
Figure 2.11 T-FIPS Time-of-Flight Simulated Efficiencies 68
Figure 2.12 Electrostatic Mirror Simulations 70
Figure 2.13 Electrostatic Harp and Electron Mirror Simulations 72
Figure 2.14 Electroformed Meshes 75
Figure 2.15 T-FIPS Start and Stop Detector Crosstalk 77
Figure 2.16 Crosstalk Particle Properties 78
Figure 2.17 Microchannel Plate Alignment Procedure 80
Figure 2.18 Microchannel Plate Alignment Tolerance 82
Figure 2.19 Photon Occulter 84
Figure 2.20 HV Bubble Time-of-Flight vs Energy Spectra 88
Figure 3.1 The Prevac IS-40E1 Ion Source 94
Figure 3.2 The HPIL Calibration System 97
Figure 3.3 HPIL Main Chamber and Beam Map Software 99
Figure 3.4 The FIPS Time-of-Flight Chamber 101
Figure 3.5 Fisheye ESA Test Setup 103

Figure 3.6 T-FIPS Prototype Time-of-Flight Chamber 105
Figure 4.1 The Composition of Earth's Ionosphere 112
Figure 4.2 Regions of Earth's Ionosphere 114
Figure 4.4 ÉPÉÉ-FPMU Comparison and Calibration Factor 120
Figure 4.5 ÉPÉE-FPMU Calibration Factor vs Spacecraft Potential 121
Figure 4.6 ÉPÉÉ-FPMU Cross-Calibration Results 122
Figure 4.7 Global Mission Average Maps – Ion Density and Spacecraft Potentials 123
Figure 4.8 Global Monthly Average Maps – Ion Densities 124
Figure 4.9 ÉPÉÉ Measurements and IRI Model Comparison 126
Figure 4.10 ÉPÉÉ Measurements During Geomagnetic Storm 127
Figure 5.1 The Heavy Ion Sensor 134
Figure 5.2 HIS RTN Coordinate Transformation 137
Figure 5.3 HIS 3D VDF RTN Transformation Results 138
Figure 5.4 HIS Coordinate Transformation Validation 139
Figure 5.5 Solar Orbiter Velocity Maps 141
Figure 5.6 Aberration Correction Calculation 142
Figure 5.7 Solar Orbiter Aberration Correction Maps 143
Figure 5.8 HIS Onboard VDF Data During CME Crossing 144
Figure 5.9 Summary of Heavy Ion Differential Streaming 148
Figure 5.10 Observations of Alpha-Proton Differential Streaming 151
Figure 5.11 O^{6+}-Alpha Differential Streaming Pearson Coefficients 153
Figure 5.12 First Observations of Oxygen 6+ to Alpha Differential Streaming 154
Figure 5.13 O^{6+}-Alpha Differential Streaming Time Series 155
Figure 5.14 O^{6+}-Alpha Differential Streaming – Positive vs Negative Distributions 157
Figure 5.15 O^{6+}-Alpha Differential Streaming – Field Angle and Secondary Population 160

Abstract

Time-of-flight (ToF) mass spectrometry is the culmination of decades of advancement in in situ plasma and radiation sensing technology. Many common versions employed today use an electrostatic analyzer to filter particles by energy-per-charge (E/q) before passing them into a ToF chamber to measure their velocity to produce mass-per-charge (m/q) spectra. However, more advanced designs include semiconducting energy detectors that give a third measurement (E/q, v, and E) to allow for the separation of spectra by charge. With proper discretization of the field-of-view, these so-called triple-coincidence ToF detectors provide a complete set of scientific information concerning particle populations in a plasma: their mass, charge, and velocity distribution functions (VDFs). With measurements of charge-resolved spectra and their VDFs a multifluid analysis of plasma can be performed in which the dynamic forces revealed within exhibit m/q dependencies. The ability to disassociate particles by charge and mass is the reason why triple-coincidence detectors are often referred to as heavy ion or composition instruments. Thus, they are unparalleled in their ability to identify plasma source regions and their initiation mechanisms. The deployment of charge-resolving ToF spectrometers to the interplanetary medium and planetary magnetospheres is necessary for answering many important science questions such as coronal heating and solar wind acceleration, the compositions of atmospheres and plumes of moons, the inflow and outflow rates and locations of magnetospheric plasma, and many more. We present the results of designing and assessing the performance of a SWaP (Size, Weight, and Power)-efficient charge-resolving time-of-flight spectrometer known as T-FIPS (Triple Fast-Imaging Plasma Spectrometer). The T-FIPS instrument is the result of minor modifications to the FIPS heritage design that flew onboard the *MESSENGER* mission to Mercury. The reduction of resource requirements and compact form factor make

T-FIPS ideal for swarm, constellation, or small probe-class missions that are envisioned for the next age in exploration of space plasmas. Our results include performance analyses of ion optical simulations using electrostatic and particle ray tracing models and engineering and design improvements using modern manufacturing techniques. Furthermore, we outline our ongoing efforts to purchase, assemble, and test the hardware for a T-FIPS prototype. We also present the results of the onboard calibration that produced data products for two plasma spectrometers: the Electric Propulsion Electrostatic Analyzer Experiment (ÉPÉÉ) that flew on the International Space Station (ISS) from March 2023 to 2024 and the Heavy Ion Sensor (HIS) that operated from January 2022 to April 2023 on the Solar Orbiter spacecraft. In addition to an overview of the cross-calibration and data product development for the ÉPÉÉ instrument we present the first results of its measurements of ions in the important top-side region of the ionosphere (~400 km). Afterwards, we describe the HIS 3D VDF calibration process for solar wind heavy ions before discussing the first results of 1-D differential streaming between the second (He^{2+}) and third (O^{6+}) most abundant ions of the solar wind. Collectively, these results demonstrate the importance of plasma spectrometers and charge-resolving time-of-flight detectors in particular for making continued scientific breakthroughs and discoveries over the upcoming decades in space exploration.

Chapter 1

Introduction

Humanity currently exists at a singular point in history that may be described, properly situated, and motivated as a critical period of the Early Space Age. Sixty-nine years ago, the first satellite was launched into orbit around Earth and four years later the first human being arrived in space. Since then, we have gone through varying degrees of commitment to space exploration and activity. The technology that enabled travel to space was first motivated by international rivalry to acquire access to unique vantage points (e.g., geostationary orbits, the lunar surface, etc.) before being driven by cooperative commitments to establish permanent presences aboard space stations. However, until recently the technology required for entry into space has been cost prohibitive and primarily limited to government agencies of nation states. Within recent decades the advent of global wireless telecommunications has opened space to commercial entities through frequent, reliable, and low-cost launch opportunities. The resulting effect was that the human psyche has been awakened to the limitless possibilities behind the commercialization of space and the feasibility of life beyond Earth.

In addition, the circumstances that created the current inflection point in the Early Space Age were arrived at through space exploration for its own sake. The government agencies that funded the otherwise unaffordable rocket launches were motivated by discovery, prestige, and unforeseeable future opportunities and had no immediate financial return to offset their costs. Agencies like the U.S. National Aeronautics and Space Association (NASA), precursors of the European Space Agency (ESA), and the

Soviet space program (later Roscosmos) first sent science missions into varying orbits about the Earth and Moon before adventuring into interplanetary space and other planetary environments. Predictably, the national and intergovernmental forays into space unlocked the commercial access of our current period through technological advancements and human understanding of what was previously unknown. Therefore, it was the motivation to explore the cosmos, create original scientific discoveries, and understand the universe through first principles that helped advance humanity into the current period of the Early Space Age. As true as it ever has been, discovery and technological advancement have generated the necessary context and possibility for unprecedented human productivity and potential for flourishing.

This research is embedded within the technology that unlocked the Early Space Age. Space detectors are the primary means of discovery for any space faring mission. In addition, they are the principal method of obtaining data and providing diagnostics for both commercial and science programs. The advancement of spaceflight detectors has coincided with the development of space launch vehicles and satellites; the first missions to space comprised simple cameras, radiation detectors, and radio transceivers to relay their data and commands. As technology progresses and mission profiles diversify (e.g., human habitation, mining, etc.) space detectors will nonetheless continue to assist with or primarily consist of mission payloads indefinitely. Space particle detectors play an important role in sampling the immediate in situ environment through or about which the space vehicle is travelling or resting. Knowledge of the particulate matter around the spacecraft unlocks information concerning their fluctuations in densities, speed, and the local natural processes occurring while also enabling mitigating actions during adverse conditions. The development of the capabilities, producibility, and requirements for space particle detectors will occur alongside all other technologies necessary for the advent and advancement of the Early Space Age.

Initial space particle detectors were unable to measure the type or composition of the atoms and molecules first discovered in space environments. In addition, they required high enough energies to induce sufficient electrical signal in premodern electronics. Later instruments were able to measure the lower energy or bulk plasma of space environs. However, it hasn't been until recent decades (e.g. AMPTE-CCE in 1984 or *Ulysses* in 1990) that instrument designs have developed enough that more diffusive species or matter of similar chemical structure are able to be disassociated from one another. The onset of particle composition measurements yielded startling discoveries that provided critical context for many regions of space (e.g., coronal charge states in the solar wind, chemical components of Enceladus' ocean world, etc.). Space particle detectors with the ability to measure composition are more complicated and have greater requirements than traditional detectors and as a result have been excluded from many science missions and nearly all commercial satellites to date. Thus, the purpose of this research has been to design and engineer a novel, resource-efficient composition detector for use in space that is comprised of known technologies established during the Early Space Age. The application of more space particle composition detectors through advancements in understanding, performance, and production will provide the development in technology necessary for continued progress during the Early Space Age.

Section 1.1 Scientific Background

1.1.1 History of Space Instrumentation

The history of spaceflight and space instrumentation go hand in hand. The first satellites launched into space (e.g., Explorer 1 & 3) carried simple science payloads designed to measure the radiation and micrometeorites in space. From the very onset of space voyages the types of questions that could be answered and the discoveries that could be made were limited by the technology available for each payload. The first detectors were Geiger-Müller counters that utilized secondary electron emission and electron avalanching to produce measurable pulse signals (see Figure 1.1). The sequence of pulses was

Figure 1.1 Explorer I and Instrumentation

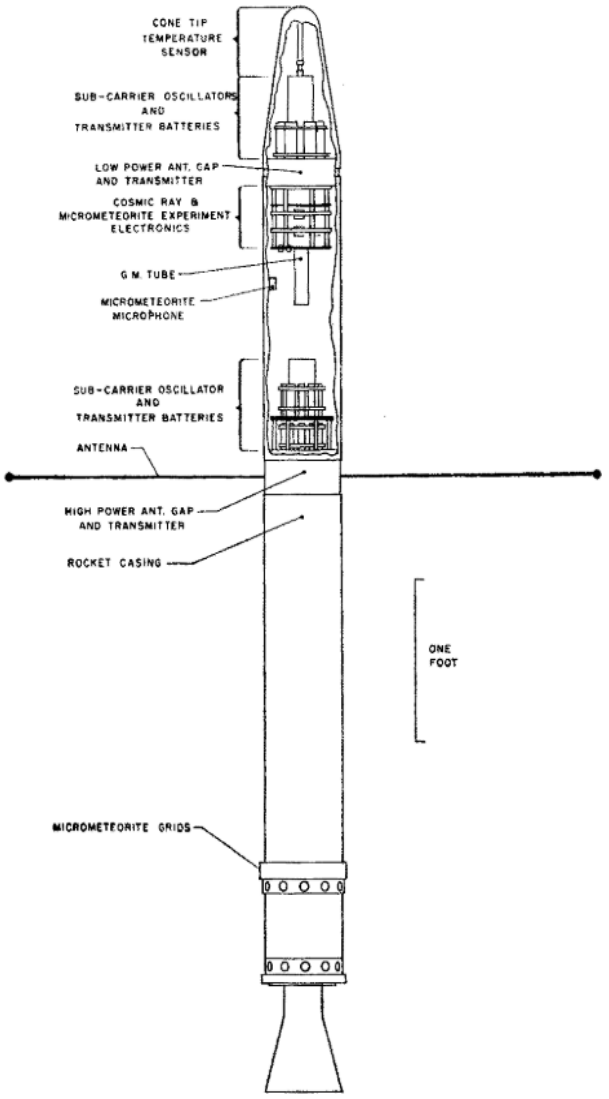

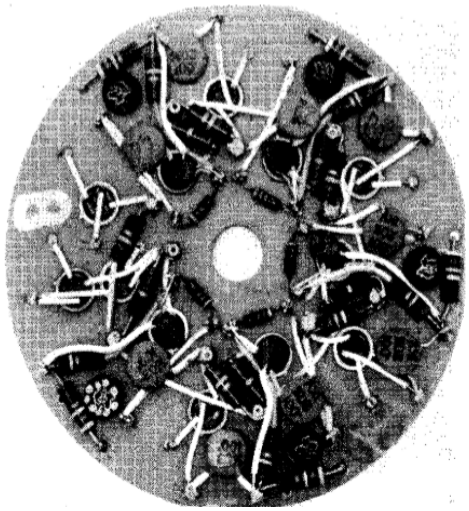

(**Left**) Drawing of Explorer I spacecraft with location of instruments. Initial payloads contained high energy Geiger-Müller radiation detectors and micrometeorite microphones. (**Above**) The electronics used for counting the pulses generated by the Type 314 halogen-quenched Geiger-Müller counters purchased from Anton Electronics Laboratories (Ludwig, 1959).

counted and the number of particles per second were determined. There were several drawbacks to these earliest detectors: (1) the necessary energy to trigger the detector was high above the thermal energy of ambient particle distributions and (2) the pulse heights produced were uniform in magnitude regardless of particle initial energy. Therefore, only the incident rate of energetic particles (> 100's of keV) could be counted and their individual energies were left unknown.[1] Consequently, only the cosmic rays and the

[1] Energetic particles (EPs) are commonly referred to as particulate radiation especially in terrestrial applications.

trapped radiation within the Van Allen belts were measured. Thus, from the inception of the Space Age our ability to learn and discover has been intrinsically limited by the capabilities of the detectors onboard.

The relationship between space instrument technology and what we know about and can achieve in space has continued throughout the Early Space Age to the present day. The Voyager Missions 1 & 2 visited the Outer Planets in the 1970's & 80's on their journey through the Solar System and beyond into the Interstellar Medium (Kohlhase & Penzo, 1977). The Low Energy Charge Particle experiments on both spacecraft continued to operate for nearly half a century until they were manually decommissioned over the past year (Krimigis et al., 1977; NASA Science Editorial Team, 2026). The particle sensors onboard the Voyager missions made many outstanding scientific discoveries while creating the first in situ measurements around several planetary magnetospheres. However, subsequent missions that have been envisioned to return to the Outer Planets were designed and motivated by what the Voyager missions and the LECP detectors were *incapable* of measuring (e.g., Cohen et al., 2023). Ultimately, the model for determining and enacting NASA science missions developed into the Science Traceability Matrix that matched outstanding science questions with instrument performance capabilities. Therefore, it was formally recognized and established that scientific discovery and technological achievement were inextricably linked. Ever since the most advanced space detectors have been proposed and constructed for the immediate use on the forthcoming science missions of any period. Examples of particle populations that often exist beyond the capabilities of standard payloads for most spacecraft missions today are low velocity particles with thermal energies below spacecraft potential, heavy ions with similar energy-per-charge (E_i/q_i) that require advanced spectrometers, and neutral particles that necessitate ionization prior to measurement. As such, it is incumbent for space instrument developers of the present day to continue advancing detector performances beyond current capabilities in order to persist in the process of scientific discovery and unlocking more regions of space for human development.

1.1.1.1 First Light in Space – Energetic Particles and Solid-State Detectors

The first particles measured in space were high energy or "energetic" particle (EP) populations (i.e., 100's of keV or more). The reason for measuring only energetic particles was that the initial instrument models that were deployed required a minimum energy threshold for detection that was well above average or bulk plasma energy distributions. The first U.S. satellites launched (i.e., Explorer 1 & 3) recorded particle measurements using Geiger-Müller counters (Van Allen, Ludwig, et al., 1958)(see Figure 1.1). These devices utilized steel tubes filled with inert gases and an electric potential applied across the two cylinder ends. When an energetic particle penetrates the chamber walls it ionizes the inert gas. The electrons liberated would energize through the electric field and strike more neutral gas particles. This process produces more electrons causing an avalanche or cascade to amplify the signal. The steel casing prevented the bulk plasma from entering the sensitive region in which detection occurs. In addition, the pulse heights were nearly uniform irrespective of inbound particle energy so that energy spectra of the EP distributions could not be analyzed. It was fairly quick (i.e., Explorer 4 & 6) that scintillator detectors were added to payloads to allow for the measurement of energy distributions (Rosen & Farley, 1961; Van Allen, McIlwain, et al., 1958)(see Figure 1.2). The plot in Figure 1.2 shows the count rate (counts per second) of the scintillator detector as a function of distance that were used on Explorer IV to measure the outer radiation belts from ~10,000 – 30,000 km above the Earth's surface. Due to the thick casing surrounding the detectors, only cosmic rays and the high energy particles of the radiation belts were measured. Scintillating detectors used for space applications are typically made of plastics and fluoresce when irradiated. The excited state of the lattice atoms release photons that are measured out using photodetectors resulting in pulse heights proportional to the irradiating particle's initial energy. As a result, the spectra of energetic particle populations were recorded. However, energy thresholds remained sufficiently high to prevent measurement of typical thermal particles, and lower energy limits remain a consistent problem in analyzing bulk plasmas to the present day.

Figure 1.2 Explorer VI Scintillator Detector

(**Top**) Picture of the first scintillator detector used in space that was flown onboard Explorer VI in 1959. Energetic particles are measured by causing the scintillator to fluoresce producing a measurable signal proportional to initial energy. (**Bottom**) Data collected of typical plasma energies in the outer Van Allen radiation belts (Rosen & Farley, 1961). The thick outer casings only allowed for high energy radiation to be detected.

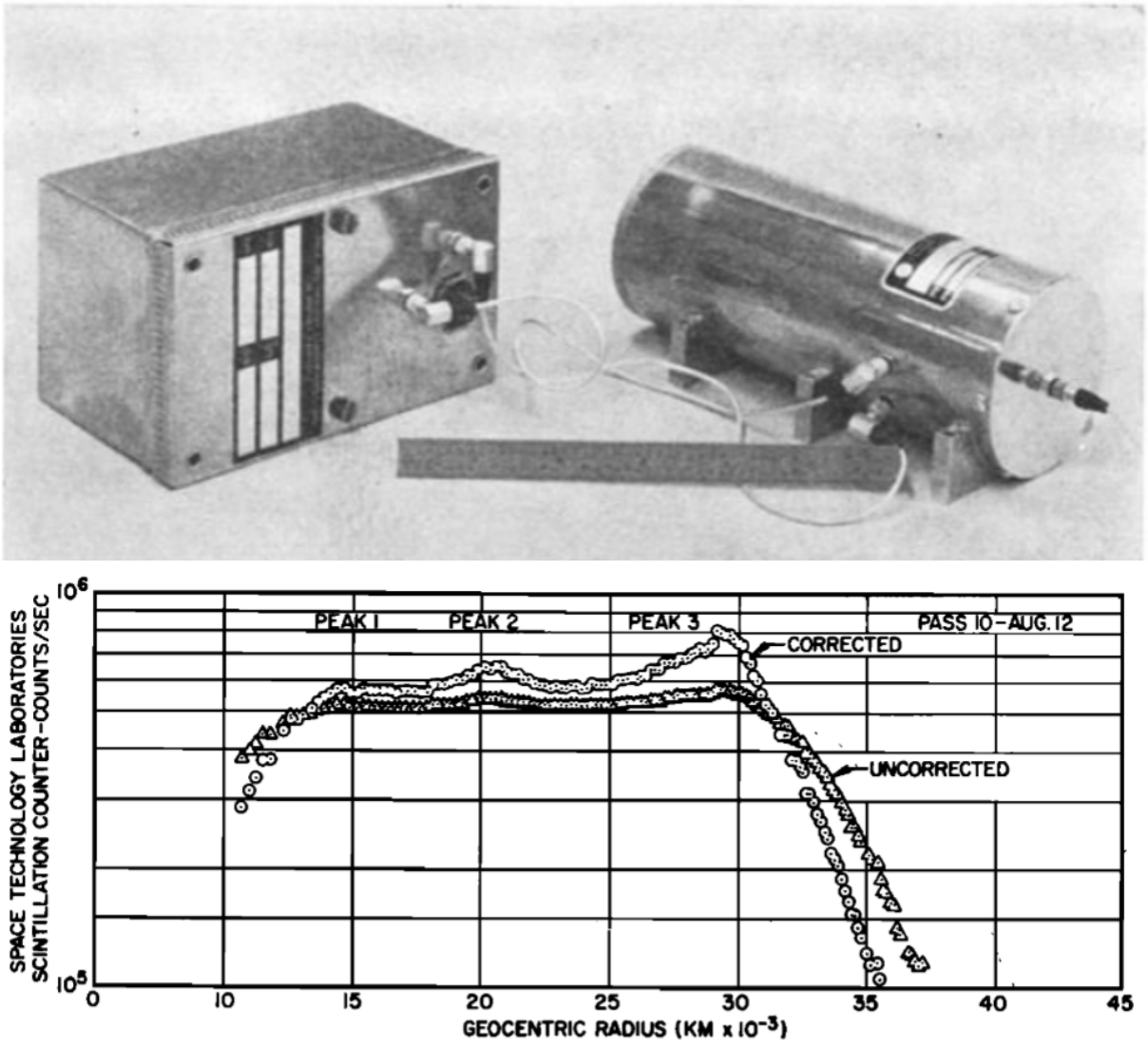

The next and most enduring advancement made in energetic particle detector technology came through the implementation of semiconducting solid-state detectors. Semiconductor radiation detectors operate similarly to scintillators in that the bombarding radiation exchanges energy with the lattice atoms. The difference between the two is that scintillating detectors produce excited states of electrons that generate light (i.e., scintillate) that is detected whereas semiconducting devices release electrons that migrate to the anode and are measured directly. Hence solid-state detectors (SSDs) have excellent energy

Figure 1.3 Early Spaceborne Solid-State Detectors

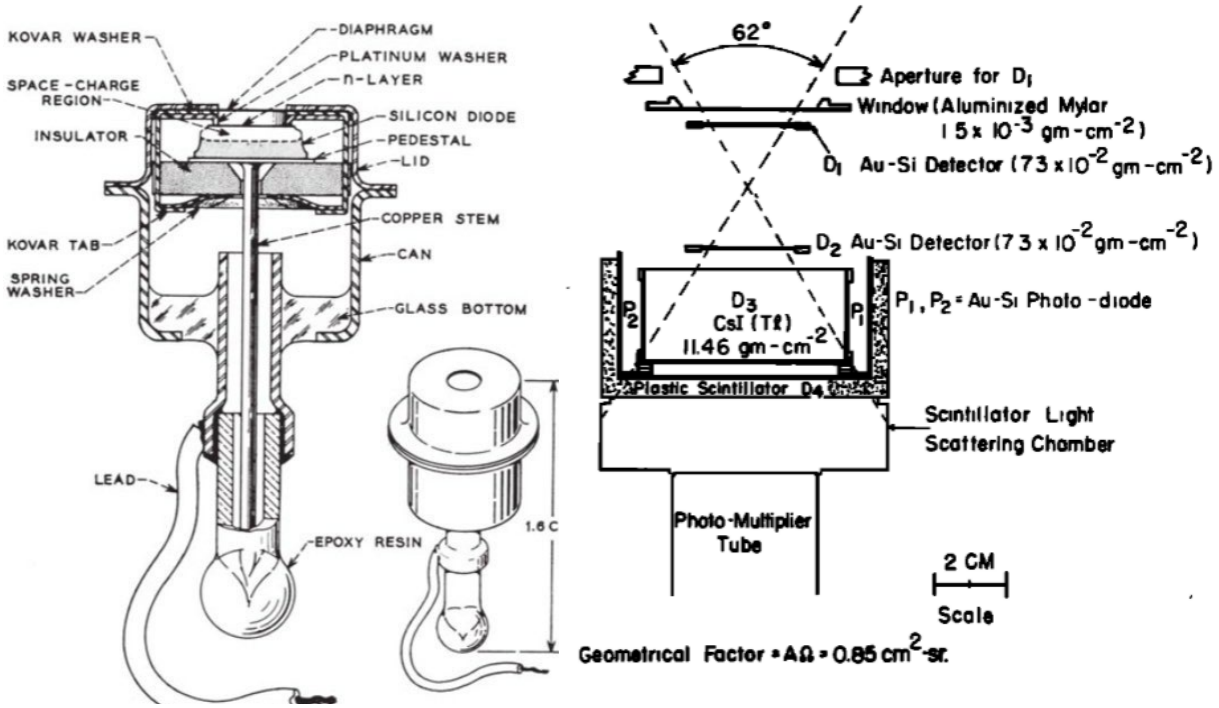

(**Left**) Simple, single waver p-n junction solid-state detector (SSD) flown on Explorer 12 in 1962 (Brown, 1965). (**Right**) Schematic for dE/dx particle telescope deployed on Explorer 18/IMP-1 in 1963 (Fan et al., 1965). The energy of ionization radiation passing through the stacked Au-Si detectors is transferred to electronic charge carriers and measured as a pulse using onboard electronics.

resolving power (e.g., Ipavich et al., 1978). The first SSDs deployed to space present in scientific literature were launched on the Explorer 15 and Telstar satellites (see Brown et al., 1963 for references to previous Air Force missions). They were used to measure energetic particles in the ring current in addition to the activity produced by the nuclear explosion detonated in the upper atmosphere on July 9th, 1962 (Brown, 1965)(see Figure 1.3). These first devices were simple single chip or wafer detectors mounted to face different directions on the spacecraft to provide information on particle trajectories. However, shortly thereafter the individual SSDs were stacked onto one another to create "charged" or "energetic particle telescopes" (Fan et al., 1965). Such SSD telescopes utilized the dE/dx method to determine the total particle energy as a function of penetration depth, and this method remains the most popular for producing energetic particle sensors today. In Figure 1.3 the earlier detector on the left utilizes

Figure 1.4 Early Spaceborne Faraday Cups

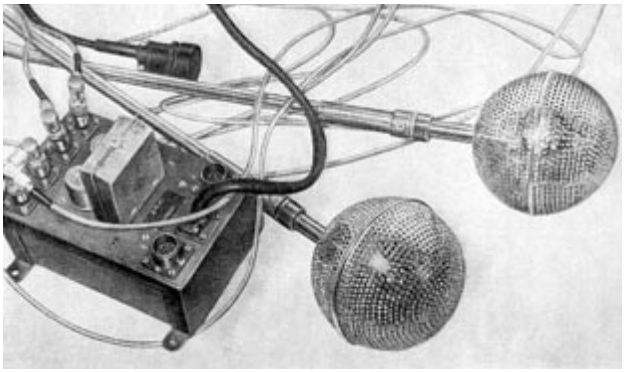

(**Left-Top**) Picture of spherical trap flown on Sputnik 3. (**Left-Middle**) Schematic of soviet style spherical ion trap (Gringauz, 1963). (**Right-Middle**) Schematic of faraday cups first flown on Explorer 10 (Bridge et al., 1960). The grids forming the retarding potential analyzers reject particles with energy lower than the applied potential.

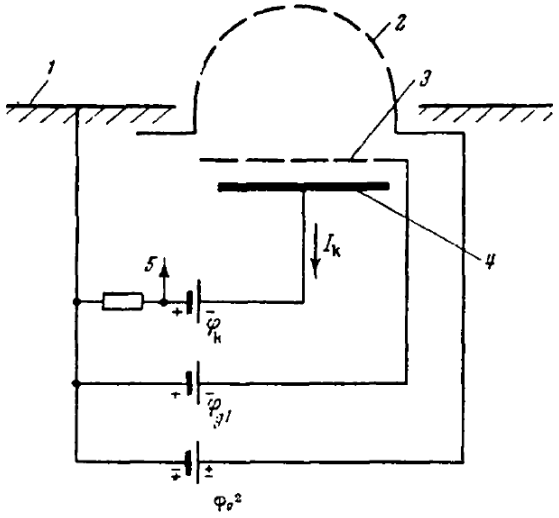

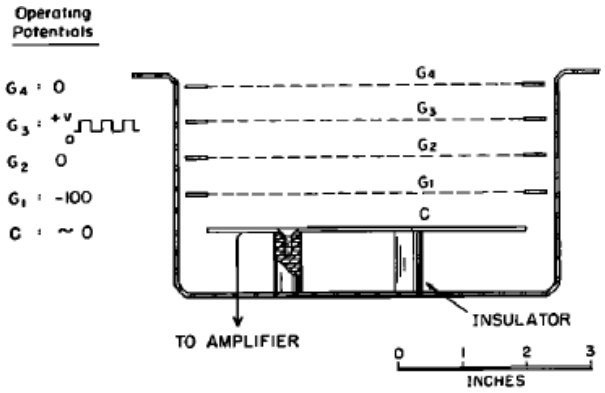

Fig. 1. Schematic representation of plasma probe.

only a single silicon diode wafer whereas the more advanced particle telescope on the right has stacked Au-Si wafers to allow for particle energy to measured by penetration depth.

1.1.1.2 First Light in Space – Ambient Plasma and Electrostatic/Magnetic Analyzers

The ambient thermal charged particles that comprised the bulk plasma of most space environments were not measured until the advent of spaceborne mass spectrometry. The initial NASA bulk plasma detectors were faraday cups that were modeled after the spherical ion traps used by the Soviet program to make the first plasma measurements in space (Bridge et al., 1960)(Gringauz, 1963)(see Figure 1.4). The faraday cup comprises conducting plates used to measure plasma that may utilize apertures or segmented anodes to determine directional information. The schematics in Figure 1.4 were drawn for the first faraday cups flown in space and depict high voltage grids as dotted lines placed in

front of the anode to prevent particles with insufficient velocities from entering. However, the energy spectrum delivered by the HV grids known as retarding potential analyzers (RPAs) utilized at the entrance aperture to filter particles were restricted in range – a limitation in their design that exists to the present day. Without curving the trajectory of the particle during filtration the k-factor or ratio of the operating voltage to the particle energy that passes through is unity (i.e., 1 kV applied to the grids rejects plasma below 1 keV). Due to the speed of the measurements recorded, faraday cups are still employed with great effect on spacecraft in the present day. Yet, most designs continue to filter particles with RPAs making their use case for plasmas > 10 keV/e impractical. An advancement in technology was necessary to extend the energy range of detection.

The next step in space particle instrumentation and knowledge of space plasmas came with the introduction of magnets and electrostatic analyzers (ESAs)(Figure 1.5). Both magnets and ESAs curve the particle path through the analyzer allowing for higher energies to be recorded. For magnet analyzers this was accomplished with permanent or electromagnets and for ESAs the same effect was induced using electrodes. Moreover, in contrast to RPA faraday cups the energy of the particle that passed through a magnet or ESA is restricted by both an upper *and lower* bound. For permanent magnets this resulted in a fixed energy passband; their use and the use of electromagnets as space plasma spectrometers quickly declined in the Early Space Age. Thus, for the ESAs that continue to be employed voltage stepping was utilized to provide intersecting passband measurements to cover the extended thermal (i.e., suprathermal) energy range they permit. Electrostatic analyzers were launched onboard the Explorer 12 and Mariner II missions (Bader, 1962)(Neugebauer & Snyder, 1962). The ESAs deployed made many of the first reliable measurements of the solar wind confirming theories predicting solar wind ubiquity and terminal velocity (i.e., solar wind vs breeze) while also providing the first observations of the fast and slow mind modes and the intermittent presence of alpha particles in significant abundances (Neugebauer & Snyder, 1962). The first ESA models were cylindrical and spherical deflector types and measured particles as a current using anodes – later models employed continuous and discrete electron multipliers (EMs) and

microchannel plates (MCPs) to allow for single particle analysis and studies of sparse, tenuous plasmas (Evans, 1965; McIlwain, 1960; O'Brien et al., 1964). Through the introduction of ESAs and spaceborne mass spectrometry the composition and suprathermal energy range of space plasmas could begin to be explored.

Over the subsequent decades two major improvements were made in the design of electrostatic analyzers to further their performance capabilities. The first was a modification of the spherical deflector

Figure 1.5 Electrostatic Analyzers and Magnets

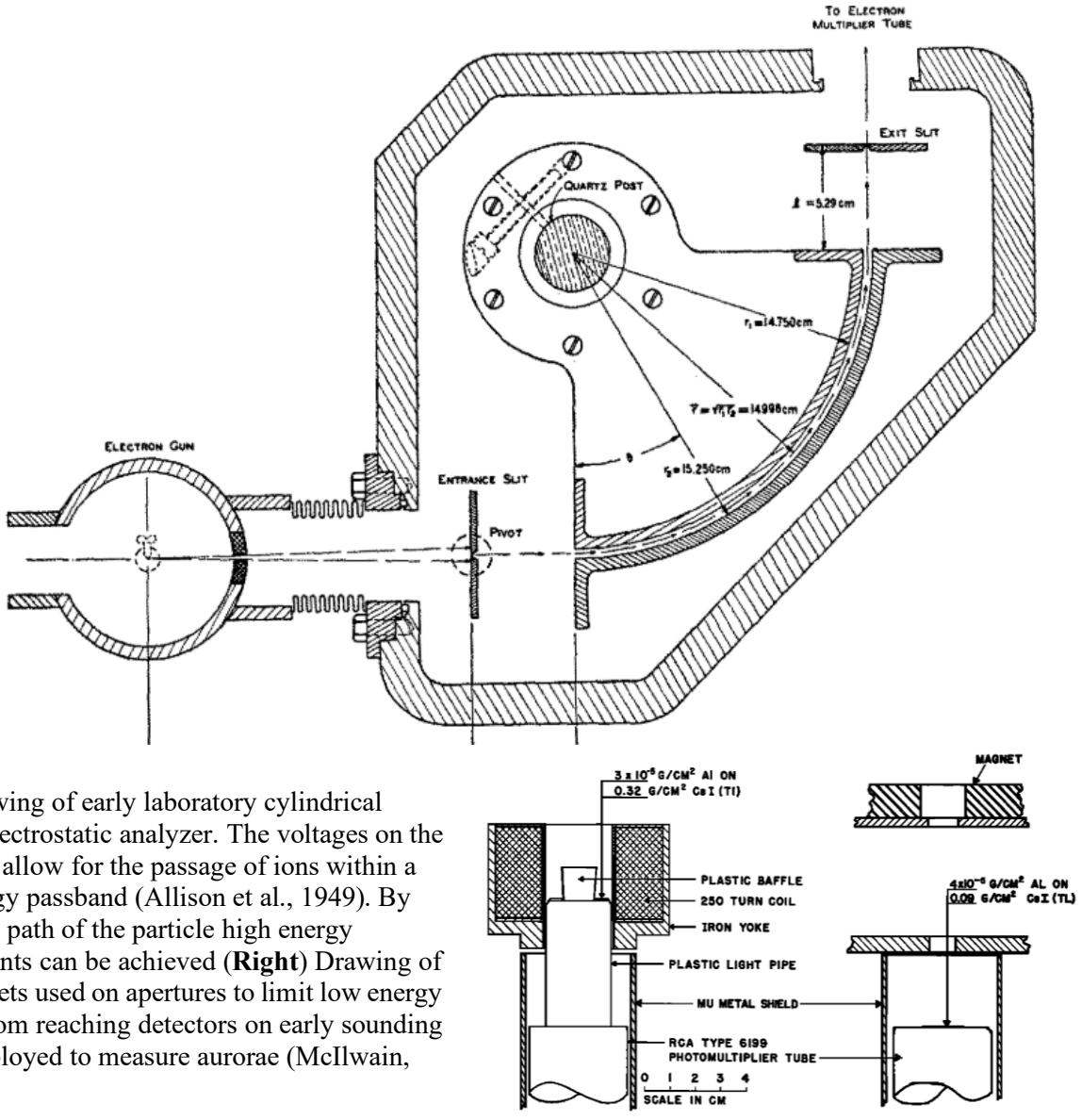

(**Top**) Drawing of early laboratory cylindrical deflector electrostatic analyzer. The voltages on the plates only allow for the passage of ions within a select energy passband (Allison et al., 1949). By curving the path of the particle high energy measurements can be achieved (**Right**) Drawing of early magnets used on apertures to limit low energy particles from reaching detectors on early sounding rockets deployed to measure aurorae (McIlwain, 1960).

type ESA was made to create the toroidal analyzer (Ewald & Liebl, 1955; Young et al., 1987). The spherical deflector ESA achieves double focusing properties when the internal cavity through which the particle travels is extended to 180°. The exiting plasma beam then nominally travels normal to the exiting surface indefinitely. The establishment of toroidal analyzers allowed for the double focusing of the outbound particles onto a surface point at any distance. The capability of focusing on separate planes became valuable for combining electrostatic analysis with further mass spectrometry techniques prior to final detection. For example, see the advanced time-of-flight system utilized with a toroidal analyzer on the IMS instrument used for the *Cassini* mission to Saturn in the bottom image Figure 1.6. Next was the introduction of the top-hat design that enabled particles to enter from both opposing sides of the spectrometer to allow for a simultaneous field-of-view (FOV) of 360° about a single axis (Young et al., 1988) – this expanded view is contained within the plane coming in and out of the page in the top diagram of Figure 1.6. The introduction of top hates came at the cost of reducing the length of particle's path through the analyzer thereby degrading the resolution with the tradeoff of faster or more complete measurements of the night sky. The most common models of ESAs deployed on spacecraft today utilize spherical and toroidal top hat analyzers to measure high resolution spectra of the thermal and suprathermal particle populations.

1.1.1.3 1.1.1.3 First Light in Space – Plasma Composition and Time-of-Flight Chambers

The next development in space plasma research came from the study of plasma composition or the disassociation of the types of particles during measurement. The shift in scientific attention towards the composition of the ambient thermal plasma came through further advances in spaceborne mass spectrometry.[2] The initial deployments of magnets and ESAs allowed for the analysis of particles via

[2] The study of the composition, or charge-state and mass spectrum, of *energetic* as opposed to plasma particles in space mostly continues to remain outside the scope of the present-day technological capabilities, beyond the successful use of the pulse height defect in solid-state detectors. This is due to the high voltages/strong magnets required to curve their trajectory.

Figure 1.6 Advances in Spaceborne Electrostatic Analyzers

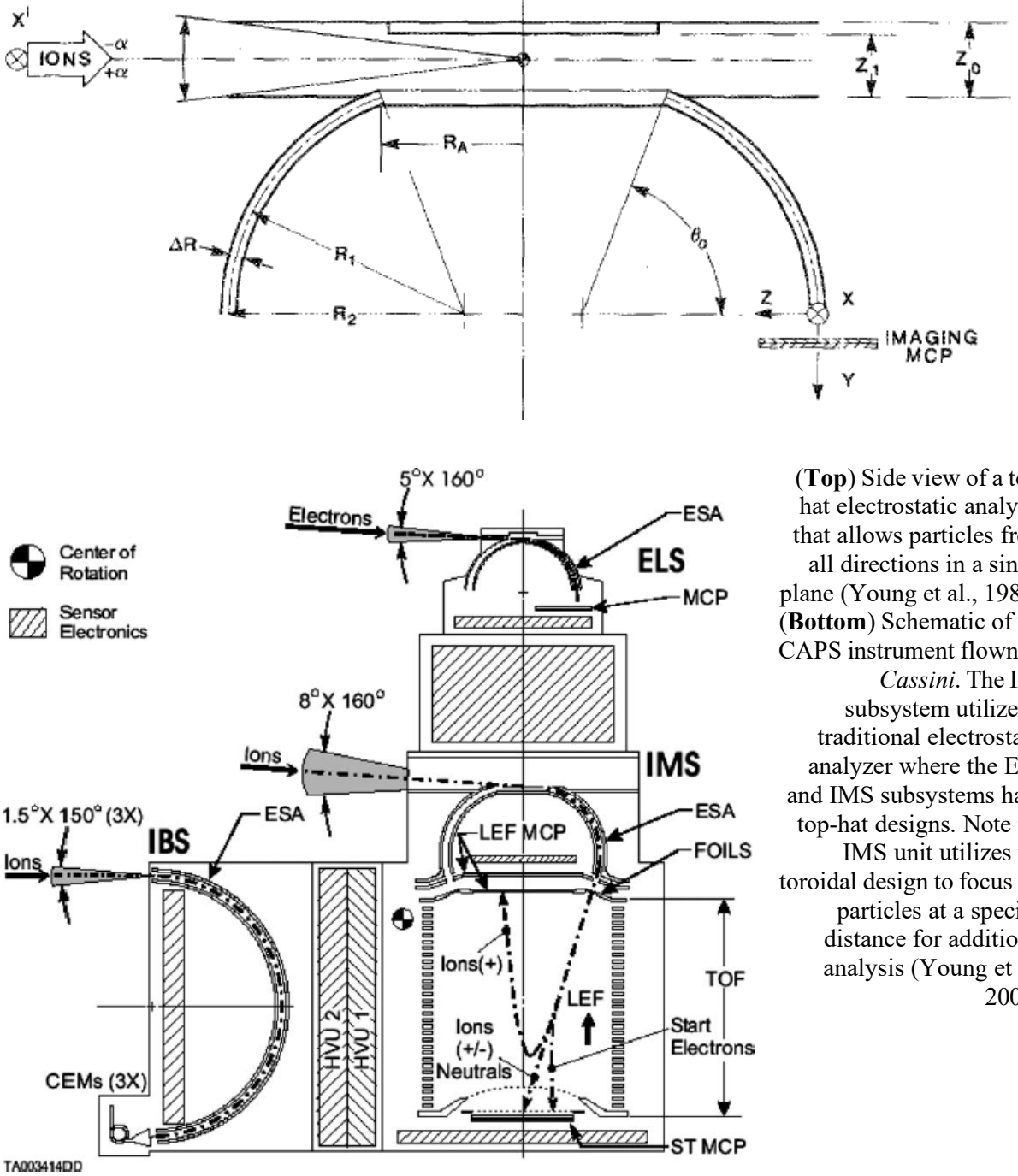

(**Top**) Side view of a top-hat electrostatic analyzer that allows particles from all directions in a single plane (Young et al., 1988). (**Bottom**) Schematic of the CAPS instrument flown on *Cassini*. The IBS subsystem utilized a traditional electrostatic analyzer where the ELS and IMS subsystems have top-hat designs. Note the IMS unit utilizes the toroidal design to focus the particles at a specific distance for additional analysis (Young et al., 2004).

their energy-per-charge (E_i/q_i). This meant that the species of particle could only be inferred by assuming distributions shifted in the energy spectrum comprised different particles moving with approximately similar velocities (e.g., Neugebauer & Conway, 1962). Thus, alpha particles were understood to be infrequently present in considerable abundances at approximately the same speed as protons because of their shift in energy due to increased mass. Similarly, the presence of various oxygen charge states, the

third most abundant element in the solar wind, were inferred shortly thereafter (Bame et al., 1968). However, for further investigation of heavy ions, analysis using energy-per-charge (E_i/q_i) alone would not be sufficient.

The in-depth exploration of heavy ions and study of advanced plasma composition came through a paradigm shift in technology. The first measurement of trace signatures of heavy ions in the solar wind came through extended exposure to foils deployed to the lunar surface during the Apollo program (Geiss et al., 1970)(see Figure 1.7). Once returned to Earth the foils were heated, and the released particles were analyzed through advanced terrestrial mass spectrometers. It was later understood by the same laboratories that the passage of particles through carbon foils produced electrons that could be subsequently measured. In result, the notion of a second coincidence or additional detection of a single particle came to the attention of space scientists (e.g., Gloeckler, 1990; McComas et al., 2004), and the time-of-flight chamber was successively developed and deployed into space to measure the velocity of particles. A time-of-flight (ToF) chamber operates by passing the particle through a foil ejecting one or more electrons upon exit that are directed toward the first coincidence detector to produce a start signal. The particle undergoing analysis is deposited onto another second coincidence detector placed at a known distance away to produce a stop signal. Thus, the passage of the particle across the chamber is clocked and the velocity is determined. Some modern uses of ToF chambers in energetic and suprathermal detectors employ only the chambers themselves (e.g., Mason et al., 1998; Rodríguez-Pacheco et al., 2020). That being said, most chambers in use today are coupled with an electrostatic analyzer to preliminarily filter particles by E_i/q_i. The following velocity measurement of the particles allows for the identification of the mass-per-charge of each particle measured.

$$\frac{EE_{ii}}{qq_{ii}} \div \frac{vv_i^2}{2} = \frac{\boldsymbol{mm_{ii}}}{qq_{ii}}$$

Figure 1.7 Foil Exposure to the Solar Wind

Picture taken by Neil Armstrong of Edwin "Buzz" Aldrin deploying the foils used to collect solar wind ions for further analysis upon return to Earth. The long exposure times allowed the heavy ions to become embedded in the foil later to be released when heated (NASA Photo S11-40-5872).

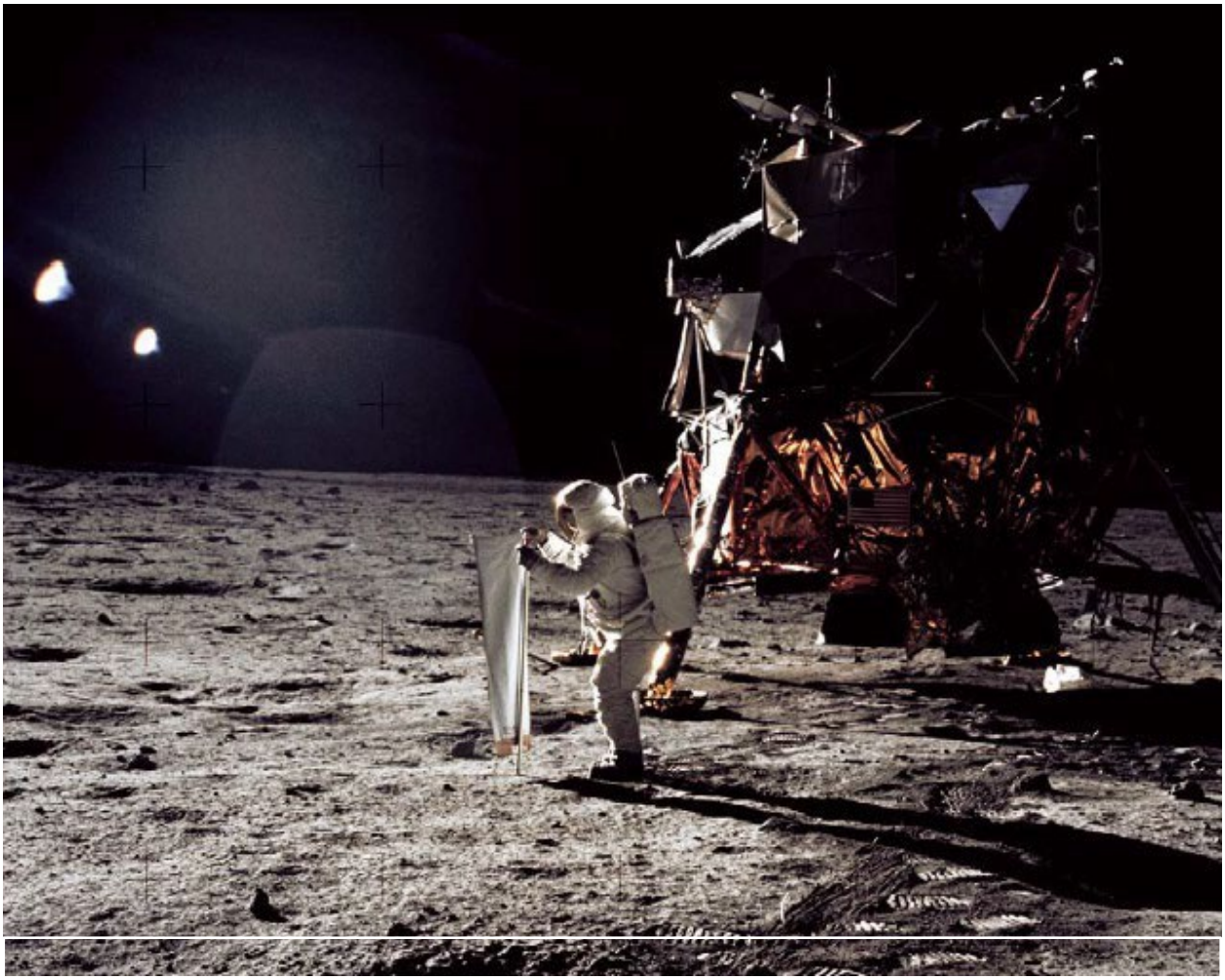

Here E_i is the kinetic energy of the particle, q_i is the charge, v_i is the velocity, and m_i is the mass. The advent of the time-of-flight chamber to spaceborne mass spectrometry provided considerably more ability to differentiate particles through the introduction of a second measurement and the subsequent recording of an additional physical characteristic of the particle. Although the necessary inference of particle charge still remained necessary it became easier for space scientists to identify various ion and neutral atoms within diverse space plasmas. The next generation of instruments that led decades of solar wind and planetary exploration were time-of-flight mass spectrometers that made unprecedented discoveries

through analysis of space plasma composition (e.g., Lepri et al., 2013; Raines et al., 2015; Waite Jr et al., 2006; Zurbuchen et al., 2016).

Through additional modifications made to time-of-flight chambers, both the charge and mass of an individual ion came to be measured separately. In particular, a third coincidence was added to measure an additional parameter. The most common method for recording a third coincidence using ToF mass spectrometers is to add a solid-state detector (SSD) for the final particle measurement. This relatively simple modification is made possible because deposition of the particle produces secondary electron emission from the detector surface. The emitted electrons are redirected to a third detector to make the stop signal (see Figure 1.8). Altogether, the particle's presence is detected three times from (1) electrons emitted during passage through a carbon foil, (2) the particle striking the SSD, and (3) electrons emitted from the SSD surface. The availability of a third coincidence results in unparalleled signal-to-noise ratio; penetrating radiation that enters the chamber at off angles to strike a single detector is easily eliminated (Gilbert et al., 2014). Critically, the addition of the SSD yields a third physical parameter.

$$EE \div \frac{EE}{qq_{ii}} = \boldsymbol{qq_{ii}}$$

$$\frac{EE}{qq_{ii}} \div \frac{vv_i^2}{2} = \frac{mm_{ii}}{qq_{ii}} \times qq_{ii} = \boldsymbol{mm_{ii}}$$

Therefore, the particle species may be unambiguously identified without the need for any inferences made on the type of particles in a given space environment. Finally, through such charge-resolving composition instruments the full complement of physical parameters became available for physicists to study space plasmas. The first advanced plasma composition instruments that utilized triple-coincidence ToF detectors were deployed on the AMPTE-CCE (Explorer 65) mission in 1984 – see in particular the CHEM and MEPA instruments (G. Gloeckler et al., 1985; Mcentire et al., 1985)(see Figure 1.8). The

Figure 1.8 Space Plasma Composition Measurements

(**Top-Left**) Schematic of the CHEM instrument – the first to be flown in space with a time-of-flight chamber. (**Top-Right**) The unprecedented charge state data of oxygen distributions measured by the CHEM instrument (G. Gloeckler et al., 1985). (**Bottom**) Large region of plasma within a coronal mass ejection containing low-charge state heavy ions believed to be the cold plasma trapped within a solar filament prior to eruption (Lepri & Rivera, 2021).

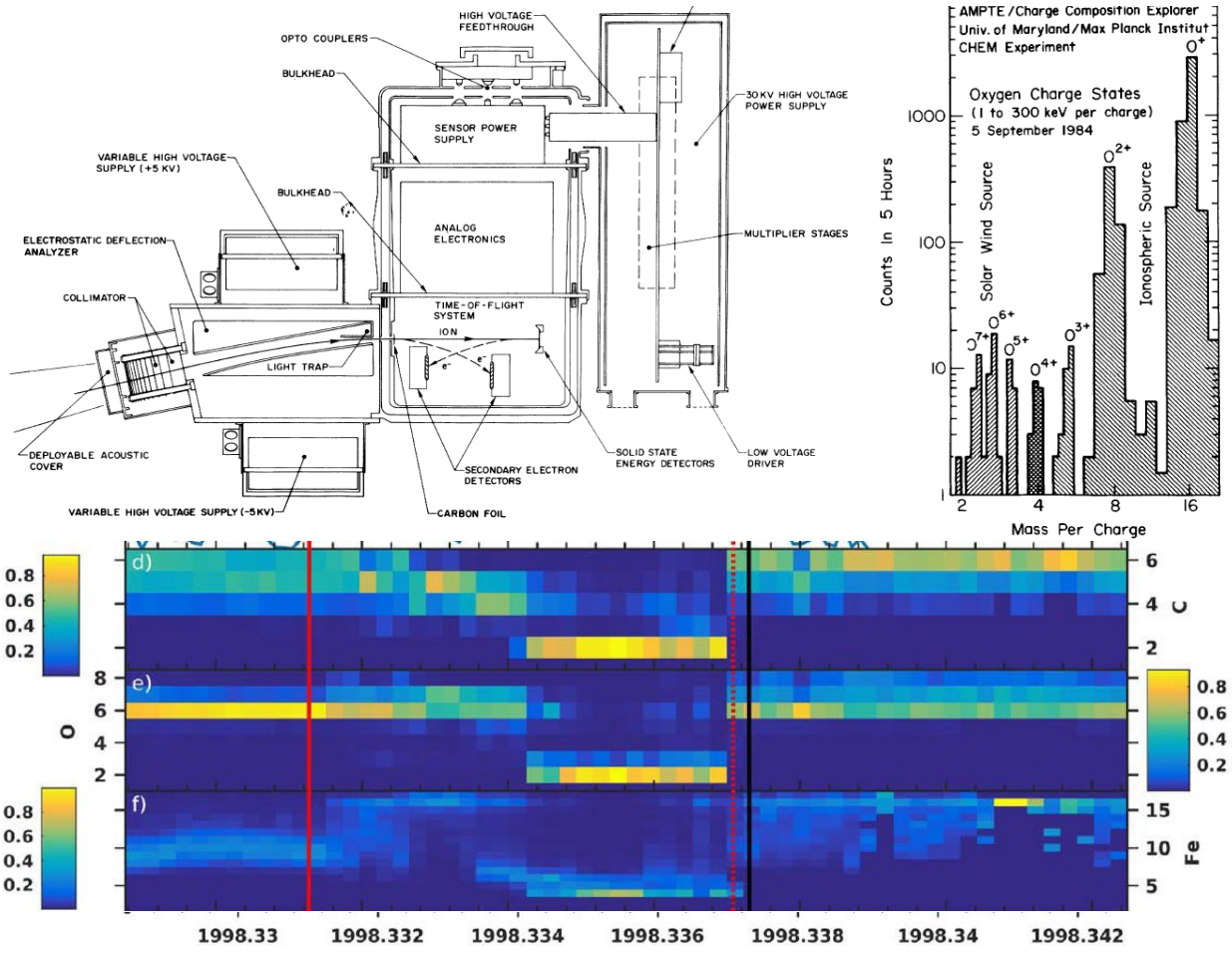

AMPTE-CCE mission released tracer gases (i.e., lithium and barium) from a secondary satellite at various points in the magnetosphere to become ionized by natural physical processes and measured by the heavy ion sensors onboard the second spacecraft thereby elucidating the topology of Earth's magnetosphere (Krimigis et al., 1982). As can be seen by Figure 1.8 in the top right plot, the accumulated measurements of different Oxygen charge states enabled the determination of plasma source identification from ionosphere upwelling (low charge states) and solar wind cusp insertion (high charge state) during a geomagnetic storm. Subsequently, the Solar Wind Ion Composition Spectrometer (SWICS) instrument

was designed and developed for three separate missions (i.e., *Ulysses* in 1990, *Wind* in 1994, and the Advance Composition Explorer in 1997) making it arguably the most successful charge-resolving ToF mass spectrometer to the present-day (G. Gloeckler et al., 1995; J. G. Gloeckler et al., 1992). The bottom plot in Figure 1.8 depicts the time series measurements of heavy ion charge states during a CME crossing. The period of noticeable decrease in charge states is the result of the passage of an intact solar filament containing plasma with charge states frozen in at lower temperatures. The use of triple-coincidence spectrometers in space has resulted in major breakthroughs in space science such as the identification of magnetospheric plasma sources (i.e., ionospheric loss versus solar wind), solar filamentary material embedded in the magnetic clouds of coronal mass ejections, and the location of heavy ion depleted plasmoids in slow solar wind (Colón-Rodríguez et al., 2025; Lepri & Rivera, 2021; Lepri & Zurbuchen, 2010; Weberg et al., 2012; Zhao et al., 2022).

Our understanding of the local space environment has evolved with the technology that enabled it. The initial forays into space in the late 50's and early 60's were limited in their capacity to measure charged and neutral particles and therefore by necessity our scientific inquiries were equivalently limited in scope. Eventually our ability to explore space and learn about the natural phenomena and dangers present within grew as our technological assets were developed. This is the fundamental process by which advancements are made in space science and therefore develop our understanding of space. The generation of technological development will be in compact designs that enable multiple spacecraft to make spatially separated synchronous measurements. The swarm or constellation missions will combine measurements from multiple observatories and provide the first measurements of the realtime mesoscale structure of the solar wind and planetary environments. Advancements in scientific knowledge continue as they have throughout human history, namely, after the observational discovery of previously unknown phenomena. As long as we remain a space-fairing people the exploration of space will always comprise the technological advancement of spaceborne detectors and their deployment to new regions.

1.1.2 Space Plasma Composition

The vast majority of space and the universe are comprised of plasma. Plasma is the most energized state of matter in which the kinetic or thermal interactions are sufficiently powerful to decompose atoms into a mixture of charged and neutral particles. It is separate from energetic particles (EPs) or radiation in that its thermodynamic traits (e.g., density, bulk velocity, temperature, etc.) define or dominate the ambient physical properties of a particular region. Plasma composition is the study of the type or species of charged and neutral particles within a plasma. In the deep space of magnetospheres and the interplanetary medium, plasmas are primarily composed of negative electrons and positive ions; neutral matter densities vary with proximity to planetary surfaces and boundaries with the local interstellar medium (Rubin et al., 2019; Schwadron et al., 2018; Swaczyna et al., 2020; Szabo et al., 2023; Vorburger et al., 2013). Additionally, the charged ions primarily exist in elemental monoatomic states i.e., H^{+}, $He^{1\text{-}2+}$, $C^{1\text{-}6+}$, $O^{1\text{-}8+}$, $Fe^{1\text{-}26+}$, etc.[3] Therefore, in effect the study of deep space plasma composition is the measurement of positively charged elemental atoms.[4] As previously mentioned it has been a relatively simple matter to measure the hydrogen and helium atoms that often comprise most ions in typical space environments – the finescale kinetic structure of their behavior is actively pursued by many space plasma physicists through turbulence research to this day. However, the measurement of the heavy ions is a relatively unexplored area of study for deep space plasmas and contains significant potential for scientific discovery.

A heavy ion has more measurable features than a simple proton and such characteristics provide considerably more information about the plasma in which the ion resides. When a heavy ion is born from

[3] By convention, X^{n} indicates element or molecule *X* has charge *n* determined by the number of electrons removed or gained.

[4] There are differences between deep space plasma and those close to neutral bodies. Plasma composition close to exospheric planetary surfaces can contain negative cations (e.g., the Moon). In addition, at higher pressures molecules can form before becoming ions or cations (e.g., OH^{-}, H_2O^{+}, NH_4^{+}, CH_4^{+}, etc.). Such regions typically require separate instrumentation (e.g., quadrupole, gas chromatograph) to measure plasma composition.

a neutral atom it has a specific number of electrons stripped away that become its charge state. The number of electrons stripped away is directly proportional to the energy released by the physical process that produced the ion: the more violent (i.e., hot or impulsive) the event the more electrons are liberated from the atom (see Figure 1.9). For example, an Oxygen atom has eight electrons with eight distinct ionization potentials that are necessary to overcome in order to remove an additional electron. Thus, the removal of each electron from an Oxygen atom gives a precise indication of the energy contribution that was achieved in the plasma generation event. Every atomic element has its own identifiable ionization potential, i.e., quanta of energy necessary to produce an ion. Therefore, measuring the charge states of

Figure 1.9 Ionization Potentials

Oxygen Ionization Potential	Energy (eV)	Temperature (K)
1st	13.61	105,198
2nd	35.12	271,459
3rd	54.94	424,657
4th	77.41	598,338
5th	113.9	880,386
6th	138.12	1,067,594
7th	739.29	5,714,319
8th	871.41	6,735,536

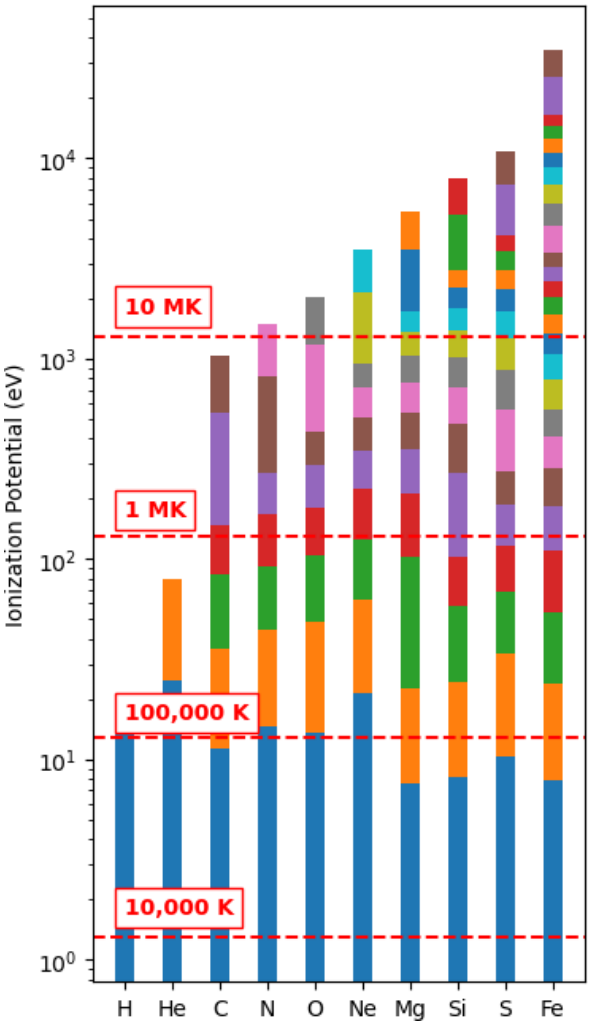

(**Above**) Oxygen ionization potentials and their corresponding energies converted to temperatures. (**Right**) Ionization potentials for the major heavy ions in the solar wind converted into cumulative temperatures. Using spectroscopy (remote) or heavy ion spectrometry (in situ) temperatures of regions can be measured.

Figure 1.10 Solar Wind Frozen Charge States

(**Left**) Plot from the original Hundhausen et al., 1968 paper that outlined the necessary conditions in the corona to preserve ion charge state shortly after acceleration. The freeze in distance is the crossover between expansion and recombination time scales. (**Right**) Modern study performing the same calculations for a variety of solar wind ions and their charge states (Gilly & Cranmer, 2020).

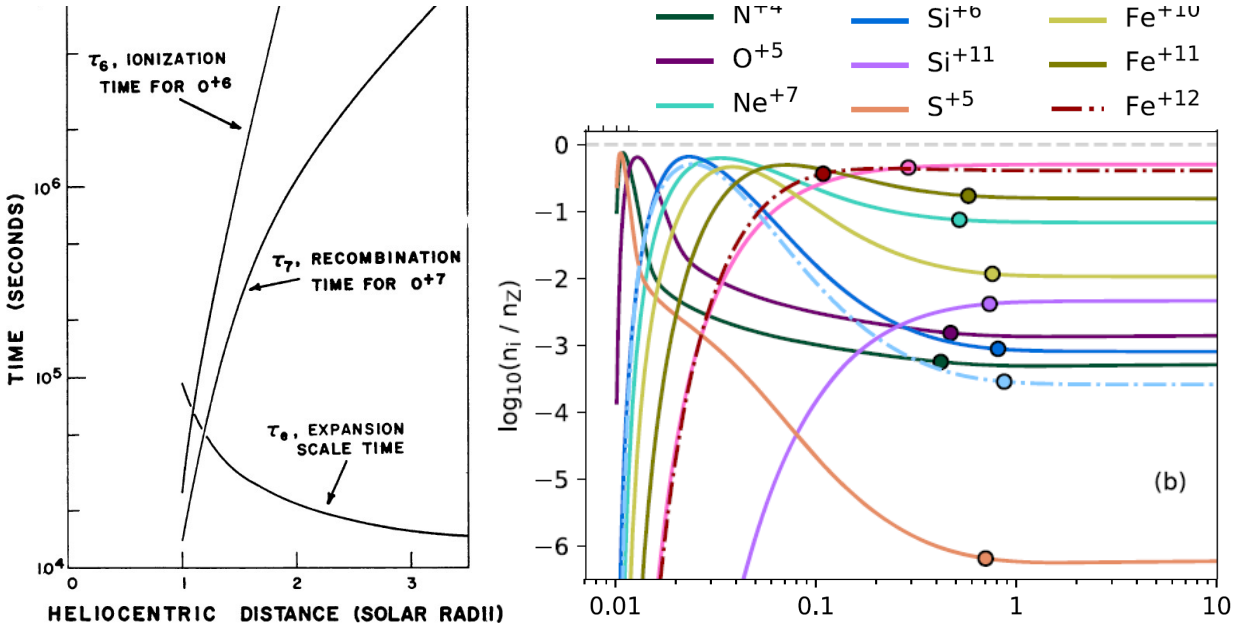

heavy ions within a plasma yields a panoply of information about its thermodynamic state or erupting process.

Fundamental to the study of plasma composition was the development of the frozen charge state theorem (Gilly & Cranmer, 2020; Hundhausen et al., 1968) This was the realization that the collision frequency between electrons and ions in deep space is sufficiently low enough to preserve the ionization state for extended durations. Without the occurrence of collisions recombination is suppressed and the charge state of heavy ions become "frozen in." In consequence, it is presumed that for most deep space plasmas that measuring the charge state of a heavy ion contains the preserved information that was imprinted by the physical process from which it was created. In Figure 1.10, the left plot is from the original paper that determined the expansion rate of solar wind plasma leaving the corona exceeds the recombination time between ions and electrons thereby freezing the charge state. The right plot uses the

same physics to predict the freeze in location of multiple heavy ions and their charge states. Additionally, the mass or species of the heavy ion is equivalent to the neutral matter from which it was generated providing another indication of source location of the plasma. For example, the abundance of a heavy ion measured in situ may be compared with the abundance of neutral matter species in various local source regions measured remotely to identify the point of origin. Thus, the higher mass and charge state values of heavy ions yield critical plasma source identification techniques made available through plasma composition measurements.

Furthermore, measuring the kinetic properties of heavy ions provides advanced information concerning the fundamental physical processes occurring in situ, or within the immediate environment of the spacecraft. The most commonly occurring processes are plasma-wave interactions that are governed by the Lorentz force equation:

$$FF_{ii} = mm_{ii}aa_{ii} = qq_{ii}\left(\vec{EE} + vv_{ii}^{\rightarrow} \times \vec{BB}\right)$$

In this equation F_i is the force exerted on the particle, a_i the resulting acceleration, and $\vec{E}$ and $\vec{B}$ are the electric and magnetic fields, respectively. Once the mass-per-charge of the heavy ion is known, measuring its kinetic properties yields information concerning the dynamic forces at play. More explicitly, if the velocity, mass, and charge state of the ions in a plasma can be determined then the electromagnetic processes that accelerate them become recognizable.

$$aa_{ii} = \frac{qq_{ii}}{mm_{ii}}\left(\vec{EE} + vv_{ii}^{\rightarrow} \times \vec{BB}\right)$$

For this reason, the detection of heavy ions provides the most scientifically relevant information when the trajectory of the particle is recorded. The equivalent is not true for single fluid, or mono-composite plasma, or of a plasma that was comprised of ions with a single mass per charge (e.g., He^{+}, C^{3+}, Ne^{5+} have

Figure 1.11 Wave-Particle Interactions

Plot of data taken by the plasma and fields instruments on the Juno mission orbiting Jupiter. The first and final three plots show the magnetic field strength, change, and frequencies, respectively. The second and third plot demonstrate the clear increase in electron energy as the waves and particle couple through resonance. The fifth, sixth, and seventh panels show the change in pitch angle, or the angle between the particle's gyromotion and magnetic field, that occurred simultaneously with the energy transfer (Daly et al., 2023). Note: it is much easier to detect electrons on the fast, kinetic timescales necessary to produce results of unambiguous particle-wave interactions demonstrated here.

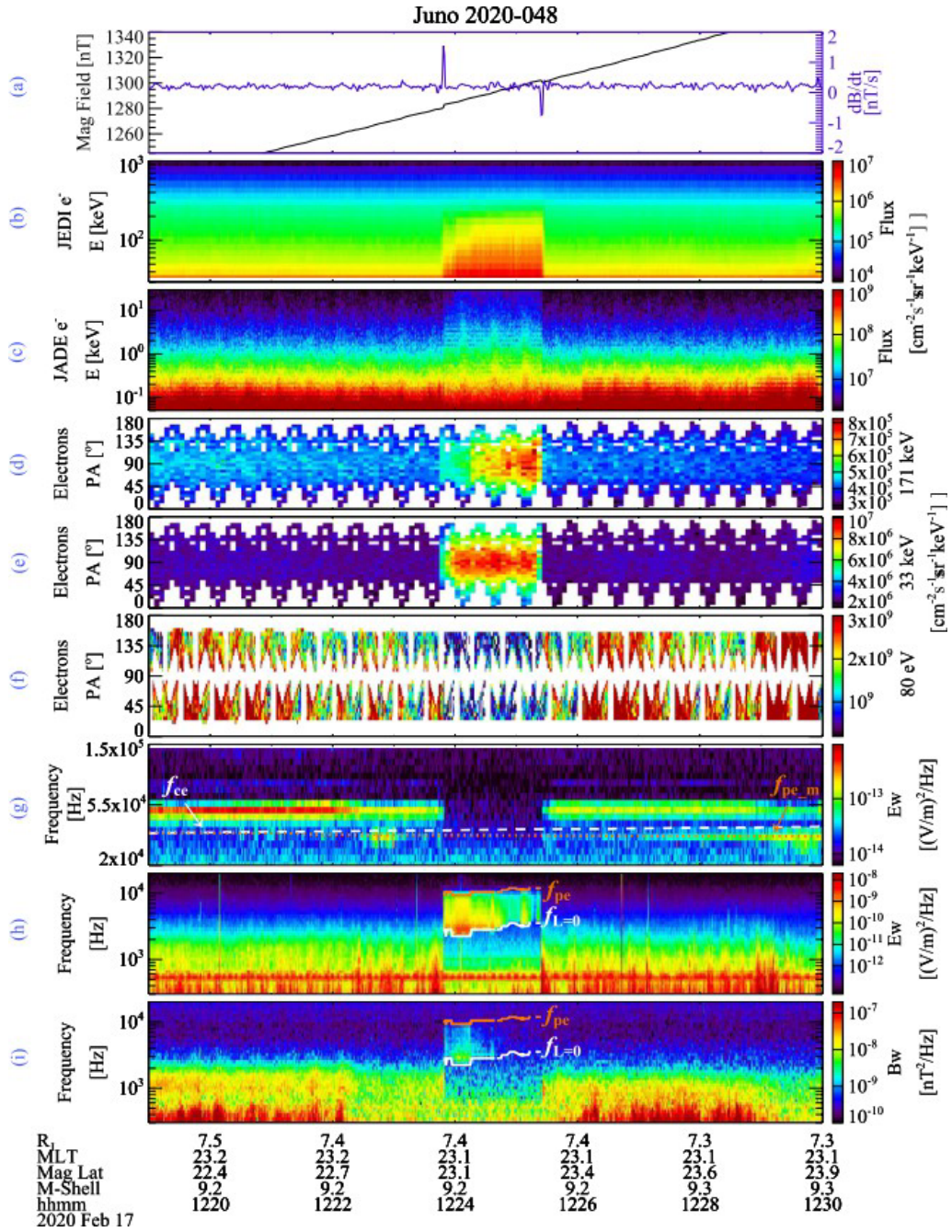

q_i/m_i = 1/4.). When the three-dimensional velocity distribution functions (3D VDFs) of heavy ions are properly measured, pertinent information relating the transfers of energy between plasma and fields is revealed. Figure 1.11 contains plots demonstrating particle-wave resonance and energy transfer occurring at Juno, albeit with the easier to detect electrons.[5] The top plot shows the magnetic field strength and the bottom three plots show the spectra of traversing waves with the electron cyclotron and plasma frequency plotted as lines. The increase in energetic electrons (second and third plot) and particles with pitch angles perpendicular to the field (fourth and fifth plots) occurs during the passage of the waves indicating energization through particle-wave resonance coupling. If similar data were collected for heavy ions the resonance frequency would be determined by the mass-per-charge of the ion producing a chorus of energy transfers at different frequencies. Thus, similar to the way frozen in charge states of different heavy ions provide multiple diagnostics for plasma source energization mechanisms, measuring the kinetics of multiply charged heavy ions provides a manifold of information by which we may learn how plasma-wave interactions occur.

1.1.2.1 The Solar Wind

The interplanetary medium is one of the two deep space environments readily available for scientific exploration through in situ plasma measurement. The solar wind is the supersonic plasma that outflows from the Sun to fill interplanetary space. It is primarily composed of ionized hydrogen, or protons, mixed with varying degrees of low abundances in helium (1 – 10% by mass)(Bame et al., 1968; Neugebauer & Snyder, 1962; Wolfe et al., 1966). The remaining 1% or less is comprised of heavier ions. In particular, the most common heavy ions in the solar wind and their relative abundances are Oxygen (O, ~42%), Carbon (C, ~24%), Nitrogen (N, ~7%), Neon (Ne, ~7%), Silicon (Si, ~7%), Iron (Fe, ~7%), and

[5] Since electrons are the only negatively charged particle in most plasma environments and have dramatically reduced masses that yield significantly different energies at equivalent speeds to heavier particles it is much easier to separate and measure them. Thus, electron detectors typically enjoy much faster time cadences.

Figure 1.12 Solar Wind Heavy Ions

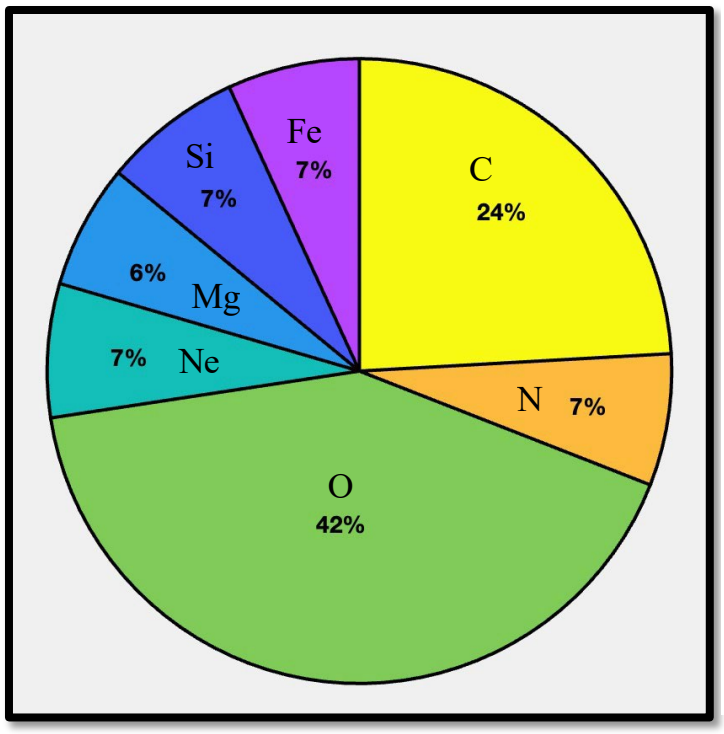

The relative abundances of the remaining ~1% of heavy ions in the solar wind after hydrogen and helium. Summed over two decades of data collected by the ACE SWICS instrument. Oxygen and carbon are the next highest in abundances and, with their heavier masses and more available charge states, make excellent diagnostics of originating coronal temperatures. Received from correspondence with Susan Lepri.

Magnesium (Mg, ~6%)(private communique, Susan Lepri)(see Figure 1.12). It has been established that the average charge states of the heavy ions found in the solar wind closely match those visible through spectroscopy within the solar corona (Asplund et al., 2021). These charge states indicate anomalously high coronal temperatures, the source of which remains a major outstanding question in solar physics to this day. The lowest visible surface of the Sun is the photosphere and is cooler (~5,700 K) than the solar atmosphere making it primarily composed of neutral matter. The photospheric matter is energized into a charged plasma and drawn upwards into the chromosphere and transition region through which the temperatures rapidly increase. Moreover, the resulting incredible pressure difference between the heated plasma of the solar corona and the surrounding interstellar space is the longstanding justification for the supersonic outflow of the solar wind (Parker, 1958). By studying in situ plasma composition emitted from the solar atmosphere we can hope to discover information concerning the underlying physics that produces the solar wind.

Figure 1.13 Solar Wind Speed and Charge Student Abundance

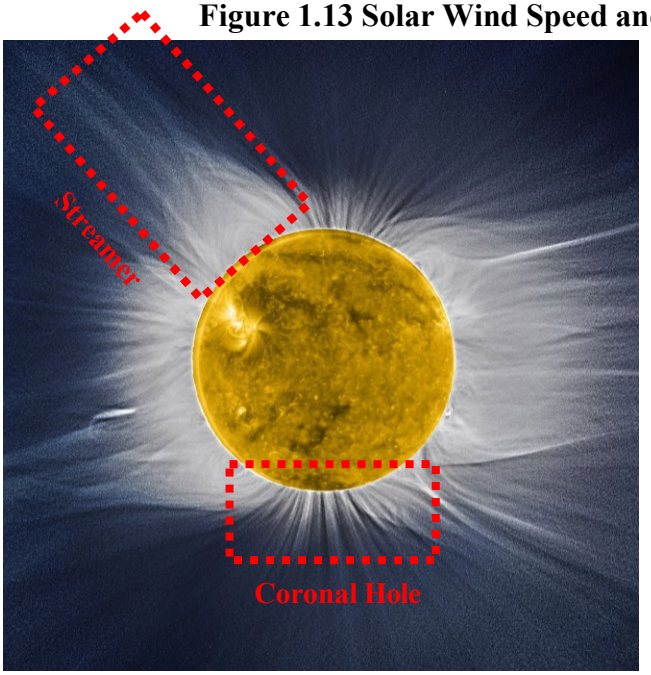

(**Left**) Image of the solar corona during an eclipse with a picture of the Sun taken at the same time overlaid. The poles are dominated by large coronal holes with plumes of fast wind emerging. The long stalk and tendril-like structures are helmet streamers and pseudostreamers which are a potential source of the slow solar wind (Poletto, 2015). (**Below**) data taken from the ACE SWICS and Solar Orbiter HIS instruments demonstrating the clear negative correlation between solar wind speed and the charge states of heavy ions contained within (Livi et al., 2023).

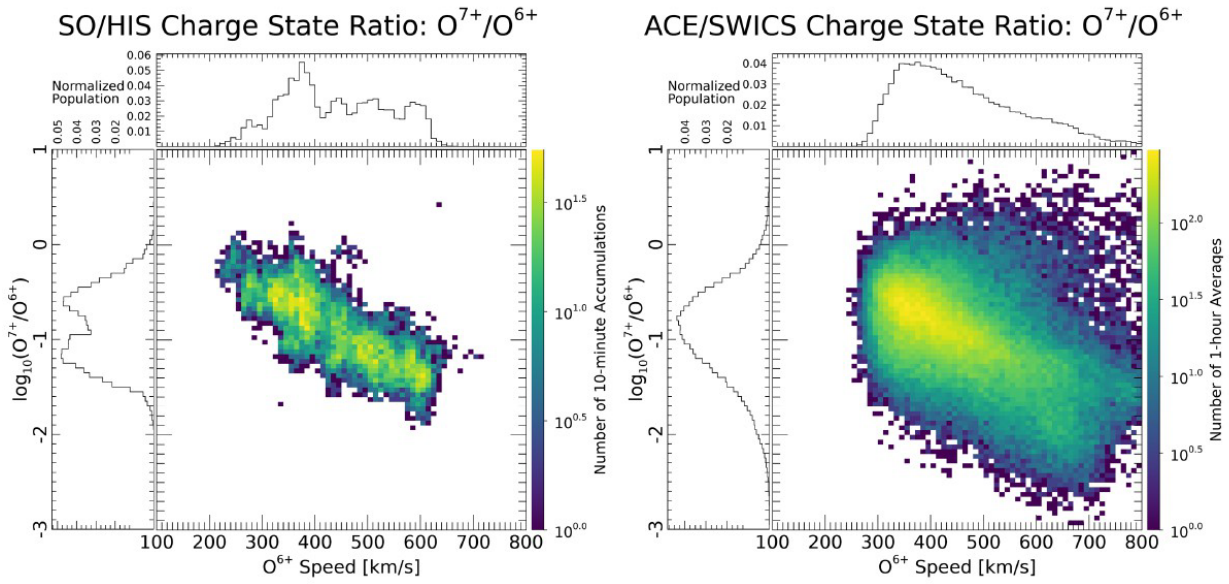

There are at least two distinct types of solar wind: the slow (~250-450 km/s) and fast wind (~450-800 km/s). The fast wind is more well understood; it is a more stable, diffuse, and heated plasma when compared to the slower wind modes. Through a combination of remote sensing and variations in situ measurements of plasma traced back to regions of the solar atmosphere we know that the fast wind comes from deep within coronal holes where plumes are seen to stream directly out from the photospheric surface (Krieger et al., 1973; Nolte et al., 1976; Poletto, 2015). Coronal holes are regions of open

magnetic field lines that stretch out into interplanetary space with no known connection point back to the solar surface. In top picture in Figure 1.13, the coronal holes appear at both poles and show plasma streams coming from lower altitudes. It is believed that it is a consequence of the fast wind plasma being emitted from the cooler photosphere that the heavy ions measured within have lower average charge states when compared to the slow wind (Alterman et al., 2025; Landi et al., 2012; Lepri et al., 2013). The lower temperatures result in the removal of less electrons before being accelerated into interplanetary space where the charge states become fixed or frozen. This can be seen in the bottom plots of Figure 1.13 with data collected from two separate missions showing that higher charge states (i.e., more O^{7+} than O^{6+}) occur at lower ion speed and decreases at higher velocities. In contrast to the fast wind is one or more types of slow wind. The reason the slow wind is more enigmatic than the fast wind is because of two factors: (1) It is highly variable meaning it fluctuates in physical parameters such as density, composition, and alfénicity.[6] (2) The source region(s) of the slow wind has not been determined with a high degree of confidence. Indeed, the slow wind becomes consistently cooler and denser about Heliospheric Current Sheets (HCS) where the magnetic polarity in the solar wind reverses. At solar minimum, the HCS can be reliably associated with helmet streamers that encircle the solar equator. Helmet streamers are regions of the Sun where closed magnetic field lines connected to the surface reverse in polarity to create a current sheet (seen as large bulbs that taper and stretch to high altitudes in the top image of Figure 1.13). At solar minimum when the helmet streamers are stable about the equator, the coronal holes coalesce into large structures at the poles and wind speed is reliably determined by heliolatitude: the slow wind is found to come from regions close to the solar equator, and the fast wind comes from the solar poles. However, as the Sun moves towards solar maximum the polar coronal holes are fractured into smaller components that move slowly toward the mid latitudes and eventually the equator before disappearing. In addition, at solar

[6] Alfvénicity is the degree to which velocities correlate with magnetic field parameters such as the alfvén speed or the presence of perturbations such as alfvén waves. The fast wind is always highly alfvénic whereas the slow wind may or may not be. The name comes from Hannes Alfvén (1908-1995) the discoverer of alfvén waves and founder of magnetohydrodynamics (MHV).

maximum pseudostreamers appear and multiple HCS can be found – the source of the fast and slow wind become intermixed and difficult to distinguish from one another.[7] For these reasons and many more scientists have proposed that there may be more than one source region for the slow wind. Examples include helmet streamers, active regions, coronal hole boundaries, and the "quiet Sun," or regions with normal levels of activity (Brooks et al., 2015; Crooker et al., 2012). Through decades of improvement in observations our current understanding of the solar wind has slowly coalesced; however, conclusive evidence to its ultimate cause remains elusive.

The physical mechanisms that transfer and heat the plasma from the photosphere and chromosphere into the corona are still hotly contested. One leading theory for solar wind acceleration is interchange reconnection (Fisk, 1996; Fisk et al., 1999; Fisk & Schwadron, 2001). Theories that employ interchange reconnection describe the solar wind plasma being first trapped along closed field lines connected to the solar surface (see Figure 1.14). Motion of the field lines causes an interaction between the closed field line carrying trapped plasma and an open field line with opposite polarity that is stretched out into interplanetary space. When the open and closed field lines interact through magnetic reconnection one leg of the closed field line is reconfigured to become an open field line and the plasma parcel is released as the solar wind. For fast wind, interchange reconnection theories describe the closed field lines as deep within coronal holes, shorter in length, and released on quick timescales (Feldman et al., 2005). Therefore, the heavy ions are trapped in cooler regions for shorter and more consistent durations. This explains the stable in situ measurements of heavy ions with lower charge state distribution in the fast wind. In contrast, the slow solar wind is believed to come from plasma trapped on closed field lines that are longer and arcade higher up into the chromosphere and corona. This plasma is heated to much higher temperatures but released intermittently as plasmoids. Thus, the slow solar wind is highly

[7] Pseudostreamers appear similar in images to helmet streamers in remote sensors but are associated with closed magnetic field lines with the same polarity and should therefore not be capable of producing current sheets.

variable containing alternating regions of sparse and dense plasma with differing charge states but higher on average. In addition to interchange reconnection, alfvén wave heating is a successful and widely accepted theory for solar wind acceleration (Alfven & Lindblad, 1947; Del Zanna & Velli, 2002; Osterbrock, 1961). Theories utilizing alfvén wave heating as a source mechanism describe the motion of magnetic field lines at the surface as creating turbulent waves that propagate up and down along the field lines scattering off one another (see Figure 1.15). This turbulent behavior creates intense heat when the energy is exchanged to the plasma particles, and is believed to be the source of the solar corona's anomalously high temperatures. It is important to note that interchange reconnection and alfvén wave heating theories both presuppose the motion of magnetic field lines along the solar surface as the instigating mechanism for generating the solar wind. Therefore, the ultimate source of solar wind acceleration is generally accepted by many to be the solar wind dynamo or the mechanism by which magnetic fields are generated and dragged along by convection and the Sun's rotation. Both interchange reconnection and alfvén wave heating have remote and in situ observations supporting their claims (Bale

Figure 1.14 Interchange Reconnection

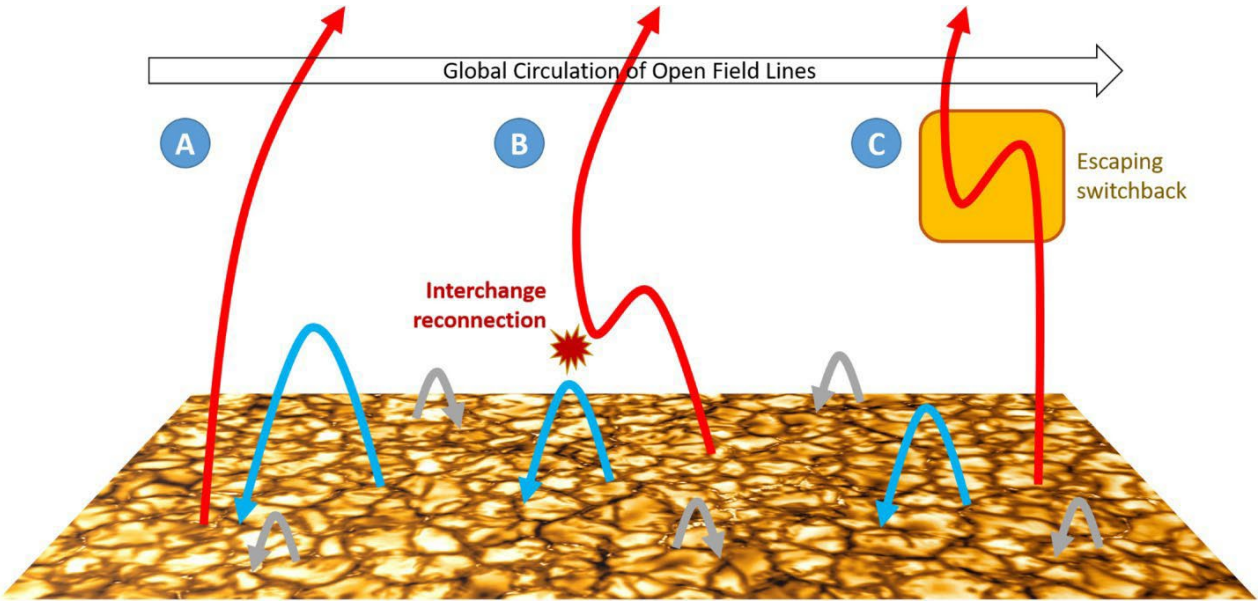

Depiction of how interchange reconnection produces the solar wind. Close magnetic field lines of opposite polarity engage with open magnetic field lines. The base of the open field line becomes the foot of the closed loop and the plasma trapped on the previously close magnetic field line becomes released (Fisk & Kasper, 2020).

et al., 2023; Drake et al., 2023; Kasper et al., 2019). However, in situ plasma composition experiments in the solar wind that would utilize differences in the behavior of heavy ion charge state to determine modes of acceleration have been limited, and explorations close to the Sun or using multipoint sampling are rare or non-existent. Thus, measuring the heavy ions of the solar wind is a key method for determining the anomalous heating of the solar corona and the acceleration mechanism(s) of the solar wind.

In situ measurements of solar wind plasma have revealed kinetic behavior that is alluring and perplexing. The solar wind proton distributions exhibit extreme temperature anisotropies that were first

Figure 1.15 Alfvén Wave Heating of the Corona

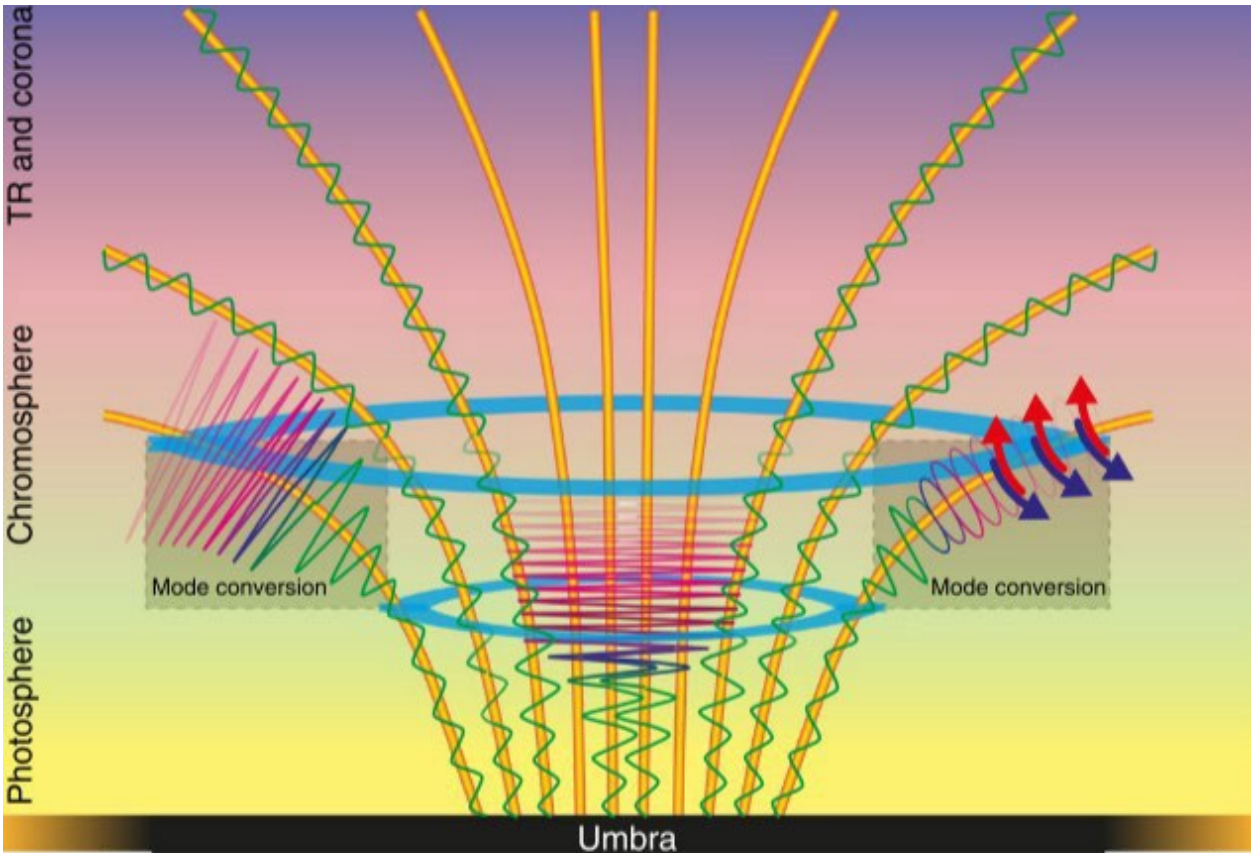

Drawing of how alfvén waves are believed to heat the solar corona to the incredibly high temperatures known through spectroscopy. The motion of the photospheric plasma below carries the magnetic field lines creating waves through their motion. The acoustic waves are eventually converted into alfvén waves that ultimately couple with the plasma to generate the significant heat necessary to produce the solar wind (Grant et al., 2018).

discovered by the Helios 1 & 2 missions in the late 1970's and early 1980's (Marsch et al., 1982). In Figure 1.16 are different contour maps produced from the measurements of solar wind proton velocity distribution functions (VDFs). Along the x-axis is the particles velocity measured in the radial i.e., pointing awa from the Sun, the y-axis is the perpendicular velocity, and the projection of the magnetic field vector is indicated using a dashed line. In both the fast and slow wind, there are secondary proton populations that stream out ahead at a faster speed. The secondary proton beam is always field aligned with a density depression in velocity space that separates the primary and secondary populations and is often referred to as the "heat shoulder."[8] However, in the slow wind around the HCS the secondary proton population becomes a well-defined, cold beam that can even exceed the nominal speed's distribution in density. The Parker Solar Probe (PSP) mission has made important advances in our understanding of proton populations through elliptical orbits with extreme perihelion (~9 solar radii) close to the solar surface. The measurements made by the SPAN-I instrument on PSP have revealed strong anisotropic heating in the faster, secondary field-aligned population known as "hammerheads" during the presence of waves (Verniero et al., 2022)(circled in grey in the right plot of Figure 1.16). The hammerhead heating is dubbed as such because its effect is to spread the velocity distribution perpendicular to the magnetic field.[9] Additionally, the rapid incarnation of a secondary, field-aligned cold beam next to the HCS has been interpreted to indicate the presence of magnetic reconnection (Desai et al., 2025, 2026). These examples of recent discoveries in the plasma kinetics of solar wind protons have revealed exciting new phenomena for study – however, our observations of such behavior have primarily been limited to the protons. The measurements that we do have that extend the mass or species beyond the proton distribution are mainly limited to the helium particles; they are still no less puzzling. The helium atoms travel reliably faster than the proton distributions despite their increased mass and the

[8] Field-aligned distributions are frequently referred to as a "parallel" temperature anisotropy (heating occurs parallel to the magnetic field).
[9] Hammerheads and similar features are known as perpendicular temperature anisotropies due to their orientation with the magnetic field.

Figure 1.16 Solar Wind Proton Velocity Distribution Functions

Plots of velocity distribution functions (VDF) of proton populations in the solar wind. (Left) Measurements taken by the Helios missions in the late 1970's and 80's. The countours signify density in phase space density. They show the field aligned anisotropies streaming along the direction of the magnetic field (black line) and the perpendicular heating occurring in the opposite direction (Marsch, 2006). (Right) Discovery of hammerhead distributions with the advanced instrumentation available onboard Parker Solar Probe (Verniero et al., 2022).

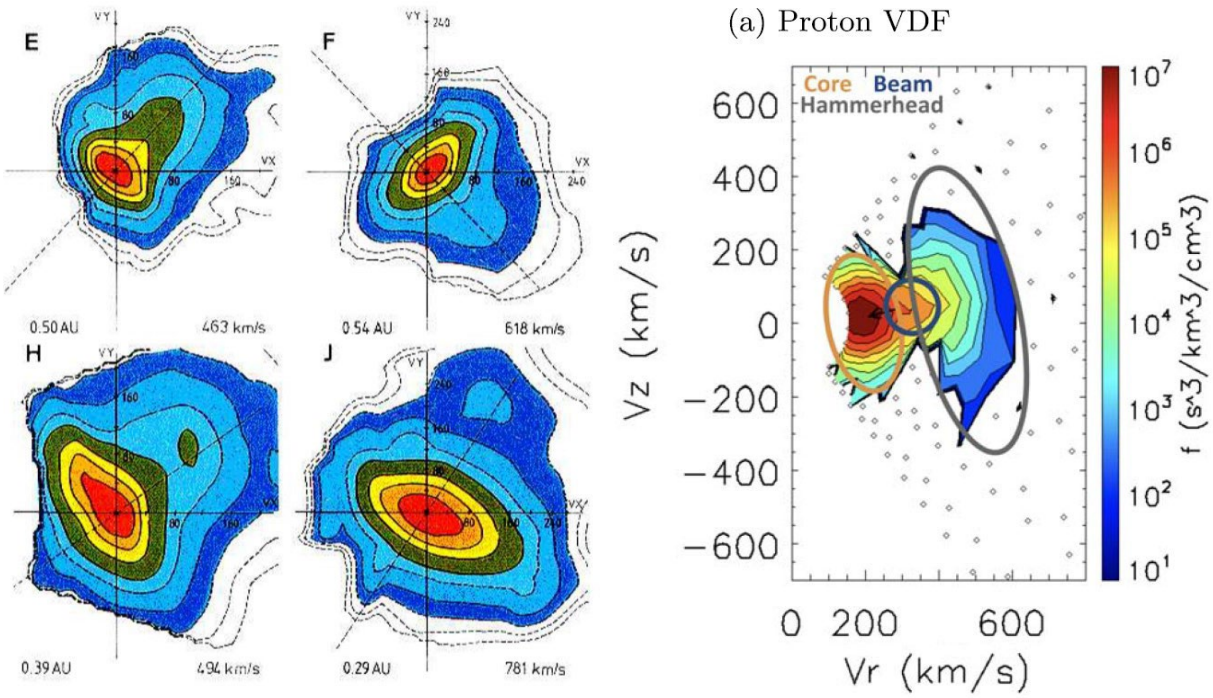

excess in energies necessary to accelerate them to such speeds. This behavior is known as the differential stream of heavy ions in the solar wind. The relative velocity difference between proton and helium ions is closely related to the local alfvén speed. In addition, the separation in velocity space is maximized at closest approach to the Sun and the distributions relax together as they propagate outwards to Earth. Thus, it is feasible to believe differential streaming is produced in the solar corona during acceleration. However, our exploration of temperature anisotropies and differential streaming has been mainly limited to protons and helium ions and the critical insights from heavy ions remain hidden (see Rivera et al., 2025 for a notable exception).

Altogether, there is a need for space detectors capable of making reliable measurements of heavy ions and their kinetics in the solar wind. By deploying plasma composition spectrometers for in situ measurements longstanding questions concerning the corona and solar wind acceleration may be resolved. In addition, heavy ion sensors capable of measuring the kinetics of particle-wave interactions will be able to conclusively determine the source of temperature anisotropies and differential streaming in the solar wind. The outstanding science questions set by scientists concerning the solar wind will be best answered by instrumentation that ranges in radial distance from the Sun and traverses across different heliolatitudes. Therefore, through advancements in spaceflight technology meaningful understanding of our Sun that has eluded scientists since the beginning of the Early Space Age will be realized.

1.1.2.2 Planetary Magnetospheres

In many ways the ability for heavy ion measurements to resolve science questions pertaining to planetary science is identical to that of the solar wind. By making plasma composition measurements and resolving the kinetics of heavy ions in planetary magnetospheres plasma source identification, energization, and transport is most readily recognizable and to a higher degree of certainty. However, the physical mechanisms under study differ in planetary magnetospheres. The plasma sources are distinct (e.g., exospheres, dust, comets, etc.) and the ionization methods are more well understood. However, exploration of planetary magnetospheres is much more an investigation of the unknown and heavy ion composition measurements still provide the most reliable conclusions for research and discovery.

The environments contained within planetary magnetospheres are wildly different even within our own solar system. The rocky inner planetary bodies, similar in many ways to the moons of the outer planets, are often exospheric or have tenuous atmospheres. Consequently, energetic radiation from the Sun and galaxy in both light and particulate forms are able to rain down on the surfaces and break apart molecules and release them to produce ions through radiolysis, photolysis, desorption, and sputtering – among other reported physics. Nonetheless, though the source mechanisms are better known the original

Figure 1.17 The Hermitian Magnetosphere and Plasma Sources

Drawing of the solar wind interactions with the Hermitian magnetosphere with various sources of the exosphere and magnetospheric plasma. In particular, it shows the injection sights at which energetic particles enter at the cusps to reach down to the surface to initiate desorption and sputtering (Slavin et al., 2009).

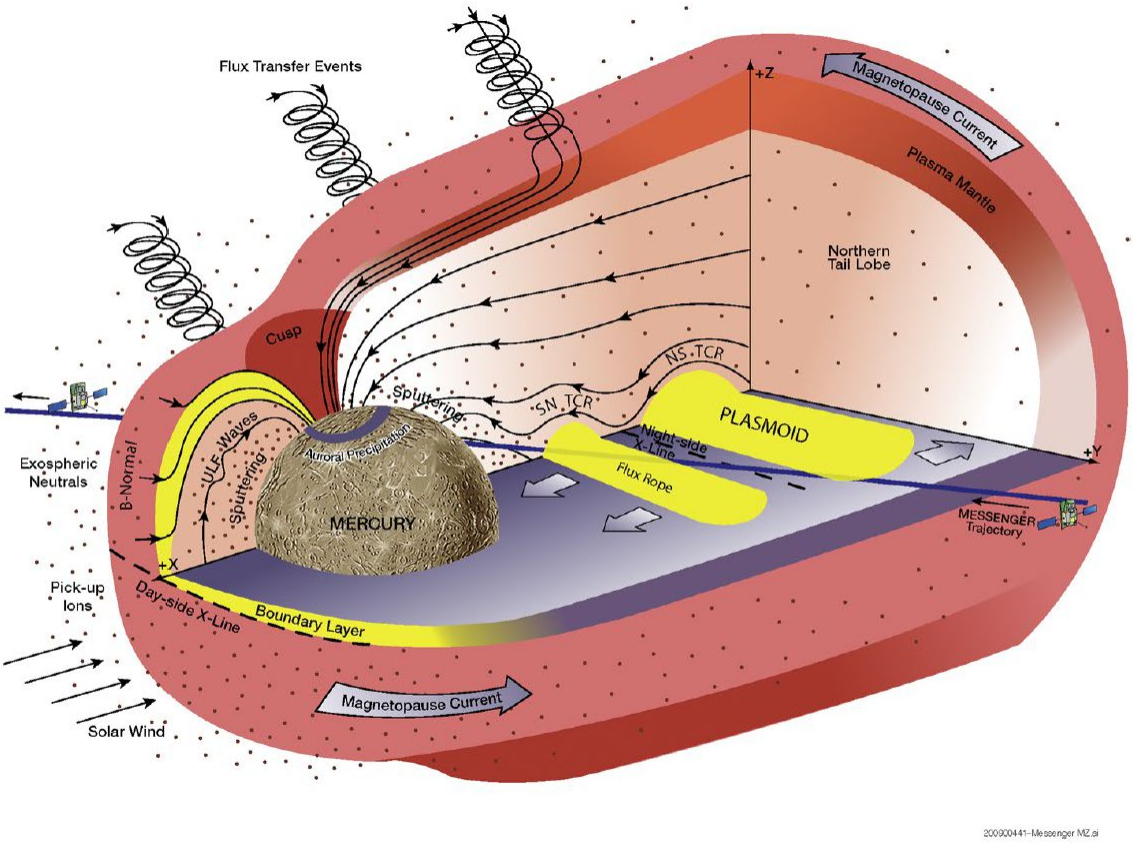

source material or even the existence of plasma source regions are more elusive. For example, prior to the arrival of a plasma spectrometer the generation and source mechanisms of Mercury's exosphere was mostly unknown. Through reliable measurements of the magnetospheric plasma scientists came to understand the role of desorption and sputtering in releasing sodium from the planetary surface (Raines et al., 2015 and references therein). The mechanics of this process is summarized by Figure 1.17 in which Mercury's magnetosphere is depicted interacting with the solar wind. Solar wind ions entering from the magnetosphere's cusps or accelerated towards the nightside surface in the tail impact the surface producing sputtering. Relatedly, rates of atmospheric escape are a pressing question for scientists researching any planet with in situ monitors (Jakosky et al., 2017; Persson et al., 2020; Szalay et al., 2021). Knowledge of the heavy ions in a plasma provides the most effective method for determining

Figure 1.18 Measurements of Enceladus' Plume

Data collected from the *Cassini* mission of Enceladus' plumes. (**Left**) Images taken of the plume emitted from the southern pole (Porco et al., 2006). (**Right**) Mass spectra taken indicating the composition of the plume and the ocean world believed to be contained within (Waite et al., 2006).

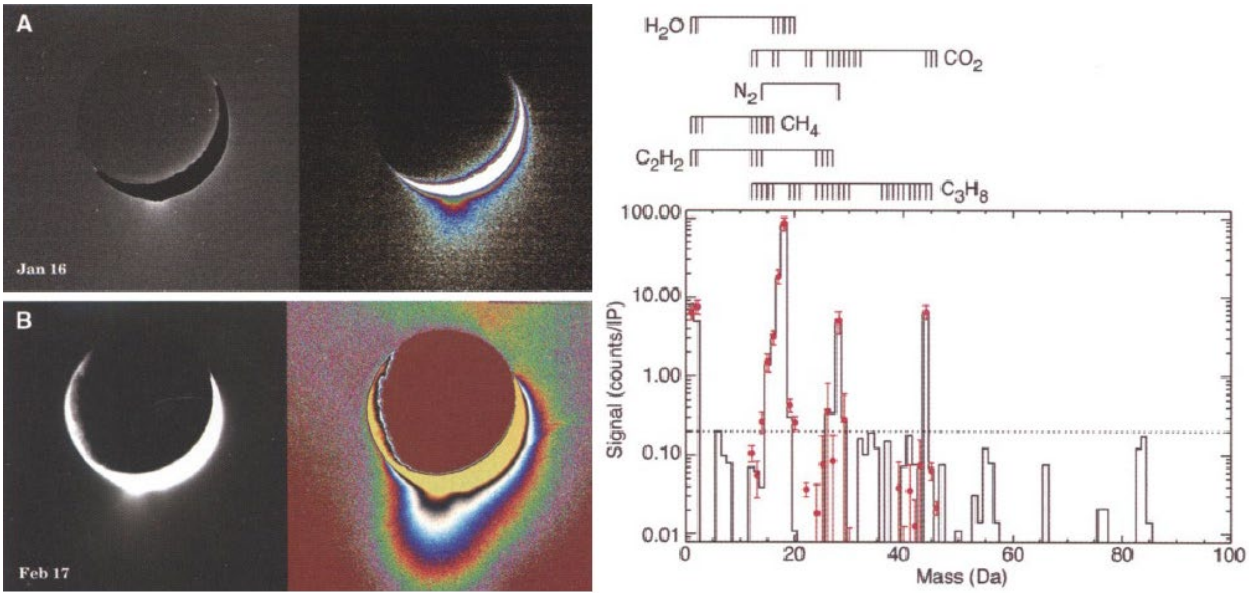

mixing rates and compositional gradients. Another example presents itself from the Cassini mission: the existence of plumes emitted from Saturn's moon Enceladus was first understood through remote sensing (Dougherty et al., 2006; Porco et al., 2006)(pictures on the left side of Figure 1.18). However, by flying through the plume and measuring the composition of its matter insights were unlocked concerning the makeup of the ocean world beneath its icy surface (Waite et al., 2006). The right plot in Figure 1.18 show the mass spectra of the accumulated measurements made during passage through the plume along with the particle species that are identified. Moreover, measurements of ring composition provide evidence for planetary formation and evolution. Example discoveries such as these redound across the planetary magnetospheres of our solar system including those of Venus, Mars, and Jupiter – they will undoubtedly continue for return missions with advanced instrumentation, as they have for explorations to comets and asteroids, and will for future missions to the unexplored outer planets. Thus, it is incumbent for all prospective missions to employ heavy ion spectrometers with the greatest performance capabilities in order to continue making unprecedented discoveries through plasma source identification and analysis.

Naturally, measuring the kinetics of heavy ions in planetary magnetospheres yields important breakthroughs in particle-wave interactions. There are examples from elementary plasma physics – the frequency of cyclotron waves (ω_{ci}), the rate of ion-ion Coulomb collisions (ν_{ii}), and polarization drift speeds (v_{pi}) are prime among them:

$$\omega_{cii} = \frac{qB}{m_i}, \qquad \nu_{iii} = \frac{q^4 n_i \ln\Lambda}{(4\pi\epsilon_0)^2 m_i^2 T_i^{\frac{3}{2}}}, \qquad v_{pii} = \frac{1}{B}\sqrt{\frac{m_i}{d}}\frac{dE}{dt}$$

In these equations lnΛ is the coulomb logarithm, the ϵ_0 permittivity of free space, T_i is the temperature of the ion, and dE/dt is the change electric field with respect to time. The relationships defined through these equations are fundamental characteristics of plasmas that exhibit mass-per-charge dependencies. So too is the motion of particles trapped along magnetic field lines. The charged particles circulating within the massive magnetospheres of the gas giants are accelerated up to incredible energies (~MeV)(Bolton et al., 2002; Nénon et al., 2025; Raptis et al., 2026). The plasma itself corotates with the magnetosphere producing global convection patters aligned with the planetary dipole. All such electromagnetic processes intrinsically exhibit a different response in each heavy ion through variations in mass and charge. Thus, the principal behavior concerning the dynamic forces in the plasmas of planetary magnetospheres is best characterized through measurements of heavy ion velocity distributions.

Explorations of the planetary magnetospheres began at the very start of the Early Space Age.[10] However, many important discoveries await future missions. Increases in instrument performances, measurements through multipoint sampling, and voyages to unexplored planets all represent opportunities for major discoveries. The Magnetosphere Multiscale (MMS) mission launched four satellites in formation to measure magnetic reconnection at the boundaries between the solar wind and Earth's

[10] Mariner flew by Venus in 1962 merely four years after Explorer I was first launched into orbit.

magnetosphere and within the tail (Burch et al., 2016). Likewise, HelioSwarm mission planned to the solar wind will use spatially separated spacecraft by magnetohydrodynamic (MHD) scale lengths to measure turbulence (Klein et al., 2023). Both missions are examples of the recent understanding arrived at by space physicists that distributed measurements However, neither mission has or was planned to be equipped with triple-coincidence, charge-resolving spectrometers. Multipoint detectors with the ability to distinguish the charge of particles will provide critical insight into the boundaries and source regions of the solar wind and the structure of CMEs and other transients. The *BepiColombo* arriving at Mercury will advance our understanding beyond FIPS measurements from *MESSENGER* in part because it will employ *two* spacecraft in different orbits that will operate in cohesion (Benkhoff et al., 2010). The multipoint mission profile coupled with greater capability in resolving particle identities in planetary environments will continue to prove critical for discovery concerning their magnetospheres, moons, atmospheres, rings, and so much more. Developing resource-efficient models will be necessary to enable any future missions dedicated toward multipoint plasma composition experiments. High fidelity measurements of plasma composition and heavy ion kinetics will provide forthcoming scientific operations to the heliosphere and planetary magnetospheres with the greatest ability to reveal new elements of space physics.

Section 1.2 T-FIPS Instrument Concept

The Triple Fast-Imaging Plasma Spectrometer (T-FIPS) is an instrument concept for a triple coincidence or charge-resolving time-of-flight plasma spectrometer. It is based on the heritage design of FIPS or the Fast-Imaging Plasma Spectrometer that successfully flown onboard the *MESSENGER* mission to Mercury (Andrews et al., 2007). The benefit to T-FIPS is its compact size and resource efficiency. It is comprised of three sub-instruments: an electrostatic analyzer (ESA), time-of-flight (ToF) chamber, and an energy detector system. It utilizes modern manufacturing techniques to improve design and production in order to build a novel instrument aligned with the goals for necessary advancement in the Early Space Age. Specifically, it is optimized for multi-point sampling of diverse space environments

using spacecraft constellations or swarms and for smaller, power- and mass-efficient probe-class missions. When properly deployed, the T-FIPS instrument would yield unprecedented results for solar wind and planetary magnetosphere science by combining advanced charge-resolving detections with a compact and resource optimized platform with reliable heritage.

1.2.1 FIPS Heritage

The T-FIPS instrument concept was developed from the original design of the Fast-Imaging Plasma Spectrometer (FIPS) detector that was flown on the *MESSENGER* mission to Mercury (Figure 1.19)(Andrews et al., 2007; Solomon et al., 2007). The top picture in Figure 1.19 shows the FIPS instrument with the electrostatic analyzer protruding from the ToF chamber on the right and the data processing unit (DPU) in front. Prior to *MESSENGER*, the only other mission to the closest planet to the Sun was *Mariner 10*; the plasma detector failed just after launch and therefore no reliable measurements were taken of the planetary magnetosphere (Bridge et al., 1960). The FIPS instrument performed exceptionally well during both the cruise phase (2004 – 2011) and within the Hermitian orbit (2011 – 2015) producing the first measurements of the magnetospheric plasma (Zurbuchen et al., 2008). In addition to determining the compositional gradients of the magnetosphere, FIPS assisted in determining the shape and dynamics of the magnetospheric cusps and discovered magnetic reconnection and fast plasma flows in the nightside magnetosphere (Dewey et al., 2018; Raines et al., 2013, 2014; Slavin et al., 2009)(see Figure 1.17). The bottom three plots in Figure 1.19 show the abundance of ions (Na^+, O^+, He^+) mapped to the location in the Hermitian magnetosphere and orientation with respect to the Sun (noon indicating Sun-pointed). The FIPS instrument operated for four years orbiting the planet as double coincidence detector; although it was able to easily identify most of the singly charged planetary ions surrounding the planet there was difficulty separating multiply charged ions, especially those with equivalent m_i/q_i (e.g., N^+ & S^{++}, Si^+ & Fe^{++}, etc.). Nonetheless, the FIPS instrument operated consistently producing remarkable discoveries until it made its final measurements during the intentional impact of

Figure 1.19 The Fast Imaging Plasma Spectrometer (FIPS)

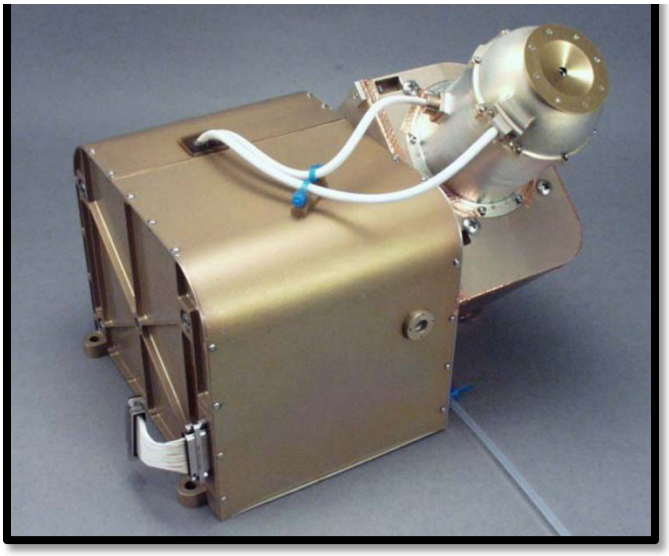

(**Left**) Picture of the FIPS instrument with electrostatic analyzer protruding from the time-of-flight chamber on the right side and data processing unit on the left (Andrews et al., 2007). (**Bottom**) Data collected by the FIPS instrument from Mercury's magnetosphere indicating the spatial distribution of heavy ions contained within (Raines et al., 2015).

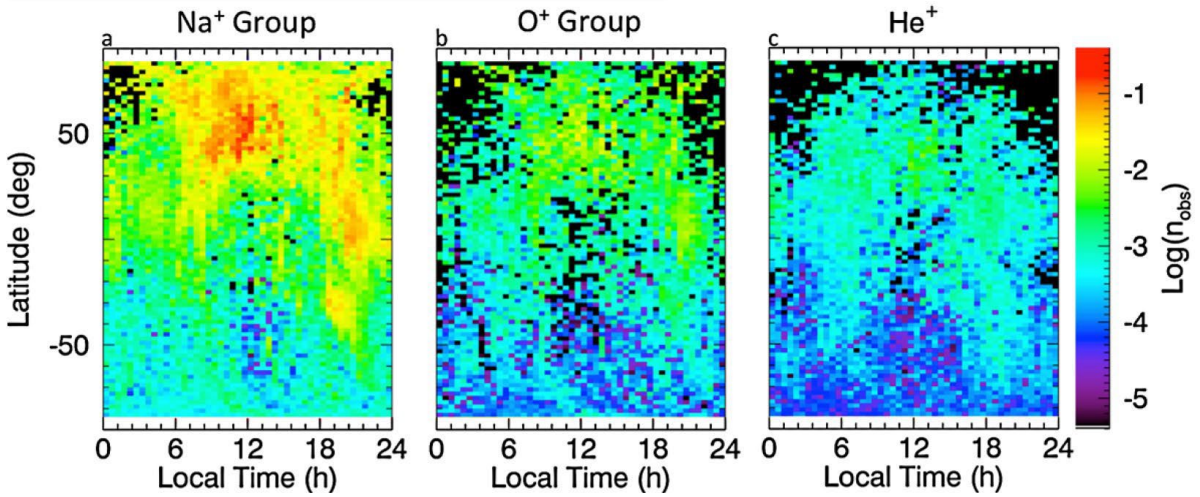

MESSENGER spacecraft with the planet's surface. The energy range was determined by the operational voltages set on the ESA that resulted in overlapping energy-per-charge passbands covering 0.05 – 20 keV/e. By convolving the resolutions of the ESA and ToF chamber, the FIPS instrument had a mass-per-charge resolution ($\Delta(m_i/q_i)/m_i/q_i$) of 0.04 and 0.08 depending on the mass of the ion (Andrews et al., 2007). The mass-per-charge range was from 1–44 amu/e. Remarkably, the FIPS instrument was only 1.8 kg and operated on 2 W of power providing an incredibly small form factor. Altogether, the FIPS instrument operated exceptionally well in an unknown environment resulting in many new and exciting scientific findings about Mercury's magnetosphere.

Figure 1.20 T-FIPS Principles of Operation

Drawing of the T-FIPS instrument concept including modifications to the original FIPS time-of-flight chamber. Particles enter through the left side via the wide view aperture and are filtered by the ESA by their mass-per-charge. Afterwards, their velocities are measured using the time-of-flight chamber. By relocating the stop detector and including an energy detector system the T-FIPS instrument becomes a triple-coincidence, charge-resolving time-of-flight plasma spectrometer.

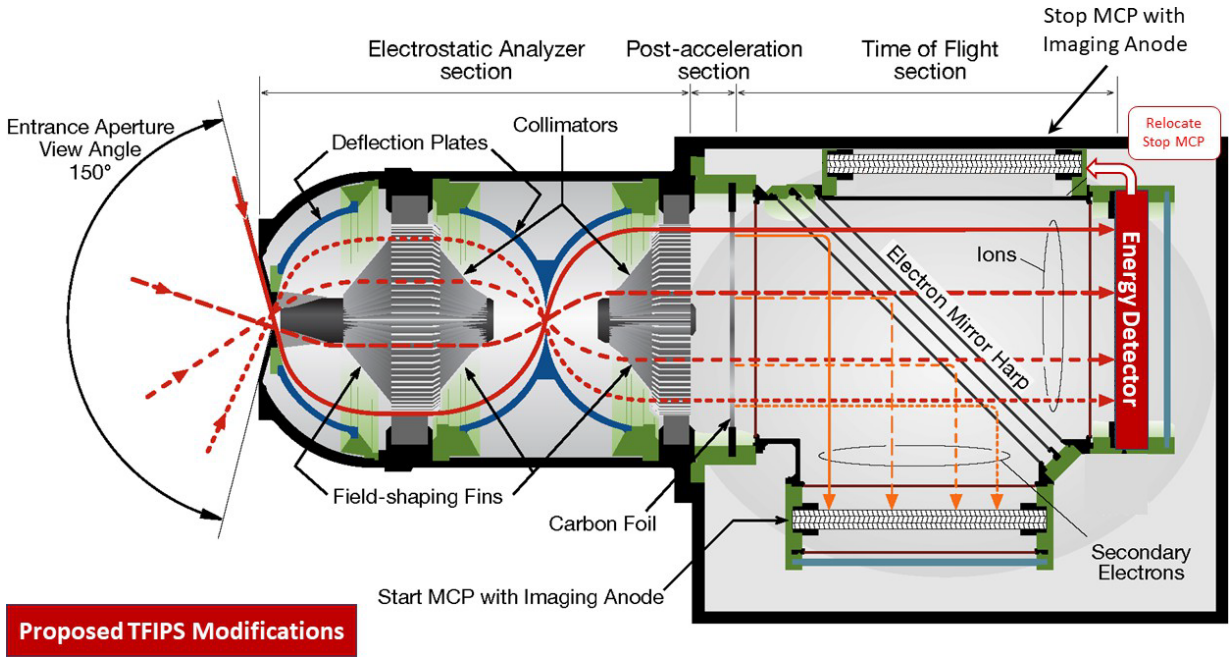

1.2.2 Electrostatic Analyzer

The T-FIPS electrostatic analyzer is the same design that was used on the FIPS instrument without any major modifications except for improvements in the fabrication and assembly methods. The design is roughly similar to a top-hat, one-and-a-half pass spherical analyzer with an expanded field-of-view. However, there are many major differences that yield enhancement in aspects of its performance compared to traditional designs. First, the aperture is more open in the nominal or ram direction down the central axis of the instrument. This expanded view towards the center is the reason for the "Fisheye" moniker and yields an unprecedented 150° × 360° instantaneous field-of-view (seen as the near semicircle on the left-hand side of Figure 1.20). In addition, compared to a traditional spherical or toroidal analyzer the interior surface electrodes of the ESA are replaced with fins; this also allows for the expanded field-of-view but also creates a nearly field-free region for the particles to travel across as they pass through the

fins.[11] Furthermore, the fins are assisted by collimators to prevent particles with rotational motion about the central boresight/ram axis by absorbing or deflecting particles without nominal trajectories so that they will not survive to the ToF chamber. The number of fins determines the angular resolution of the instrument (i.e., 24 fins grants 15° angular resolution). A natural benefit of all ESAs (and magnets) is their ability to prevent energetic photons from reaching the detectors due to the bending of the particle's path during analysis.[12].[13] In general, instrument developers design their detectors to prevent energetic photons from reaching the detector within three reflections (see e.g., Gershman & Zurbuchen, 2010; Herrero, 1992; Hooks et al., 2024). Therefore, the electrodes of the Fisheye ESA are blackened using a surface treatment to suppress reflections. The interior components of the ESA are held together using a stacking pin that aligns them when being compressed together; this pin results in a 15° blind spot at the central axis. However, the most important capability of the novel Fisheye design is its ability to preserve information concerning the heading of the particle. The different paths of particles are shown as dotted, dashed, and solid red lines in Figure 1.20. If a particle enters at a wide angle with respect to the central axis – nearly perpendicular with the boresight/ram direction – it will embark on large, swooping paths through the ESA closer to the outer walls. This aspect and the symmetries of the design result in the particle arriving in a straight-line trajectory nominal to the ESA exit aperture with a large radial distance away from the central axis. In contrast, a particle that enters with a small entrance angle close to the boresight/ram direction will pass through the ESA via small arcs close to the stacking pin. Thus, when the particle exits it is also on a straight-light path nominal to the exiting plane albeit radially close to the central axis. In result, the design of the Fisheye ESA naturally converts particle trajectory i.e., entrance angle into radial distance from the center axis. With this performance feature, the heading of the particle

[11] As a consequence of the fins along the interior surface their electrostatic fields resemble more of a trapezoid than a sphere.
[12] Microchannel plates and channel electron multipliers are sensitive to ultraviolet light and any electromagnetic waves with higher frequencies.
[13] Microchannel plates and channel electron multipliers are sensitive to ultraviolet light and any electromagnetic waves with higher frequencies.

Figure 1.21 The 3D Cam Electrostatic Analyzer

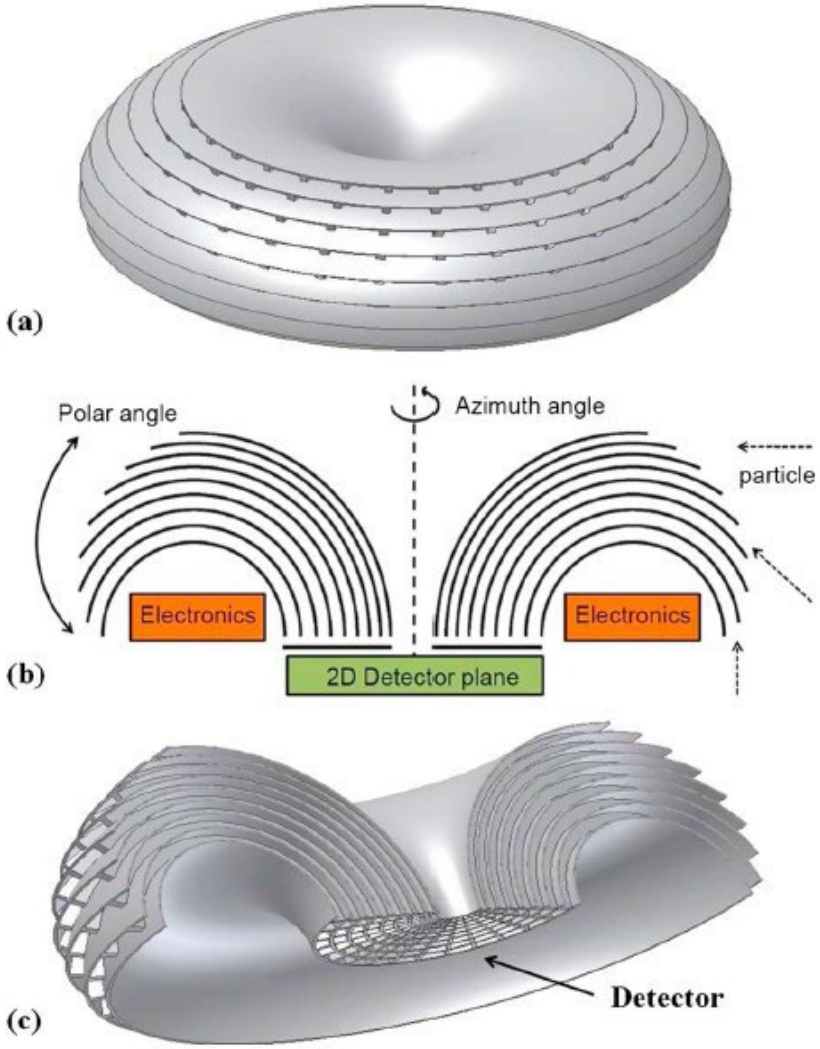

Drawings of the 3D Cam electrostatic analyzer developed by the Laboratoire de Physique des Plasmas (LPP) in France (Morel et al., 2017). The multiple circular apertures enable a 360° × 180° field-of-view. The external flux of particles is imaged down onto a single plane within the interior. Using a concentric einzel lens (Chapter 2) the image was focused down and mated to the T-FIP ToF chamber for enhancements in performance characteristics and applicability for various science missions.

is easily determined via its position on the detector. Collectively, the wide instantaneous FoV, novel electrode designs, and symmetries that preserve particle trajectory provide the Fisheye ESA with intrinsic performance advantages that are not found in standard electrostatic analyzers.

In addition to the original FIPS ESA we investigated using another ESA in conjunction with the T-FIPS ToF chamber that was developed by colleagues at the Laboratoire de Physique des Plasmas (LPP) at the Sorbonne University in France (Morel et al., 2017). The novel design known as the 3D Cam ESA allows for an exception 180° × 360° simultaneous FoV or half the night sky. This was accomplished using a toroidal shape with separate channels of entry along the outer surface that arc down onto a single

inner plane. As can be seen in Figure 1.21, the entrance apertures completely encircle the torus allowing particles to entry at any angle along each individual channel. In addition, many of the parameters (e.g., number of channels) could be quickly altered and produced because the 3D Cam ESA is manufactured using 3D printing and surface metallization techniques. In a number of features the 3D Cam outperformed the FIPS Fisheye ESA besides an increased field of view. It had an improved k-factor meaning lower voltages for higher particle passband energies and larger overall energy range (up to 40 keV/e). Furthermore, the geometric factor was higher by several orders of magnitude (i.e., 10^{-5} to 10^{-3} cm^2 sr eV/eV).[14] The higher energy range enables measurement of faster moving particles (e.g., suprathermal solar wind particles) and the larger geometric factor allows for deployment to space environments where the expectant flux of particles is low. Therefore, different versions of the 3D Cam ESA were explored as options to be mated to the T-FIPS ToF chamber. The ability to produce two versions of T-FIPS dependent upon the entrance ESA enables more opportunity for deployment on future science missions.

1.2.3 Time-of-Flight Chamber

Once the particles pass through the electrostatic analyzer they encounter the time-of-flight (ToF) system. The T-FIPS ToF chamber has undergone significant modifications compared to the FIPS ToF chamber in order to incorporate the energy detector system; the modifications to the ToF chamber that include the addition of a third detector as an energy acquisition subsystem transform the T-FIPS instrument into a charge-resolving mass spectrometer (see Figure 1.20). First, the particles exiting the ESA are energized by a post-acceleration system; the post-acceleration functions through high voltage connections to the entrance and body of the ToF chamber. The entrance to the ToF chamber is covered with a carbon foil that produces electrons when the ion enters the chamber. By "floating" the carbon foil

[14] The geometric factor of an instrument in essence is the factor by which to multiply the number of particles entering an instrument to determine how many will create a measurement. However, there are many aspects that determine the "survivability" of a particle (e.g., entrance angle, initial energy, mass, charge, etc.). Therefore, the definition of an instrument's geometric factor is variable and can be determined by how advanced of calibration it has undergone.

and ToF body to high voltages the particle exiting the ESA at ground is accelerated towards the carbon foil. Once the ion enters the carbon foil with a boosted velocity it is encompassed by the ToF chamber body and aperture grids so that the floated potentials appear as the new ground. Moreover, the majority of ions that pass through carbon foils exit as a neutral particle and are therefore electrically blind to any subsequent fields (Gonin et al., 1995a, 1995b; Kallenbach et al., 1995). The purpose of accelerating the particle before it enters the ToF chamber is twofold: (1) it helps overcome energy lost by the ion as it passes through the foil (i.e., energy "straggling") that decreases with higher initial energy and (2) it aids in overcoming the dead layer of the energy detectors (details below). The electrons produced by the carbon foil are steered perpendicular to the entrance onto the Start detector using an electrostatic mirror. The electrostatic mirror is a relatively novel ion optical component employed on a limited number of instruments (see Rodríguez-Pacheco et al., 2020b; Wilken & Stüdemann, 1984 for other examples). It operates by sandwiching a high voltage grid between two grounded grids. This design results in moderately low field leakage beyond the grounding grids that creates a field-free region beyond but between the grids are electric field lines 45° to particle travel (see examples in Figure 2.3 next chapter). The much lighter electrons are reflected with high fidelity, preserving their original location from the carbon foil onto the Start detector (see example in Figure 2.10 next chapter). The initial position of the ion undergoing measurement is actually extracted using the electron's location on the carbon foil that is imprinted onto the Start detector. The much heavier ions mostly ignore the electric fields inside the mirror and pass through towards the far side of the chamber. In the original FIPS design, there are two microchannel plates (MCPs) that are the Start and Stop detectors. The Start detector is located prior to the electrostatic mirror and 90° to the central axis in order to detect the redirected electrons from the carbon foil. Since the original FIPS design is only a double-coincidence ToF spectrometer it only has two detectors – the Stop MCP is located opposite to the entrance and records the position of the ion. However, the fundamental alteration to the FIPS heritage design is to move the Stop detector to be located 90° with respect to the central axis, after the electrostatic mirror, and symmetrically opposite to the Start detector (indicated on the right-hand side of Figure 1.20); put in its previous location is the energy detector system

at the chamber exit opposite the carbon foil. When ions strike an energy detector electrons are emitted and accelerated back towards the electrostatic mirror. The same single mirror steers the Stop electrons "upwards", or in the opposite direction of the Start detector, perpendicular to the central axis, onto the Stop detector. Therefore, the modifications that produce the T-FIPS ToF chamber yield three separate detections per ion measurement and determine both velocity and energy signatures. The velocity, energy, and energy-per-charge combine to provide unambiguous references to the mass and charge of the ions undergoing investigation.

1.2.4 Energy Detector System

The energy detector subsystem is the third and final component of the TFIPS instrument. As described above it is integrated directly into the ToF chamber. The energy detector subsystem consists of an array of detectors mounted onto a surface facing the direction of ion travel and held at a standoff distance via isolators from the ToF chamber exit. The electronics for signal processing are mounted on the backside of the detector mounting plate and opposite the ToF chamber. The modular design of the energy detector subsystem may incorporate two different types of energy detectors: solid-state detectors (SSDs) and/or avalanche photodiodes (APDs). As described in the history of spaceflight detectors, solid-state detectors have been flown and operated in space for over half a century since the onset of the Space Age. Consequently, SSDs benefit from a high degree of spaceflight heritage or confidence in their ability to operate after launch in deep space environments. However, SSDs are slower (~1 ms / 1 MHz) than the detection rate readily achievable by the MCP Start and Stop detectors (~1 ns / 1 GHz)(Knoll, 2010; Ogasawara et al., 2016). In addition, they have a dead layer or non-depleted region that the particle must pass through before being detected and is the region on the left of the detector volume drawn in Figure 1.22. Semiconducting energy detectors operate by placing a voltage across the detector creating an electric field within the interior that clears a portion of the detector volume of its conductance band electrons; when particles strike the lattice atoms in this region they liberate charge carriers (electrons and

Figure 1.22 Solid-State Detectors and Avalanche Photodiodes

(**Left**) The physics occurring within the interior volume of a solid-state detector. The depleted region measures the energy of particles. The non-depleted region or dead layer is not cleared of conductance band electrons and therefore recombination occurs before a signal is produced (Texas A&M University / Nuclear Safeguards Education) (**Right**) The differences in energy resolutions between an SSD and APD. Note also that resolution increases with smaller size detectors; this is a result of improved signal to noise with reduced surface area (Ogasawara et al., 2016).

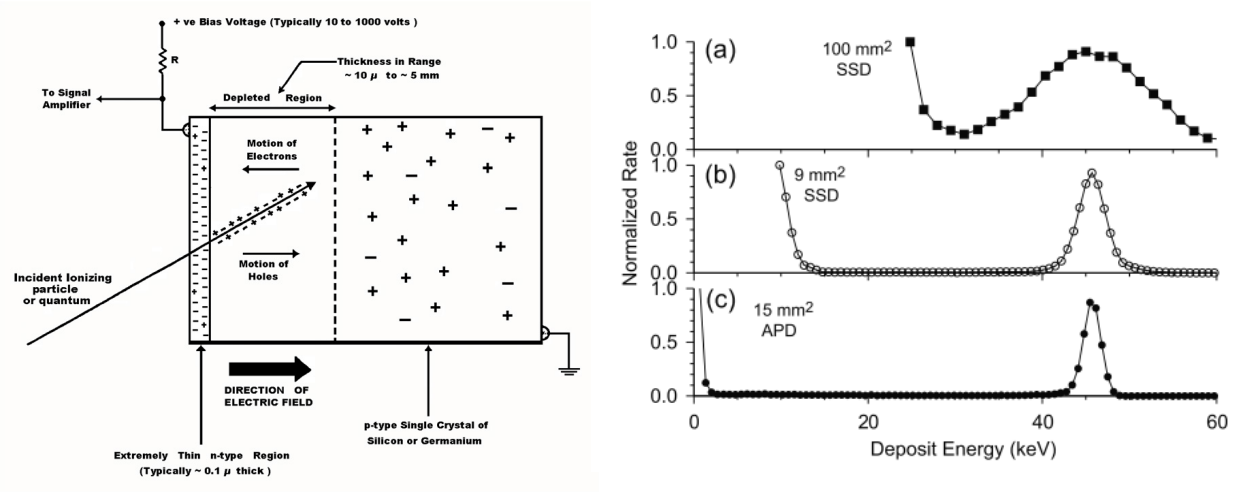

electron holes) that are measured by the electrodes through the bias current.[15,16] The non-depleted region or dead layer is indicated by the region filled with +'s and –'s in the right-side drawing of Figure 1.22 and is the portion of the detector volume where the conductance band electrons are not removed; electrons and electron holes in this section recombine with lattice ions before being measured thereby quenching the signal that denotes the particle energy loss in that region of the detector. The non-depleted region/dead layer is the portion of the detector volume facing towards the ToF chamber. Therefore, the particle must pass through the dead layer before entering the sensitive or depleted region for measurement. Particles

[15] Liberated electrons drift towards the positive electrode, and their charge becomes extracted and visible through the bias current. An electron hole is the lack of presence of an electron and drifts in the opposite direction. The negative electrode on the opposite side of the detector replenishes the electron hole with an electron also producing a measurable current. The combination of absorbing the charge of liberated electrons and replenishing the charge of electron holes produces the energy signature pulse and is proportional in height to the initial energy of the measured particle.

[16] The bias current is the current necessary to maintain the voltage across the detector volume. With no energetic particles present to activate the sensor the "dark current" is the standard rate of replacing electrons/electron-holes due to thermodynamic vibrations of the lattice and determines the background noise the energy signals must overcome.

without sufficient energy are not recorded; this property of the detector introduces an energy threshold below which particle measurement cannot occur.[17] Solid-state detectors have a high energy threshold i.e., 20 -30 keV depending on particle mass below which an ions energy is absorbed completely without signature because it never passes into the depleted region (Knoll, 2010). In contrast, avalanche photodiodes are specially doped in order to produce an avalanching or cascading region within the detector volume (Knoll, 2010). Similar to the behavior described in Geiger-Müller counters, the liberated electrons gain enough energy through the applied electric field to ionize additional lattice atoms inducing an exponential increase in measurable charge.[18] The resulting increase in charge results in a larger, more defined pulse that increases energy and timing resolution allowing for detection rates approximating those of MCPs (i.e., 1 ns / 1 GHz)(Knoll, 2010). In the plot on the right of Figure 1.22 the decrease in width of the energy distribution indicates an increase in resolution that results from an increase in capability to distinguish measurements from one another. Moreover, the dead layer in APDs is smaller so that lower energy particles can be detected. However, the gain of an APD is temperature dependent producing floating energy signal that must be counteracted through temperature control or an active biasing system in addition to extensive preflight calibrations (Ogasawara et. al., 2016). Furthermore, the energy resolution of APDs decreases at very low temperatures (~20 °C); in contrast SSDs increase in resolution at lower temperatures due to reduced dark currents and better signal to noise (Ogasawara et al., 2016). In sum, SSDs enjoy extensive heritage, stable energy signatures, and perform better in more thermodynamic environments whereas APDs provide a lower energy threshold, fasting timing, and higher energy resolution. Therefore, our designs for the energy detector system are currently agnostic to which detector type is utilized allowing for the greater applicability of the T-FIPS instrument to more diverse science targets and space environments.

[17] The energy threshold was a secondary reason for the post-acceleration system between the ESA and ToF chamber.

[18] The factor by which the charge is exponentially increased is known as the detector's gain. For the APDs explored in this study the gain is typically ~10-50 (Ogasawara et al., 2012).

The T-FIPS instrument utilizes three subcomponents to become a triple-coincidence, charge-resolving time-of-flight plasma spectrometer. These include the original Fisheye ESA, modified ToF chamber, and a new energy detector system. The most important facet is that all three subsystems are predicted to utilize only 5 W of power. In addition, the form factor is expected to fit within 6U or 60 cubic centimeters. Finally, the mass is expected to be around 5 kg. The T-FIPS instrument form factor and energy draw is significantly reduced with respect to all other known charge-resolving spectrometers.[19] Overall, the compact, resource-efficient qualities of T-FIPS position it as an exceptional detector for plasma composition studies on future Heliophysics and planetary sciences mission.

[19] For example, the SWICS instrument on ACE and the HIS sensor on Solar Orbiter (Andrews et al., 2007; J. G. Gloeckler et al., 1992).

Chapter 2

Designing and Optimizing the T-FIPS Sensor

The primary objective of this research was to develop the T-FIPS instrument concept. There are important facets of the design and optimization of the mechanical model and performance characteristics that are simulated using numerical modeling that must take place prior to the fabrication of. In addition, there were a number of engineering challenges and different versions that were considered throughout the evolution. The revision process ultimately narrowed down onto a single model with small modular features in the energy detector system to allow for adapting performance metrics to various mission profiles. The final T-FIPS design utilizes all the advanced components and subsystems necessary to produce a triple-coincidence time-of-flight mass spectrometer but in an unprecedentedly small form factor. Whereas enough of the mechanical development has advanced to begin manufacturing of a prototype, much of the conceptual development still awaits the hardware tests that will follow. Eventually, the combination of simulated and experimentally determined performance metrics will provide the data necessary to finalize the spaceflight design to be proposed for future science missions; the T-FIPS instrument will be optimized to answer a new era of science questions that center upon multipoint sampling and mesoscale physical processes.

Section 2.1 CAD Development

The design, development, and production of a spaceflight detector is wholly centered upon the mechanical design and is typically constructed using computer aided designs (CADs). The first step to

Figure 2.1 The T-FIPS Computer-Aided Designs

(**Top**) CAD of the dual harp "Extend-o-FIPS" model. (**Bottom Left**) CAD of the T-FIPS external housing and protruded electrostatic analyzer. (**Bottom Right**) CAD for the single harp T-FIPS instrument concept. The CADs were developed using FIPS heritage designs and developed by Charles Via, Marcello Lara, and Jayveer Phull with the leadership of Louis Marr.

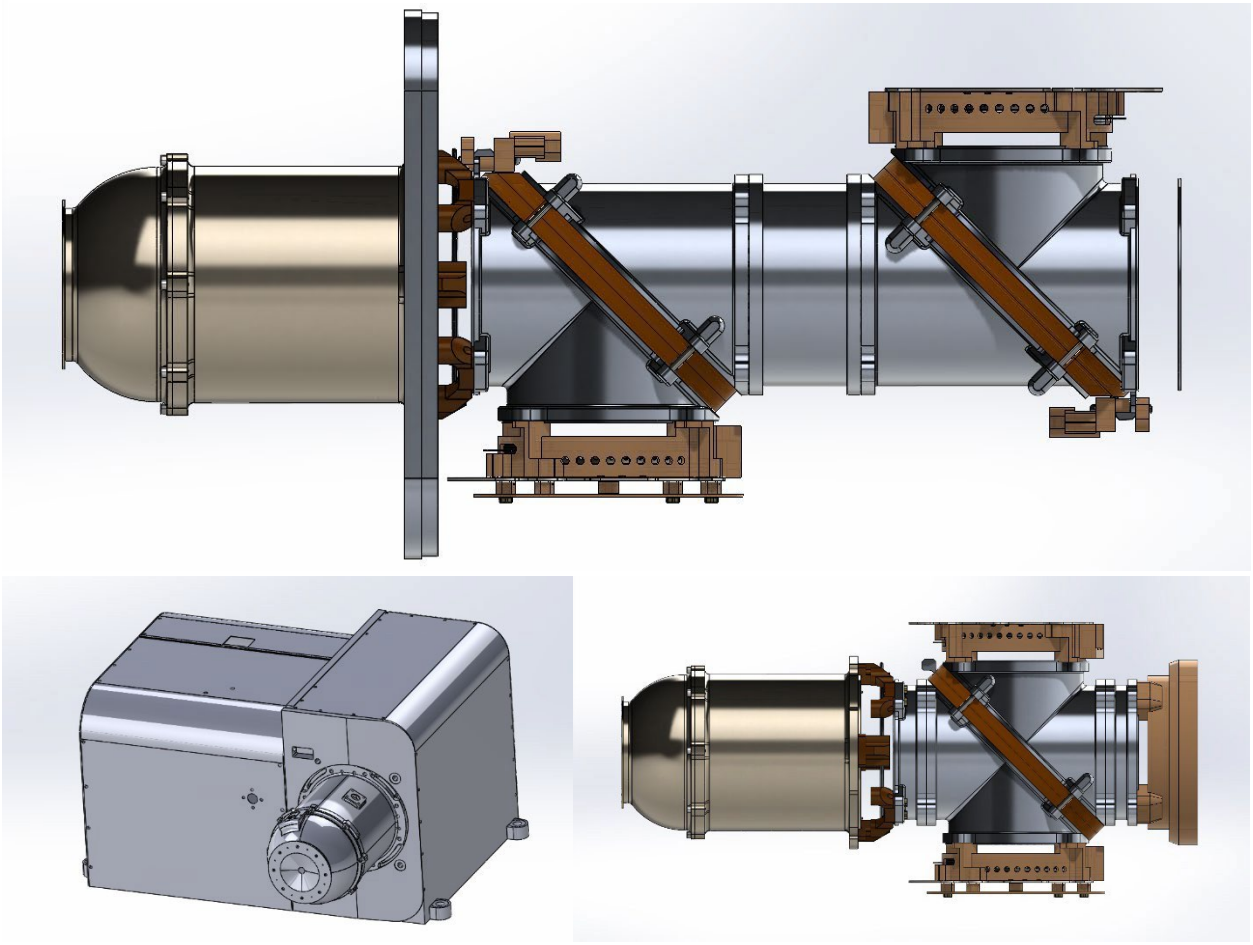

advancing the T-FIPS instrument was generating the CADs for the new time-of-flight (ToF) chamber; thankfully, the FIPS electrostatic analyzer needed only minor updates from the CAD developed for the *MESSENGER* mission before incorporating it into the T-FIPS model. However, the T-FIPS ToF chamber required significant alterations to the second half that came after the electrostatic mirror.[20] The original FIPS ToF chamber CAD was used to start the project, and the symmetry of the system significantly reduced the number of new components. In essence, the latter half of the FIPS ToF chamber that came

[20] The T-FIPS ToF chamber CAD was first developed by then University of Michigan students Charles Via and Marcello Lara. The design was finalized by SPRL mechanical engineer Louis Marr and prepared for manufacturing by University of Michigan student Jayveer Phull.

after the electrostatic mirror was discarded and replaced with a copy of the leading half of the chamber that is rotated symmetrically opposite the mirror. Altogether, the modifications extended the chamber distance from 7.5 cm to 10 cm, creating a longer flight path for analyzed particles. The result is the single-mirror design seen in the bottom right of Figure 2.1 and the exterior structure developed in the bottom left. In time-of-flight chambers, extending the flight path or increasing the duration of particles between start and stop signals enhances the timing resolution of the instrument at the cost of additional weight and size. Moreover, in the early stages of designing T-FIPS there were two ToF CADs under consideration: (1) the single mirror design and (2) a double mirror design with an additional flight tube in between colloquially called Extend-o-FIPS (seen the top image of Figure 2.1). The need for the extended version was to remove the possibility of crosstalk between the Start and Stop detectors. Once it was determined the crosstalk would not be a primary concern for the prototype (see section 2.3.2 for further discussion) the number of designs was reduced and further studies proceeded with the single harp detector only. Nonetheless, the early developments of the ToF chamber CADs were critical in determining the initial design features such as the distance between the carbon foil and mirrors, between the mirror and the Start and Stop detectors, and between the mirror and energy detectors (and consequently the full ToF length). With the completion of the first drafts for the ToF chamber CAD the production of electrostatic and ion optical models could begin.

Section 2.2 Electrostatic and Ion Optical Simulations

Since the advent of high-speed computing, the simulated performance of an instrument has become fundamental to the design and calibration process. At its essence, the modeled performance of an instrument uses the same physical laws that were used to envision its theory of operation. In other words, our simulated results are as good as our understanding of physics and our ability to import them into computers – and they do quite well. In particular, particle instruments employ electromagnetics, particle dynamics and kinematics, and radiation interactions with solid matter. For many years SIMION and

SRIM (Stopping and Range of Ions in Matter) have been the primary software tools to simulate particle instrument performance for electrostatics with particle ray tracing and interactions between radiation and matter, respectively (SIMION.com/SRIM.org). However, for this research we instead used the COMSOL Multiphysics software package to model the electrostatic fields and the particle motions through them (COMSOL.com). In the next few sections we will outline the processes by which the simulations were produced and their results thereby determining the key performance metrics of the instrument prior to hardware development. The great benefit to this is that the impacts of design changes may be quantified and determined prior to experimental testing. Collectively, the T-FIPS simulations demonstrate the robustness of its design and the quality of its performance to answer science questions on future planetary and heliophysics missions.

2.2.1 Numerical Modeling Background

Simulating the performance of an instrument must be broken into a series of subcomponents. This is primarily because the complexity of the entire behavior under investigations is beyond any single domain – the separate physics, regions, and scales – length and temporal – are best divided up for individual analysis and joined together. For example, the behavior of an ion passing through a carbon foil occurs at the atomic scale (~0.1 nanometers or 10^{-10} m) and the flight path of the particle that exits into the time-of-flight chamber is 10 cm (or 10^{-2} m). The level of detail of the former example cannot be propagated out to the scale of the latter in order to analyze both using a single model. Moreover, an individual simulation may be broken into steps (e.g., meshing, potentials, particles – see below). However, the first principal physics of every model remains the same.

The initial step to building a simulation is determining the geometry of the object. Several toy models were developed to investigate the behavior of the T-FIPS instrument (see Figure 2.2). A toy model is a geometric structure developed within the COMSOL software itself without the use of a CAD.

Figure 2.2 Toy Ion Optical Geometries and Simulations

Examples of various toy models of ion optical simulations used to explore early design features of the instrument. These used native COMSOL objects to develop and had less detail than the CADs. (**a**) Dual harp ToF chamber model. The trajectory color is particle energy but the dark blue are ions and the lighter teal colored trajectories are Start and Stop electrons. (**b**) Simulation of electrostatic fins similar to those used in the Fisheye ESA. Note the nearly uniform potential and therefore approximately field-free region in between. (**c**) Alternative Fisheye ESA model that attempted preserve its primary performance features. (**d**) Electrostatic mirror simulation using square grids.

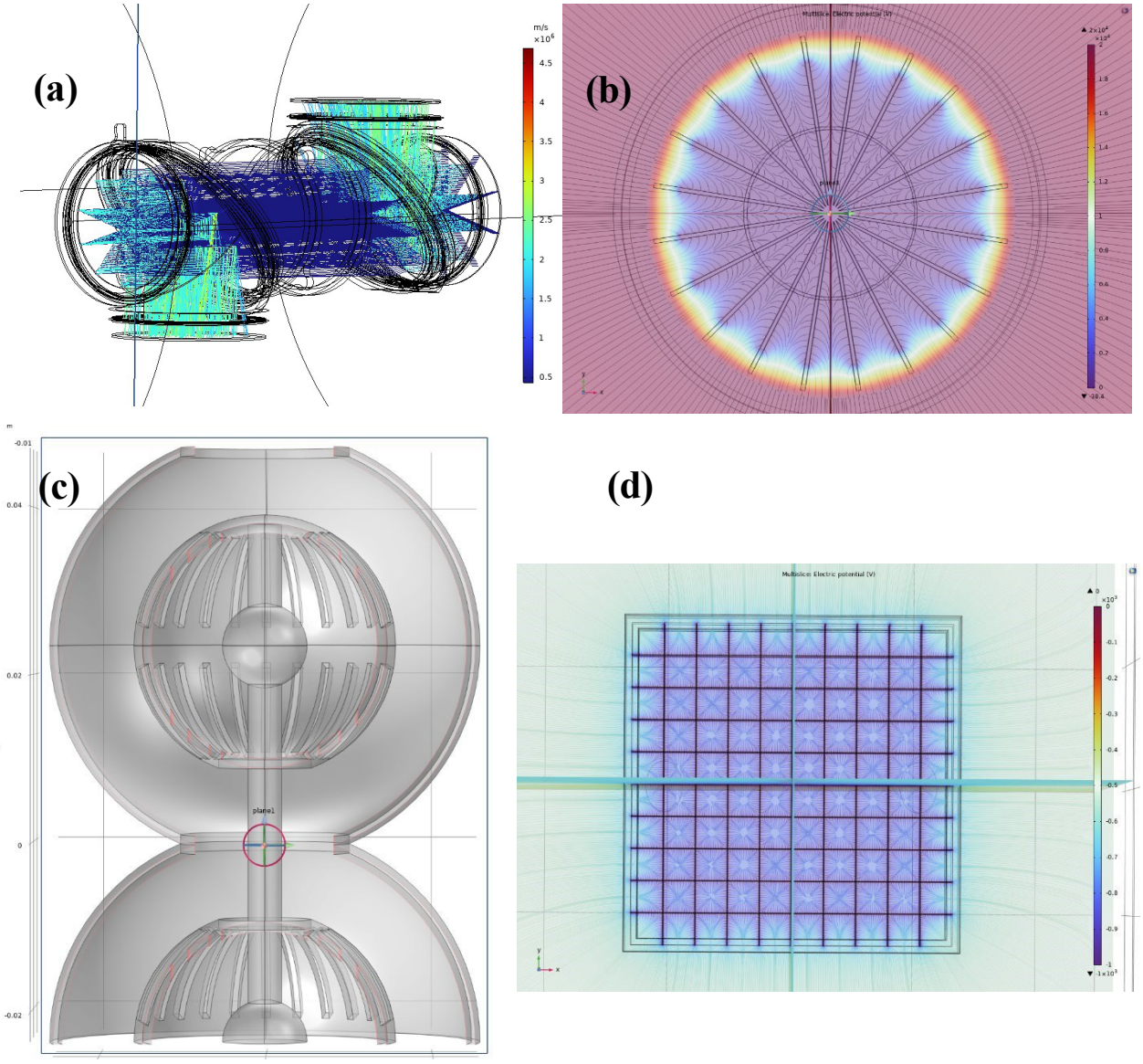

The use of toy models was useful in determining the initial behavior or feasibility of a concept; examples of these include early explorations of the dual harp ToF chamber design (Figure 2.2 a), alternative versions of the front-end electrostatic analyzer (Figure 2.2 b and c), an ion optical lens for the 3D Cam ESA (Figure 2.6 in section 2.2.3), and the electrostatic mirrors (Figure 2.2 d and Figure 2.12, in section

2.2.5). The electrostatic analyzer and later versions of the ToF chamber were integral components that necessitated a CAD for the most reliable performance analyses using simulations. Whenever possible the CAD should be used for ion optical modeling in order to match the performance features to the geometry with the highest fidelity i.e., the mechanical assembly used for manufacturing. Still, a CAD used for assembly typically has far too many features for use in ion optical modeling. For instance, the mechanical drawing will include fillets, chamfers, or fastener holes that are critical for mass reduction, high voltage surfaces, and instrument assembly but do not impact the electromagnetic fields enough to alter instrument performance. These features nonetheless take considerable computational power to include and are thus best removed prior to introducing it to the model. Considerable work must go into defeaturing a CAD before it is prepared for simulations.[21] In some instances, such as with the electrostatic mirrors, entire assemblies must be removed completely and replaced by native COMSOL objects (see blue shaded region in the top design in Figure 2.8 and section 2.2.4 for further details). Nonetheless, the accuracy of the model is maintained by subdividing into various performance domains and maintaining loyalty to the original geometry where it counts. Through these processes the geometries for the CAD and toy model simulations are constructed.

After the geometry is built or imported, the mesh of the simulation must be overlayed. The COMSOL software is a finite element model meaning that it creates a pixelated mesh of the simulation domain by which partial differential equations can be solved. The edges, points, and volumes of the mesh are the nodes at which the physical model can be solved. Luckily, the COMSOL simulation has an automated adaptive meshing that can overlay most geometries and domains. The tessellation of the domain is seen in the pixelated image the dual-harp geometry in the bottom left of Figure 2.3. For difficult areas, user input can solve inconsistencies in boundaries or surfaces but just as often the

[21] The development of the CADs used for this study and their simulation-ready counterparts was aided by Charles Via, Marcello Lara, and Louis Marr.

component features are removed completely. The shape of the mesh pixels can be altered but are typically trapezoidal and the size of the pixels determines the spatial resolution of the model. The same mesh is utilized for both the electrostatic and particle ray tracing simulations. Altogether, the simulation mesh is a critical facet in the development and quality of the T-FIPS performance models.

The behavior of particles as they move through the instrument is theorized using ion optical models. An ion optical model is divided into two components: electromagnetic fields and particles trajectories.[22] Our models need only generate electrostatic fields – however, magnetic and time varying fields are necessary in other particle instruments (see introduction). The electrostatic fields are created by solving the Poisson equation:

$$\nabla^2\phi\phi = \frac{\rho\rho}{\epsilon\epsilon_0}$$

Here $\nabla\nabla^2$ is the Laplace operator (divergence of the gradient), ϕ is the electric potential, ρ is the charge density, and ϵ_0 is the permittivity of free space. In effect, the charge is zero everywhere in free space so that the Laplace equation is recovered and the initial voltages are set by quantifying values at the surfaces of the electrodes. The regions between the electrodes are iteratively resolved by averaging the values in between. The electrostatic model is solved when the numbers stabilize. The 3D spatial derivative or gradient of the electrostatic potential is the electric field and is perpendicular to the lines of equipotential. The top left diagram in Figure 2.3 shows the electrostatic potential in color ranging from -1 kV (blue) to ~10 kV (dark red). The carbon foil, center mirror grid, and energy detector face are slightly negative with respect to instrument ground in order to accelerate electrons. The electric field lines in white are calculated by taking the gradient of the potential and depict the fringe fields that appear at the apertures;

[22] The flux of particles through the instrument is never high enough to necessitate considering the charge density and its impact on the electromagnetic fields within the instrument.

Figure 2.3 The COMSOL Simulation Process

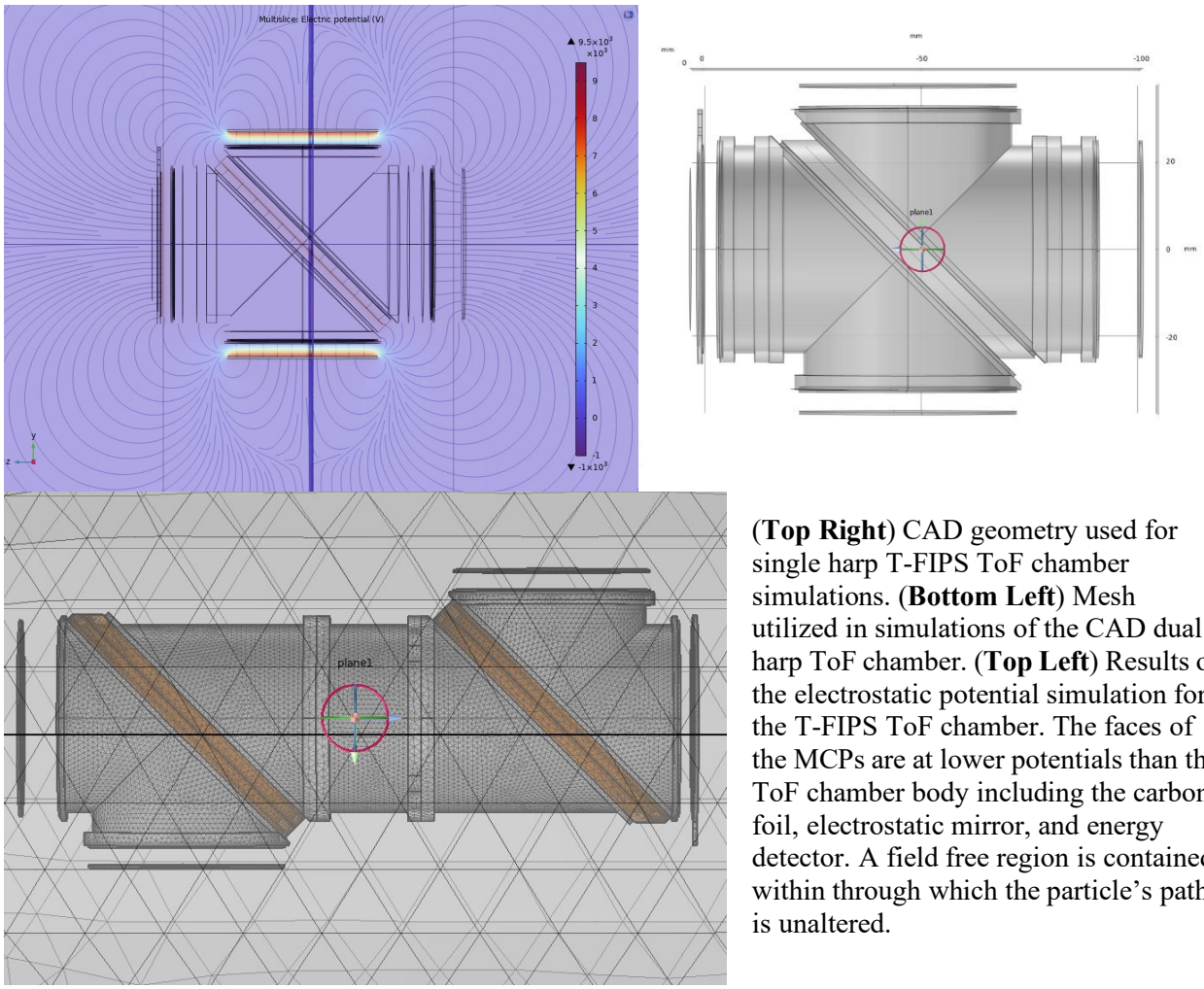

(**Top Right**) CAD geometry used for single harp T-FIPS ToF chamber simulations. (**Bottom Left**) Mesh utilized in simulations of the CAD dual harp ToF chamber. (**Top Left**) Results of the electrostatic potential simulation for the T-FIPS ToF chamber. The faces of the MCPs are at lower potentials than the ToF chamber body including the carbon foil, electrostatic mirror, and energy detector. A field free region is contained within through which the particle's path is unaltered.

this electrostatic model is was developed prior to the insulating caps discussed in section 2.2.4. Critical to producing a quality instrument that employs ion optics is determining where the field lines terminate. Many stray lines will deviate towards the grounded surfaces of the instrument and result in undesirable trajectories for particles. These are known as fringe fields and occur frequently at the edges of entrance and exit apertures. This region is found in the gaps between the four chamber openings and the carbon foil (left plane) and detector faces (top, bottom, and right planes) in the top right diagram in Figure 2.3 Proper utilization of grounding grids or electrodes can modify fringe fields to create field lines truer to the original intent of the design. Assessing the electric fields is also important for the electromechanical design of the instrument in order to ensure proper standoff distances and surface geometries to prevent

electric discharge or arcing. In addition to determining particle behavior, electrostatic simulations are important tools for instrument analysis in their own right.

The second component of an ion optical model is the particle ray tracing – the tracking of the particles path through the electromagnetic fields. The particle tracing module is a time-dependent model that iteratively steps through the particles' motion as a function of time. The particles trajectory is determined through a combination of dynamic force interactions with the fields and individual particle kinematics. For each time step the field strength and direction is determined by the particle's location. Then the force on the particle is calculated and the momentum of the particle is adjusted. The momentum adjustment is turned into a mass-dependent velocity and converted into a distance that is determined by the time step – the particle's path is predicted (see Figure 2.2 a, Figure 2.7, and Figure 2.10 for examples). The process continuously repeats until the full trajectory is determined. Naturally, the size of the time step fixes the temporal resolution of the simulation and is typically on the order of 10's picoseconds. Sufficient spatial and temporal resolution is achieved when decreasing the spacing/time steps does not alter the trajectories. The important metrics are determined by which particles are capable of traversing the instrument and arriving at the detector. By recording the characteristics of the population of particles that survive the instrument the performance is evaluated. The resulting resolutions (i.e., timing, mass, energy, etc.) are calculated by measuring the narrowness of the distribution that is recorded. Note that the geometric factor, or the likelihood of a particle to produce a measurement, and resolution which is the accuracy of determining particle characteristics, are in constant tension.[23] Particle ray tracing is pivotal for determining anomalous aberrations or undesired deviations in the particle image.[24, 25]

[23] In a perfect instrument the geometric factor would have a delta function probability at the exact particle energy under investigation.
[24] In ion optics the object is the collective initial conditions for the particles entering a device and the image is resulting product that exits.
[25] In mass spectrometry many aberrations are desired. The smearing of an image by energy-per-charge, for example, is the essence to how an electrostatic analyzer functions.

Finally, there are points in simulating the performance of an instrument in which the interaction of particles and fields occur at the atomic scales i.e., within solid matter. These are primarily considered during passage through the carbon foil and during particle deposition into the energy detector. In this research the SRIM/TRIM model was extensively utilized. The particle interactions are modeled by using simplified calculations of the momentum exchange between the bombarding radiation and atomic lattice (Ziegler et al., 2010). The interactions with the carbon foil and resulting energy and angle distributions were used in the ToF chamber simulations. The predictions in measurable energy signals within the SSDS were also critical in determining key components of the instrument design (see discussion on HV bubble below). Thus, the simulation of radiation with solid matter is a fundamental component for evaluating instrument performance.

The use of numerical models to determine the performance characteristics of an instrument includes the employment of many separate simulations. Furthermore, each simulation is comprised of a sequence of steps to facilitate their construction. In the next section we will review the results of these simulations and their application to individual instrument subassemblies.

2.2.2 Fisheye Electrostatic Analyzer

The Fisheye electrostatic analyzer is the original FIPS ESA that was utilized for the life of the *MESSENGER* mission. As discussed in previous sections, it has many advantages over a typical top-hat spherical or toroidal ESA such as a wide instantaneous FoV and preservation of information concerning the initial particle trajectory. However, there were no modifications to the T-FIPS ToF chamber entrance directly after the Fisheye ESA exit aperture and thus no need to modify the original Fisheye design. That being said, slight improvements in in the model that were considered to ease the assembly process and improve HV surfaces and standoff distances in order to achieve higher energy ranges. To facilitate this, electrostatic simulations were developed using the CAD that was initially produced for the *MESSENGER*

mission. The high voltage or grounded potentials were applied to all respective surfaces and used to identify locations of potential HV breakdown – and therefore areas for potential improvement. In the top image of Figure 2.4 the grounded potential is demarcated in blue and the ESA operating potential located primarily along the outer ESA cups is in dark red. The fins along the interior are grounded and appear as dark blue rectangles in the center. The electric field lines are drawn in white lines indicating the direction of force experience by charged particles and potential paths or electron leakage or field emission, or locations of potential electrical breakdown. In the bottom image of Figure 2.4, the colored lines indicate the strength of equipotentials. Compression or bunching of lines along surfaces indicates high fields strengths and regions of interest. The colored map in Figure 2.5 indicates the scalar magnitude of the electric field strength – the dark red regions indicate spaces containing high electric field densities. The results indicated key regions where HV breakdown were particular concerns: the outer edge of the ESA cups where they are mechanically attached to the frame created high density fields in tight volumes. In addition, the tip of the cone that comprises the fins is a region of high electric field density. The region of interest about the fin cones is not near a mechanical attachment point and would therefore necessarily occur across a vacuum gap rather than across any surface. The remaining section of concern for high voltage breakdown is between the first outer ESA cup and the grounded entrance aperture. This region's susceptibility was well known to the MESSENGER FIPS engineers and was reinforced with insulating material. Altogether, the Fisheye entrance aperture, outer ESA cup attachments, and fin cone apices are all locations worth consideration for design changes to achieve higher potentials and particle energy range, in order of importance.[26] In addition, toy models were explored to find replacements for the fins that would produce equivalent electrostatic properties and particle trajectories without the use of thin plates that are more vulnerable to electrical breakdown (see Figure 2.2 design b and c). Ultimately, the

[26] It would also not hurt to provide additional space between the entrance outer ESA cup and the grounded housing.

Figure 2.4 Fisheye ESA Electrostatic Models

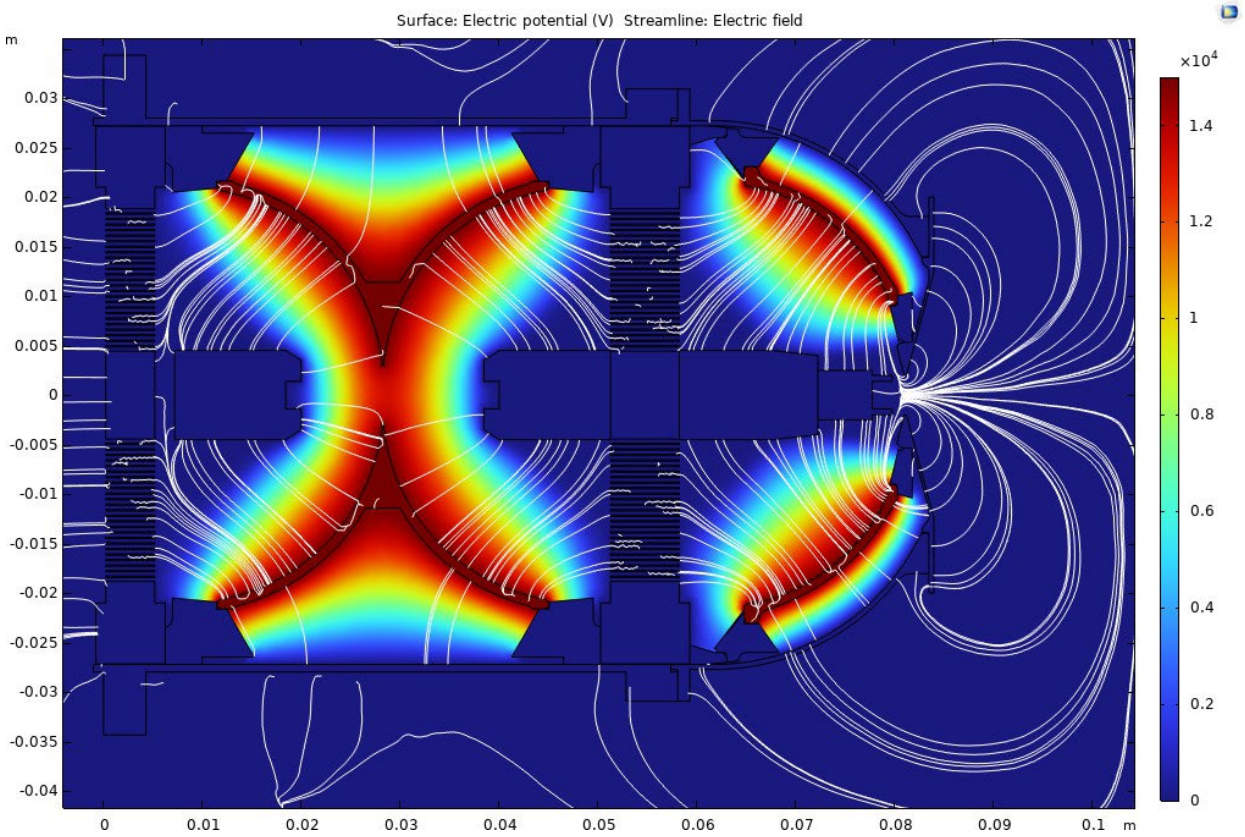

(**Top**) 2D slice through the Fisheye ESA depicting voltage strength in color and field lines in white. (**Bottom**) Contour map of the electric potential around key regions showing draping and regions with high field densities.

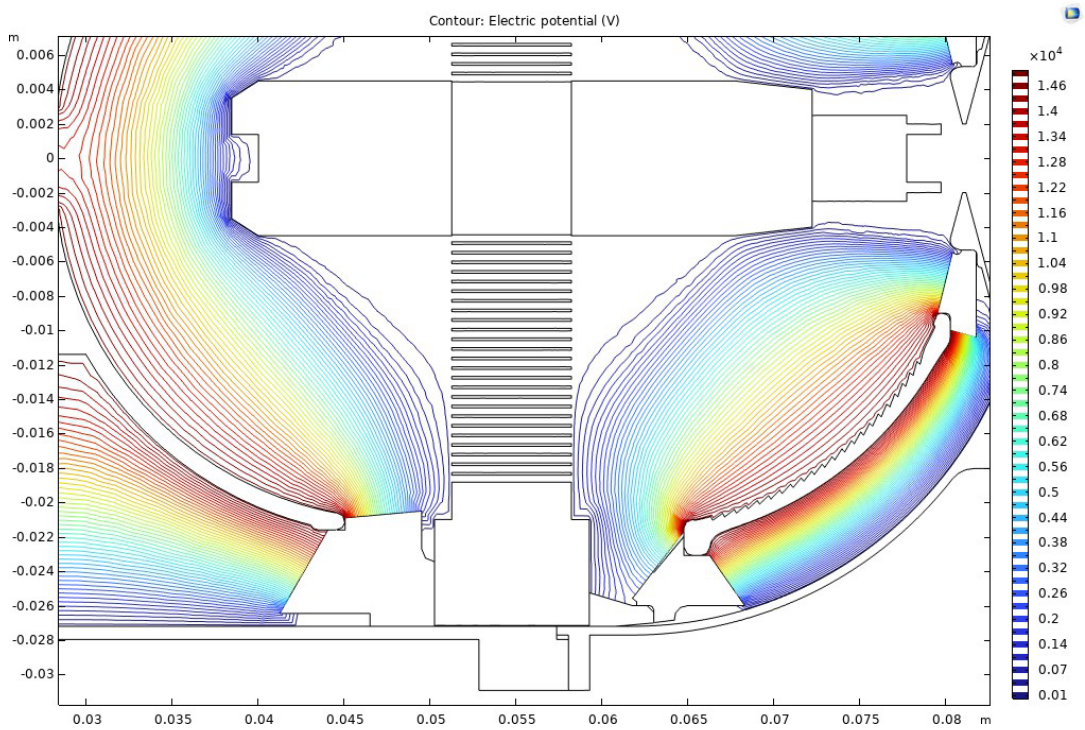

Figure 2.5 Fisheye ESA Electromechanical Study

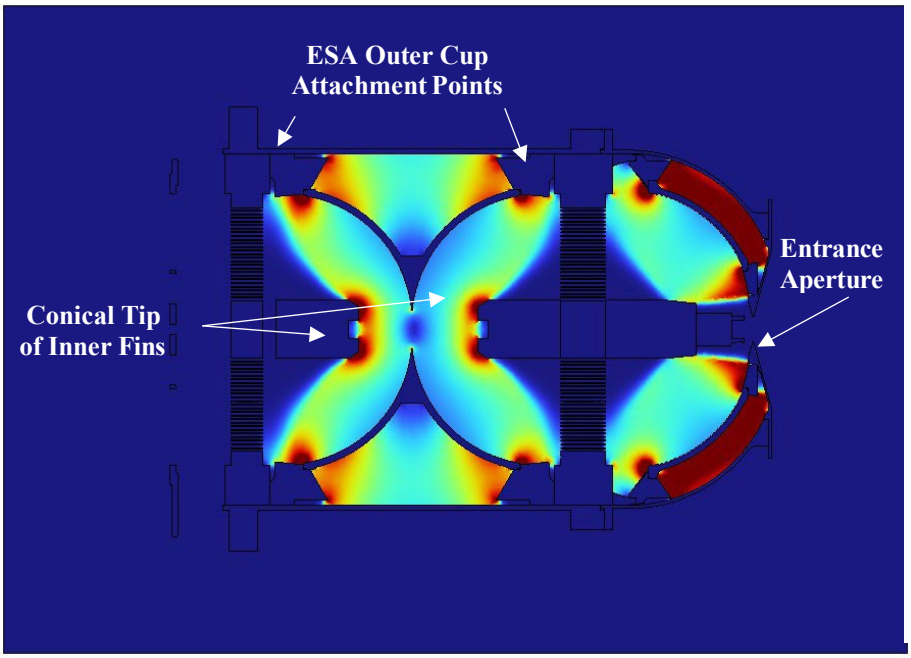

Plot of a 2D slide through the Fisheye ESA of the electric field strength. It is clear there are regions for potential breakdown near the outer cup attachment points, fin apices, and entrance aperture. The dark red regions between the cup and housing near the aperture indicate this is another region of potential improvement.

requirement to extend the energy range for the prototype sensor was set aside for future investigation in lieu of exploring uses with the 3D Cam ESA and only slight modifications to the mechanical design were made by SPRL engineer Louis Marr to improve manufacturing and assembly. Although there are already experimental tests being performed on flight spare Fisheye ESAs (see chapter on laboratory research) there are plans to begin production of a new model with the recent modifications in the near future. The electrostatic simulations of the Fisheye ESA demonstrate the success of its design using modern software and its readiness for continued application in space sciences missions.

2.2.3 3D Cam ESA Concentric Einzel Lens

In addition to the T-FIPS design that utilizes the Fisheye ESA we explored the ability to mate the T-FIPS ToF chamber to the 3D Cam ESA developed by colleagues at LPP France (see introduction). The primary concern for assembling the two together was the difference in size; the output of the 3D Cam ESA was approximately double the size of the T-FIPS ToF chamber entrance. While the size of the 3D Cam is easily scalable due to the 3D printing manufacturing techniques used to fabricate it there are electromechanical limitations that bind how small it can be made. Increasing the size of the T-FIPS ToF

chamber in order to expand the acceptance would introduce necessary alterations to the carbon foil frame and elliptical mirror harp mounts to maintain mechanical stability. Therefore, we chose to investigate an electrostatic lens that would reduce the spatial scale of the exiting particle image by roughly one half. Naturally, we chose as our initial template the einzel lens due to its longstanding primacy for such applications.[27] An einzel lens reduces the width of a beam using three cylindrical electrodes in series with the outer sleeves grounded and an inner positive sleeve for positive particles. The field lines penetrate radially inward before arcing back towards the leading and trailing grounded sleeves to create a focusing effect on particles. However, the lack of focusing power in a traditional einzel lens would extend the overall instrument length too far (we placed a restraint that the lens could not exceed the length of the ToF chamber). Due to these considerations, we developed a concentric einzel lens: a traditional einzel lens with an inner sleeve for an opposing potential. The inner and outer cylindrical sleeves are seen in the geometry in the top left image of Figure 2.6. The opposing potentials are color-coded red (approximately +7.4 kV) and blue (approximately -2.1 kV) in the bottom left image. In a concentric einzel lens the field lines are able to connect radially across onto the center sleeve thereby removing much of the need for field lines to arc backwards to the grounding sleeve, and away from the desired particle motion. The bottom right image in Figure 2.6 demarcates the new, entirely radial field lines that were created and the traditional field lines that arc back to the outer sleeve. The new ion optical design significantly increased the focusing power and reduced the required length of the device. As seen in Figure 2.7 and the resulting particle trajectories, the reduction in composite size of the image was successfully accomplished while preserving the particle arrangement in the original object. The output of the 3D Cam ESA was simulated using four concentric particle rings initiated at the exit aperture of the ESA channels. The simulated ions were protons initially imparted with ~15 keV and the color of the trajectory lines indicate the magnitude of the particle velocity (proportional to the square root of the energy) at that point in the particle's path.

[27] The only well-established alternative being the quadrupole lens that utilizes either electrostatic or magnetic fields. The quadrupole is conceptually more complicated and produces severe aberrations when not properly calibrated.

Figure 2.6 3D Cam ESA Concentric Einzel Lens Geometry and Electrostatics

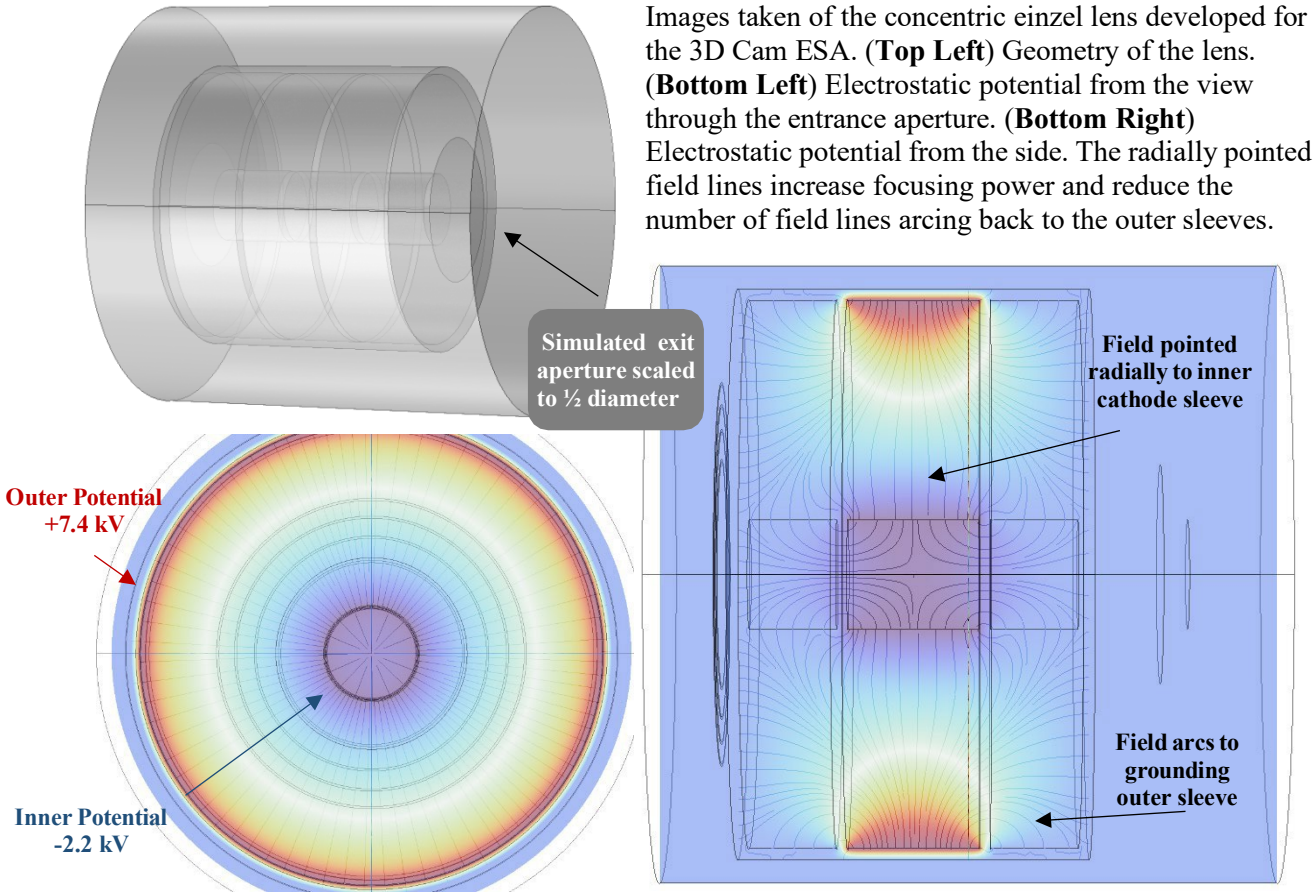

Images taken of the concentric einzel lens developed for the 3D Cam ESA. (**Top Left**) Geometry of the lens. (**Bottom Left**) Electrostatic potential from the view through the entrance aperture. (**Bottom Right**) Electrostatic potential from the side. The radially pointed field lines increase focusing power and reduce the number of field lines arcing back to the outer sleeves.

The four rings comprising the object are focused down onto an output image plane that is scaled down to half the diameter (i.e., the disc placed at the exit aperture in the top left image in Figure 2.6) with their relative interspacing maintained. The subsequent post-acceleration system (-15 kV) would accelerate the particles into a collimated beam thereby preserving the final image. By employing the concentric einzel lens not only was the overall path length and therefore instrument dimensions reduced but the necessary voltages were kept low by maintaining a k-factor of ~2 i.e., only 10 kV was needed on the outer sleeve to accept particles with 20 keV/e. Ultimately, the concentric einzel lens demonstrated the feasibility of mating the 3D Cam ESA to the T-FIPS ToF chamber for future missions to explore the solar wind or planetary magnetospheres.

Figure 2.7 3D Cam ESA Concentric Einzel Lens Particle Ray Tracing

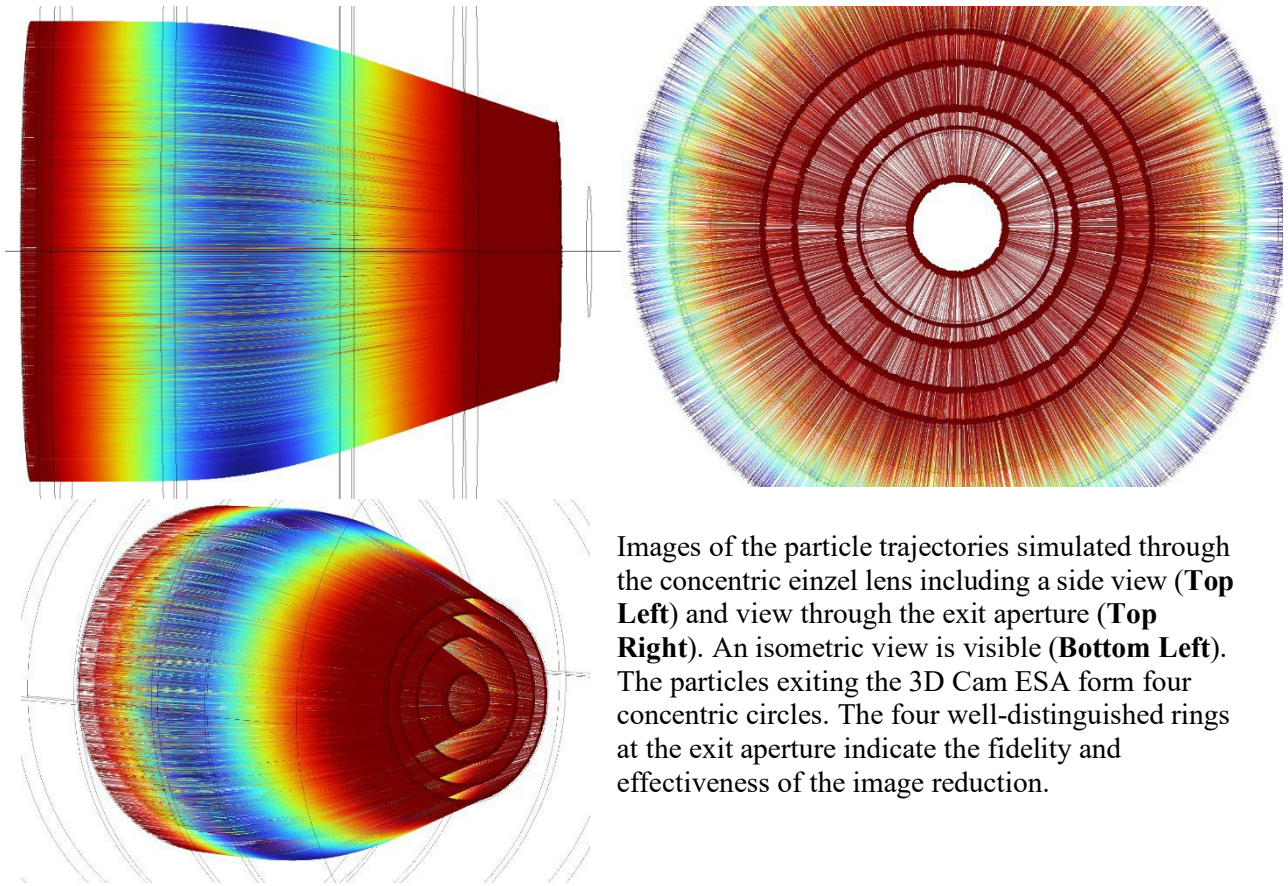

Images of the particle trajectories simulated through the concentric einzel lens including a side view (**Top Left**) and view through the exit aperture (**Top Right**). An isometric view is visible (**Bottom Left**). The particles exiting the 3D Cam ESA form four concentric circles. The four well-distinguished rings at the exit aperture indicate the fidelity and effectiveness of the image reduction.

2.2.4 T-FIPS Time-of-Flight Chamber

The technical advancement of the T-FIPS ToF chamber was the primary focus on this research. As a consequence, considerable effort was made towards the development of its performance model. Initial toy models were used to explore both the single harp T-FIPS model and the dual harp "Extend-o-FIPS" version (see e.g., top left image in Figure 2.2). Additionally, a CAD model was created for each in order to conform the results to the true mechanical structure (Figure 2.1 and bottom left image of Figure 2.8). After defeaturing, certain assemblies were removed because of their complicated structure and inability to produce quality simulation domain meshes. These included the carbon foil and electrostatic mirror mounts. In their place were generated COMSOL native planar circles or ellipses. For the case of the electrostatic mirror a cylindrical sleeve was placed around the three consecutive plates that replace grids in order to encapsulate the fields similar to the original design. The remodeled electrostatic mirror is

Figure 2.8 T-FIPS Time-of-Flight Chamber Configurations

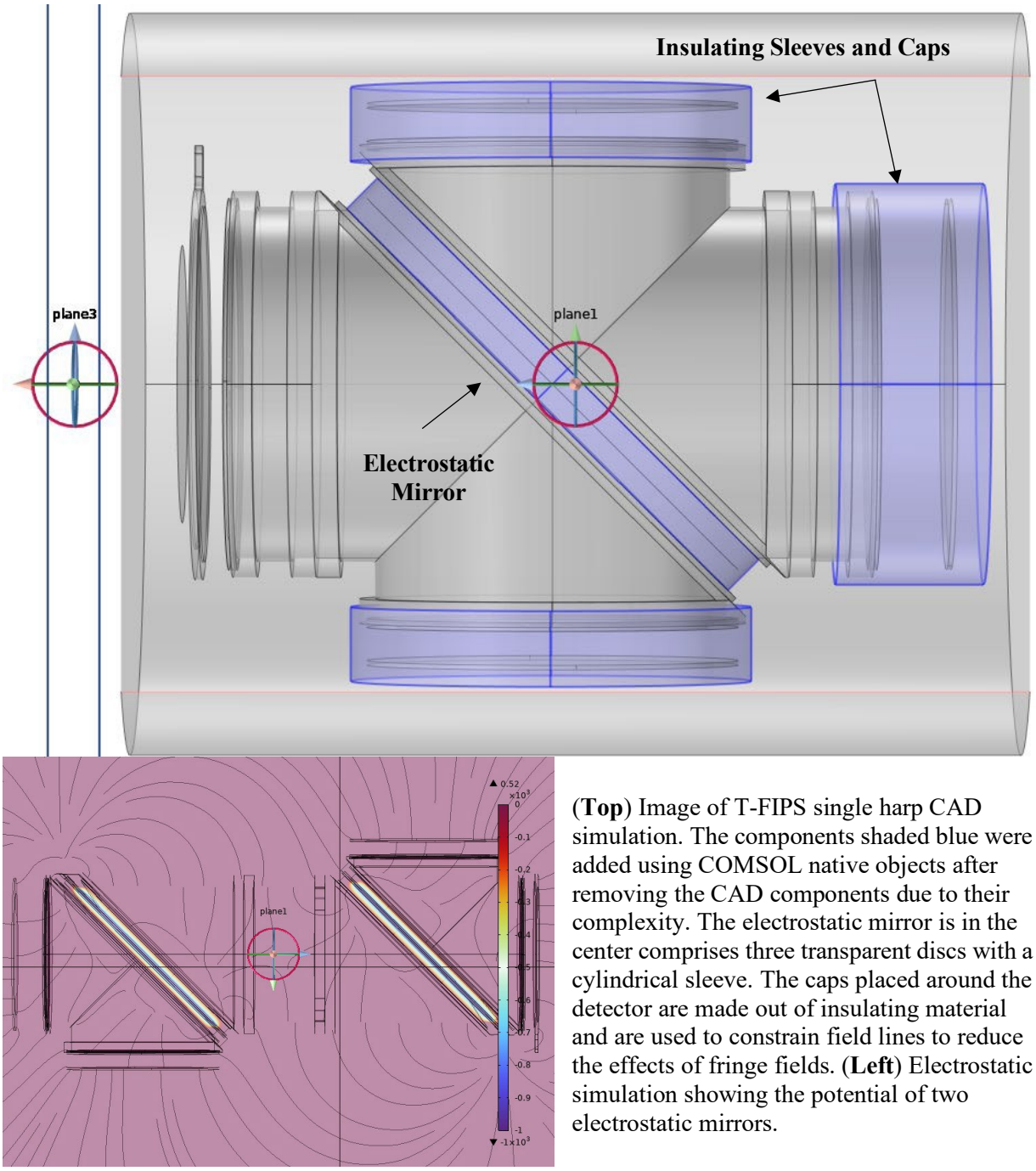

(**Top**) Image of T-FIPS single harp CAD simulation. The components shaded blue were added using COMSOL native objects after removing the CAD components due to their complexity. The electrostatic mirror is in the center comprises three transparent discs with a cylindrical sleeve. The caps placed around the detector are made out of insulating material and are used to constrain field lines to reduce the effects of fringe fields. (**Left**) Electrostatic simulation showing the potential of two electrostatic mirrors.

shown as the blue shaded region at the interior of the chamber in the top geometry in Figure 2.8. The interior planes were made transparent to particles so that they behaved similarly to the carbon foil and electrostatic grids. In order to simulate the effects of passage through a carbon foil on the particle's energy and scattering angle TRIM simulations were produced for the ions H^{+}, $He^{1\text{-}2+}$, $C^{1,4\text{-}6+}$, $N^{1,5\text{-}7+}$, $O^{1,6\text{-}}$

Figure 2.9 Time-of-Flight Chamber Particle Distributions

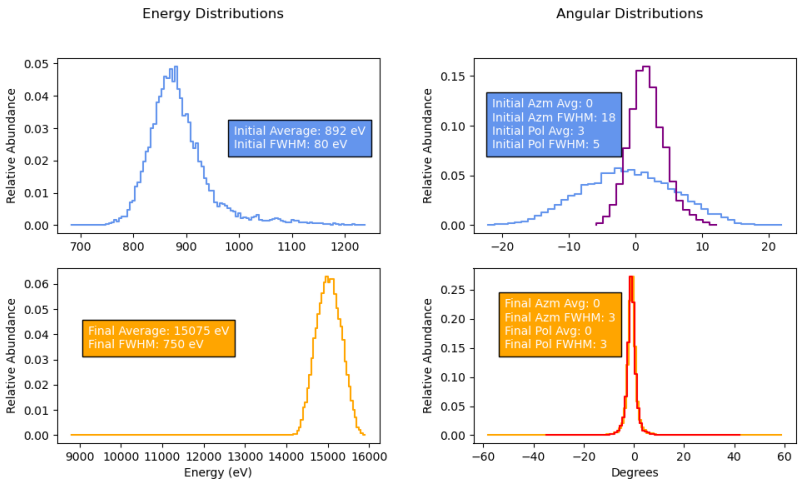

Energy and angle distributions of proton particles exiting an ESA and after energization through the post-acceleration system and passing through an 100 Angstrom thick carbon foil. The post-acceleration collimates the particles into a beam. There is less scattering and energy straggling in the results than expected in the real instrument.

$^{8+}$, $Fe^{1,8\text{-}16+}$ using a foil thickness of 100 angstroms. The initial particle energies that were explored matched those capable of passing through the entrance ESA at 5, 10, and 15 keV/e (e.g., N^{7+} = 10 kev/e × 7e = 70 keV initial energy). The initial (left side) and post-processed particle (right-side) for proton distributions are plotted in Figure 2.9. The particles are first boosted in energy by the post-acceleration system. In addition, the relatively wide angular distributions that exit the ESA are collimated by the acceleration into a tight beam prior to entering the foil. However, the TRIM simulations resulted in less energy straggling and tighter angular distributions than expected indicating the results underestimate the scattering and stopping power experienced during transition through the carbon foil. The resulting particle energies and trajectories were imported into the COMSOL particle ray tracing model as initial conditions for particles passing through the foil. The results of the particle ray tracing model are shown in Figure 2.10. When an ion (blue particle) passed through the plane representing the foil an electron (red particle) was generated.[28] The carbon foil is slightly negative in potential with respect to the ToF chamber body or relative ground; this results in a considerable acceleration boost for the low mass electrons away from the foil towards the electrostatic mirror. Evidenced by the blue block-M particles in the top image in

[28] Transiting proton particles typically produce 1-3 electrons with ~ 1 eV energies upon exit and increase in number with particle mass (Allegrini et al., 2003). Nonetheless, our simulations were simplified to only produce one electron at the foil for each ion entering the chamber.

Figure 2.10 T-FIPS Time-of-Flight Chamber Ion Optical Model

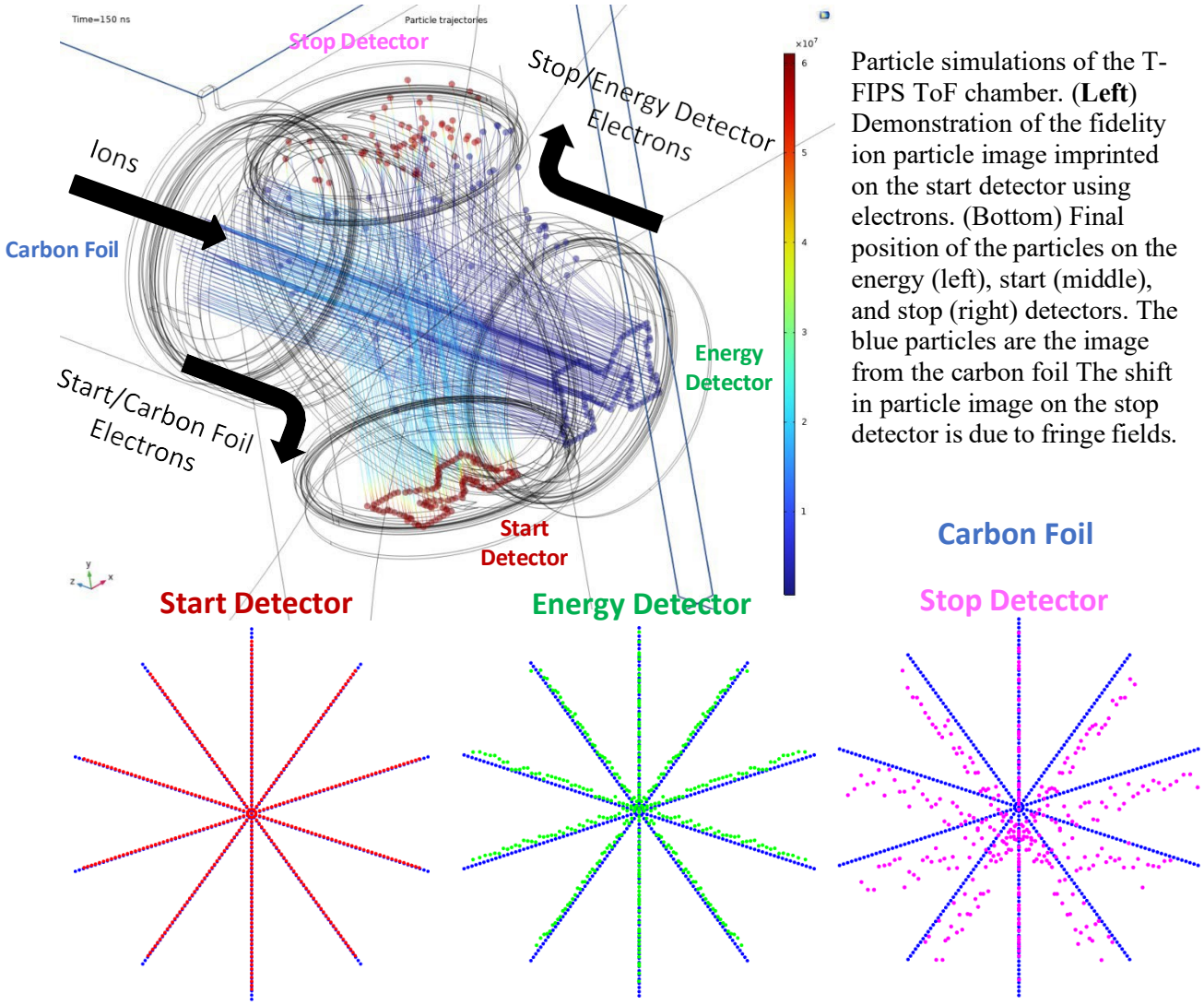

Particle simulations of the T-FIPS ToF chamber. (**Left**) Demonstration of the fidelity ion particle image imprinted on the start detector using electrons. (Bottom) Final position of the particles on the energy (left), start (middle), and stop (right) detectors. The blue particles are the image from the carbon foil The shift in particle image on the stop detector is due to fringe fields.

Figure 2.10, ions pass through the electrostatic mirror with minor deviations in trajectory resulting from the field within the mirror. The symmetry of the sandwiched grids results in a correction on the latter half that roughly offsets the deviation that occurs in the first (see e.g., energy exchange that occurs in the bottom plot of Figure 2.16). Nonetheless, the ions' behaviors are relatively unchanged and for higher energies and masses the interaction with the mirror disappears altogether. In contrast, the paths of the electrons (red particles) are dramatically altered as predicted – the angle of redirection is nearly 90° exactly. In addition, there is a substantial voltage drop from the Start MCP exit aperture and the detector face that assists in pulling the electrons into straight paths (see top left image of Figure 2.3).

Figure 2.11 T-FIPS Time-of-Flight Simulated Efficiencies

Number of Ions		5000
Detector	**Transmission**	**Percent Efficiency**
Start	5000	100%
Energy	5000	100%
Stop	4499	90%

Consequently, as seen by the red particle block-M (top) and the red star pattern (bottom-left) in Figure 2.10, the electron image is nearly a perfect mirror of the original object produced at the carbon foil at individual ions' transit locations. Because of the spatial precision of microchannel plates and the quality of the image on the Start detector, the particle position is recorded using the electrons reflected by the electrostatic mirror from the carbon foil. When the ions exit the ToF chamber opposite to the entrance they strike another planar disc representing the energy detector sensitive area (i.e., green star pattern in Figure 2.10). The detector is also slightly negative with respect to the ToF chamber body, and the secondary electrons generated through the simulation are boosted back towards the mirror, similar to the carbon foil. Nevertheless, as witnessed by the magenta star pattern the fidelity of the original image at the Stop detector from the carbon foil is at that point nearly destroyed – whereas the number of electrons arriving at the Start detector is equivalent to the number of ions passing through the foil only approximately 90% make it from the energy detector to the Stop detector (see Figure 2.11). However, these efficiencies are high because of the idealized mirror that are simulated using planar discs instead of grids that would result in field leakage and more scattering. The electrons that do not make it to the Stop detector are lost due to the effects of fringe fields along the detector edges (see e.g., pre-modified ToF chamber simulation in top-left of Figure 2.3). Additional components were added to reduce the impact of fringe fields between the ToF chamber exit apertures and the Start, Stop, and Energy detectors. The modifications to regions around the detectors are shaded blue in Figure 2.8 and include insulating sleeves with caps to trap and redirect field lines toward the chamber; the improvements led to modest increases in triple-coincidence measurements and improvement in image quality on the Start detector, especially at the edges. Future versions of the T-FIPS ToF chamber will likely incorporate insulating sleeves like those built in the model using native objects to assist in reducing fringe fields and enhance performance. Eventually, the results of the simulation will be joined with the experimental results produced in the

laboratory to accurately predict the behavior of ions not available for terrestrial calibrations (e.g., corrosive oxygen, ions with charge greater than +1, etc.). Overall, the numerical models for the T-FIPS ToF chamber were successful and useful through the development cycle of the design and production of the prototype hardware.

2.2.5 Electrostatic Mirrors

The electrostatic mirror is an integral component of the T-FIPS ToF chamber and relatively novel device used in space particle detectors. In previous instruments, grids were modeled using transparent planes like the one used in ToF chamber simulations.[29] However, it is possible to produce individual simulations containing a small portion of an electrostatic grid. The term small in this case refers to the number of wires – the complexity of the grid scales quadratically with square frames and the intersection points require considerable computational power and memory to mesh and solve for physics models. Nevertheless, quality simulations of small meshes are possible with COMSOL and explored during this research. The initial simulations studied the extension of the electric field into the ToF chamber body. The theory of operation for the T-FIPS Tof chamber includes two field-free regions – the first region is enclosed by the entrance aperture, first mirror grid, and Start detector exit aperture and the second region is enclosed by the last mirror grid in addition to the Stop and energy detector exit apertures. This is accomplished through grounding grids at all six locations and is visible as the two field free triangular regions within the chamber in the top-left image of Figure 2.3. In theory, particles move unchecked through these regions because there are no electric fields with which to interact. In reality, particles interact with complicated network of field lines emanating and terminating at various points on the network of square borders creating the surface. The shape of the electric fields is evidenced by the white lines terminating on the grids in the top frame in Figure 2.12. The results of the simulation indicate a

[29] This is the only method available for large-scale SIMION simulations as well.

Figure 2.12 Electrostatic Mirror Simulations

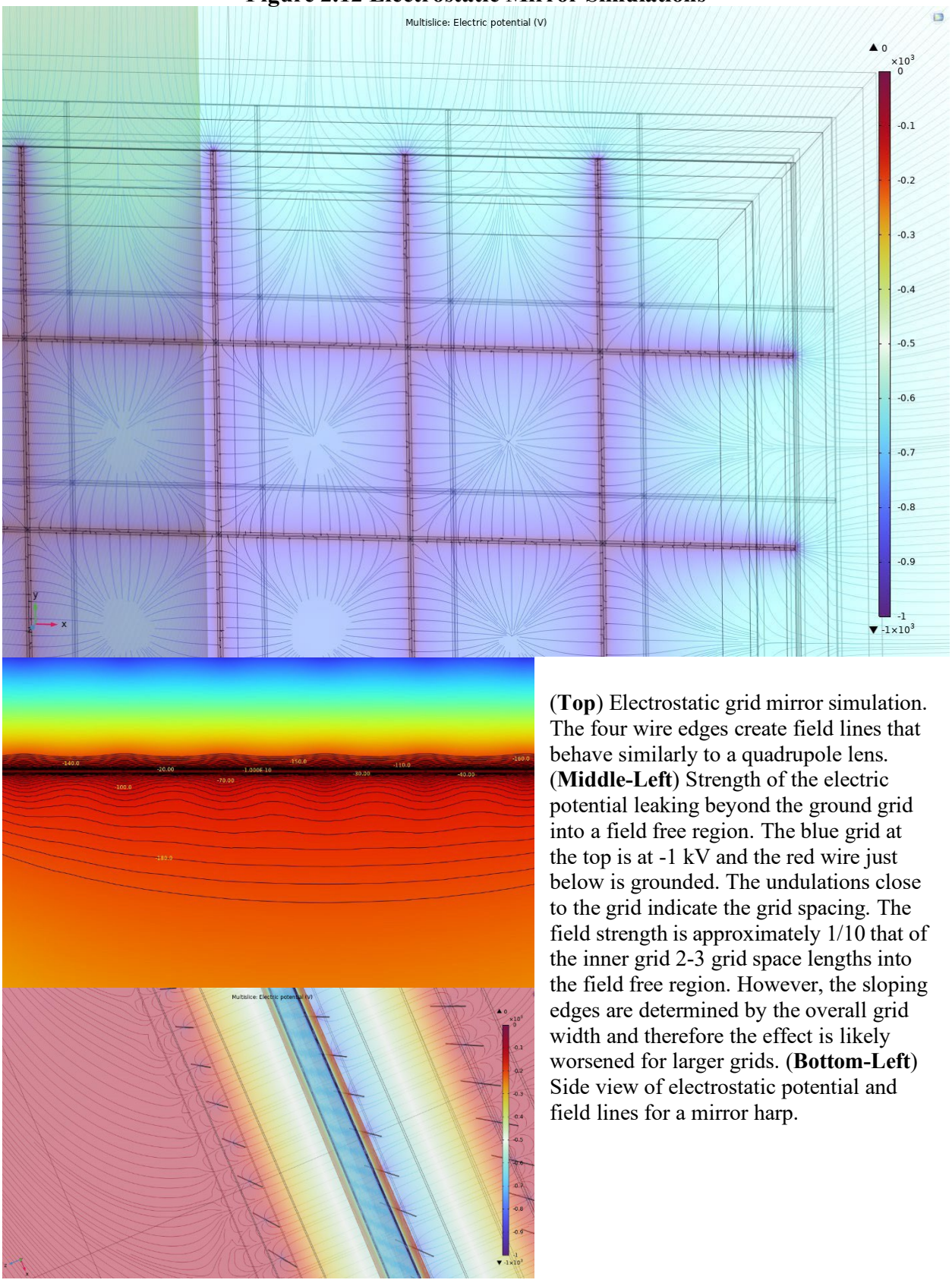

(**Top**) Electrostatic grid mirror simulation. The four wire edges create field lines that behave similarly to a quadrupole lens. (**Middle-Left**) Strength of the electric potential leaking beyond the ground grid into a field free region. The blue grid at the top is at -1 kV and the red wire just below is grounded. The undulations close to the grid indicate the grid spacing. The field strength is approximately 1/10 that of the inner grid 2-3 grid space lengths into the field free region. However, the sloping edges are determined by the overall grid width and therefore the effect is likely worsened for larger grids. (**Bottom-Left**) Side view of electrostatic potential and field lines for a mirror harp.

similar field topology as an einzel lens – each pixel acts like a squared lens. This makes sense considering the mirror uses a grounded=energized-grounded series configuration similar to the cylindrical sleeves of an einzel lens (see section 2.2.3 for discussion). Furthermore, not all the lines terminate within the surface layer containing the grid; a portion leaks out into the field-free region before arching back towards the nearest grounded wire on the grid. The depth of this penetration was analyzed by plotting the equipotential lines extending off the grid surface in middle-left image in Figure 2.12. For example, it can be seen that for a voltage of -1 kV (colored blue at the top of the simulation domain) on the inner grid of the electrostatic mirror there is a 2-3 grid space length penetration into the field free region (the bottom region containing black undulating lines). The grid spacing can be inferred by the spatial separation between waves in the equipotential. Moreover, the slope back toward the grounding grid at the edges of the simulation are caused by the grounded mirror mount (not seen). Therefore, it is probable that the penetration into the field free region is worse for larger grids that are beyond basic simulation capabilities. Additionally, the difference in electric field lines between grids and harps, or meshes with unidirectional wires, were investigated. Examples of harp simulations are shown in the bottom-left of Figure 2.12 and the top and bottom-left of Figure 2.13. Naturally, it was recovered that the rectangular lensing effect is reduced to only a single focal plane. The field lines in this focal plane are shown in black in the electrostatic simulation in the bottom left of Figure 2.12. From these results, it is reasonable to assume that the scattering produced by electrostatic mirrors using grids will be eliminated along the axis parallel to the harp wires; this hypothesis can be investigated using additional studies using charged particle ray tracing. In sum, the electrostatic models of individual grids yielded important information concerning the behavior of electrostatic mirrors.

Further exploration into the behavior of grids was made through charged particle simulations. In particular, electrons were scattered off a simulated electrostatic mirror using 3D modeled grids to deduce the behavior of those sent to the Start and Stop detectors. The results are depicted in the bottom-left (harp) and bottom-right (grid) simulations in Figure 2.13. The particles are partially deflected prior to passing

Figure 2.13 Electrostatic Harp and Electron Mirror Simulations

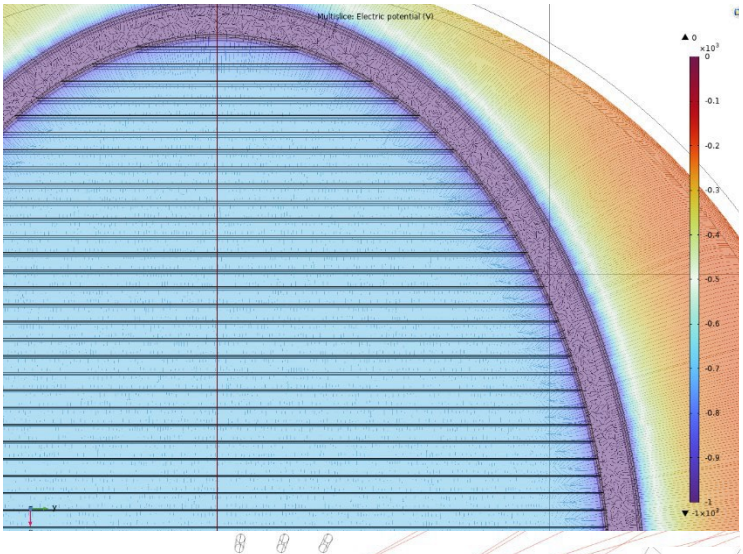

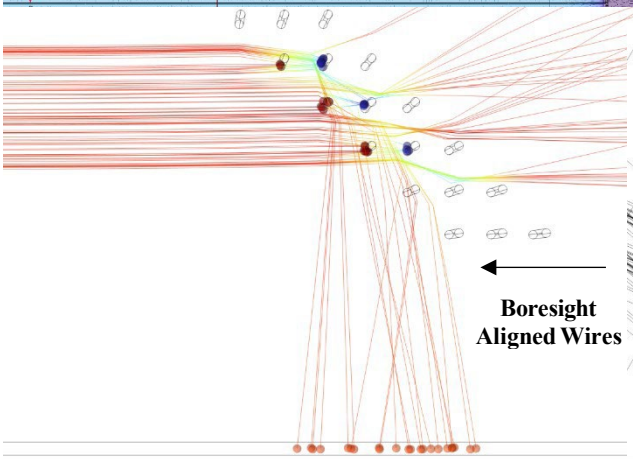

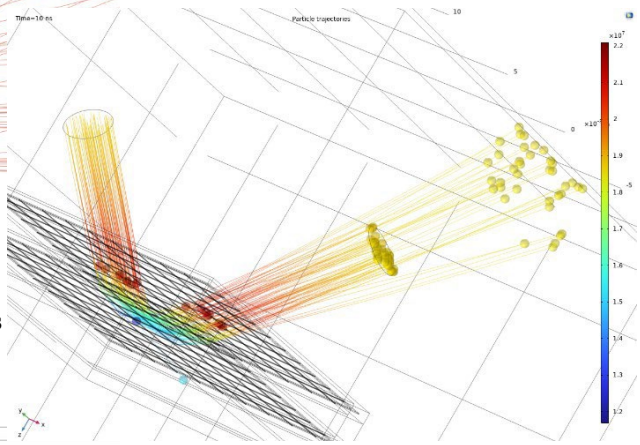

(**Top Left**) Simulation of an electrostatic mirror harp. The lensing effect is reduced to a single plane. (**Bottom Left**) Simulation demonstrating the adverse effects of boresight aligning the grid wires – and therefore field lines. Some particles are reflected down but many pass through unlike simulations with 45° alignment (**Bottom Right**) Particle ray tracing simulation results of an electrostatic mirror grid. Most of the electrons land directly on the plate symmetric to their origin.

the initial grounded by leaking fields. Once inside the mirror the majority of particles redirected perpendicular to their original trajectory along a single axis before exiting. The spatial separation seen in the exiting image demonstrates the scattering and some particles are lost through contact with the wires. Thus, the models display a faithful representation of the behavior we expect to see in the electrostatic mirror. Furthermore, the alignment between the wires of the three grids comprising the mirror was studied using particle trajectory models. For example, in the bottom-left harp simulation in Figure 2.13 the wires are boresight aligned and produce field lines pointing anti-parallel to the particles inbound path in contrast to being 45°-aligned. The simulation results show that the greatest number of particle reflections occur when the grid wires in the mirror stack are aligned 45° to the particle trajectories bisecting the inbound and outbound motion. Thus, the placement of the individual arrays within each grid does seem to impact

performance. Grids with both boresight and 45° wire alignment were purchased for experiment testing in the T-FIPS prototype analyzer to test these results. Collectively, the investigations using numerical models showed the differences in realistic versus idealized simulations. Yet, they accurately portrayed the desired effects we hope to see in grids reinforcing their importance in precision ion optical devices and thus spaceborne particle detectors. For such reasons, it is hopeful that future 3D studies into electrostatic grids will be continued by coupling their simulated performance with experimental results.

Section 2.3 Ancillary Developments

In addition to the CAD development and ion optical models there were numerous calculations, meetings, and decisions that went into designing the T-FIPS instrument. These entailed trade studies, their own individual simulations, and in some instances designing entirely new components. Such were the necessary steps to take once production and assembly began and abstract concepts met reality. For example, the use of either avalanche photodiodes (APDs) or solid-state detectors (SSDs) as the energy detector was a critical design consideration, as was determining the voltage at which to place the energy detector system with its supporting electronics. Nearly all of these decisions have been finalized and the pathway to completing the prototype detector is almost clear. Nonetheless, the thought and time put into the decision-making process is a testimony to the intricacy of the instrument design.

2.3.1 Electroformed Grids[30]

A major improvement in the T-FIPS design when compared to its original FIPS heritage is the introduction of electroformed meshes. On the FIPS instrument sent to Mercury the ToF chamber utilized harps rather than grids in both the entrance and exit aperture and the electrostatic mirror. The harps were hand wound using thin, high tensile strength wire and with relatively low lines per inch (LPI). The results

[30] Research and trade studies into various meshes were done at behest and guidance of SPRL mechanical engineer Louis Marr.

were delicate and highly effective yet the labor hours it took to produce a small number of working harps was enormous. Fundamental to the start of the T-FIPS enterprise was envisioning the use of modern engineering and production techniques to improve performance and ease manufacturing and assembly; the hand wound harps were components whose design and revision contained significant potential to achieve these goals. At first two alternatives were considered: electroformed and photoetched meshes. Photoetched meshes are produced using lithography – a mask is placed over a thin sheet of metal covering the regions that are meant to be removed. A coating known as the photoresist is spread over the metal in order to overlay the regions left exposed by the mask. The photoresist is baked into a protective layer, and the mask is washed away to leave bare metal beneath. Then the sheet is sprayed with a chemical etchant that dissolves away the unprotected, previously masked regions leaving on the locations with the photoresist. Using this process, it is possible to create thin metal meshes. One benefit of the photoetching process is that it can be used on nearly any metal (e.g., steel, aluminum, copper, etc.). This provides a range of material properties to explore for benefits such as tensile strength and conductivity. However, the photo etching product naturally produces wires with square cross-sections: the initial surface of the sheet is flat, and the chemical etch removes metal directly below along a vertical path. A rectangular or bar shaped wire is not conducive for high voltages.[31] Furthermore, they do not provide suitable surfaces upon which to adhere carbon foils (source: discussions with manufacturers). Therefore, electroformed meshes were chosen for immediate study and testing for the possible benefits of photo etched versions was left to be explored in the near future. Whereas photoetching is a subtractive manufacturing technique, electroforming is additive. A base conductive layer known as a mandrel is submersed in a electrolytic cell, i.e., a container of solution containing dissolved metals. Currents are passed through the solution into the mandrel drawing and depositing the dissolved metals onto the mandrel at the same time. The process coats the mandrel atom by atom creating a uniform, smooth

[31] The potential for high voltage breakdown is increased at sharp corners or points due to the electric field concentration it generates.

Figure 2.14 Electroformed Meshes

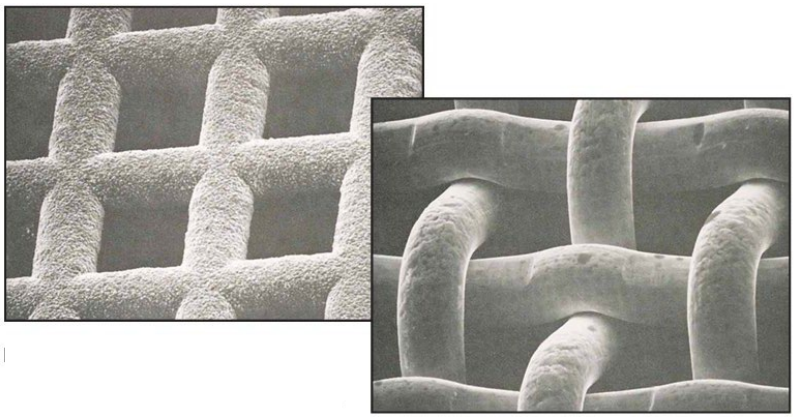

High resolution photographs showing the finished product of electroformed (**Left**) and woven (**Right**) meshes. The electroforming process natural creates wires idealized for high voltages and placement of carbon foils (Parkinson, n.d.).

surface. The final product has ideally curved surfaces even about the mesh vertices that are well-suited for high voltage applications. The differences in quality with respect to woven meshes can be seen in Figure 2.14. Additionally, the cost of electroformed and photoetched meshes are comparable and well below the cost of producing hand wound harps. However, the metals available for the electroformed meshes are limited – effectively nickel is the only applicable material for spaceflight detectors.[32] Furthermore, electroformed meshes are the preferred substrate onto which carbon foils are placed. The number of wires was determined to approximate the transparency of the original FIPS harps. The option of producing a harp (unidirectional) rather than grid (square lattice) meshes using photo etching and electroforming processes was explored; it is possible to produce electroformed harps but would have some design limitations and would require some research performed at the manufacturing level.[33] Thus, grids will be employed in the T-FIPS prototype design. Special mounts were developed to grow, support, and contain the wires. The final decision was to determine the best grid alignment for the electrostatic mirror; either the wires of the three elliptical meshes could be boresight aligned to maximize transparency or align 45° to the boresight and particle motion to produce the most ideal electric field lines.[34] Although simulations indicate greater performance for 45° aligned wires both options were purchased for testing in the

[32] The other standard options are gold and copper.
[33] It is not likely that any harps can be produced using additive or subtractive manufacturing without some form of a mechanical support structure bisecting the frame.
[34] Boresight aligned wires produce an electric field pointing opposite to the initial particle trajectory and back towards the entrance aperture. In theory, this would reflect the particle backwards.

prototype chamber (see discussion in previous section for further details). In conclusion, the development and design of electroformed meshes for the T-FIPS prototype and future instruments was an important process that dramatically reduces cost and improves assembly. Future tests in the laboratory will determine the performance characteristics of electroformed meshes and their differences with handspun harps, if any.

2.3.2 MCP Crosstalk

Significant time and planning went into preventing MCP crosstalk in the T-FIPS ToF chamber. MCP crosstalk occurs when particles that are adsorbed onto the surface of the Start or Stop MCP interact with an electron – likely from the carbon foil or energy detector – and are released through electron stimulated desorption (ESD). Due to the high voltages within the device it is feasible for the released particle to become energized enough to produce a measurable signal if it were to strike another detector. Placing the Start and Stop MCPs so that their sensitive areas are directly opposing each other significantly reduces the overall size of the ToF chamber while increasing the chance of MCP crosstalk. In the worst-case scenario, the desorbed ions could create a runaway feedback loop potentially becoming a significant noise source. To investigate the possibility of ESD-caused crosstalk we designed 2D (top-left) and 3D (bottom-left) ToF simulations seen in Figure 2.15. Indeed, it was shown using the ion optical simulations that the voltages in the chamber naturally promote this behavior; the same force that pulls the electrons onto the MCP plate accelerates ions in the opposite direction back towards the mirror. In Figure 2.16 we have plotted the position and energy of the desorbed ions as a function of time. The ions liberated from the Start detector by carbon foil electrons are shown on the left side of the dotted red line occurring during the 5-65 ns interval. They are born with low energy (5 eV) and pass through the harp and strike the opposing Stop detector. The ions pick up speed through the HV grids and are accelerated to high energies (15-16 keV) into the electrostatic mirror. After traversing the mirror, the ions are decelerated to low energies (5 eV) by the HV grids of the Stop detector but still strike the detector face liberating adsorbed

Figure 2.15 T-FIPS Start and Stop Detector Crosstalk

(**Top Left**) 2D simulation demonstrating ESD producing crosstalk across the Start and Stop detectors (credit, UM student Marcello Lara). (**Bottom Left**) 3D simulations showing the same effect. (**Right**) Diagram for the placement and alignment of the electrostatic mirrors and MCP detectors in the Suprathermal Ion Spectrograph (SIS)(Rodríguez-Pacheco et al., 2020a). It is clear from the arrangement that if crosstalk between the detectors was an issue it should have been visible in the SIS data.

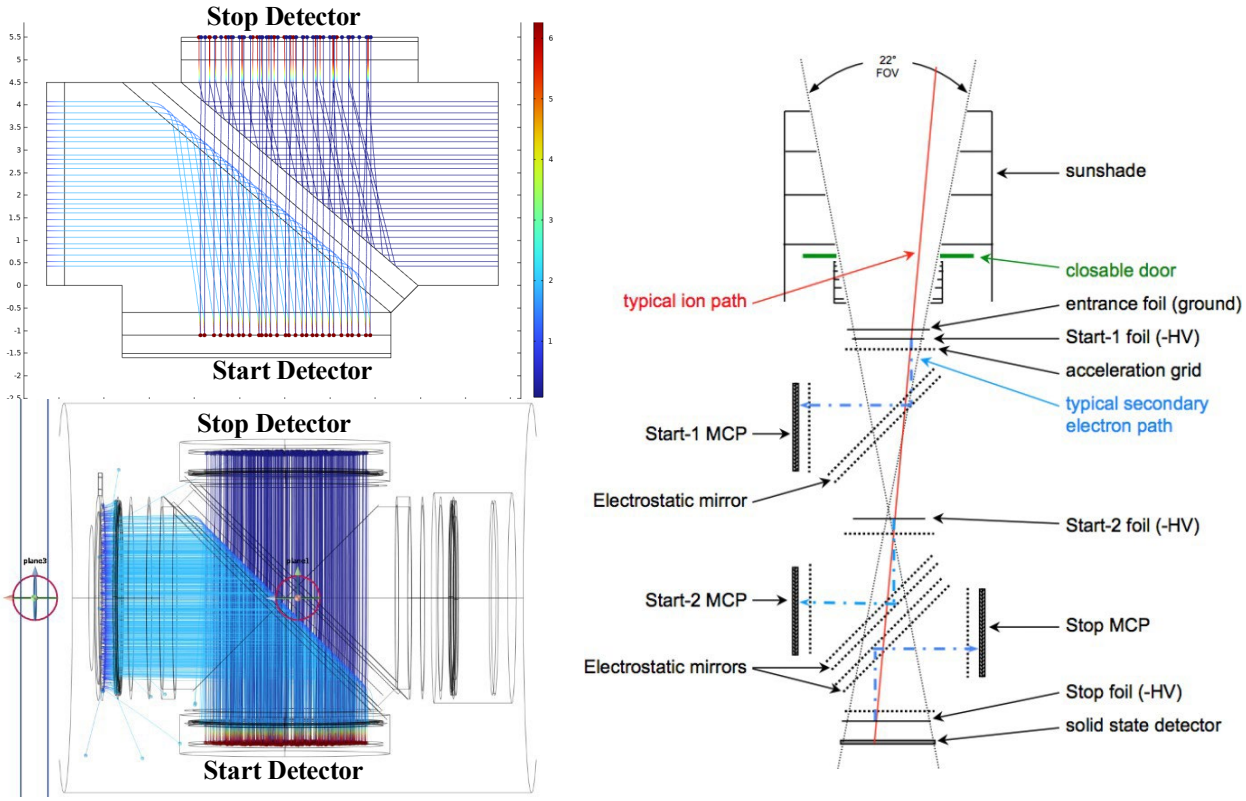

ions (at ~65 ns). The ions are accelerated in the opposite direction and back towards the Start detector during ~65-120 ns. Therefore, to prevent runaway crosstalk two initial ToF chamber versions were developed: a single and dual harp.[35] However, the primary advantage of the T-FIPS instrument has over other charge-resolving spectrometers is its compact size and reduced mass (see Introduction). In addition, there were discussions with other instrument developers who have utilized electrostatic mirrors with opposing facing detectors that indicated that this issue was not prevalent in the instrument (source: George Ho, SIS Principle Investigator). In the left diagram in Figure 2.15 it can be seen that the MCPs

[35] The dual harp model was colloquially called Extend-o-FIPS because of the extra length added to the chamber to accommodate the second harp.

Figure 2.16 Crosstalk Particle Properties

The position and energy of desorbed particles study for detector crosstalk. At approximately 5 nanoseconds the carbon foil electrons liberated adsorbed ions from the Start MCP. The particles are accelerated across the HV grid before being decelerated and striking the Stop detector. Then adsorbed particles are released from the stop detector and accelerate back to hit the Start detector. The ions achieve higher energies inside the harp at separate intervals. Some particles strike the mirror grid and become trapped resulting in flatlined positions and energies.

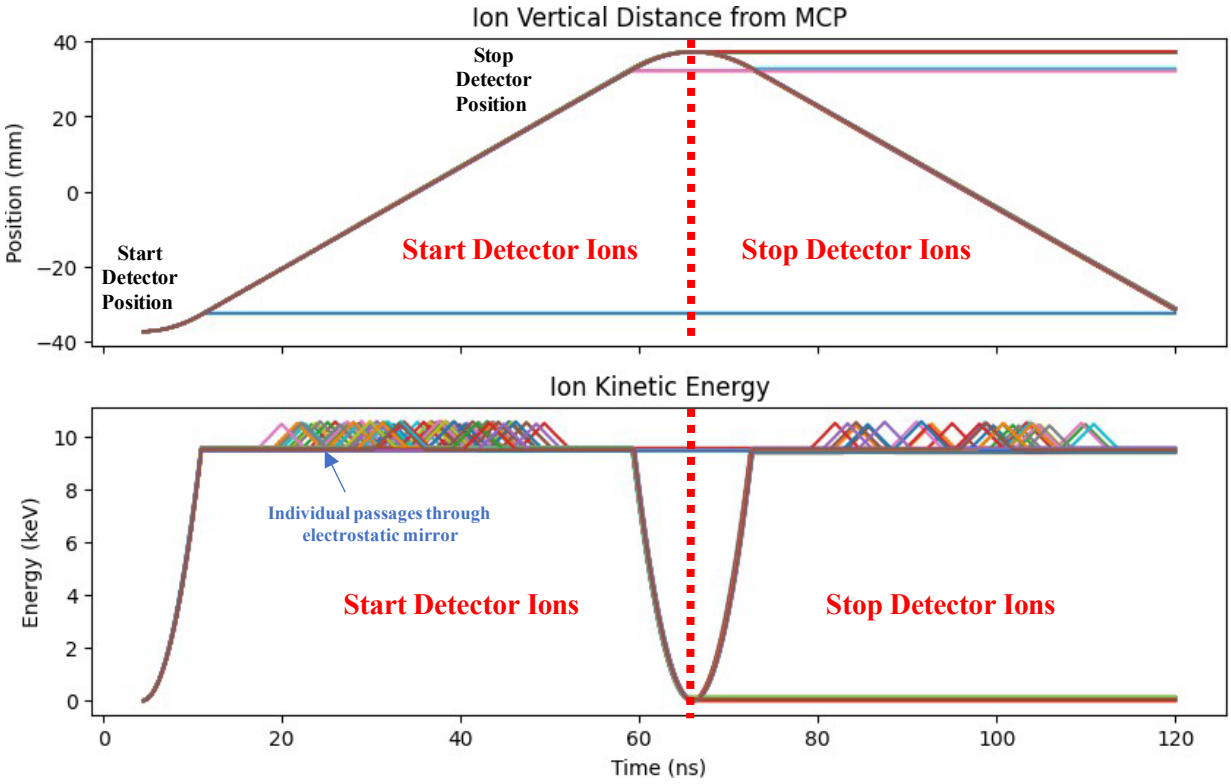

used in the Suprathermal Ion Spectrometer on the Solar Orbiter spacecraft are positioned opposite to each other similar to T-FIPS. The lack of crosstalk could be due to the low energies at which adsorbed ions arrive at the opposing detector limiting the likelihood of ESD. Therefore, the investigations into the dual harp model were abandoned and the single harp design was selected for prototype development. While the concern for MCP crosstalk has not been completely invalidated, future experimental tests will determine if and by how much it will produce noise signatures.

2.3.3 Microchannel Plate Alignment

The alignment of microchannel plates is a critical facet of assembling any space particle detector that utilizes them for particle counting or imaging. Microchannel plates are incredibly fast (~GHz rate)

and are excellent for position sensing (~μm resolution). They became an industry standard for laboratories and consequently spaceborne instruments because of the regularity in pulse width and speed due to the simple and relatively uniform signal production process. Similar to channel electron multipliers (CEM), microchannel plates are made out of insulated ceramic or glass that is coated with a semiconducting material. A CEM is comprised of a single tube that opens to a wide aperture to provide a large acceptance for single particle detection. An MCP in contrast is comprised of many small glass capillaries compressed together to make a high-density array of small apertures that enable its position sensitivity. The top left drawing in Figure 2.17 depicts the signal production process which begins when a particle strikes the outer surface of the plate or enters a capillary with sufficient energy to strike produce an electron. A voltage is applied across the plate nearly parallel to the capillaries that accelerates the liberated electron down into the device. As the electron gains energy and strikes the inner walls of the capillary it produces more electrons resulting in a large gain ($\sim 10^{3\text{-}4}$). The resulting electron cloud is emitted out the backside of the capillary and recorded using a position sensitive anode to collect the charge. Eventually, the gain achieved by a plate becomes saturated because the space charge density of the electron cloud in the capillary prevents additional electrons from being released. Consequently, many detectors stack multiple thin plates on top of one another with a slight gap in between that allows for the electron cloud in a single tube to spread and enter multiple capillaries thereby allowing for further increase in charge. This process naturally trades spatial resolution as the electron cloud spreads out for larger pulse signals.[36] Both the FIPS and therefore T-FIPS instrument utilize three MCPs stacked together known as a Z-stack detector. The name Z-stack comes from the fact that the capillaries are not aligned perfectly straight up and down i.e., they form a small deviation from a straight line bisecting the plate

[36] In practice, the spatial resolution is determined by the electronics which increase in size and power with more refinement. The spatial resolution in space instruments never achieves that which is capable of the plates themselves – nor is it commonly necessary! Mass spectrometers using Rutherford backscattering are a rare example otherwise.

Figure 2.17 Microchannel Plate Alignment Procedure

(**Top Left**) Depiction of how electron gain occurs in MCPs. Additionally, a second plate can be placed below with an 180° opposing bias angle to make a chevron stack (a third yields a Z-stack). (**Bottom Left**) CAD of the MCP alignment fixture used to assemble the MCP detectors. Teflon pegs were added to the sides of the Teflon sleeve to slide up and immobilize the plates (seen in picture laying on the platform). The CAD was developed by Marcello Lara and assembled by Marcello and Isaac Fertig. (**Bottom Right**) Demonstration of how the MCP alignment fixture operates with a light shone below (note: prototype detector assembly occurred in a cleanroom). (**Top Right**) Results from alignment tests using a light and photometer. A second peak did not occur at 180° as expected. However, alignment can be achieved at the minimum value. The light experiment was designed and recorded by Anusha Banninthiya.

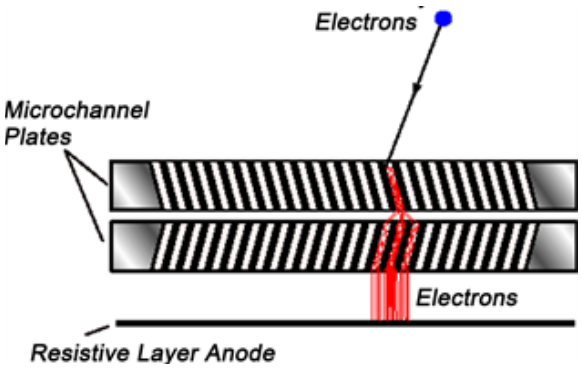

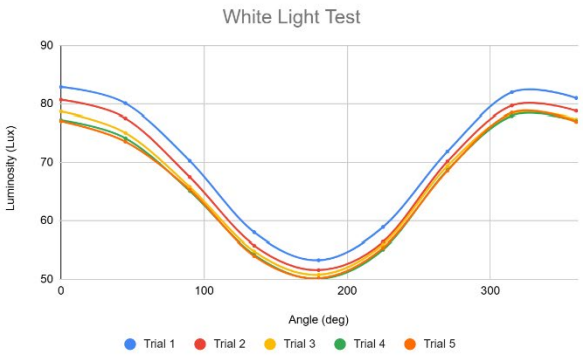

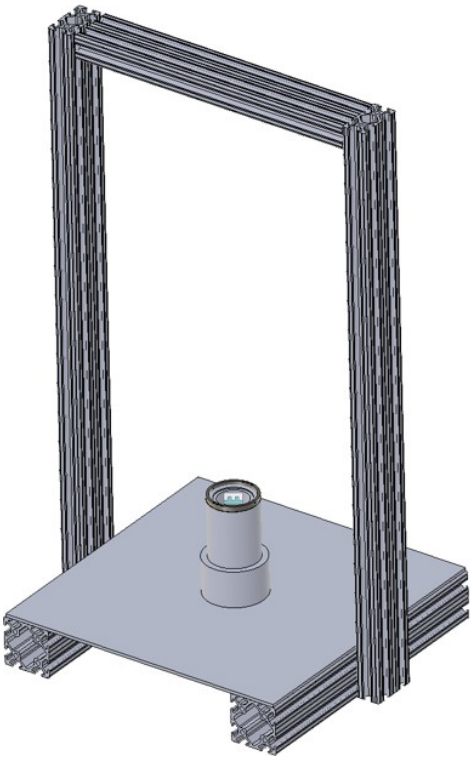

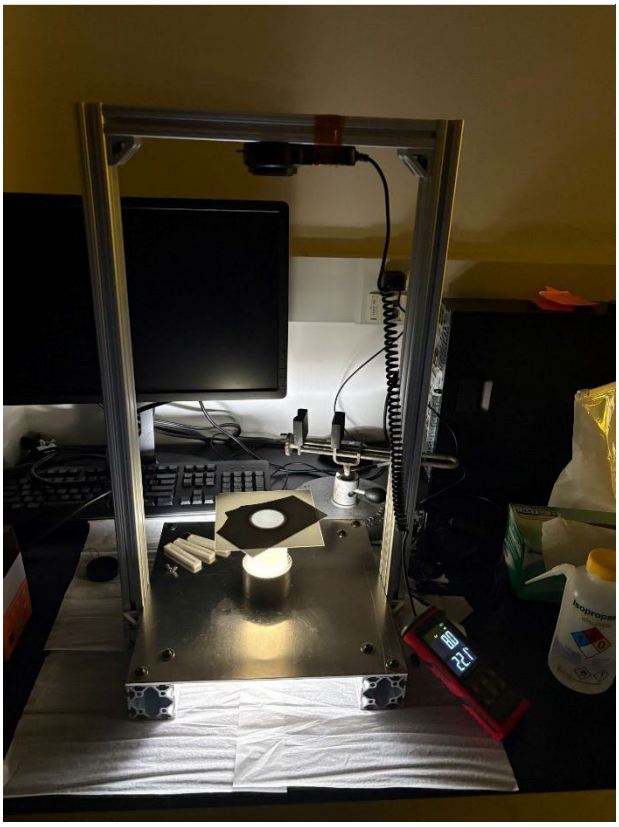

surface known as a bias angle. The bias angle prevents feedback from desorbed ions within the plate becoming accelerated back towards the capillary entrance. In order to be properly aligned the bias angle of each plate in the Z-stack must be 180° opposite to the one adjacent so that they form a Z-shaped pattern in the profile. For the similar reasons, detectors that stack two plates like the top left drawing in Figure 2.17 are known as chevrons. Therefore, aligning the plates properly during installation is a critical feature of assembling the detector.

Initially, we were concerned that not aligning the bias angles of the plates would cause an alteration in the recorded image. A diagram illustrating the alignment process and the calculations that were derived is provided in Figure 2.18. The resulting figures indicated that the slightest deviation in orienting the plates would result in a spatial relocation that far exceeds the micrometer spacing of the pores. From this it was realized that the mechanical tolerance of the MCP mounts themselves could not maintain vertical alignment of the MCP pores in a stack and that misalignment in the plates would not distort the image and that the primary for aligning the bias angles is achieving the highest gain; by not aligning the plates the electrons become choked as they necessarily rotate rather than scatter straight down. Therefore, a special mounting fixture was designed and built to aid in the alignment of the MCP plates during assembly.[37] A CAD and picture of the mounting fixture are provided in the bottom-left and bottom-right of Figure 2.17, respectively. The mounting fixture or (assembly jig) comprised a single hallowed Teflon tube mounted on a plate with a diameter equivalent to the plates. It is a well understood feature that when the MCP plates are aligned the passage of light through the stack increases (correspondence with INCOM manufacturer). Therefore, a light was shone from below up through the Teflon tube into the MCP stack while it was being assembled to confirm proper alignment before immobilization the plates together. Furthermore, a light sensor was placed above the MCP to record the

[37] Design and assembly were provided by laboratory technicians and University of Michigan students Isaac Fertig and Marcello Lara.

Figure 2.18 Microchannel Plate Alignment Tolerance

The alignment of the plates is necessary to ensure the capillaries are anti-aligned to one another.



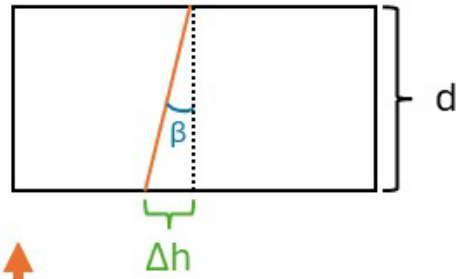

The maximal displacement (Δh) is limited by the bias angle (β) and thickness of the plate (d). For a bias angle of 8° and plate thickness of 0.60 mm the maximal displace is $\Delta h = d \cdot \tan(8°) = 84.3\ \mu m$.

Example:
For a maximal displacement of 84.3 µm and misalignment angle of 5° the total displacement is 52.34 µm. For complete misalignment (90°) the total displacement is 842.53 µm.

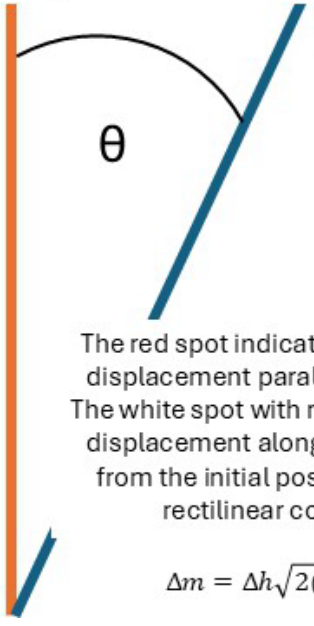

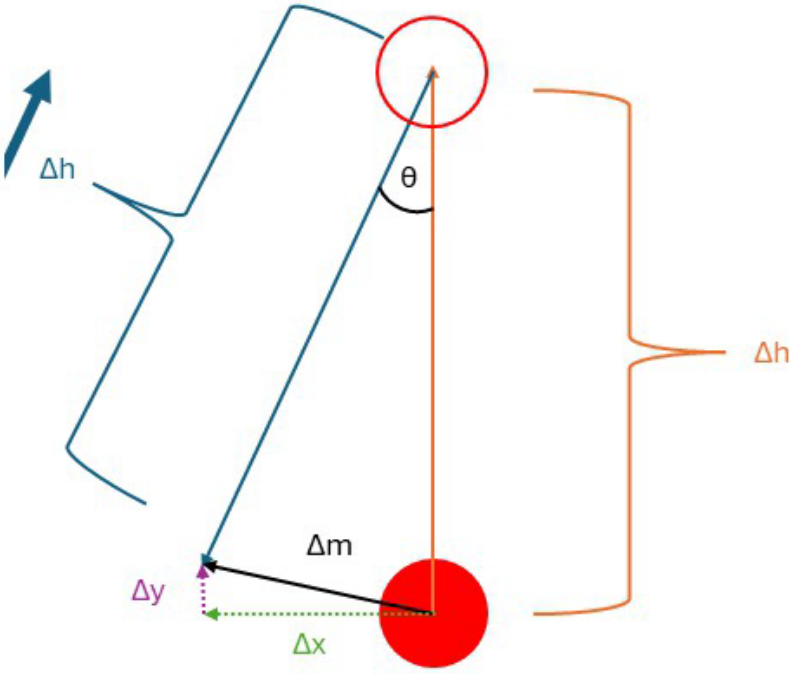

The red spot indicates the initial impact position on the first plate. The orange arrow is the displacement parallel to the plate surface as the electrons move down the first capillary. The white spot with red outline is the position on the second plate and the blue arrow is the displacement along the second capillary. The black arrow (Δm) is the total displacement from the initial position and the green and purple arrows (Δx, Δy) is the displacement in rectilinear coordinates. For a given misalignment angle (θ) these values are:

$$\Delta m = \Delta h\sqrt{2(1-\cos\theta)} \qquad \Delta x = \Delta h \sin\theta \qquad \Delta y = \Delta h(1-\cos\theta)$$

intensity of light that passes through for quantitative analysis.[38] The amount of light passing through MCP plates as a function of the rotation angle of the upper plate is plotted in the top-right of Figure 2.17. However, as can be seen a second peak was not discovered when the plates were opposingly aligned (i.e., by 180°) as expected.[39] Therefore, the plates were aligned by eye using a fiduciary mark on the outer edges. Further studies will continue to explore the efficacy of using a light source to align the plates by attempting to use different wavelengths, filters, and meters. A procedure for assembling and aligning the plates was completed and used to produce the T-FIPS Start detector.[40] The MCP fixture, procedure, and alignment process will continue to support T-FIPS testing and operations throughout its evolution as a prototype and instrument.

2.3.4 Photon Occulter

Early in the development of the T-FIPS instrument there was an exploration into alternative electrostatic analyzers for the instrument (see top-right and bottom-left of Figure 2.2 for examples). During investigations into designs inspired by the Fisheye ESA there were generalizations that were sought after with respect to its desired performance features. One in particular was its ability to occult the detector from solar electromagnetic radiation. Broadly, an important feature of ESAs are their ability to prevent light from travelling through and into the interior of the instrument; it is common to roughen or blacken the inner surfaces of the electrodes to capture or absorb light rays. A three-reflection principle is used as a general rule: a photon should not be able to reach a detector before three reflections off interior surfaces of the instrument. For a spherical or toroidal ESAs the process is relatively straightforward,

[38] The light sensor was research, developed, and validated by University of Michigan student Anusha Banninthiya.
[39] It in fact occurred at a low point in luminosity. Ironically, this still provides a quantitative value for when the plates are aligned.
[40] The original MCP assembly procedure was written by University of Michigan student Jayveer Phull.

Figure 2.19 Photon Occulter

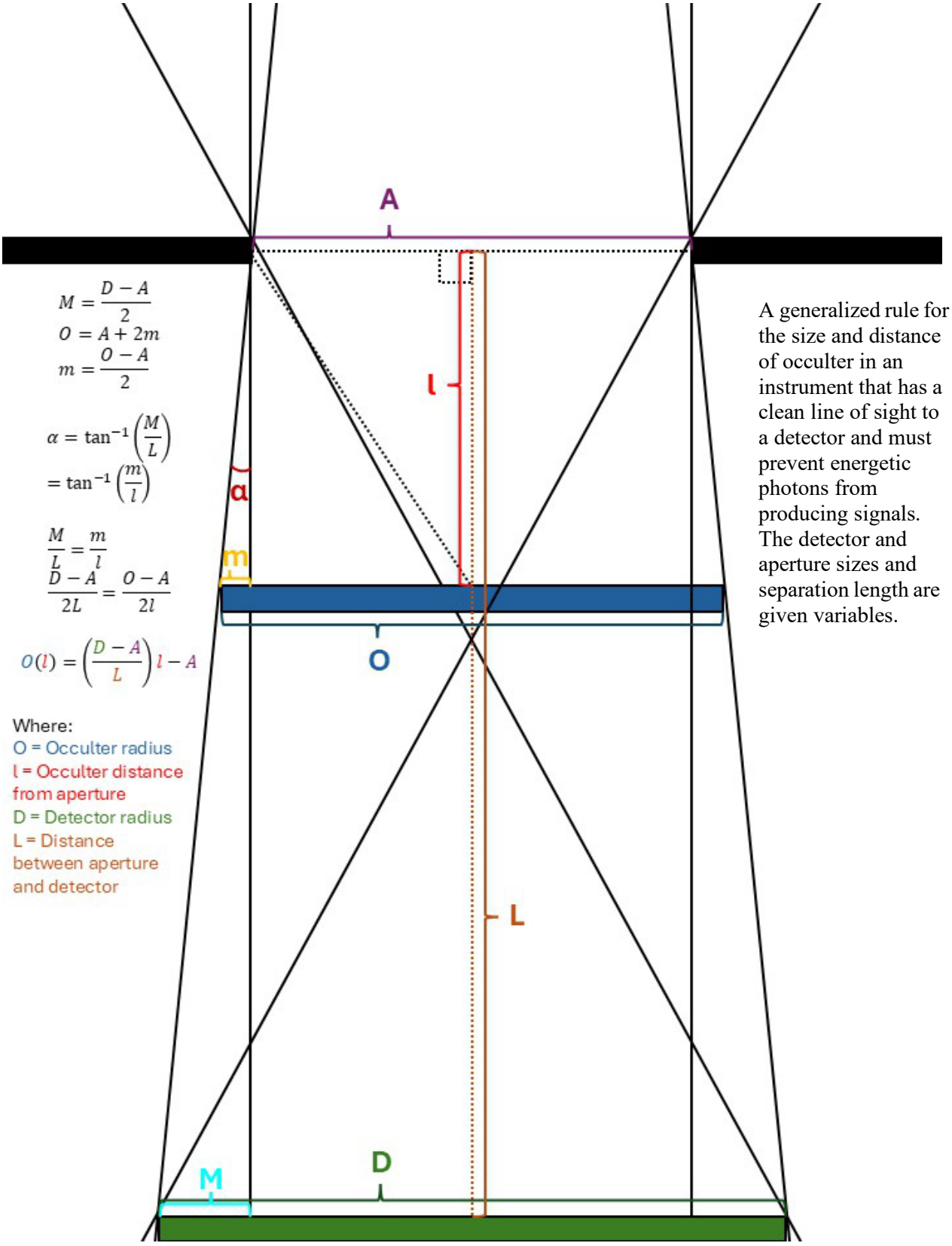

A generalized rule for the size and distance of occulter in an instrument that has a clean line of sight to a detector and must prevent energetic photons from producing signals. The detector and aperture sizes and separation length are given variables.

however, the Fisheye ESA has a near straight line trajectory through the instrument but for the stacking pin in the center occulting the aperture. Therefore, designs that sought to remove the stacking pin would need an occultation plane installed into its place. Figure 2.19 shows a simple analysis for developing an occulter to prevent the direct passage of light onto a detector. Light (and particles) enter the instrument at the top through the aperture (labeled A). The occulter (labeled O) effectively shadows an area on the detector face (labeled D). A generalized principle relating the size of the occulting disc and distance from the aperture seen on the let-hand side was devised that uses detector, aperture size, and distance between as input variables. This formula was applicable for a variety of ESA designs that are similar to the Fisheye ESA and that might envision removing or reducing the size of the stacking pin. Additional measures are necessary to prevent the transmission of photons that bounce off interior surfaces towards the detector. Nonetheless, the occulter dimension analysis provides a strong foundation by which to prevent noise signatures in newly devised ESAs.

2.3.5 Energy Detector System

The energy detector system is the major difference between the FIPS instrument and the T-FIPS charge-resolving upgrade. Consequently, it has consisted of many of the most in-depth analyses and design reviews that has occurred thus far in the development of T-FIPS. In principle, the addition of an energy detector is simple – in practice it's a complicated engineering endeavor. Implementing an energy detector is a convoluted task because of the existence of the post-acceleration system. Recall that the post-acceleration system operates by floating the ToF chamber walls, aperture grids, and carbon foil up to a high negative potential. Thus, upon exiting the ESA an ion is accelerated dramatically into the ToF chamber with a velocity proportional to the inverse of its mass-per-charge (qi/mi). Therefore, two options present themselves: (1) place the energy detector system at the same voltage as the ToF chamber or (2) place it at the spacecraft and instrument ground same as the ESA. If the energy detector system is floated to the same potential as the ToF chamber the electronics used to process the signal must be at the same

voltage; the reason for this is that the signal produced by the energy detector must be passed to a preamplifier quickly before it is lost into transient noise signatures that frequently occur. Once amplified the signal is shaped and discretized using an analog-to-digital converter (ADC) or similar device. This digitization process is often performed by an Application-Specific Integrated Circuit (ASIC) and is best done at the same potential as the detector so that information is not lost when it is passed through the voltage gap. Hence, the task stretches from placing an energy detector inside the high voltage bubble to installing the entire detector system with support electronics. Incorporating the energy detector system onto the chamber at the same potential necessitates additional measures to transmit power and signal across the voltage gap along with revisions in the exterior housing. Naturally, therefore, we explored techniques for not floating the detector at the same potential as a chamber (Option 2). Placing the detector at spacecraft and instrument ground means the electronics are at the same potential as the system and transmission of power and signal is done easily with simple connections. Moreover, the electromechanical challenges are transferred from a voltage gap between the energy detector system and external housing to the ToF chamber and the detector system itself. This is not wholly without its own challenges: placing the energy detector system at ground requires significant design twoards isolators that would be used to keep the two structures separate. The reason for an advanced, specialized design is to prevent high voltage breakdown while minimizing the distance between detector system and ToF chamber to inhibit fringe fields and enhance ion optical performance i.e., particle transmission. Nevertheless, this design challenge of developing isolators for an energy detector at ground is much smaller than redefining the back end of the instrument and outer housing to create a sufficient vacuum gap around a floated detector. However, placing the energy detectors at ground means that the ions undergo the opposite effect of when they enter; the ions are decelerated by the same quantity they were accelerated by at the carbon foil. First, the deceleration implies that the lowest energy particles will not have enough energy to penetrate through the dead layer to produce an energy signal. Second, the majority of the ions that are transmitted through the ESA and penetrate the carbon foil are neutralized as a result. Therefore, they will not be decelerated by the voltage drop at the energy detector and will produce a

second energy signal that is separated from the ions of the same species by an energy difference equivalent to their original charge multiplied by the post-acceleration voltage; the ions and neutrals will have the same time-of-flight signature but different energy measurements. This will appear as two different spectra overlapping in the E-ToF space used to separate particles thereby reducing the ability to distinguish particles. Plots of the overlapping behavior in Figure 2.20 show simulated measurements of heavy ions as ellipses with horizontal width denoting the timing resolution (Δt) at 10 ns and vertical width denoting the energy resolution ($\Delta E/E = 0.12$). These fixed values were used as for initial study in place of better values collected by future simulations or experiments. The charge of the particles is indicated by the color of the outer boundary of the ellipses for neutral (blue) and +1 ions (red). The plots show the spectra with time-of-flight on the x-axis and energy on the y-axis for three ESA voltage settings at 0.05, 0.18, and 0.36 keV/e in the top, middle, and bottom plots, respectively. It can be seen that at higher energies the spectra become more overlapped in E-ToF space. Significant research was devoted toward a more advanced forward model for predicted spectra using the abundances of heavy ions within the solar wind utilizing an energy detector system at ground.[41] In addition, the updated model included energy resolutions derived from TRIM simulations. The improved results further validated the significant degradation in resolution to the overlapping of particle measurements. Ultimately, two factors determined that the energy system would have to be placed inside the high voltage bubble and not at the spacecraft ground: (1) the ion and neutral spectra were too close in E-ToF space to faithful deconvolve for the species and abundances in the solar wind and (2) the electrons sputtered from the energy detector used for Stop signals would not be capable of overcoming the potential necessary to make it into the ToF chamber. This latter fact became obvious under investigation of the system using ion optical simulations. As a

[41] The forward model was extensively tested and developed by University of Michigan student Renin Asirvatham with the guidance of Dr. Erik Fischer.

Figure 2.20 HV Bubble Time-of-Flight vs Energy Spectra

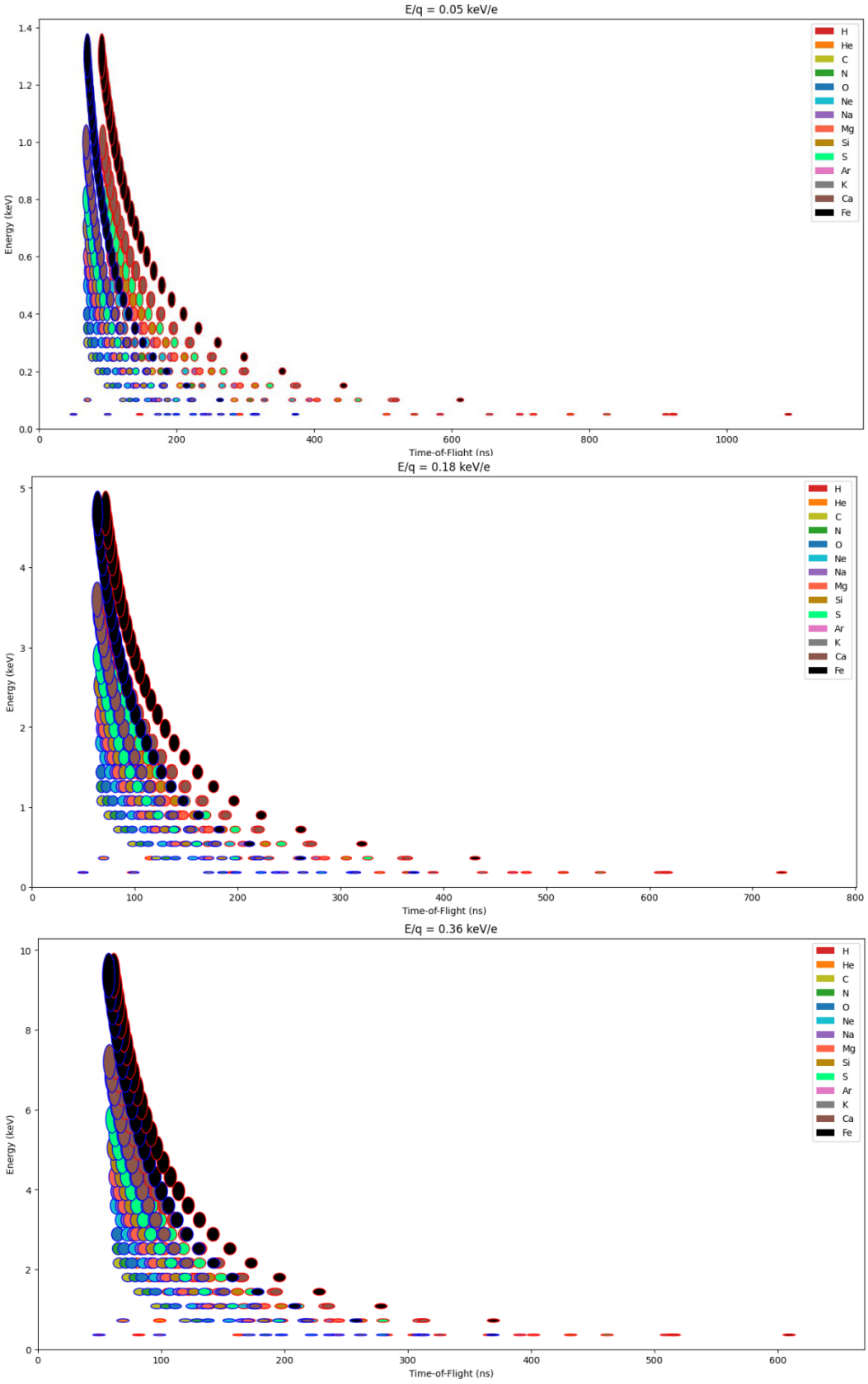

Plots of the energy vs time-of-flight (E-ToF) spectra simulating the performance of the instrument with the energy detector system at ground. By viewing from top to bottom it can be seen that the ions (red perimeter) slowly blend into the neutrals (blue perimeter) completely at higher energies, thereby distorting the spectra of each and making species identification impossible. Higher quality investigations were performed by Renin Asirvatham that included TRIM simulations of the energy detector signals that confirm these results.

result, the only feasible method for producing a start signal with the energy detector system at ground is to place another carbon foil at the exit aperture of the ToF chamber.[42] With the addition of a carbon foil the engineering modifications necessary for implementing an energy detector at ground rise to a comparable level to placing the system within the post-acceleration voltage bubble. Further, utilizing the backside of a second carbon foil is a more novel consideration with less heritage when compared to using the detector surfaces as electron sputtering sources themselves. Therefore, the choice was made to place the energy detector system inside the ToF chamber at the post-acceleration voltage. Considerable time and focus were invested in determining the placement and operating voltage of the energy detector system; the energy was worthwhile and leaves an implementation strategy for producing hardware for the prototype detector relatively straightforward.

In addition, there were several other important considerations made toward developing the energy detector system. First, the prototype needed a mock energy detector to produce electrons to begin testing while the system was being designed, purchased, and assembled. The mock detector is known as the electron production plate and was developed primarily using existing components.[43] The electron production plate mount is a repurposed MCP stack mount. The surface used to produce electrons is a simple aluminum plate with the same diameter as the microchannel plates held together by a wave washer and Teflon ring. By reusing an MCP mount, the diameter and attachment points naturally align to the chamber. Attachment of a HV cable to the plate enables application of different bias potentials to test their impact on electron trajectory and transmission. The selection of the type of energy detector was an additional challenge. As outlined in the introduction, the choice of using solid-state detectors (SSDs) or avalanche photodiodes (APDs) contained different benefits and detractions: SSDs have greater heritage, stable energy signatures, and operate better at colder temperatures but produce slower measurements and

[42] Electrons are sputtered from both the front and back of a carbon foil when ions pass through.
[43] The design of the electron production plate was led by University of Michigan student Isaac Fertig.

have high energy thresholds. In contrast, APDs have increased timing and energy resolutions with thinner dead layers but produce temperature dependent energy measurements with decreased resolution at lower temperatures. Research into the temperature profiles achieved by the energy detector system for specific missions was performed in order to quantify the effect on the APDs.[44] The results indicate that it is possible to utilize APDs for diverse missions. In fact, there are two methods for mitigating the temperature dependency of the energy signal – an active biasing system or environmental control system. An active bias system works by reducing the detector bias voltage for higher temperatures thereby negating the gain increase. However, an environment control system would regulate the temperature by heating the detectors during cooler conditions, producing signals that are more stable and regular energy signals. Altogether, the T-FIPS prototype detector will use APDs, and a thermal regulation system will be developed and tested during experiments in the laboratory. However, the long-term intention is to produce a modular design that can easily incorporate two different detector systems of each type, SSD and APD; the ability to use either detector increases the applicability of the instrument to more science missions. Moreover, the detector system will comprise multiple detectors to provide redundancy and reduce detector size.[45] Thus, in principle it is possible to include both types of detectors to garner the benefits of each for a single mission similar to other detectors. The next, and final step for the T-FIPS prototype development is to purchase the APDs and begin design and production of the energy detector system and its supporting electronics.

The development and construction of the T-FIPS sensor have been the primary purpose of this research and its conceptual evolution has constituted many studies, decisions, and learning processes. The development of the CAD and ion optical models of various subassemblies were pivotal in determining their performance abilities and solving design challenges. Moreover, many obstacles and improvements

[44] Research into the thermodynamic characteristics of the instrument during lunar and solar orbits was performed by University of Michigan student Theodore Saenger.
[45] The background noise of a semiconducting detector scales with size. In particular, the best signal-to-noise ratio is achieved when detector surface area divided by its volume is maximized for fixed volumes (Ogasawara et al., 2012).

were incorporated once theory and design met with production and assembly. Collectively, this has generated a body of work comprising the documentation and research results that accurately portray the T-FIPS instrument and its capabilities as well as outlining the next steps for continuing production. As manufacturing and assembly progresses and experimental tests begin these results will guide the continued development of the instrument and tell the story of how it advanced along the way.

Chapter 3

Hardware Developments and Laboratory Testing

The most important component in an instrument's maturation is its experimental testing and calibration. Experimental analysis must occur in the laboratory and necessarily comes after most of the challenges concerning the conceptual development and assembly of the instrument have been overcome. Nonetheless, it has just as many trials and uncertainties. Many of the technical processes that occur mimic that of the instrument itself: supplying high voltage power, detector operation, signal transfer and processing, etc. In addition, there are the difficulties that come with the terrestrial application of space detector calibrations. For example, the testing of particle instruments on Earth requires the production and maintenance of ultra-high vacuum (UHV) chambers, the generation of heavy ion plasmas, and full motion control of the instrument. Altogether, the task of performing ground calibrations for an instrument requires an intimate understanding of instrument design and experimental physics and therefore it naturally advances alongside developments that occur in the broad application of both fields. Advancements in radiation detectors, mass spectrometry, vacuum systems, plasma production, etc., are important for space particle detectors and must be incorporated onto future science missions for maximal growth and performance. Therefore, research in spaceborne particle detectors is as much of an engineering undertaking as it is a scientific endeavor. The next few sections will outline the hardware developments and experimental tests that occurred during and alongside the development of the T-FIPS instrument. They are a critical start to the final progression of the T-FIPS instrument from an initial

concept to becoming a prototype, and will prove the exceptional quality and lifespan of the instrument through their continued application.

Note: The experimental and laboratory work performed for this research was a team effort and contributed to by many University of Michigan students and SPRL engineers. Many thanks to the students and lab technicians Christopher Bert, Karthik Kamaraj, Marcello Lara, Gaston Wlodawer, Arjun Sharma, Ben Miller, Isaac Fertig, Jaccob Bell, and Jayveer Phull as well as SPRL Engineers Samantha Vaughn (HPIL lab manager), Fernando Saca, Louis Marr, Ryan Barnhart, Jon Reid, Brad Angelocci, and Brian Ferguson for all the work, support, and guidance over the years that led to the results enumerated below (as well as many others).

Section 3.1 Laboratory Improvements

In preparation for the T-FIPS prototype calibrations a number of improvements were made to the Heliospheric Plasma Instrumentation Laboratory's (HPIL) testing facility. In sum, they entail a complete overhaul of the original system that was developed to test the FIPS instrument in the late 90's and early 00's; these include transfer from analog to digital electronics and computer-based system control and monitoring. In addition, most of the equipment was upgraded to more advanced, modern designs. Overall, the improvements to the (HPIL) calibration system elevate it to an equivalent standing to the best space particle testing facilities in the world and position it well for proving out the T-FIPS system.

The most important upgrade to the calibration facility was the addition of the Prevac IS-40E1 heavy ion source. In Figure 3.1, the IS-40E1 is shown attached to a test chamber via a large (~300 kV ceramic break). The IS-40E1 is primarily designed to be a bombarding source used for etching and surface preparation and therefore yields a high flux particle beam – up to 10 mA emission current from the filament and a beam current of 1 μA at 32 mm from the exit aperture. The emission current (and neutral gas density) determine(s) the ion density generated in the ionization chamber prior to acceleration

because the IS-40E1 is an electron ionization source; electron ionization occurs when an electron interacts with an atom destabilizing the orbit of the electrons in its valence shell causing one to separate and produce a singly charged ion. The IS-40E1 comes with its own optical refinement and manipulation system including an internal energization system (up to 5 keV), a wien filter, two foci, and deflection plates. The particles are filtered by mass using the wien filter – or E × B filter, that selects a particle by velocity.

$$FF = qq\vec{\square} + v\vec{} \times \vec{\square} = 0$$

Figure 3.1 The Prevac IS-40E1 Ion Source

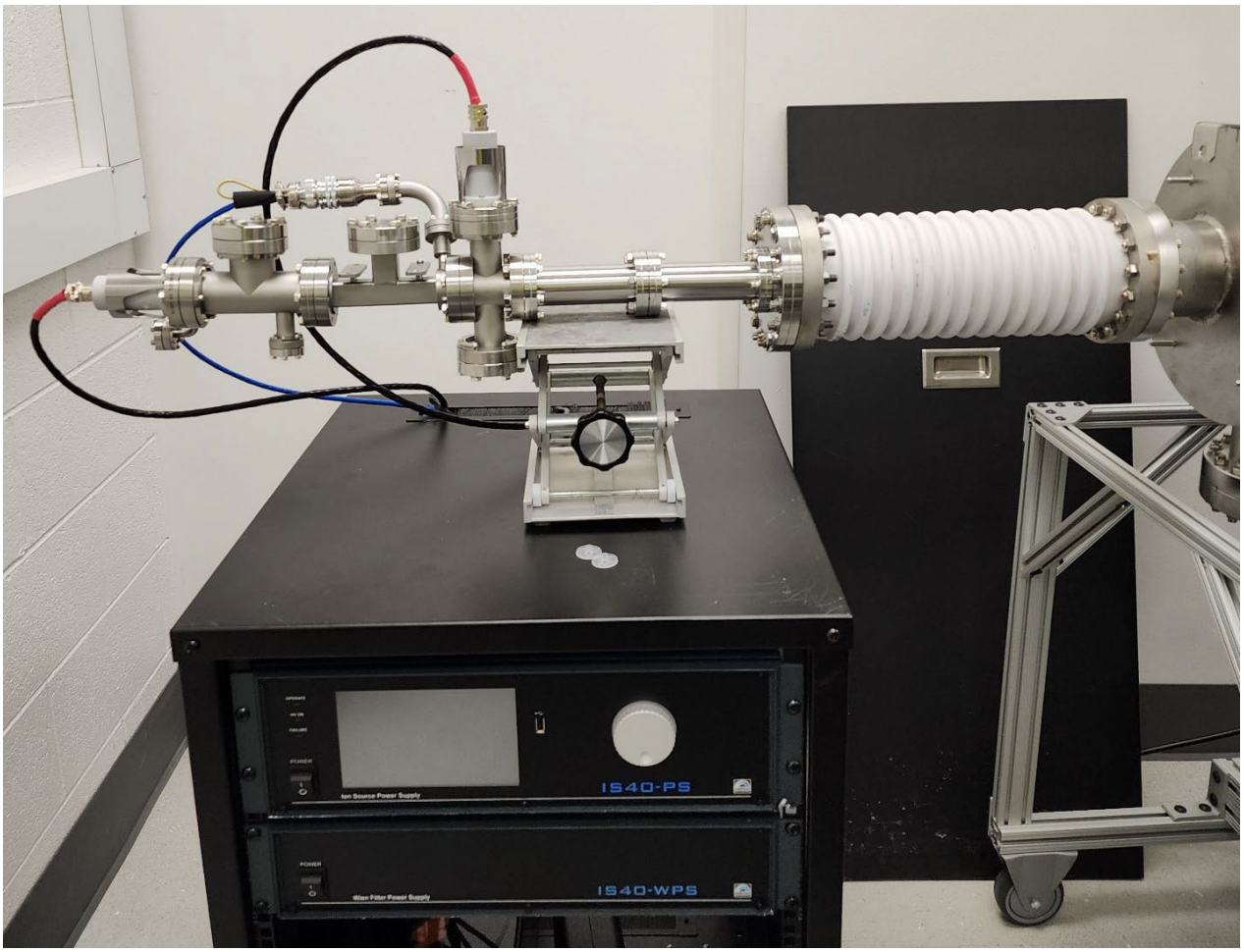

Image of the Prevac IS-40E1 ion source attached to a 450 kV ceramic break. The wein filter is installed in the center without the magnet. The power supplies used to operate the instrument are mounted beneath.

$$\vec{F} = -v\vec{v} \times \vec{B}$$

$$|vv| = \frac{|EE|}{|BB|}\csc\theta\theta = \frac{VV}{\Delta xx \cdot |BB|}\csc\theta\theta$$

Here θ is the angle between the velocity vector and magnetic field and the electric field strength has been converted to a voltage difference (V) and electrode separation length (Δx). Therefore, we have the condition for when the force on the particle is zero. The electric field is always pointed opposite to the force generated by the motion of the particle through the magnetic field. The function has a minimum at $\pi/2$ or when the velocity and magnetic field are perpendicular (and therefore perpendicular to the electric field as well). Thus, for a 1 keV nitrogen atom, a 0.4 tesla magnet, and 1 cm gap between the electrodes one need only apply 469.5 V across the electrodes to allow the passage of the particle.[46] All other particles with different velocities will have their trajectories overwhelmed by the electric (too slow) or magnetic (too fast) fields and not escape through the filter aperture. If a plasma of mixed composition is generated and extracted from the ionization chamber using an energization potential all the particles will acquire a kinetic energy commensurate to their charge alone ($K = q \cdot E \cdot L = -q \cdot [V/\Delta x] \cdot L$).[47] All the plasma particles will achieve the same energy resulting in separate, mass dependent velocity distributions. Therefore, there is a simple relationship between extraction energy and wien filter potential:

$$\frac{\sqrt{2 \cdot KK}}{mm} = \frac{VV}{\Delta xx \cdot |BB|}\csc\theta\theta$$

[46] The IS-40E1 has two options for magnets to mount at the wien filter – 0.04 and 0.4 teslas.
[47] Here K is the kinetic energy of the particle, V is the extraction voltage, Δx is the distance between the ionization chamber walls and the extraction grid, and L is the average path length of a particle to the extraction grid. Not to be confused with the wien filter equation.

$$mm(KK, VV) = 2KK \left(\frac{\Delta xx \cdot |BB|}{VV} \sin \theta\theta \right)^2$$

The selection of the particle via its mass using the wien filter can be achieved for any desired kinetic energy with the correct electric potential identified through the relationship above. The neutral particles are fed into the chamber using a gas leak system and allow for the calibration of instruments using different heavy ions. Once particle mass and energy are selected the resulting beam can be focused or deflected using the sources internal ion optical system. It is also possible to convert the ion gun into a sputtering source by mounting various pellets in front of the source and extracting and filtering the sputtered ions using an electric potential and beam magnet in series. The Prevac IS-40E1 ion gun provides a robust and flexible plasma source for experimental testing of space particle detectors in the calibration facility.

In addition to the ion source there are many other components that were integrated into the calibration system. The ion source is assisted in energizing the plasma by the acceleration system.[48] Figure 3.2 contains images of the CADs developed for the acceleration system (bottom) and complete calibration system (top-left). The acceleration system operates by electrically isolating the portion of the vacuum chamber in which the plasma is generated from the other sections of the chamber (as well as the rest of the laboratory) in order to surround it within a high voltage bubble. This is accomplished using ceramic breaks to isolate chamber surfaces from one another, a polycarbonate tabletop upon which to mount the ion source and support systems, and faraday cage to protect technicians from the high voltages. On the electrically isolated table surface is a copper sheet connecting the ion source, power supplies, a turbomolecular pump, and batteries to operate everything for ~12 hours. A high voltage cube built out of

[48] The acceleration system was developed by University of Michigan student Arjun Sharma with the guidance of Prof. Steve Battel.

Figure 3.2 The HPIL Calibration System

Calibration System

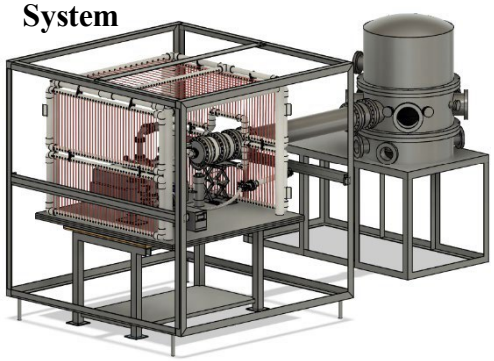

(**Left**) Calibration system with acceleration table and main chamber. (**Bottom**) Close up of the acceleration system. The sides are open on the high voltage cube to allow for visibility into the interior. The chamber side inside the acceleration system is isolated from the rest of the chamber and everything on the able top is floated up to higher potentials to produce acceleration. CAD developed by University of Michigan student Erin O'Malley.

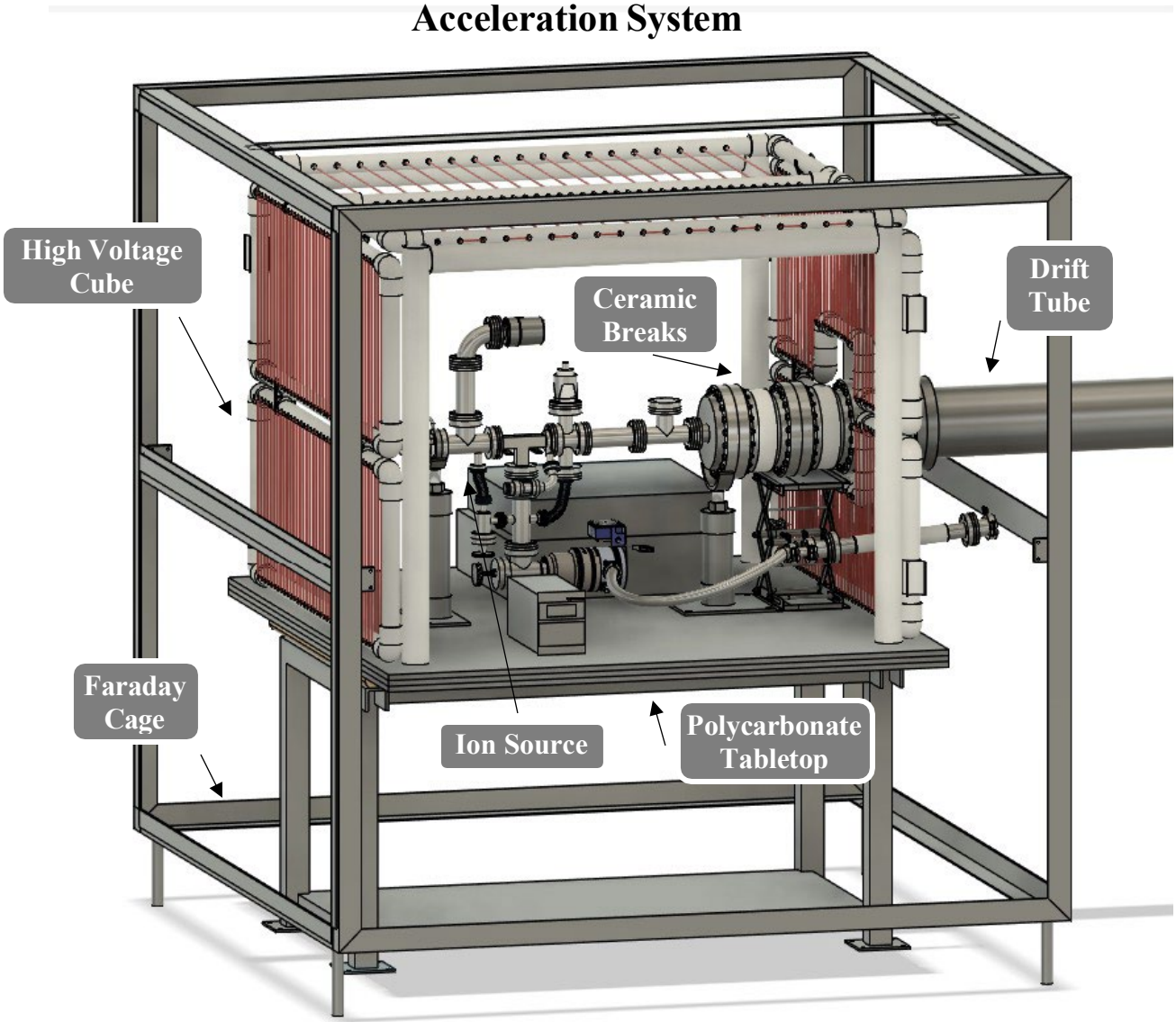

PCV pipe interwoven with high voltage cables are placed around the ion source and acceleration system on top of the copper sheet in order to encapsulate all the components in a single equipotential volume.[49] Up to 40 kV can be supplied to the table safely. When this is done the chamber in which the plasma is generated has a system ground equivalent to the potential supplied to the acceleration system; the equipotential volume produces a reference frame in which neutral particles that become ionized perceive their surroundings as electrically neutral. From the charged particle's perspective, the voltage supplied to the acceleration system is ground and the chamber side that is electrically neutral in the laboratory frame has a negative potential. Accordingly, if the particle is allowed to travel from one side of the chamber to the other it will become energized by the value supplied to the table (i.e., up to 40 keV).[50] This is sufficient for simulating the bulk plasma and suprathermal particles in most space environments.

Once a plasma is generated, refined, and energized it is passed into the main chamber for instrument analysis. The instrument is manipulated using a 4-axis control system – X-Y motion in a plane perpendicular to the particle travel and two rotation axes. This is accomplished using two 300 mm linear and two rotary Zaber motion stages that are operated from a computer terminal. A picture of the linear motion stages inside the main chamber is located left in Figure 3.3 and a CAD containing all four motion stages (linear and rotary) is found in Figure 3.5. In addition to the instrument undergoing calibration the carriage can be equipped with one of two detectors: a faraday cup for current measurements and a channel electron multiplier (CEM) for single particle analysis. In left image in Figure 3.3, the CEM is mounted at the top of the vertical linear motion stage. The faraday cup has a high voltage grid for analysis of beam energy distributions up to 1 keV. Either detector in place allows or flux measurements of the beam that are used to calibrate against the particle measurements of the instrument. Furthermore, a software

[49] A ceramic break is used to transfer the turbomolecular pumps exhaust to a roughing pump. The ion source turbo pump system was developed by Western Michigan University student Ben Miller. The ion source is operated wireless through the faraday cage at a computer terminal.
[50] Ionization of a plasma above singly charge ions is not feasible with electron ionization alone and is not easily accomplished in any terrestrial laboratory setting. Thus, calibration systems able to multiply charge ions are very rare.

program was developed to map the beam by vertically and horizontally stepping the detector position through a grid and sequencing the measurements at each into a single image.[51] An example plot reduced after running the beam mapping software is provided in the top-right of.Figure 3.3 The x- and y-axis indicate horizontal and vertical detector position, respectively, and the color indicates the flux of particles measured at each location. The signals generated inside the chamber are passed out using feedthroughs into an electronics control rack. Analog measurements from the faraday cup are recorded using a preamplifier and ammeter. Single particle analysis occurs via pulse height discriminators and counters to produce a count rate and converted into a flux using the detector aperture size. Analog-to-digital converters (ADCs) and multichannel analyzers (MCAs) are used for pulse height analysis. Many of the supporting electronics use traditional NIM Ortec devices. However, nearly all the processes described can be also performed using a Moku lab-based field-programmable gate array (FBGA). The chamber operates using a series of roughing, turbomolecular, and cryo pumps and can achieve an ultimate pressure of

Figure 3.3 HPIL Main Chamber and Beam Map Software

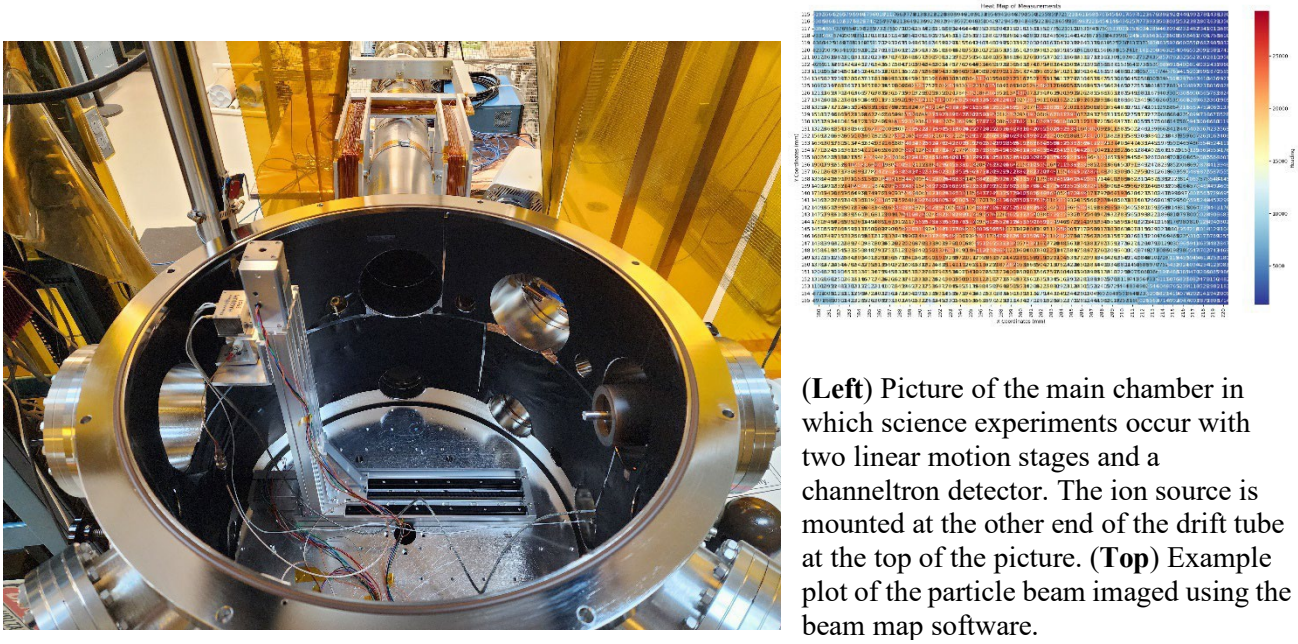

(**Left**) Picture of the main chamber in which science experiments occur with two linear motion stages and a channeltron detector. The ion source is mounted at the other end of the drift tube at the top of the picture. (**Top**) Example plot of the particle beam imaged using the beam map software.

[51] The beam map software was initially developed by University of Michigan student Gaston Wlodawer and the final version was written, tested, and implemented by Jaccob Bell.

~5×10^{-8} torr.[52] Lastly, an ISO class 7 clean room was built around the calibration system's main chamber to maintain contamination control during tests. Furthermore, an ISO 5 clean room station was constructed adjacent to the chamber with a nitrogen purge cabinet to safely assemble and store hardware.[53] Collectively, the revisions to the calibration facility replace nearly all the major components besides the chamber and pumps themselves. Additionally, the facility upgrades allow for system commands and data recording to occur from the computer terminal through digitization and state of the art electronics. The HPIL calibration facility is highly capable system idealized for space plasma instrument performance testing.

Section 3.2 Experimental Tests

3.2.1 FIPS Time-of-Flight Chamber[54]

The first tests performed using the improved calibration facility were on a FIPS flight spare time-of-flight chamber produced during the *MESSENGER* mission. The purpose of testing the flight spare was to (1) further calibrate the instrument to reanalyze existing *MESSENGER* data for the upcoming *BepiColombo* mission back to Mercury and (2) prepare for calibrating the T-FIPS prototype ToF chamber by performing similar experimental tests. A picture of the FIPS ToF spare is shown in Figure 3.4. The entrance is pointed away and covered with red cap to protect the carbon foil. The Start detector is mounted to the bottom left and the mirror mount bisects the chamber. The Stop detector was removed in this picture due to a prior failure that occurred in 2018 and was replaced with a white cover. The hope was to perform tests and determine the cause of the failure. The detector was reattached, and high voltage conditioning was achieved up to -15 kV but the detectors could not be brought to operating voltages with

[52] Particle collision lengths at this pressure are much longer than the chamber dimensions enabling the plasma used for calibrations to be collimated into a well-behaved beam.
[53] The clean room tent and facilities were developed by Isaac Fertig and Marcello Lara and was assisted in its early stages by Karthik Kamaraj, Gaston Wlodawer, and Arjun Sharma.
[54] The work done to test the FIPS spare ToF chamber was accomplished with University of Michigan student turned lab technician Isaac Fertig.

Figure 3.4 The FIPS Time-of-Flight Chamber

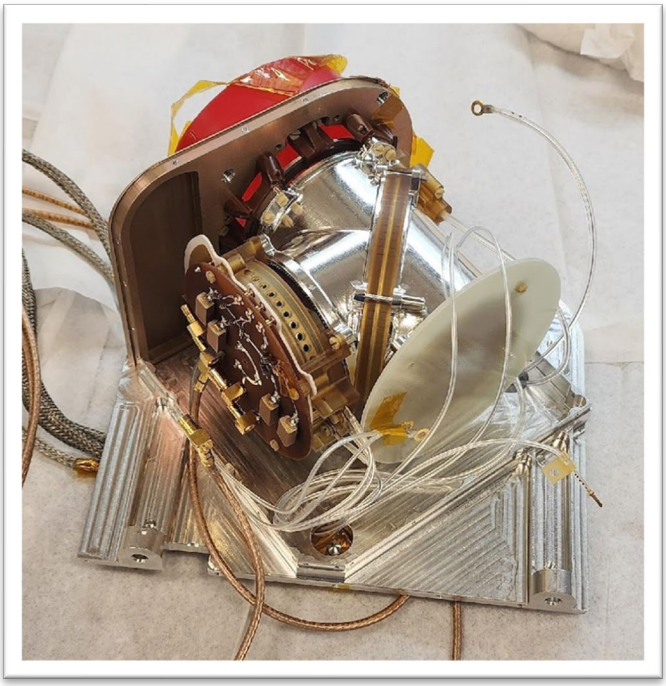

Picture of the FIPS flight spare ToF chamber prior to the Stop detector being reattached and tested in the improved calibration chamber. The entrance and carbon foil are on the far side protected with a red cover and Kapton tape. The start detector is assembled and mounted to the bottom of the chamber.

causing electrical breakdown. Tests were performed using the MCP plates at operating voltages with the post-acceleration system at lower voltages so that breakdown did not occur, but no measurements signals could be found from the plates. It was decided to disassemble the detectors and reassemble them with new microchannel plates for use on the T-FIPS prototype detector (see details in hardware section below). The tests using the FIPS ToF flight spare chamber were ultimately not successful, however, in the process the sputtering ion source variation of the calibration system was developed.[55] Also, valuable knowledge was gathered concerning the ToF chamber operation and electronics.

[55] The work developing the ion sputtering source was performed by Karthik Kamaraj, Arjun Shun, and Gaston Wlodawer, Isaac Fertig, and Jayveer Phull.

3.2.2 T-FIPS Fisheye Electrostatic Analyzer[56]

In addition to a flight spare ToF chamber, a spare Fisheye ESA was tested for use on the T-FIPS prototype sensor. A CAD of the experimental test setup inside the chamber was developed and is shown in Figure 3.5. The 300 mm linear motion stages along the bottom and left-hand side provide horizontal and vertical translation indicated by red and blue arrows, respectively. The rotary stages are mounted perpendicular to one another and mounted to the motion stage carrier to provide rotations along two axis with respect to the incoming particle beam. The ESA was cleaned and mounted in the chamber and tested up to operating voltages (~12 kV). The aperture was manipulated using a 4-axis controller that allowed for testing the ESA at all particle trajectories contained within its 150° × 360° FoV (see Figure 3.5). The particles that passed through the instrument and were thereby selected for their energy-per-charge (E_i/q_i) were recorded using a Quantar MCP detector. Transmission through the instrument was successfully recorded for particles measured at 4 keV with a voltage setting of 3 kV. This indicates an instrument k-factor of 1.33 in keeping with measurements taken from the Fisheye ESA flown onboard the *MESSENGER* mission. At the time of this writing the T-FIPS ESA tests are currently ongoing.[57] Accurate characterization of the Fisheye ESA and T-FIPS prototype ToF chamber separately before being incorporated together will provide the best testing and calibration data to outline the instrument's response.

[56] The design and work done for the T-FIPS Fisheye ESA was done with lab technician Isaac Fertig.
[57] There was a failure from the Quantar detector's multiparameter multichannel analyzer. Additional tests of the Fisheye ESA await diagnosis and repair of the detector.

Figure 3.5 Fisheye ESA Test Setup

Diagram of the experimental set up for the FIPS Fisheye ESA tests. The XY motion are delivered by two 300mm Zaber linear motion stages. The two Zaber rotary stages allow for testing particle trajectories along perpendicular rotation axes allowing for a complete determination of the systems performance. The ESA is mounted to a Quantar MCP detector.

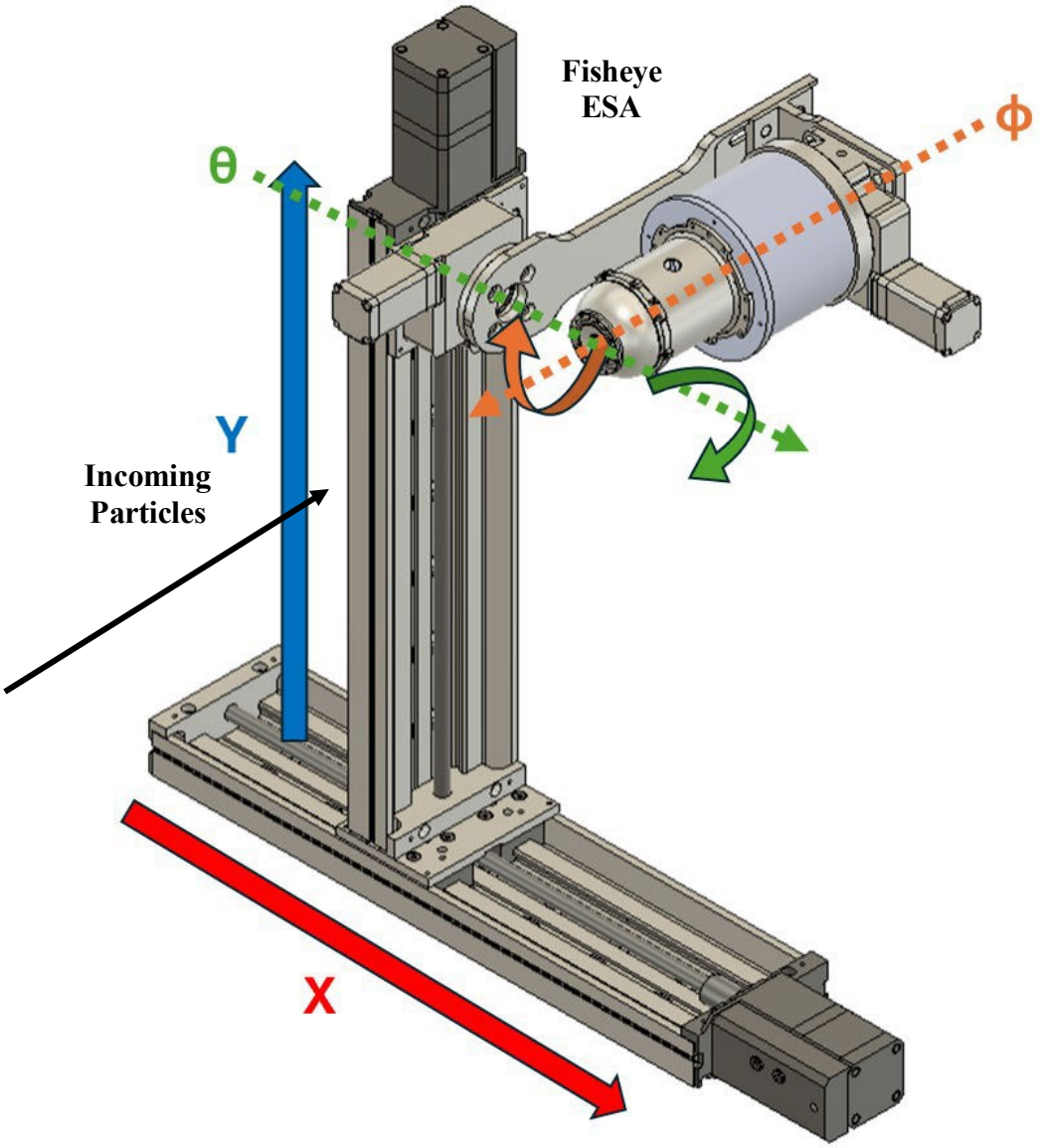

Section 3.3 Hardware Development

3.3.1 T-FIPS Start Detector

After tests were concluded on the FIPS flight spare ToF chamber the Start and Stop detectors were disassembled for parts to use on the T-FIPS prototype ToF chamber.[58] This began with the purchase of new microchannel plates (MCPs) to replace the old spares from the *MESSENGER* mission. The original mission used MCPs produced by Photonis (previously Burle) and still remain available for standard purchase. However, the new prototype MCPs were chosen to come from Incom because of previous work done with them on other sensors, in addition to the desired features that result from their manufacturing techniques.[59] The resistance on the Z-stack plates was minimized in order to facilitate the fastest timing possible. This does make the plates more susceptible to saturation from penetrating radiation during the most severe space weather events, however, it is unlikely that increasing resistance would result in improved resiliency worth the timing degradation. The bias angle, plate width, aspect ratio, and open-air ratio were matched to the original FIPS instrument specifications.[60] The HPIL clean room was developed in order to assemble and store the new components for the T-FIPS prototype ToF chamber. The Start MCP detector was disassembled, and the old plates were removed. At the same time the new plates were installed and aligned (see chapter 2). The newly assembled T-FIPS prototype Start detector awaits testing after the FIPS Fisheye ESA and will be subsequently incorporated onto the T-FIPS prototype chamber along with the Stop detector.

[58] Assembly of the T-FIPS prototype Start detector was accomplished with lab technician Isaac Fertig and SPRL Engineer Jon Reid.
[59] Incom MCPs do not need scrubbing/scrabbing before use because the outer semiconducting layer is implanted using bombardment that results in surface deposition. This removes the alkali layers believed to cause MCP scrubbing/scrabbing (Popecki et al., 2016).
[60] The aspect ratio is derived from the MCP channel diameter and length and the open air ratio comes from the sum total open area of the channel pores and the total detector surface area.

Figure 3.6 T-FIPS Prototype Time-of-Flight Chamber



Pictures of the newly manufacturing T-FIPS ToF chamber. There is a single entrance aperture and three exit apertures for the Start, Stop, and Energy detectors. The space between used to conjoin the two pieces together is where the electrostatic mirror grids will be mounted using insulators. The chamber CAD was developed by SPRL engineer Louis Marr and manufactured by SPRL machinist and Frank Palumbo.

3.3.2 T-FIPS Time-of-Flight Prototype Chamber[61]

The final version of the CAD for the T-FIPS ToF chamber was produced after early investigations into its design and performance using ion optical simulations (see Chapter 2). Figure 3.6 contains pictures of the ToF chamber that was machined with the modifications to the Stop detector location. The result are two sections that are nearly identical to one another. Key features were improved along the way including improved high voltage connections and mounts for the new grids and mirror. Assembly of the T-FIPS prototype chamber awaits burnishing of the chamber and arrival of the newly ordered electroformed grids.

[61] The T-FIPS prototype chamber was designed by SPRL mechanical engineer Louis Marr and manufactured by SPRL machinist Frank Palumbo. The drawings were produced by University of Michigan student Jayveer Phull.

3.3.3 Summary of Future Work

The development of the T-FIPS prototype instrument is well underway. Once the FIPS Fisheye ESA testing is complete the performance of the energy-per-charge (E/q_i) filtering will be well characterized. With the arrival of the new electroformed grids for the apertures and mirror, and the fabrication of the Stop detector using the FIPS flight spare components similar to the Start detector, the ToF chamber can be assembled. Early tests can begin soon after the attachment of the electron production plate (see Chapter 2) and connections made for power and signal transfer; these will characterize the image performance of the Start detector and electrostatic mirror as well as the efficiency for triple-coincidence measurements for the Stop detector. At the same time, development of the new energy system can progress and can be tested separately and in conjunction with the new prototype ToF chamber. This will initially include new ground support electronics to amplify and shape the signals from the energy detector, soon to replaced with later versions of the system designed with the prototype instrument signal processing hardware. Finally, bringing the full instrument together with Fisheye ESA, modified ToF chamber, and energy detector system will yield the full capabilities of T-FIPS as a compact triple coincidence time-of-flight plasma spectrometer.

Overview:
The Importance of In-Flight Calibrations and Observational Analyses

The processes of designing, producing, and testing the diverse types of space instrumentation are as unique and numerous as the instruments themselves. However, the purpose and metric for success are all the same: observational data products. Producing an instrument's data products requires an intimate knowledge of the device with a physicist's understanding of space science and phenomena and takes continuous iterations of in-flight calibrations. While creating modern space plasma spectrometers can be a challenge and take several years to complete the result must be a product available for any scientist throughout posterity. Therefore, the conversions between electrical signals produced by the instrument and the perceived scientific conditions in a space environment must be published and reproducible in order to decrease the likelihood of mistakes and maximize the potential for discovery. Ultimately, the role of an instrument developer is one in service to the broader capacity found within the community of their scientific peers.

As outlined in the introduction, our capability to explore and understand space is thoroughly tied to the proficiency of the instrument suites that are available to be flown. The performance metrics of instruments define what can be known about a region under study and advances in technology have been sufficient reason enough to return to many space environments. The relationship between exploration and instrument performance capabilities exists because the latter determines the type and quality of observational data products generated during a mission. The observational data taken by instruments enables the study and detection of space weather for determining safety conditions and preventing societal

impacts. For these reasons, since the Space Age's inception the principal investigators of spacecraft instruments have been space physicists. Building a space plasma instrument is fundamentally an undertaking in engineering and experimental physics. Nevertheless, because the ultimate purpose is the production of observational data to answer science questions the development is led by someone with an understanding of space plasmas and phenomena. Thus, every instrument developer is guided by the goal of producing the most useful data products for performing scientific analysis.

Thus far this research has outlined the steps from instrument conception to prototype development. Once ground-based performance evaluations are complete environmental testing occurs.[62] Environmental tests are designed to prove the instruments durability and resilience. After launch the remaining step is in-flight calibrations. In-flight calibrations are equivalent in importance and wholly linked to the terrestrial calibrations and simulated performance. The known measurements made from within vacuum chambers or simulated in computers are used to match and interpolate between measurements made in space. Furthermore, in-flight calibrations often require comparisons with other detectors onboard; it is always beneficial to produce instrument suites with overlapping performance ranges for this reason. Likewise, analysis between instrument measurements and pre-existing data sets from past missions to ensure consistency between the results is a valuable and critical technique. At their core, in-flight calibrations transfer the manifold of settings, conditions, and signals into observational measurements through a recondite understanding of spacecraft and instrument design and operation. Hence, it is typical to release data products at different levels, or in other words, the results of different intervals in the calibration. For example, level one data products are typically the raw signals from the sensors. Level two may be physical results in their most basic form (e.g., distributions of flux or count rates at individual detectors) and level three are often calculated products such as MHD fluid moments like bulk flow velocity, density, and temperature. By publishing the steps for in-flight calibration and

[62] Environmental testing includes thermal cycling, vibration tests, and determining electromagnetic interference.

releasing the data products for each the instrument team empowers the scientific community to make the greatest use of the data. In recent years there has been significant growth in open data practices that have resulted in a more informed and instrumentally literate scientific community and less embarrassments from retractions.[63] Possibly of greater importance, by publishing calibration techniques the instrument teams from different institutions are able to learn best practices from one another resulting in an overall increase in consistency and quality. In short, during the Early Space Age the results of space science mission have evolved from the ad-hoc, cryptic techniques of individuals to more a universal, open consensus made by the scientific community. Nonetheless, in-flight calibrations are full of challenges unique to each instrument that are best met and explained by the expertise of the instrument developers. Overall, in-flight calibrations are the final, significant step to releasing observational data products to the scientific community.

The final two chapters of this research cover the results of both in-flight calibrations and observational data analysis. The calibrations and analyses are performed on the data collected from two instruments: (1) the Electric Propulsion Electrostatic Analyzer (ÉPÉE) that flew on the International Space Station (ISS) in the top-side ionosphere and (2) the Heavy Ion Sensor (HIS) that was launched as part of ESA's Solar Orbiter mission. In this chapter, we cross-calibrations for the ÉPÉE instrument with the Floating Potential Measurement Unit (FPMU) langmuir probes before analyzing global distributions of ionospheric plasma and nighttime/daytime conditions during a geomagnetic storm. In Chapter 5, we outline the studies that assist in the calibration of 3D velocity distribution functions before performing the first analysis of differential streaming between solar wind alphas and O^{6+}. There are similarities between the two instruments: ÉPÉE and HIS utilize electrostatic analyzer to filter particles prior to detection to measure the energy spectra of space plasmas. However, they operate within completely different space

[63] In the early space age and until very recently data products were considered the proprietary work of the instrument team and were often released to NASA only as post-calibrated science data with few requirements imposed on it.

environments (Earth's ionosphere and interplanetary space) and therefore under very different conditions to study related but unique and disparate phenomena. This research assists in the release of new data products for each instrument and the scientific analysis performed for each mission. The overarching theme that ties all these works together is the transfer of novel technologies into unprecedented discoveries that further our knowledge of our local space environment and the best practices to survive within it.

Chapter 4

EPEE Calibration and Measurements of Top-Side Ionosphere

Section 4.1 Earth's Ionosphere

The terminus and most important facet of space weather is its effect on the ionosphere. The broad definition of space weather is the impact of solar-terrestrial relations on humanity or society. There is nothing that causes more widespread influence over human activities than the change in conditions within the ionosphere as energy from the Sun cascades down into Earth's system. The ionosphere itself is generated by the continuous fluence of high energy electromagnetic radiation emitted from the Sun;[64] the ultraviolet rays raining down on the neutral atmosphere produce a primarily singly charged oxygen (O^+) rich ionosphere (Hoffman, 1967). As mentioned in the introduction, the greater pressures experienced about planetary bodies result in the ability for complex molecules to form. Therefore, ionized and neutral forms of molecules such as O_2 and NO exist as well. Furthermore, the ionosphere and neutral atmosphere blend over a large distance (~400 km) with often dramatic transformations in density and composition. The results of the simulated ion densities are shown for solar maximum (a) and minimum (b) in the top left of Figure 4.1. The cyclical variations in solar activity result in changes in the relative abundances of

[64] The term radiation confusingly refers to both corpuscular/particulate radiation and electromagnetic wave (or photon) radiation. It comes historically from both types of radiation's ability to ionize or alter the chemistry of neutral matter and thereby cause damage.

Figure 4.1 The Composition of Earth's Ionosphere

(**Top-Left)** Plots of ion composition from the NRLMSISE-00 model during (a) solar maximum and (b) solar minimum (Emmert, 2015).

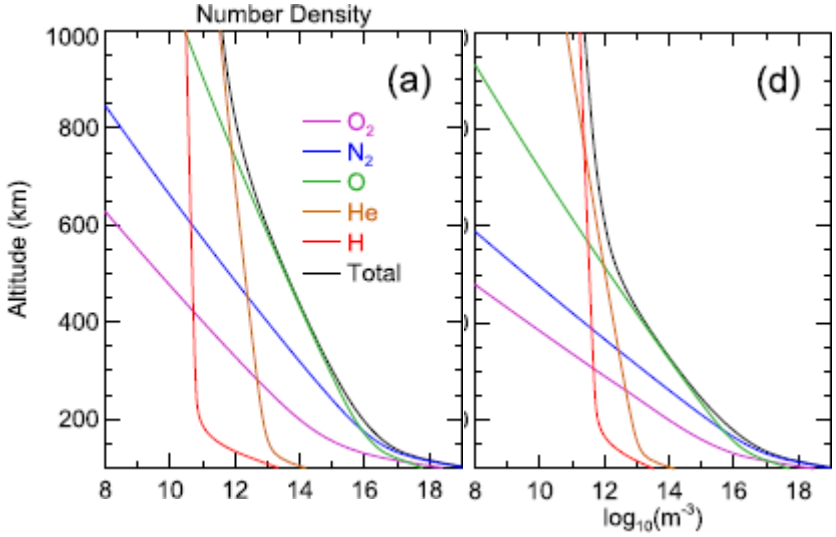

(**Bottom-Left**) Composition measurements during a geomagnetic storm in 1972 measured by the ISIS-II IMS instrument. The increase in N is evidence of upwelling from lower regions (Hoffman et al., 1974)(Lin & Ilie, 2022). (**Bottom-Right**) Diagram of the mechanisms in the ionosphere that cause ionization, gravitational settling, and diffusion (Lin & Ilie, 2022).

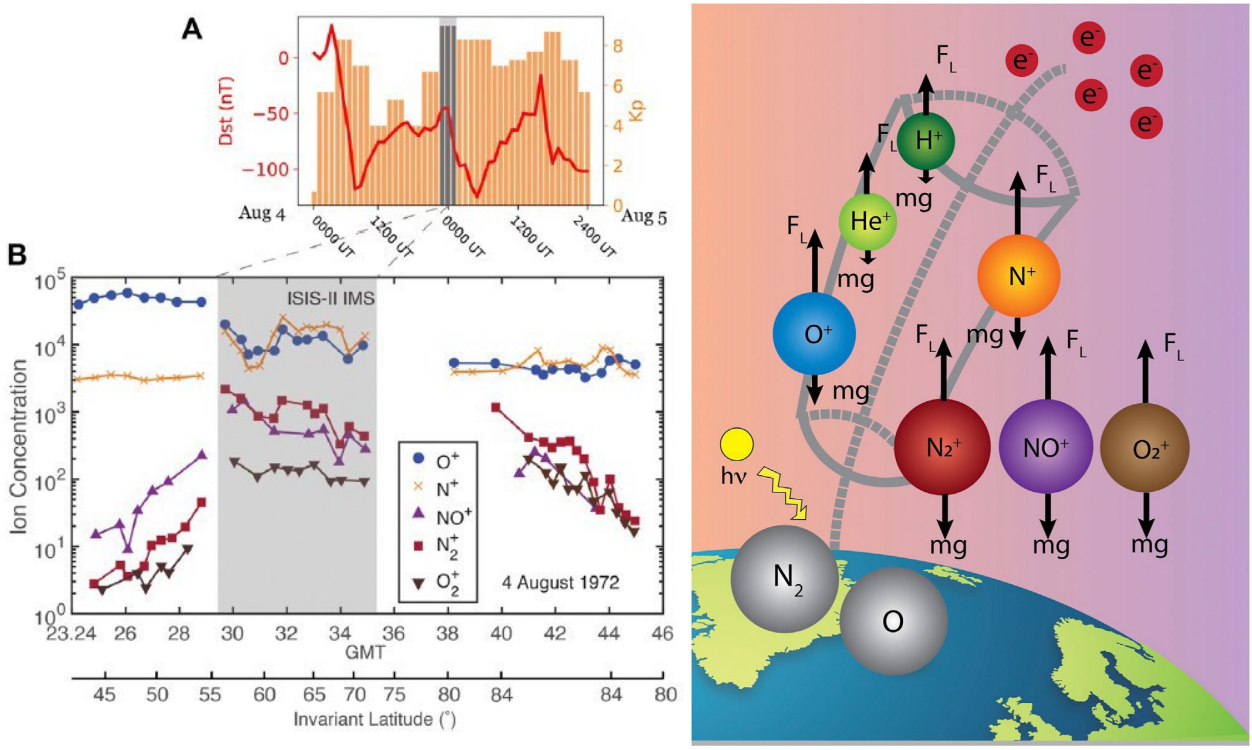

ions. Whereas the straight-line trajectories of the light emitted from the Sun result in a constant influx of ions to the daytime of the planet, the relocation or injection of hot electrons or precipitating ions from transient phenomena – often caused by space weather – create local enhancements in plasma densities.[65] The bottom left plots (A and B) in Figure 4.1 show composition measurements of the ionosphere during a geomagnetic storm (Hoffman et al., 1974; Lin & Ilie, 2022). The increases in N^+, N_2^+ NO^+, and O^+ are caused by upwelling from below. The diagram in the bottom left of Figure 4.1 depicts the behavior of ions during periods of upwelling understood to be caused by the injection of electrons. Moreover, the strength of electromagnetic fields increases at closer distances to the planet creating powerful transport mechanisms. Since the early twentieth century the ability to bounce radio waves off the ionosphere has enabled long-distance communication between places with line-of-sight connections blocked by Earth's curvature; they are still an important form of communication today especially for agriculture and military operations. The ability to reflect signals off the ionosphere at specific frequencies is derived from the electron densities impact on the plasma frequency and the index of refraction.

$$nn = \sqrt{1 - \left(\frac{\omega\omega_{pp}}{\omega\omega}\right)^2}, \qquad \omega\omega_{pp} = \sqrt{\frac{NN_{ee}ee^2}{\varepsilon\varepsilon_0 mm_{ee}}}$$

Here n is the index of refract, ω_p is the plasma frequency, ω is the frequency of the wave, N_e is the electron density, ε_0 is the permittivity of free space, and m_e is the mass of an electron (Gurnett & Bhattacharjee, 2017). This property is a result of the ability of the electromagnetic waves to transmit through plasma which is determined by the inertia of the charged particles within. Since the much heavier ions move significantly slower than the electrons it is the electron density that effectively modulates the waves. Furthermore, satellite communications pass their signals at higher frequencies into the ionosphere due to their ability to *transmit through* the plasma. Therefore, both types of communication can be

[65] A prime example being the northern and southern aurorae.

degraded by rapid changes in electron densities in the ionosphere. Figure 4.2 shows the various regions of the ionosphere depicted through altitude and electron density. The F2 peak changes in altitude and density during daytime-nighttime transitions and geomagnetic storms and obscures remote signals used for measurements. The locations and pointing direction of satellites (above looking down) and ground radar instruments (below pointing up) result in frequent interference from the F2 region. In addition to being critical for communication systems the ionosphere plays an important role in transferring energy into the atmosphere. During geomagnetic storms the heating of the ionosphere is transferred into the atmosphere causing it to inflate and expand up to higher altitudes; the density increase at Low Earth Orbit (LEO) creates more drag on satellites shortening mission lifetime through orbital decay –sometimes abruptly (T. E. Berger et al., 2023)(see e.g., lower left plots A and B in Figure 4.1). More broadly, the transfer of energy between the ionosphere and atmosphere is widely recognized but still not fully understood and the ultimate contribution between the two is still under investigation (e.g., Nwankwo & Ridley, 2025). Despite the importance of the ionosphere and its proximity to Earth's surface there is still much concerning its dynamics that we do not understand. The lack of information comes from the sparsity of observations from the topside of the ionosphere. Using the same physics that allows radio propagation and satellite relays it is possible to observe electron densities through slices of different regions of the

Figure 4.2 Regions of Earth's Ionosphere

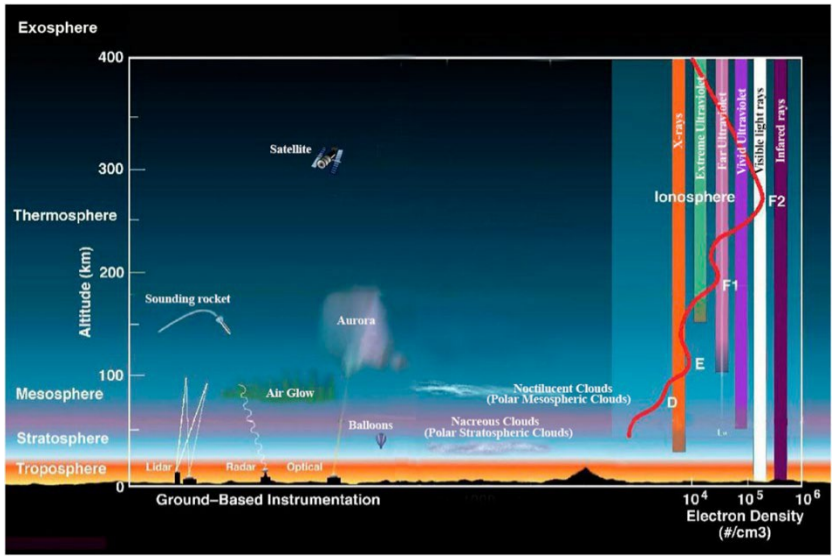

Depiction of methods for observing the ionosphere overlayed with a plot of basic characteristics. The critical point around 200-400 km is difficult to reach using either in situ and remote instruments. The F2 electron density peak obscures signals from either side and is one of the many dynamic features of the ionosphere plasma environment (source: Wikipedia).

ionosphere; for example, using ground-based radio transceivers (or ionosondes) the bottom of the ionosphere can be studied using this method (see Figure 4.2). However, remote sensing techniques are primarily limited to line-of-sight electron observations that are attenuated by regions above and below, and information concerning the ions is left unknown.[66] Furthermore, the ability to measure plasma in situ below LEO is limited due to the atmospheric drag experienced by satellites orbiting in this region. Therefore, measurements taken from the top-side ionosphere are critical for determining the outstanding science questions concerning ionosphere-atmosphere coupling.

Section 4.2 Description of the ÉPÉÉ Spectrometer

The Electric Propulsion Electrostatic Analyzer (ÉPÉÉ) is a SWaP-efficient plasma spectrometer that flew onboard the International Space Station (ISS) from March 30th, 2023 to April 21st, 2024 as part of the Defense Space Test Program (STP-H9). The ISS flies in a LEO orbit at an altitude ranging between 340-417 kilometers with approximately 90-minute periods. The location of ÉPÉÉ spectrometer on the spacecraft is indicated in the bottom left image of Figure 4.3. The ÉPÉÉ instrument has an energy range of 1-180 eV and completes a full measurement cycle at 1 Hz; the ISS orbits at ~7.4 km/s yielding about 8 kilometers spatial separation for observations. A photograph of the instrument is shown in the top left of . Figure 4.3. An exploded diagram displaying the internal components is found in the top right. The ÉPÉÉ spectrometer is comprised of a collimator, electrostatic analyzer, and anode detector with a nominal viewing angle and size less than 1U (10 cm × 10 cm × 5 cm). The electrostatic analyzer is the fourth generation of the laminated style analyzer and was developed in collaboration between Los Alamos National Laboratory (LANL) and the United States Air Force Academy (USAFA)(see Maldonado et al., 2025 and references therein). The laminated ESA has small entrance and exit apertures (~10s of microns)

[66] The F2 electron density peak obscures observations of the lower electron densities on the opposing side from any remote sounder. To add to the issue, the peak experiences dramatic changes in density and altitude (nominally ~250 kilometers)(see Figure 4.2).

that sandwich two electrodes that generate an electric field in the transverse direction of the particles trajectory. The simulation results in the bottom right of Figure 4.3 depicts the behavior of ions as they base through the ESA cavity. The deflection and offset of the apertures limit the particles that pass through by energy-per-charge (E_i/q_i) thereby acting as an energy bandpass filter for the primarily singly charge ions in Earth's ionosphere. The collimator only allows particles with nominal trajectories to pass through while also rejecting photons. The geometric factor for the instrument is 4.8×10^{-4} sr cm^2 eV / eV effectively limiting the extremely dense plasma (~$10^{9\text{-}12}$ m^{-3}) and allowing for an energy resolution ($\Delta E/E$) of ~20%. The measurements recorded by the ADC from the anode detector are converted into currents and ultimately ion densities, spacecraft potentials, and eventually temperatures (see details below). Altogether, ÉPÉÉ was an effective and rugged instrument that provided quality measurements of the topside ionosphere during the important period of solar maximum.

Section 4.3 Calibration of the ÉPÉÉ Data Products

The first step for this research was to generate the instrument data products through in-flight calibrations of the instrument. This was accomplished by performing cross-calibration with the Floating Potential Measurement Unit (FPMU) that was operated infrequently during the same intervals as ÉPÉÉ. The location FPMU on the ISS is shown in the bottom left image of Figure 4.3. The FPMU is a series of langmuir probes that were developed by the Space Dynamics Laboratory at the Utah State University (Barjatya et al., 2009; Wright et al., 2008). Due to its placement within the ionosphere, the ISS like other satellites in the regions experiences large spacecraft potential swings (up to 40 V) as result of changes in solar exposure and conditions in the surrounding plasma. Ultraviolet light and photons with higher energy from the Sun cause emission of electrons when they strike the exterior surface of the spacecraft creating a positive potential.[67] Furthermore, the spacecraft will naturally accumulate enough charge to stabilize the

[67] The same phenomenon is observed in the photoelectric effect experiments.

flow of charged particles between the vehicle and the surrounding plasma. The so-called plasma potential is determined by the collisional cross-section and therefore the density and temperature of the charged particles in the plasma.[68] Due to the faster speed of the lighter electrons in a thermodynamically stable plasma the electrons are more likely to interact with the external surfaces; the spacecraft charges up negative in order to deflect electrons away.[69] In addition to natural fluctuations, the high voltage solar panels flown onboard the ISS operate up to 160 V making the large, cumulative variations in spacecraft voltages potentially dangerous to astronauts during spacewalks. The primary purpose of the FPMU was to monitor these potentials while secondarily measuring plasma characteristics such as plasma potential and electron densities. To calibrate ÉPÉÉ assumptions were made concerning the surrounding plasma. First, the motion of the ISS (v_{iss}) significantly exceeds typical bulk flow velocities ($vv_{iiiiii}^{ppppppppppppp}$) in the top-side ionosphere; the particle velocity ($vv_{iiiiii}^{ppiiiiiaaeee}$) that produces the current measured by the anode is assumed to be produced by the ram of the spacecraft alone.

$$vv_{iiiiii}^{ppiiiiiaaeee} = vv_{iiiiii}^{ppppppppppppp} + vv_{IIIIII}, \qquad vv_{IIIIII} \gg vv_{iiiiii}^{ppppppppppppp} \rightarrow vv_{iiiiii}^{ppiiiiiaaeee} \approx vv_{IIIIII}$$

Second, the ionosphere plasma is assumed quasi-neutral meaning that the total charge density (Q_{plasma}) of ions and electrons balance to zero:

$$QQ_{ppppppppppppp} = \sum_{ii} qq_{ii} nn_{ii} - eenn_{ee} \approx 0$$

[68] The plasma potential like all potentials requires a reference point (i.e., the spacecraft) in order to be defined. The spacecraft potential charges equal and opposite to the plasma potential and the value is determined by the likelihood of the particles to interact with the spacecraft.

[69] The potential difference results in a plasma sheath around the spacecraft that, in contrast to the electrons, accelerates ions towards the spacecraft. This effect artificially increases the flow of ions into the instrument aperture and must be accounted for in the calibrations (see below).

$$\sum_{ii} q_{ii} nn_{ii} \approx nn_{ee}$$

Above q_i is the charge of the ion, n_i is its individual number density, e is the elementary charge, and n_e is the electron density. This enables the direct cross-calibration between ÉPÉÉ ion densities observations and FPMU electron density measurements. The assumption that the ions are dominated by singly charged oxygen atoms is made as well. Finally, any deviations between the FPMU recorded densities and ÉPÉÉ measurements are presumed to be the result of fluctuations in spacecraft potential. As the spacecraft charges up to high negative potentials the ions are accelerated across the sheath into the aperture artificially increasing the anode measurements relative to the pristine ambient plasma. With these assumptions the current measurement of the anode becomes,

$$II = eennee vvIIIIII AAεε(ϕϕIIIIII)$$

In this equation, I is the current measured by the anode, e is the elementary charge, n_e is the electron density measurements made by FPMU, v_{ISS} is the velocity of the spacecraft, A is the surface area of the instrument aperture, and ε is the calibration factor presumed to be a function of spacecraft potential (ϕ_{ISS}). The results are inverted in order to find the value of the calibration factor.

$$εε(ϕϕIIIIII) = \frac{II}{eennee vvIIIIII AA}$$

Since the goal is to determine the calibration factor as a function of spacecraft potential, the spacecraft potential data product is calculated next. The ÉPÉÉ instrument is a plasma spectrometer and measures the (presumed) singly charged ions of the ionospheric plasma as a function of their energy. With the individual particle motion neglected compared to the vehicle speed the measured energy is a function of the spacecraft's ram speed and the potential drop through the sheath produced by spacecraft charging.

$$EE_0 = \frac{1}{2} mm_{ii} vv_{IIIIII}^2 + ee\phi\phi_{IIIIII}$$

The value for E_0 is taken from the ESA passband setting that achieves the highest current measurement on the anode which is the point at which the average ion thermal energy overcomes the spacecraft potential. Again, by inverting the function we find the spacecraft potential as a function of average particle thermal energy.

$$\phi\phi_{IIIIII}(EE_0) = \frac{1}{ee}\left(EE_0 - \frac{1}{2} mm_{ii} vv_{IIIIII}^2\right)$$

With this relationship in place the spacecraft potential was processed for the life of the mission and released as a data product. Moreover, with the spacecraft potential evaluated the density calibration factor could be analyzed as a function of vehicle charging effects. The ÉPÉÉ and FPMU data were cross calibrated over September 28-29, 2023. The density calibrations were analyzed for concurrent timesteps resulting in a time series calibration factor that was subsequently matched with corresponding spacecraft potentials. The comparison between the pre-calibrated ÉPEÉ and FPMUS data is shown in Figure 4.4. The top plot shows two separate FPMU electron density measurements made by the Wide-sweep Langmuir Probe (WLP) and Plasma Impedence Probe (PIP) in purple and green, respectively, and the raw ÉPÉÉ anode current measurement in blue. The calibration factor was calculated for the densities from both FPMU instruments and plotted as a function of time below. Next, the impact of spacecraft potential on the calibration factors was analyzed using the plots in Figure 4.5. It was broadly recognizable that there was a linear trend between the calibration factor and spacecraft potential, however, two off-nominal periods were identified. The off-nominal periods are demarcated by the two blue boundaries in the left plot. The anomalously high values for the calibration factor at low spacecraft potential (i.e., top-left box) were determined to occur during reoccurring passes through an Equatorial Plasma Bubble (EPB) on the

nightside of the planet.[70] This region is delineated by red dotted vertical lines in the time series plots of Figure 4.4. An EPB is a local depletion of plasma that is believed to convect upwards from lower regions in the ionosphere. The presence of EPBs occurs naturally as a result of the diurnal rotation or at larger scales during geomagnetic storms (C. S. Huang, 2023; Xiong & Lühr, 2023). Nonetheless, the ultimate causes of EPBs remain unknown and an important topic for ionospheric studies using in situ measurements from the topside ionosphere. For initial calibrations, the portions of the data recorded during the EPB crossing were removed. Secondly, an off-nominal section of the data was identified for low calibration factor values at high voltages. This data is found in the bottom right blue ellipse in the left plot in Figure 4.5. This is believed to be an effect of the spacecraft shunting mechanism that is used to

Figure 4.3 ÉPÉÉ-FPMU Comparison and Calibration Factor

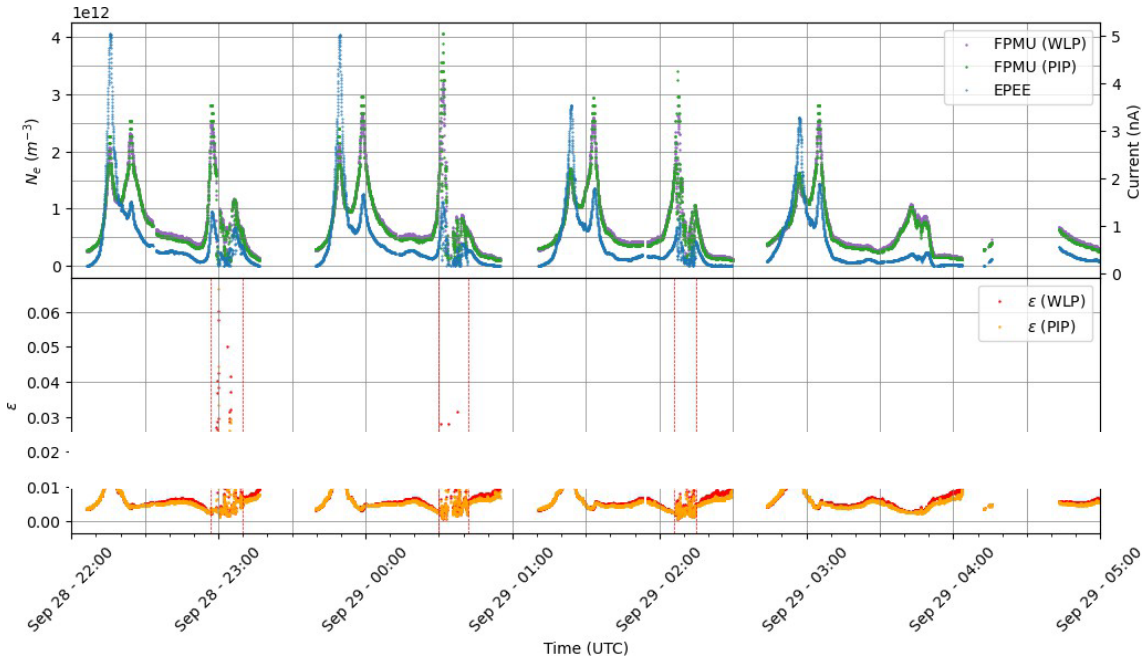

Plots of the cross-calibration between ÉPÉÉ and FPMU. The top plot has the non-calibrated ÉPÉÉ anode current measurements and the green (PIP) and purple (WLP) separate langmuir probe electron density measurements. The bottom plot shows the individual calibration factors that were calculated from each. The variations in the calibration factor result from differences in the spacecraft potential increasing the flux of ions at the anode. The regions bracketed in red vertical line in which the calibration factor becomes unpredictable occurred during separate orbital transits through the same equatorial plasma bubble (EPB)(90-minute intervals). Inside the EPB the ion density drops precipitously, and the assumptions made for the calibration calculations no longer hold.

[70] The EPB crossing was recognized through private communications with FPMU PI Dr. Aroh Barjatya.

Figure 4.4 ÉPÉE-FPMU Calibration Factor vs Spacecraft Potential

(**Left**) The calibration factor as a function of voltage displays a linear trend with two off-nominal periods. The left blue box indicates anomalous factors that occurred during successive EPB crossings. The right box occurs during spacecraft shunting during charging from the high voltage solar arrays. (**Right**) Linear fit that was applied once the off-nominal regions were removed.

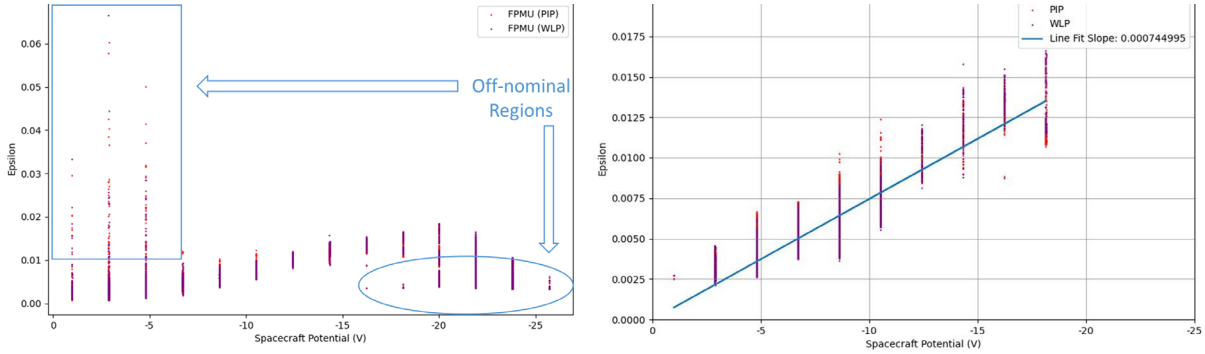

reduce the impact of spacecraft charging from the high voltage solar arrays. Both off-nominal regions were removed and the resulting data set is shown in the right plot in Figure 4.5. Also shown is the linear fit that was calculated for calibration factor data as a function of spacecraft potential. The linear fit was used to predict the ion densities of the plasma. The resulting calibrated ÉPÉÉ ion densities were matched to observations from the FPMU data that accurately filled in the data gaps where the latter instrument was turned off as seen in the updated time series plotted in Figure 4.6. The shaded regions in the plots indicate times when the spacecraft was eclipsed (i.e., on the night side of the planet). The bottom plot shows the comparison between the spacecraft measurements derived separately by the ÉPÉE and FPMU instruments. The density enhancements and spacecraft potentials correctly reflect the diurnal activities and changes in plasma conditions expected for measurements taken from the night and dayside ionosphere. With the calibration factor in hand the ion densities were processed for the lifetime of the mission using the spacecraft potential. Using these steps the in-flight calibration was accomplished and the level two data products for ÉPÉÉ instrument were released.

Figure 4.5 ÉPÉÉ-FPMU Cross-Calibration Results

The final product of the cross-calibrations in which the resulting ÉPÉÉ ion densities (**Top**). Nighttime/eclipse periods are shaded in blue. The observations appear to faithfully reconstruct periods in which FPMU was turned off. The regions in which the ISS were in the EPB produce low quality measurements due to the breakdown in assumptions for the calibration factor. The bottom plot show the results of the spacecraft potential calculations in comparison to the FPMU measurements. The diurnal variations are caused from higher densities on the dayside resulting in the spacecraft charging to higher negative potentials to deflect contact from electrons.

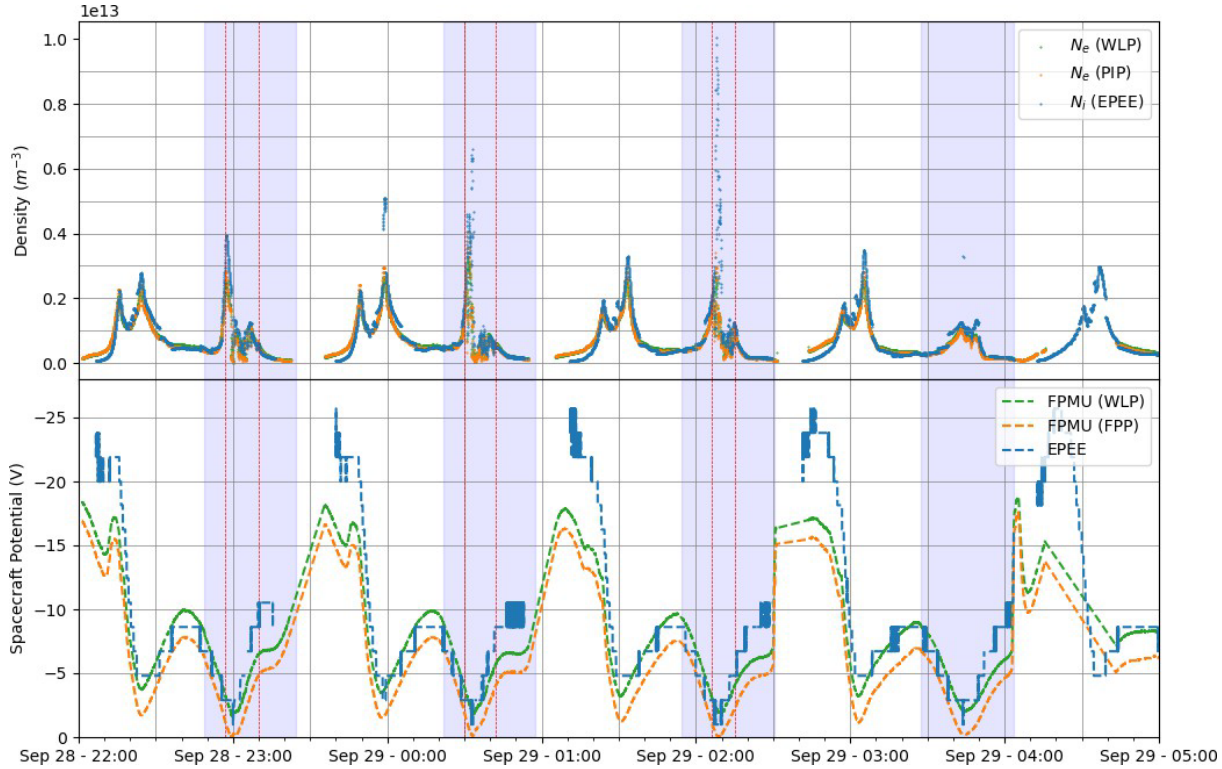

Section 4.4 Analysis ÉPÉÉ Measurements and the Topside Ionosphere

Once the spacecraft potential and ion density data products were derived, we proceeded with the first analysis of on-orbit plasma measurements. The first step was to produce global maps of the plasma characteristics in the topside ionosphere by matching the densities and ISS potentials to the position of the spacecraft. To accomplish this, the density and potential measurements for each position were summed and normalized by the number of measurements. The resulting data are plotted in Figure 4.7. In both the spacecraft potential (top) and ion density (maps) the x-axis shows the longitudinal position and the y-axis the latitudinal position of the spacecraft. The color indicates the magnitude of the spacecraft potential and

Figure 4.6 Global Mission Average Maps – Ion Density and Spacecraft Potentials

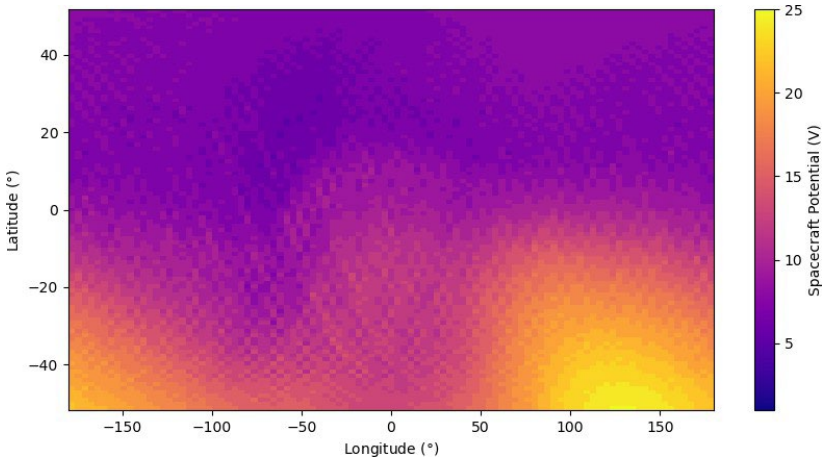

Global maps of the average spacecraft (**Left**) and ion density (**Bottom**) measurements made by ÉPÉÉ. The spacecraft charging at high latitudes is believed to result from less UV sunlit exposure to the spacecraft. The Equatorial Ionization Anomaly is visible at the equator indicating the calibration was effective.

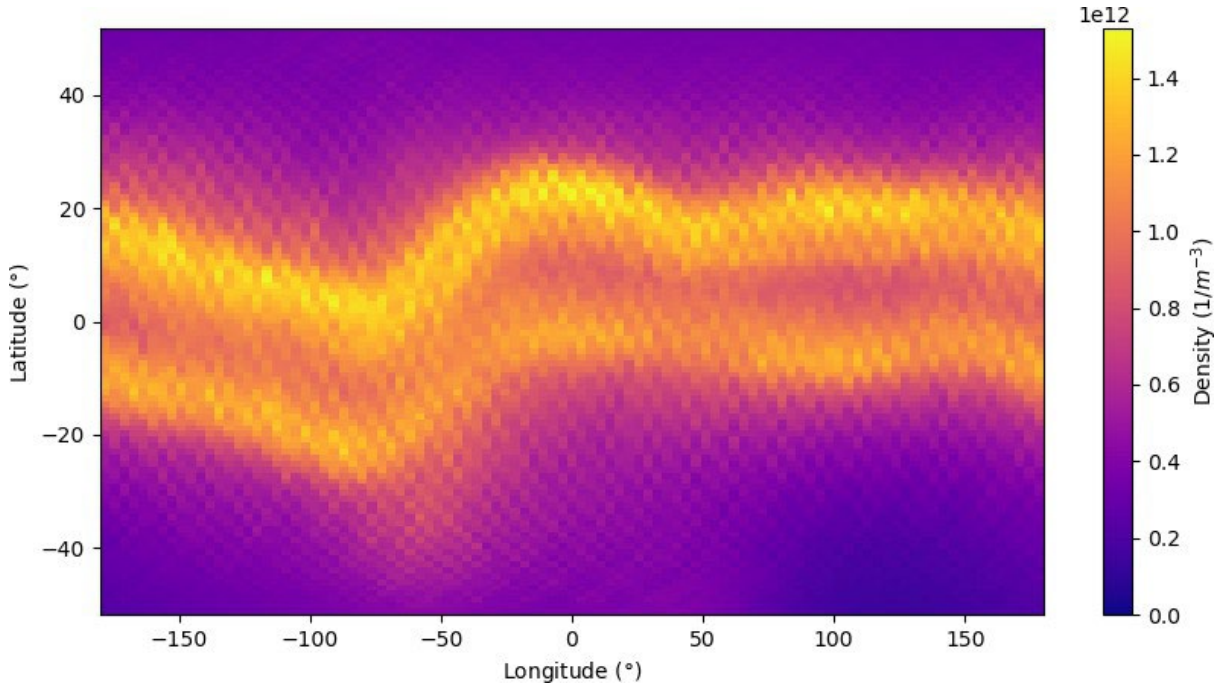

ion density, respectively. The high spacecraft potentials near the poles (especially southward) shown in the top plot are believed to be caused by the lack of Sun exposure resulting in lower plasma densities and less electrons liberated from UV radiation. The location of the Appleton Equatorial Ionization Anomaly (EIA) was clearly visible in the bottom density plot as two parallel enhancements running longitudinally in the data. The EIA is a naturally occurring region comprising two crests running longitudinal (±15° latitude) at the equator that straddle a plasma trough (Appleton, 1946; Namba & Maeda, 1939). The EIA is generated by a complicated process involving ion-atmosphere coupling; strong high altitude neutral

Figure 4.7 Global Monthly Average Maps – Ion Densities

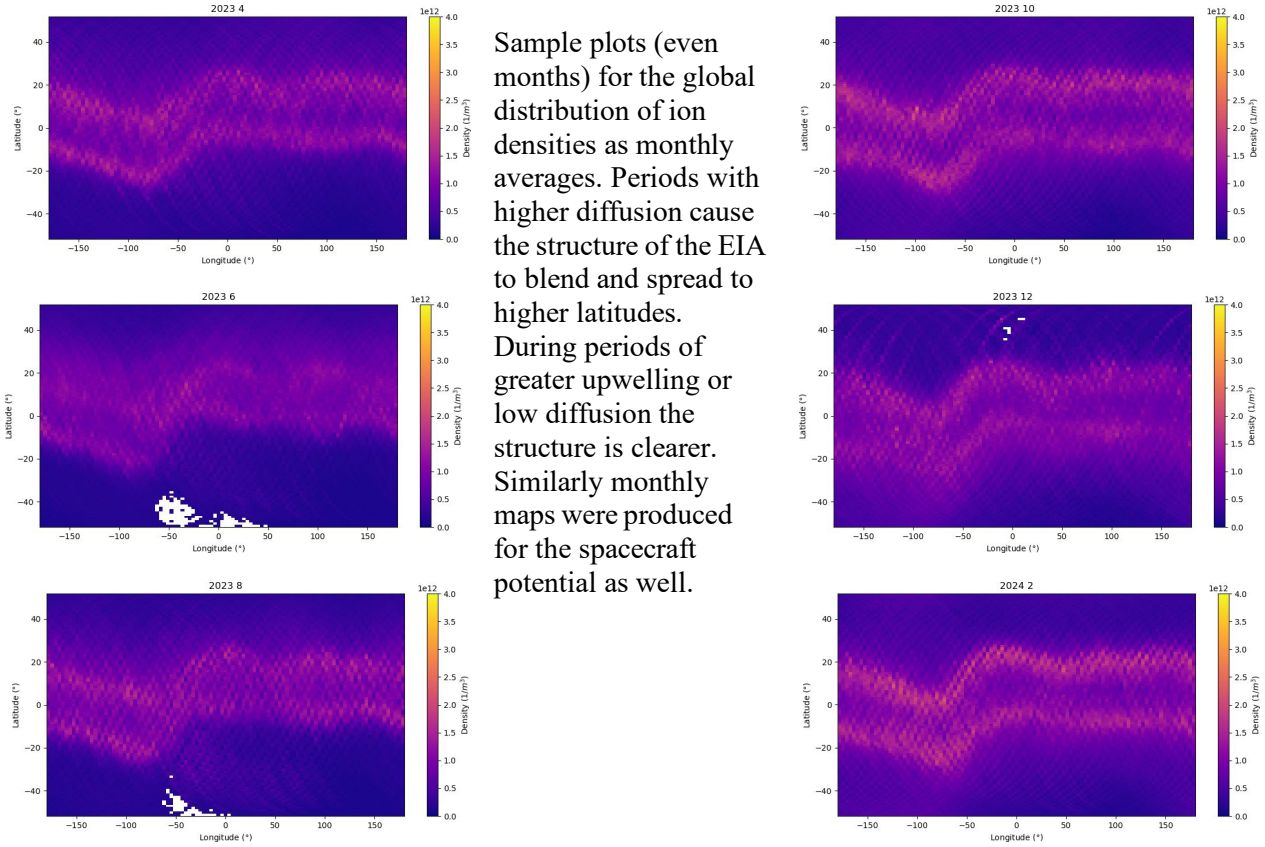

Sample plots (even months) for the global distribution of ion densities as monthly averages. Periods with higher diffusion cause the structure of the EIA to blend and spread to higher latitudes. During periods of greater upwelling or low diffusion the structure is clearer. Similarly monthly maps were produced for the spacecraft potential as well.

winds at the equator generated by solar heating tht push charged particles at different speeds producing an easterly directed electric field perpendicular to the pole-aligned geomagnetic fields. The resulting E×B drifts are vertical causing ions to upwell from lower regions before diffusing along field lines toward the lower plasma pressures at the poles (Hanson & Moffett, 1966; Martyn, 1954; Mitra, 1946). This process is known as the Equatorial Plasma Fountain and results in the EIA measurements. Naturally, the complex mechanisms that results in the EIA experience dramatic seasonal and geographic changes as the planet rotates on its axis and revolves about the Sun. For this reason, monthly plots were produced for comparison and shown in Figure 4.8. The plots are similar to that in Figure 4.7 except the data is averaged for separate months. The color bar depicting density is constant across each map. Differences in plasma densities throughout the months are apparent with noticeable increases in the northern hemisphere trough. Furthermore, variations in diffusion rates cause the twin crests to lose their structure resulting in blending

between the two crests or expansion towards the poles. Overall, the initial observations demonstrated quality measurements of the spacecraft potential and ion densities in the ionosphere.

In addition, the data calibrated data were compared with model results. Specifically, the International Reference Ionosphere model was used to compare with the observations recorded by ÉPÉÉ (Bilitza et al., 2024). The simulation was run for the duration of the mission producing 3D (longitude × latitude × altitude) maps of ionospheric densities. The trajectory of ISS was used to slice the data through the maps for direct comparison with the in situ, singe-point ÉPÉÉ measurements. The results are plotted in Figure 4.9 were found to be in good agreement with one another. The top plot show the model and instrument data together as a time series during the same interval used for the FPMU cross-calibration. The ÉPÉÉ measurements are plotted in blue and the predicted measurements from two separate versions of the IRI mode,l namely, NeQuick and Corr2, are in plotted in orange and green, respectively. The variation between observed and model densities was analyzed by taking the ratio of each other; this scale factor is plotted a function of time in the bottom plot of Figure 4.9. The major differences occurred during the peaks and troughs that occur naturally at the day- and night-side – naturally the conservative model results under predicted the extrema in either circumstance. Additionally, the greatest discrepancies occurred during the nighttime and near the equator which could be a result of the EPB that was located in this region. The ratio between the ÉPÉE and IRI ion densities was calculated for the life of the mission and shown in the histogram in the middle-left of Figure 4.9. As can be seen, nearly half (~49.6%) of the data are within a factor of two of each other indicating the model closely approximates the observed conditions in the ionosphere. Further cross-analysis of ÉPÉÉ data with ionosphere models will provide critical restraints for enhancing their predictive capabilities.

Finally, the data was used to conduct studies of storm time conditions that occurred on November 4th and 5th, 2023. During this period the Earth was struck by a halo-CME that erupted from an M1.8-class solar flare on November 3rd. Halo CMEs are appropriately named because they produce a ring- or halo-

Figure 4.8 ÉPÉÉ Measurements and IRI Model Comparison

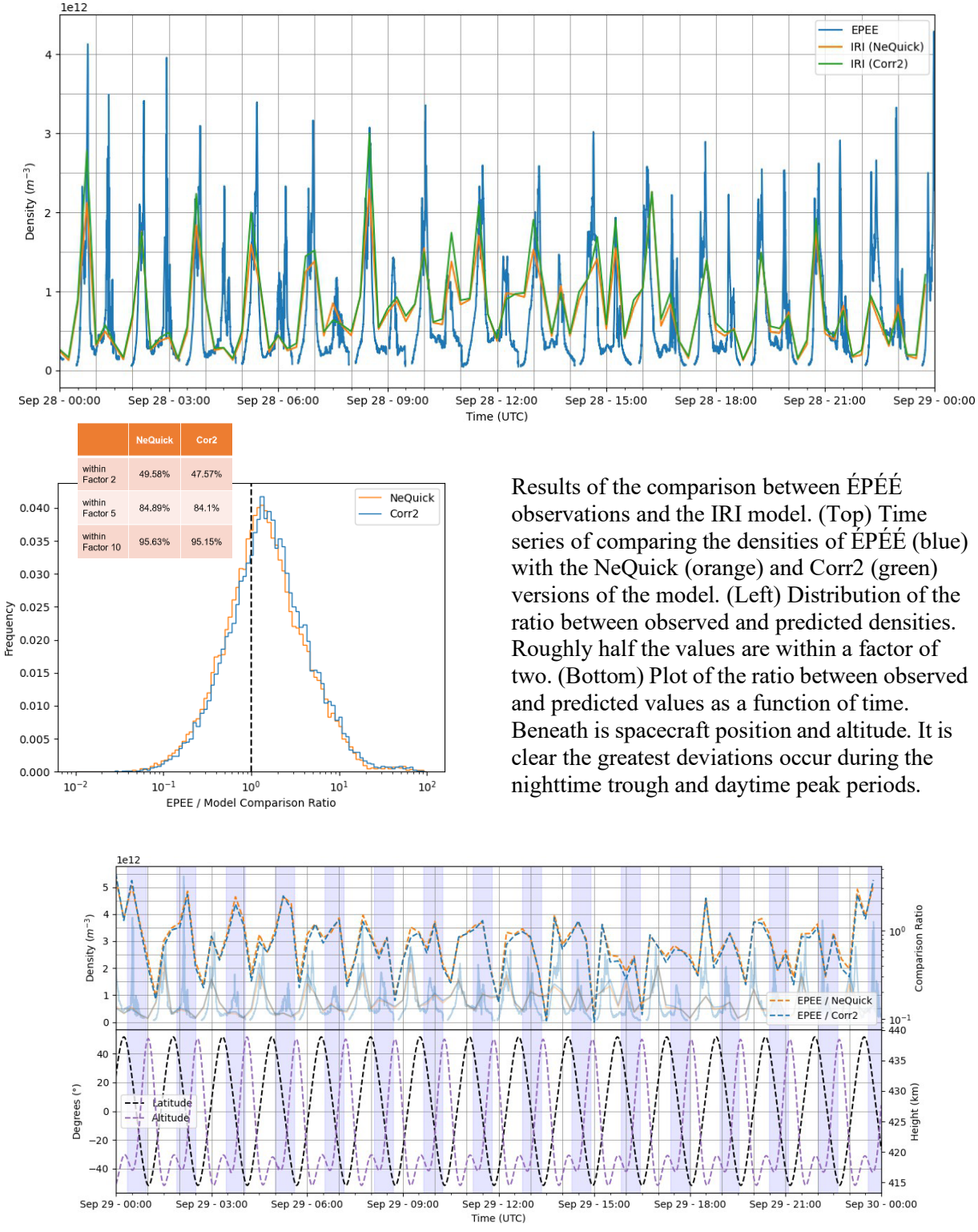

Results of the comparison between ÉPÉÉ observations and the IRI model. (Top) Time series of comparing the densities of ÉPÉÉ (blue) with the NeQuick (orange) and Corr2 (green) versions of the model. (Left) Distribution of the ratio between observed and predicted densities. Roughly half the values are within a factor of two. (Bottom) Plot of the ratio between observed and predicted values as a function of time. Beneath is spacecraft position and altitude. It is clear the greatest deviations occur during the nighttime trough and daytime peak periods.

Figure 4.9 ÉPÉÉ Measurements During Geomagnetic Storm

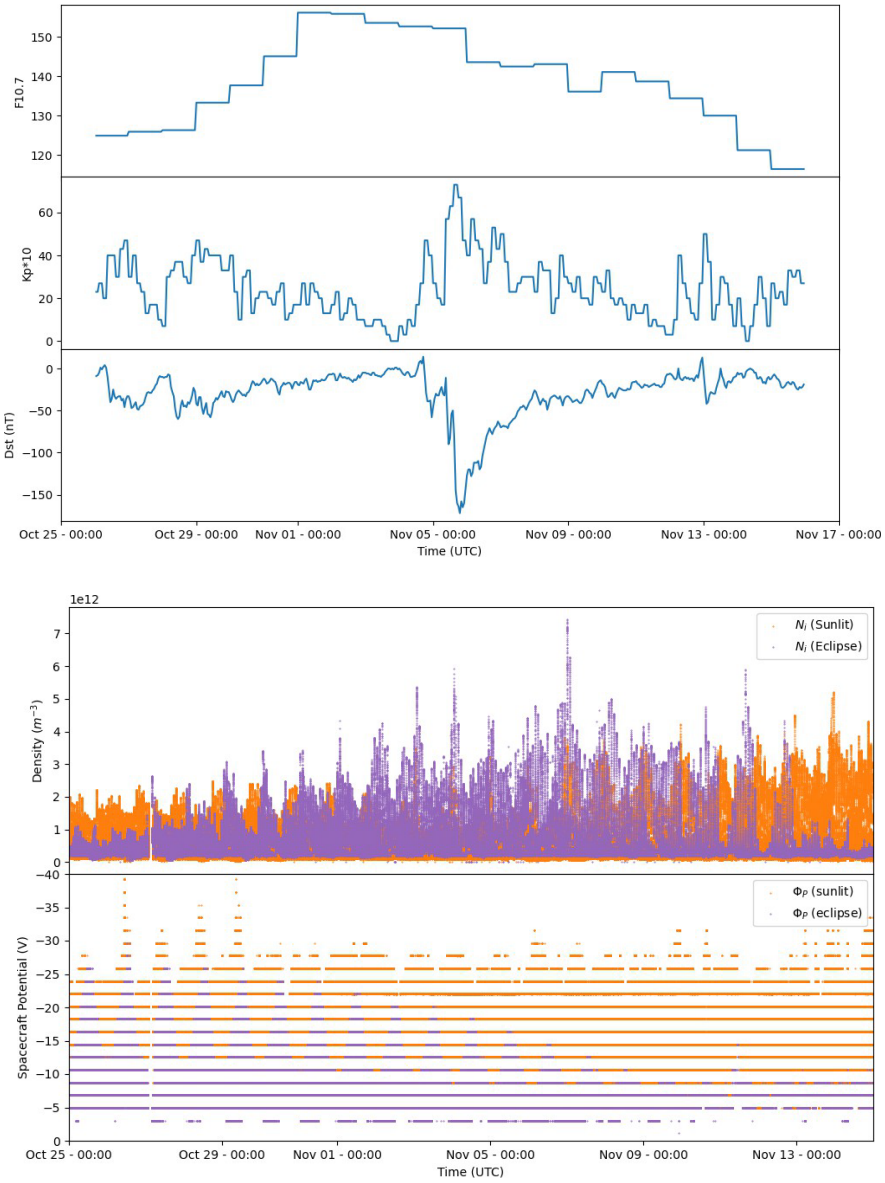

Stormtime conditions in the ionosphere that were studied during November 4-5, 2023. (**Top**) The F10.7 during this period which indicates the quantity of solar electromagnetic radiation achieved on the dayside. The Kp and Dst are indices used to indicate the level of magnetic disturbance during a storm. The peak of the storm occurred around on November 5th at apprxomitately 1500 UTC. (**Bottom**) Density and spacecraft potential measurements taken during the same period. During the peak of the storm the nighttime (purple) densities rose higher than the daytime (orange) densities while spacecraft potential appear nominal. This appears to indicate the presence of substorm plasma coming from the magnetotail – however, further validation of the data is necessary.

like structure in cameras at Earth as the plasma cloud travels straight towards the planet indicating imminent onset of a direct hit. The Kp and Dst indexes are different methods for calculating the severity of geomagnetic storms by measuring the increase in magnetic field strength at various points on Earth's surface that result during compression of the magnetosphere. This compression drives particle motion in the interior causing geomagnetic storm activity in the ionosphere. Both the Kp and Dst indices

are plotted as a function of time during the storm period in top plot of Figure 4.10. In addition, the F10.7 index which indicates solar luminosity is provided as well. Two moderate storms occurred (G1 and G3) with the second and larger of the two storms achieving a Kp index of 7.3 and Dst index of -162.6 nT around 1500 UTC. The density and spacecraft potential are plotted during the peak of the storm activity in the bottom of Figure 4.10. The measurements taken from the dayside are plotted in orange and the nightside observations are plotted in purple. As can be seen, nighttime enhancements occur during the same peak in storm activity seen in the Kp and Dst plots. Further validation is needed to confirm the timing intervals of these measurements. Nonetheless, the peak in densities occur simultaneously with lower spacecraft potentials further indicating the plasma enhancements occurred in the nightside. The density measurements recorded by ÉPÉÉ indicate an enhancement in the EIA as a result of the storm-time conditions that raised the F region of the ionosphere to higher altitudes. At the same time there were no obvious changes in spacecraft potential. The plasma measurements recorded by ÉPÉÉ during a geomagnetic storm provide important insight concerning ionospheric dynamics and transport mechanisms that occur as a result of space weather. Collectively, the global maps, model comparisons, and storm-time studies demonstrate the efficacy of the in-flight calibrations and the quality of ÉPÉÉ as a SWaP-efficient plasma spectrometer for topside ionosphere monitoring.

Understanding the upper ionosphere is a critical piece to completing the puzzle for our knowledge of space storm's impact on human society. Whereas the solar dynamo's production of the solar wind and transients such as flares and CMEs (see Chapter 1) represent the initial trigger for the domino of events that create space weather, the impacts on the ionosphere represents the hammer fall at the end. The complex system combines variations in the neutral atmosphere with the plasma motion generated by external drivers. Despite the proximity of the ionosphere the practical implications of LEO continue to prevent complete understanding of the physical mechanisms that occur within. Thus, the deployment of plasma spectrometers such as ÉPÉÉ to the topside ionosphere provide promising experimental results that are needed to complete our understanding; the in-flight calibrations, resultant data products, and first

analysis of the ÉPÉÉ data demonstrate this point. Further calibrations will yield ion temperature data products as well. Importantly, the STP-H9 payload was only one of a series of tests used to improve and prove the efficacy of the laminated style ESA. The measurements made provide important insight for instrument performance that was folded into the design of the Autonomous Ion Mass Spectrometer (AIMSS) that returned to the ISS to begin operation earlier this year. Critically, the AIMSS utilizes the laminated style ESA in conjunction with high powered magnet, and the anode detector is replaced by a position sensitive MCP. These improvements dramatically improve the instrument's energy and mass resolution enabling easy distinction between the different ions of the ionosphere. The upgrade to include plasma composition measurements will allow for pivotal source region identification in order to determine which regions and species rise to higher altitudes during upwelling events. Overall, the development of ÉPÉÉ instrument and fidelity of its measurements comprise an important step towards our understanding of Earth's local space environment that has continued to elude space physicists since the onset of the Early Space Age.

Chapter 5

Heavy Ion Sensor Calibration and Observational Analysis

Section 5.1 Heavy Ions of the Solar Wind

The heavy ions of the solar wind are an important diagnostic for solving most outstanding science questions concerning the solar wind plasma emitted from the Sun into the interplanetary medium. They provide valuable signatures as to the source locations of the solar wind such as coronal holes, active regions, helmet or pseudostreamers, or the quiet Sun (Brooks et al., 2015). In addition, their charge states denote key details concerning the electron temperatures, densities, and ion freeze in distances that occur as a result of the elusive acceleration mechanisms that produce the solar wind (Gilly & Cranmer, 2020; Hundhausen et al., 1968). Beyond being a remote analytic tool for plasma source regions and conditions, heavy ion observations reveal critical insight into the in situ kinetic behavior of particles. For example, since the first missions into interplanetary space we have known that the heavier alpha (He_{2+}) particles often move faster and are hotter than the lighter bulk plasma protons (H^{+})(Neugebauer & Snyder, 1962). The cause and nature of the differential streaming and non-thermal equilibrium heating of ions are an important indicator of how the solar wind becomes accelerated, and potentially drives heating mechanisms that occur as it propagates outward to 1 Au (Ďurovcová et al., 2017; Kasper et al., 2008). Thus, heavy ion measurements of the solar wind are important for understanding the fundamental mechanisms that drive coronal heating as well as solar wind acceleration and transport. (see Chapter 1 and the individual subsections below for further details on the scientific importance of heavy ions).

The value of heavy ion measurements is partly fueled by the lack of available observations. Due to their size, complexity, and resource requirements, the deployment of composition instruments to interplanetary space on science missions has been frequently neglected. Not only this, but the sparse densities of many heavy ions necessitate long accumulation times for reliable statistics. Thus, in depth calibrations are required prior to the release of data products and longer exposure to the plasma results in successive revisions as performance improves. Until recently, the three iterations of the SWICS instrument on the *Ulysses*, ACE, and *Wind* spacecraft have produced the majority of heavy ion studies in the solar wind (G. Gloeckler et al., 1995, 1998; J. G. Gloeckler et al., 1992). The measurements produced by the SWICS instruments, while fundamental to our modern understanding of solar wind heavy ion behavior, have been inherently limited in their nature. First, the SWICS instruments are primarily constrained to observations from 1 Au or beyond; the ACE and *Wind* spacecraft operate from Lagrange Point 1 (L1) whereas *Ulysses* made three consecutive passes over the solar poles that occurred outside of Earth's orbit. Second, the SWICS instruments' FoV and the orientation at which they were mounted on the spacecraft provided solar wind observations in the radial direction only. Therefore, the velocity distributions functions (VDFs) and temperatures that are provided are restricted to the radial direction and the perpendicular behavior of heavy ions (e.g., in and out of the ecliptic plane) have been left unstudied. Thus, the study of heavy ions has been limited by the natural conditions within the solar wind plasma and the practical considerations of instrument design.

The deployment of the Heavy Ion Sensor (HIS) on the Solar Orbiter mission is an important opportunity to increase the type of available heavy ion observations in the Solar Wind (see instrument details below). First, the spacecraft orbits between 0.3 – 1 Au thereby enabling HIS to produce the first heavy ion measurements of the inner heliosphere. Second, the HIS instrument is capable of measuring solar wind plasma perpendicular to the radial direction and can provide novel 3D VDF observations of anisotropic heating and differential streaming. Prior to the release of the 3D VDF measurements a thorough calibration of the data and instrument orientation must be undertaken. In this study, we describe

the calibration pipeline that has been developed to produce the HIS 3D VDF data products. Second, since the final 3D VDF calibrations are still incomplete we provide the first ever detailed analysis 1D differential streaming between oxygen 6+ (O^{6+}) and alpha (He^{2+}) particles in the radial direction and its behavior at varying distance from the Sun. Collectively, the HIS 3D VDF calibrations and 1D differential streaming analysis represent important progress in the use of HIS observations to make fundamental breakthroughs in the physics of heavy ions in the solar wind.

Section 5.2 Description of the Heavy Ion Sensor

The Solar Orbiter spacecraft (SolO) was launched on February 10th, 2020 by the European Space Agency (ESA) to study the Sun and solar wind over a confluence of radial distances and heliolatitudes. The spacecraft carries a suite of remote and in situ instruments that provide observations during orbits ranging between 0.3 – 1 AU and rising above and below the ecliptic plane by ±24°.[71] The Solar Orbiter uses white light and ultraviolet imagers, coronographs, spectrographs and other remote sensors to study the photosphere and outer regions of the solar atmosphere (e.g., chromosphere, corona, etc.) while measuring the particulate radiation and solar wind plasma populations that flow into the interplanetary medium by using a compliment of radio wave and magnetic field sensors with energetic and bulk plasma detectors. Significantly, SolO operated with a plasma composition instrument known as the Heavy Ion Sensor (HIS) that measured the heavy ions in the solar wind (H, ^{4}He, ^{3}He, C, N, O, Mg, Ne, Si, Fe and their charge states) over an energy range from 0.5 – 78 kev/e (Livi et al., 2023; Owen et al., 2020). A diagram of the Solar Orbiter instrument with instrument locations labeled in the top right of Figure 5.1. The HIS instrument is mounted top right (labeled SWA) and peaks over the heatshield to face the oncoming solar wind. The native time resolution for the measurements was 30 seconds and entailed a full cycle through the spherical ESAs 64 logarithmically-spaced voltage settings and 16 elevation angles

[71] During the extended phase of the mission the spacecraft is scheduled to travel up to ±33° heliolatitude.

dictated by the voltages applied to deflectors at the entrance aperture. The bottom right picture in Figure 5.1 is of the HIS instrument with the ESA entrance at the top. The FoV is approximately 96° × 34° (azimuth by elevation) and the particle trajectories are recorded after passage through the ESA, post-acceleration system, and ToF chamber using using the Start MCP position and an array of 32 SSDs. The HIS instrument is a triple-coincidence plasma spectrometer that uses secondary electrons to measure heavy ions with three separate detections to achieve unparalleled signal to noise ratios and mass resolution (see chapter 1). The drawing in the top left of Figure 5.1 illustrates the individual components that comprises the HIS instrument with the ESA at the top, ToF chamber below, and the base of the instrument comprising the electronics. HIS is amongst the most powerful composition instruments to be deployed to study the solar wind to date; it has an extended energy range to measure suprathermal particles and plasma heated by solar wind transients and unprecedented time cadence. However, the most novel performance feature is the ability for HIS to produce three-dimensional velocity distribution functions (3D VDFs) of the solar wind plasma. The elevation angle selection provided by the entrance deflectors and wide FoV of the HIS instrument enable it to produce the first ever 3D VDFs of heavy ions in the inner heliosphere that include particle trajectories out of the ecliptic and perpendicular to the radial direction. The plot in the bottom left of Figure 5.1 shows the HIS FoV perpendicular above and below the ecliptic plane. By applying different voltages to the deflector electrodes at the entrance particles are measured at the individual elevation bins to provide angular distributions within this plane. The bin widths are from initial ground calibrations, and the regions colored purple indicate overlap between the bins and blind spots are colore grey. The importance of 3D VDFs results from the scientific value of vector coordinate observations. For example, particle wave interactions result in anisotropic heating that occurs perpendicularly and parallel to interplanetary magnetic field (Marsch, 2012; Verniero et al., 2022). While the existence of parallel and perpendicular heating has been long established the ultimate causes are still being investigated (J. Huang et al., 2020; Marsch et al., 2009; Tu et al., 2004). To study the influence of fields on particles and vice versa requires measurements in vector coordinates for both particle velocities and the magnetic field to discern relationships between field orientation and

Figure 5.1 The Heavy Ion Sensor

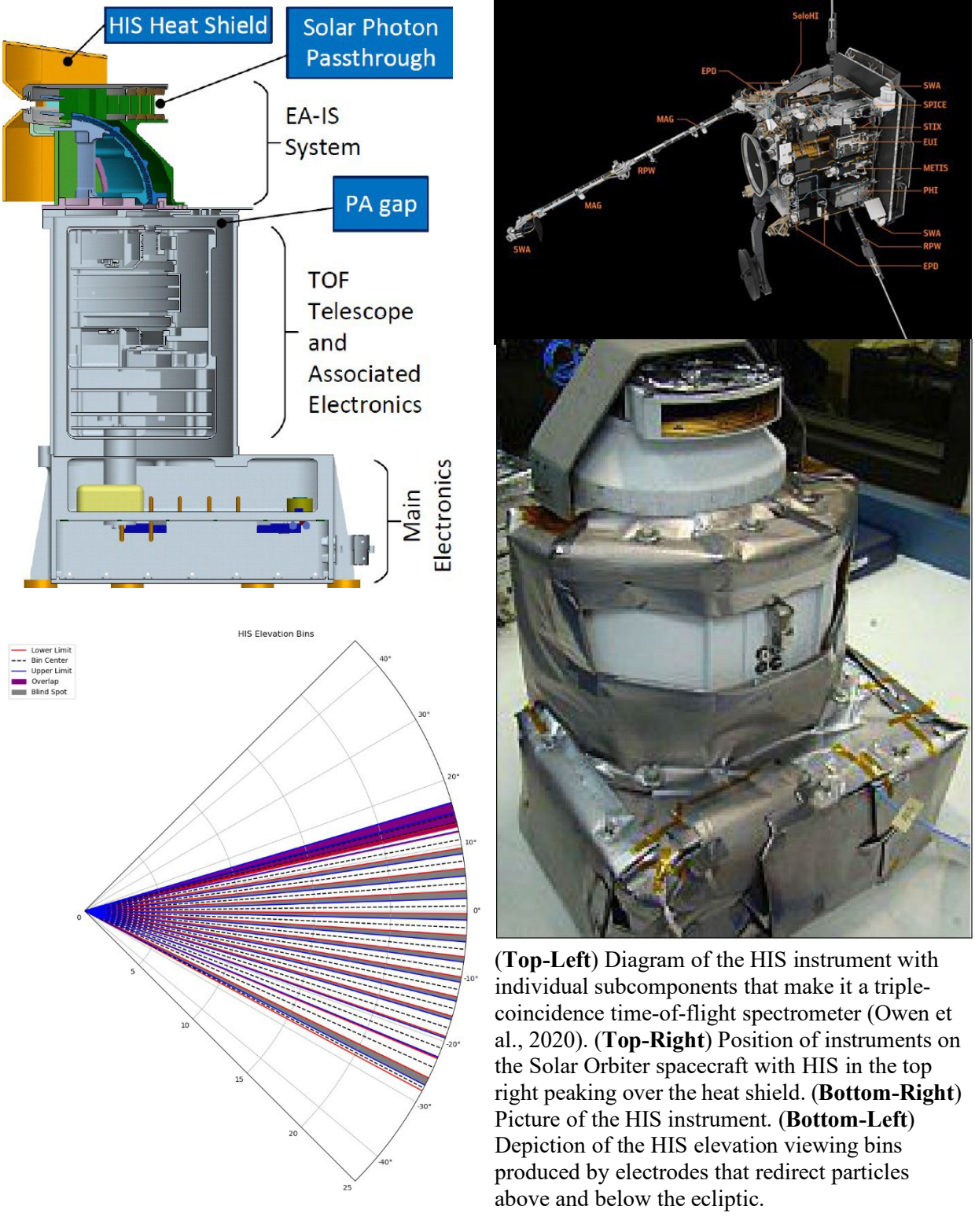

(**Top-Left**) Diagram of the HIS instrument with individual subcomponents that make it a triple-coincidence time-of-flight spectrometer (Owen et al., 2020). (**Top-Right**) Position of instruments on the Solar Orbiter spacecraft with HIS in the top right peaking over the heat shield. (**Bottom-Right**) Picture of the HIS instrument. (**Bottom-Left**) Depiction of the HIS elevation viewing bins produced by electrodes that redirect particles above and below the ecliptic.

perturbations with changes in particle speed and direction. In addition, as discussed in the chapter introduction the only differential streaming measurements have occurred in the radial direction (see e.g., L. Berger et al., 2011; Mostafavi et al., 2022). Therefore, the ability to measure heating and differential streams along axes perpendicular to the radial motion contains high potential for scientific discovery; since observations are limited to the radial motion the degree to which differential streaming is determined by the bulk flow velocity and magnetic field orientations is still unknown. With the production of 3D VDFs of heavy ions the analysis of differential streaming perpendicular to the radial direction and during deviations in the bulk flow and magnetic field vectors can be undertaken. Thus, the addition of HIS to the Solar Orbiter mission and the faithful calibration of its data products is a necessary step to understanding the plasma source origins and heavy ion kinetics in the interplanetary medium.

Section 5.3 Heavy Ion Sensor 3D VDF Calibration[72]

The calibration of the HIS heavy ion 3D VDFs is a multistep process that requires a thorough understanding of the spacecraft. The SolO spacecraft is 3-axis stabilized meaning it has complete control of its attitude and orientation and rotates itself accordingly to assist with communication transfer and remote observation campaigns. To resolve the 3D VDFs, the spacecraft attitude, instrument placement and FoV, and the relative motion of the spacecraft with respect to a global, fixed reference frame all need to be taken into account. The first step is to map the instrument's position and viewing angle to the nominal pointing direction of the spacecraft which is typically radially pointed at to Sun. Second, the spacecraft position and pointing direction have to be properly oriented in the Heliosphere to produce data products with the solar wind in the optimal reference frame for analysis by the scientific community. In a heliographic coordinate system, the x-axis is defined by the radial vector between the Sun and orbiting object. The normal vector points out of the ecliptic plane, and the third tangential vector is perpendicular

[72] The HIS 3D VDF calibrations were completed with the guidance and mentorship of Dr. Ryan Dewey.

to both (R,T,N). These transformations are enacted using the SPICE (spacecraft, planet, instrument, C-matrix, events) kernels that are developed by the mission's operation team (C. Acton et al., 2018; C. H. Acton, 1996). The SPICE kernels contain not only information on the placement of instruments and FoVs for different missions, but also hold information concerning the motion of the spacecraft and the scientifically relevant surrounding bodies (e.g., the Sun, planets, stars, etc.). In order to convert the data into a desirable reference frame it is important to begin with properly defining the HIS FoV before applying the sequence of transformations to rotate the vector coordinates of the grid; in practice, translating the instrument's FoV to different reference frames is done by rotating the individual pixel corner vector vertices using transformation matrices. A diagram of the coordinate transformation process is supplied in Figure 5.2. The individual steps of the pipeline are listed at the top and in the bottom are samples of the HIS FoV reference transformation by 30° rotations along different axis. The original FoV are the black grids and the transformed FoV are red. The transformation matrices are supplied by the SPICE kernels and are calculated for each measurement time step. The process of tracking and matching the rate of time onboard a spacecraft with the time cadence on Earth is a complex engineering feat that is constantly improved through advancements in technology and signal processing. Due to completeness of the SPICE kernels and technical expertise of the mission operators the transformation of observations becomes a simple process of calling a series of functions that operate on the data using the SPICE kernels. The SPICE kernel software has been developed for a number of programming languages in addition to wrappers written for new languages such as Python; the Python language was used to perform the HIS 3D VDF calibrations for this study. The revised 3D VDFs are rotated into the Solar Orbiter-Sun heliographic coordinate system. An example of the resulting VDF data product with coordinate transformation is shown in the plots of Figure 5.3. The dimensions of the FoV are provided along the x-axis (azimuth) and y-axis (elevation). The top plot shows the raw, untransformed data measured by the instrument in color overlaid with a white grid denoting the individual pixel locations. The bottom plot shows the transformed data with the revised FoV demarcated by a red grid. In addition, the motion of the center or boresight of the HIS FoV as a function of time was assessed to determine the changes in HIS pointing direction on

Figure 5.2 HIS RTN Coordinate Transformation

1. Convert from Elevation-Azimuth to Polar-Horizontal.
2. Transform to rectangular coordinates.
3. Rotate to Spacecraft RTN.
4. Transform to spherical coordinates.
5. Convert from Polar-Horizontal to Elevation-Azimuth.

Step 3 Matrix Algebra

$$\vec{v}_{SRTN}^{cart} = R_{SRTN} \cdot (-\vec{v}_{HIS}^{cart})$$

Note: The cartesian vector is inverted to convert from the instrument view frame to the frame of an incoming particle.

Breakdown of the method used to rotate the HIS 3D VDFs into SolO-Sun RTN coordinates. The plots show how the HIS FoV is transformed via test matrices along three axes. The actual rotations are performed using the SPICE kernels matrices.

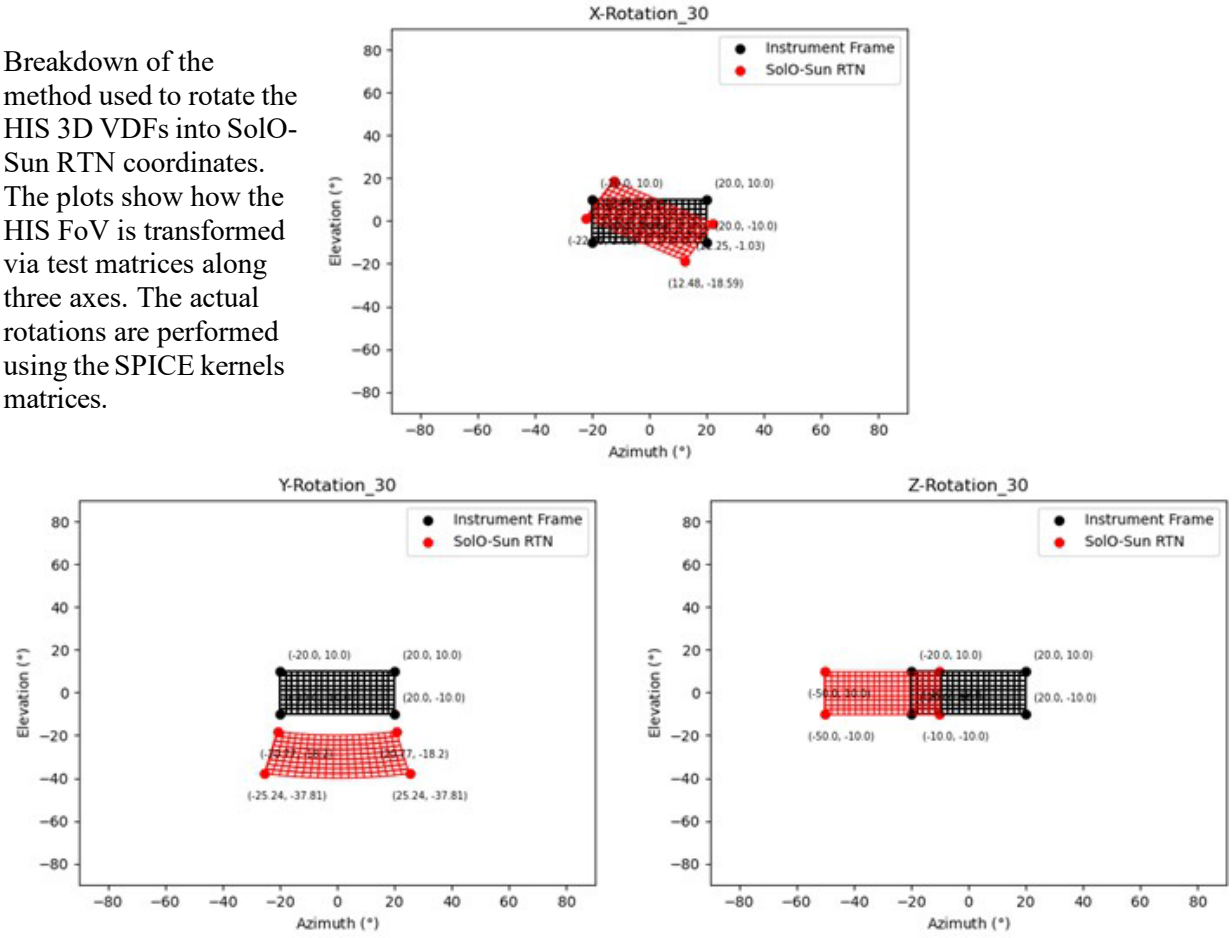

Rotations along x, y, and z-axis by +30°.

orbit – a plot of the boresight motion as a function of time is plotted in Figure 5.4 for the life of the mission. The top plot shows the spacecraft position in orange and the tilt in the elevation angle in black. The SPICE analysis indicates the spacecraft lists from side to side depending on whether it is moving along an inbound or outbound trajectory; inbound trajectories move toward perihelion and outbound trajectories are during travel to aphelion. Furthermore, as evidenced by the middle plot of

Figure 5.3 HIS 3D VDF RTN Transformation Results

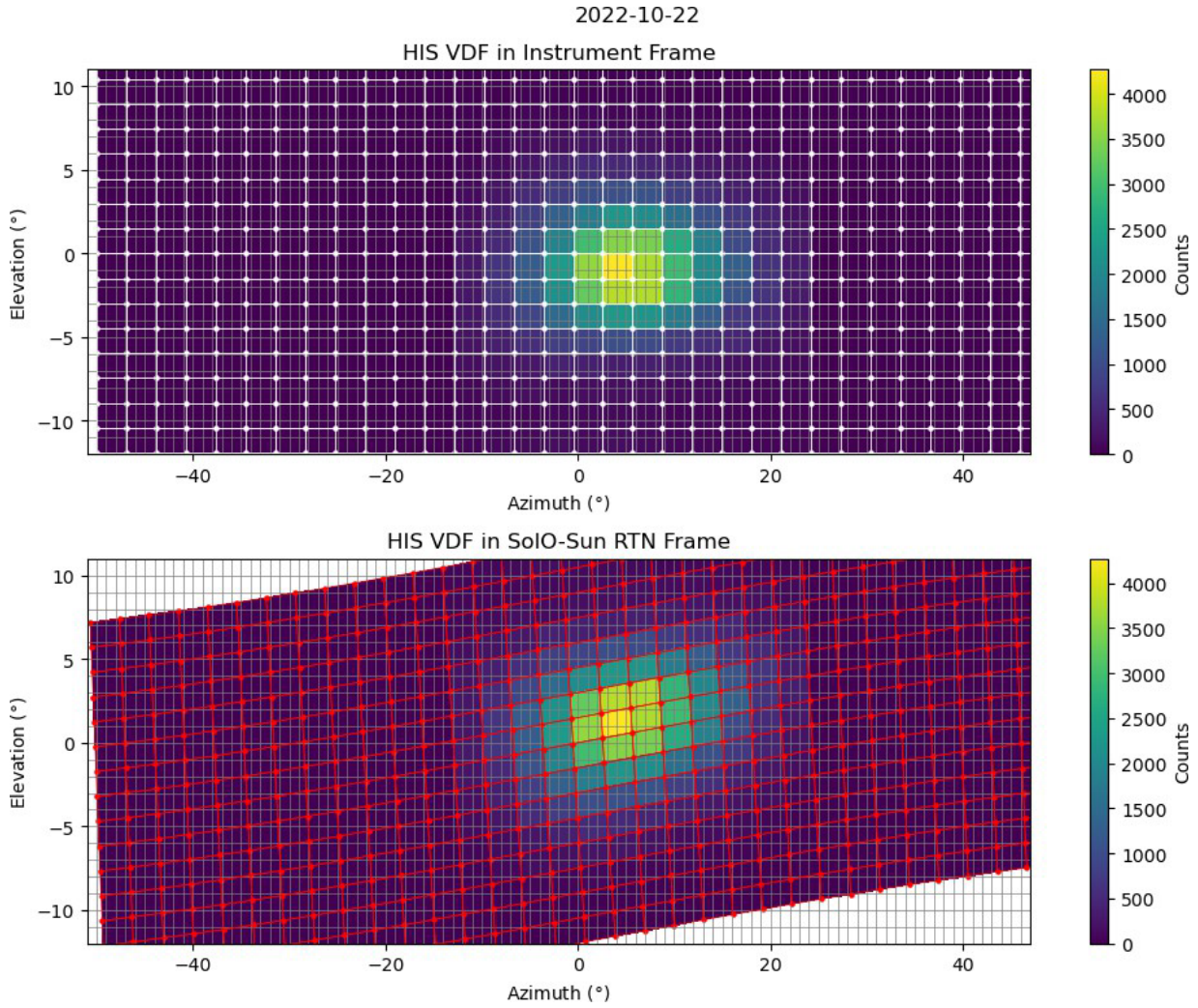

Example of the results of the 3D VD coordinate transformation from instrument frame to SolO-Sun RTN coordinates. The top plot shows the raw data and the bottom plots shows the transformed data in the transformed FoV. The spacecraft appears to list from side to side depending on its position along its orbit.

Figure 5.4 HIS Coordinate Transformation Validation

Position and pointing direction of the HIS instrument. The top plot shows spacecraft position (black) and the FoV elevation title or list angle (orange). The results indicate the spacecraft tilts left on inbound trajectories and right on outbound. The middle plot shows the instrument boresight azimuth (in ecliptic) and elevation (out of ecliptic motion. The bottom plot shows the results of the velocity aberration corrections.

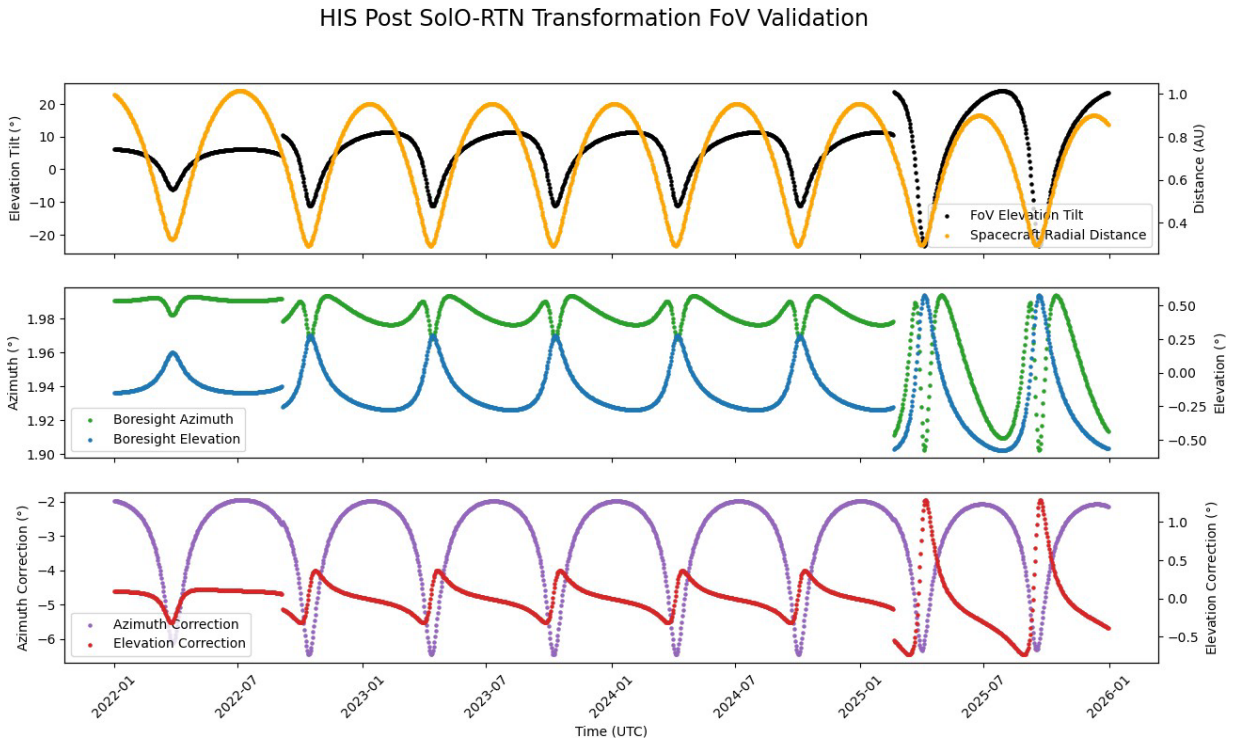

Figure 5.4 the HIS FoV pointing direction changes in both azimuth and elevation as a function of radial distance as the spacecraft slightly adjusts (< ±2°) its position to stay aligned with the Sun. The orientation of the spacecraft is typically dictated by the science goals of the remote sensors' instrument teams. As can be seen from the plots showing position and viewing angles in Figure 5.4 (as well the position maps in Figure 5.5 and Figure 5.7), the jump in radial distance and shift of the orbit in the vertical plane indicate a significant change in spacecraft orientation September 4th, 2022 when the spacecraft was boosted to higher orbital inclinations via a gravity assist maneuver about Venus. From this observation, the coordinate transformations appear to reconstruct the spacecraft's motion in the HIS FoV boresight direction. Altogether, the SPICE transformations for the HIS 3D VDFS were validated using the time series investigation of the FoV motion and spacecraft position and orientation.

In addition to the spacecraft position and pointing transformations, corrections must be applied to the data to account for the influence of the spacecraft's motion on the trajectories recorded for particles. This is known as the spacecraft velocity aberration correction.[73] In order to account for the velocity aberration, the spacecraft attitude and its motion in the radial, normal, and tangential direction must be determined. The normal and tangential velocities correspond to latitude and longitude in the heliographic coordinate system, respectively. This is accomplished using the data provided by the SPICE kernels and their corresponding function used to call the spacecraft position and velocity. To validate the velocity measurements, the spacecraft trajectory was plotted with colors that correspond to the magnitude of individual velocity components and is shown Figure 5.5. White arrows indicate the direction of the spacecraft travel. The two larger plots on the left show an out of ecliptic view with the x-axis in the ecliptic plane and the z-axis pointing perpendicular above and below; here we have the normal velocity indicated by color to show the latitudinal motion of the spacecraft. The smaller three maps on the right show the top down motion within the ecliptic and are colored by the total, tangential, and radial velocities from top to bottom. As expected, the spacecraft is traveling fastest in the radial and tangential directions during its perihelion passes of the Sun. In addition, when the spacecraft moves to higher latitudes there is a noticeable positive increase in the normal velocity as expected, indicating the R/T/N velocities can be used to accurately determine the velocity aberrations. Thus, from the plots it is clear that the spacecraft velocities will be effective in predicting the necessary correction for the spacecraft motion in the measurements.

First, the apparent (or measured) particle velocity ($vv_{\text{ß}}^{iiiiii}$) must be modified to remove the effects of aberration caused by radial motion of the spacecraft ($vv_{\text{ß}}^{IIiippSS}$).

[73] A good analogy is feeling for the direction of the wind with your hand outside of the window of a moving vehicle.

$$vv'_{RR} = vv^{iiiiii}_{RR} - vv^{IIippSS}_{RR}$$

The motion of the particle is first recorded as an energy-per-charge (E_i/q_i) by the ESA before being converted into a velocity and is therefore mass dependent and different for each ion. Second, the aberration angle is calculated using the geometry of the spacecrafts motion with respect to the radial direction (see diagram in Figure 5.6 geometry of calculation).

$$\theta\theta_{NN} = \tan^{-1}(VV_{NN}/VV'_{RR}), \qquad \theta\theta_{TT} = \tan^{-1}(VV_{TT}/VV'_{RR})$$

Figure 5.5 Solar Orbiter Velocity Maps

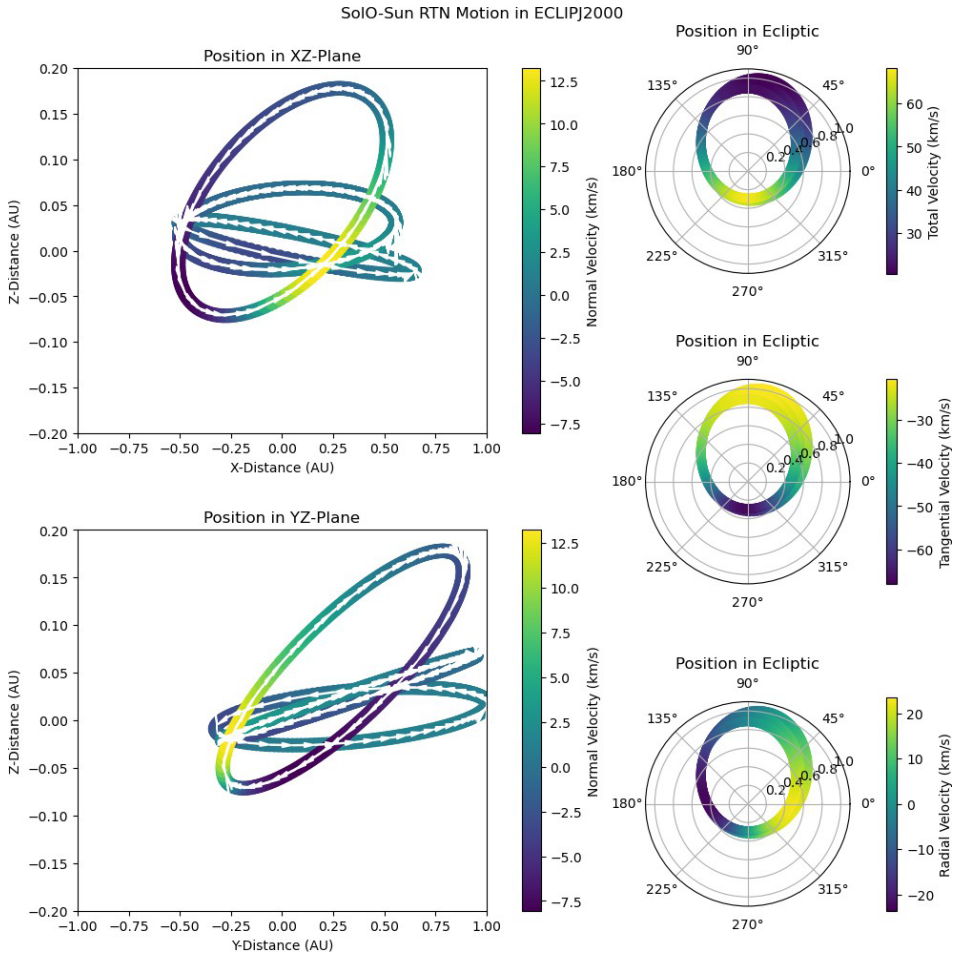

Maps of the position of the Solar Orbiter spacecraft colored by spacecraft velocity. The left two plots indicate the heliolatidudinal position sliced along two perpendicular planes colored by normal velocity with white arrows indicating the direction. The right three plots are top down looking at motion projected onto the ecliptic plane and colored by total velocity (top), tangential velocity (middle) and radial velocity (bottom). All velocities behave as expected of the spacecraft orbital motion.

Figure 5.6 Aberration Correction Calculation

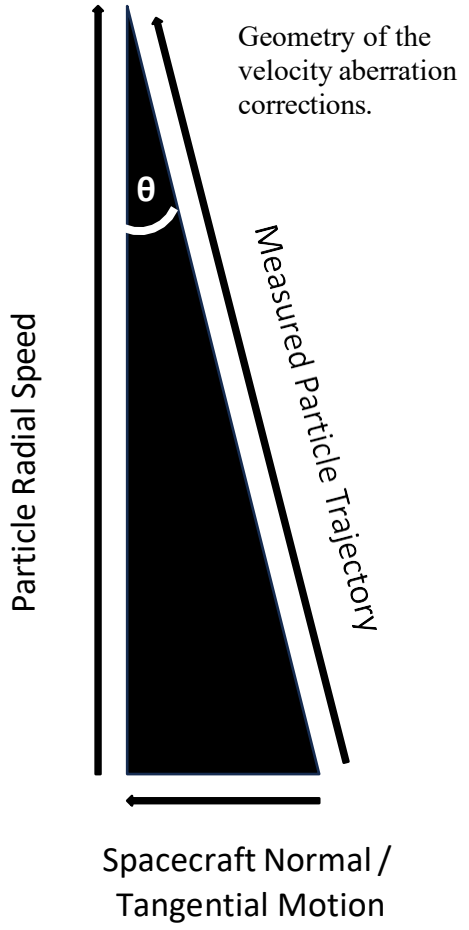

Here $\theta_{N/T}$ are the aberration angles and V_N, V_T, and V'_R are the normal, tangential, and modified radial velocities, respectively. With the angular distribution of the FoV placed onto a rectilinear grid the calculated aberration corrections become simple linear shifts in the coordinate system. Daily calculations of the velocity aberrations were made for the instrument's operation lifetime and plotted onto the spacecraft trajectory similar to the R/T/N velocity maps; these trajectory maps are shown in Figure 5.7. In addition, the azimuth and elevation corrections as a function of time are plotted in the bottom of Figure 5.4 for comparison with other spacecraft parameters. The azimuth corrections range from -2° to -6° degrees depending on the tangential velocity of the spacecraft i.e., the greatest values occur at perihelion and the small values at aphelion. Likewise, the aberration due to the lower normal velocities produces less aberration ($< \pm 1°$). Therefore, the alterations used to fix velocity aberrations correctly match the motion of the spacecraft about the Heliosphere. Altogether, Figure 5.4 to Figure 5.7 indicate the individual steps and final results of the 3D VDF calibration pipeline are correct. The total magnitudes of the boresight tilt and velocity aberration corrections require further validation prior to the release of data products to the scientific community that were not completed during this study. Nonetheless, the results thus far are promising and provide the majority of the framework necessary for completing the data transformation.

The addition of the HIS instrument to the Solar Orbiter payload is an important step towards producing essential observations for plasma source identification and in situ plasma kinetics; these data

Figure 5.7 Solar Orbiter Aberration Correction Maps

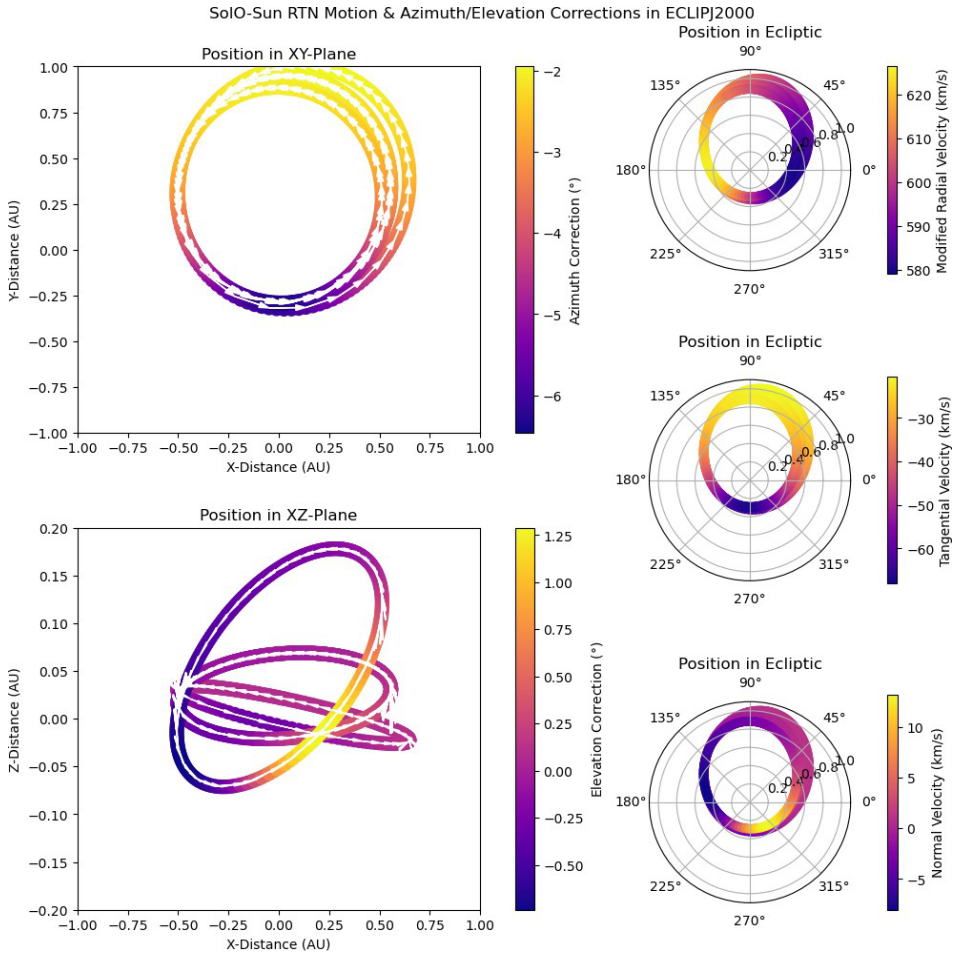

Maps of the position of the Solar Orbiter spacecraft colored by velocity aberration corrections. The individual plots match the same orientations as Figure 59. When the spacecraft moves upward the corresponding correction removes the apparent downward motion of the particles. Likewise, along the tangential direction. Thus, the behavior appears correct although the magnitudes require further validation.

will provide insight into the elusive acceleration mechanisms and help confirm existing theories for solar wind heating by providing measurements along axes perpendicular to the radial direction. To that effect, major milestones were made in the 3D calibration, but further validation and the final steps to produce the publicly available data products await. Future work to help accomplish this will include tests of the coordinate transformations using more minute increments that will elucidate more detail in spacecraft motion. For example, deviations in spacecraft pointing that occur as the high-powered antennae are directed toward Earth to assist in the transmission of data should appear in the boresight transformations. The final step of the calibrations will be to incorporate the geometric factor as a function of energy-per-charge and elevation deflector settings. This will entail any corrections that result from overlapping in the

Figure 5.8 HIS Onboard VDF Data During CME Crossing

Plots of the onboard (pre-calibrated) 3D VDFs of alphas (top) and O^{6+} particle distributions just before and after a CME shock crossing that occurred on September 6th, 2022. The out of ecliptic elevation measurements are summed over and plotted onto the ecliptic plane. The white dotted lines indicate the instrument FoV and azimuthal look direction. The data are summed over 30 minute intervals and have an hour and half separation in between. The populations are clearly heated as a result of the shock crossing indicating the important science that can be done with the HIS VDFs.

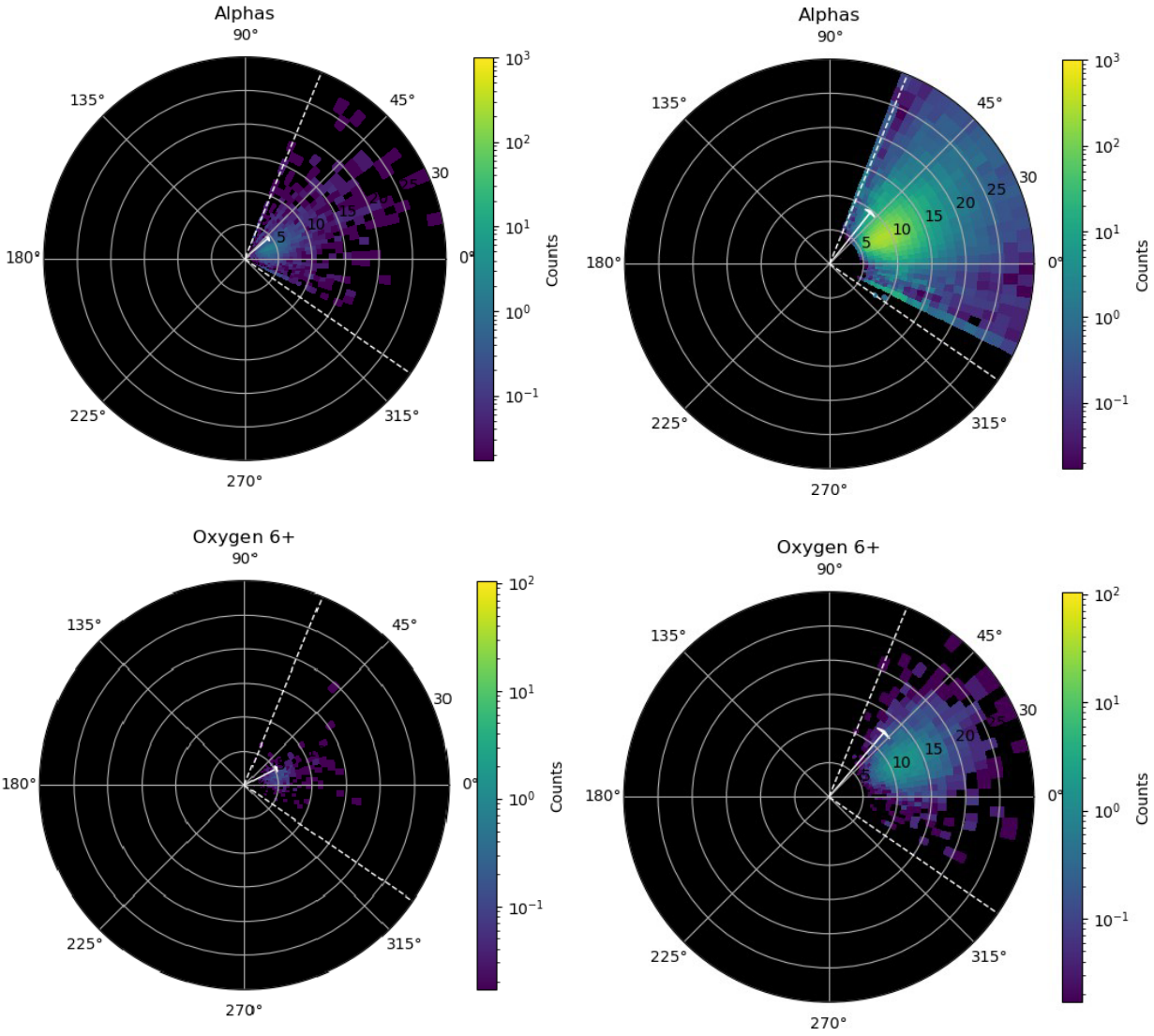

elevation bins (seen in Figure 5.1) and will incorporate the results of pre-existing ion optical models developed during the HIS instrument's development. In addition, improvements to the geometric factor can be made by cross-calibrating the individual elevation bins between HIS and the PAS sensor for the low mass ions that are measured by both instruments (i.e., protons and alpha particles). Already, the detail revealed by the onboard VDFs relay important physics occurring the solar wind, such as the heating of

O^{6+} during the crossing of a CME shock. The plots in Figure 5.8 show the data collected for alphas (top) and O^{6+} (bottom) just prior (left-side) to and after (right-side) the spacecraft passed a shock on September 6th, 2022. The data is overlaid onto a polar plot with the instrument FoV delineated by white dotted lines and the elevation bins summed and projected onto the ecliptic plane. The color increase indicates higher particle counts and the further distance from the center indicates increase in energy. The extreme heating that occurred in both particle species is evidenced by the large spread in velocity space that occurs as the particle temperatures are boosted. The orientation and shape of the contours indicate the extent to which anisotropic heating occurred and enable close comparison with the magnetic field orientation. By incorporating the VDF transformation and calibration pipeline to the existing data the HIS heavy ion 3D VDFs will undoubtedly unlock important secrets in how charged particles are produced and energized in the interplanetary medium.

Section 5.4 Heavy Ion Sensor Radial Differential Streaming

The flow of ions in the solar wind is full of unpredictable behavior. If the particles accelerated by the corona into interplanetary space are imparted with equivalent energies the resultant mass-dependent velocities would be greater for lighter ions. Or, alternatively, acceleration mechanisms that may result in terminal velocities would at least have them moving at equivalent speeds. However, during early explorations into the Heliosphere it was recognized that the heavier alpha particles typically travelled faster than the more abundant, lighter protons (Neugebauer & Snyder, 1962). Additionally, later observations taken during the Helios 1 & 2 missions found that the magnitude of the differential streaming between the two ions was greater with closer proximity to the Sun (see Figure 5.9). Moreover, they found that differential speed between alphas and protons often approaches but rarely exceeds the alfvén velocity, or the speed at which alfvén waves propagate, in the solar wind plasma. This indicated a potential relationship between waves moving through interplanetary magnetic field and acceleration of ions to differential speeds. Also, the highest speeds of alpha-proton differential streaming occur in the fast

wind and a general positive correlation between differential speed and the bulk flow was recognized. The middle plot on the left of Figure 5.9 shows the magnitude of proton-alpha differential streaming on the y-axis and distance from the Sun on the x-axis. In addition, the data is binned by wind speed and plotted separately by color. The fastest wind speeds exhibit the greatest differential streaming. Moreover, all wind speed types display the highest proton-alpha speed separation at closer proximity to the Corona. Since the strength of differential streaming is inversely related to distance from the Sun it is reasonable to interpret that the offset in particle energies is produced within the corona during solar wind acceleration. Nonetheless, like the source of solar wind acceleration, the ultimate cause of differential streaming is still not fully understood and, consequently, the differential streaming of heavy ions has been an important topic for solar wind research for several decades. More recent studies develop the notion of collisional age which classifies the solar wind by the number of coulomb interactions that have occurred since emission from the corona (Kasper et al., 2008). The plot in the top right of Figure 5.9 displays the ratio of alpha to proton perpendicular temperature in color with the collisional age along the abscissa and magnitude of differential speed along the ordinate. The helium ions experience higher heating when they move at the speed of protons due to the enhanced resonance with alfvén waves. By employing collisional age to analyze data from the *Wind* mission the authors recognized that as the solar wind propagates outward the separation between the speed of the particles slowly decreases as the two, presumably mostly parallel, ion beams relax towards thermodynamic equilibrium through scattering. More recently, data from the SWICS instrument was used to determine if differential streaming with respect to the bulk proton plasma extends to ions heavier than alphas, such as the third most abundant species oxygen 6+ (O^{6+}). L. Berger et al., 2011 provided further analysis of differential streaming by including heavy ions in the radial direction at 1 Au and found the ions did move separately with respect to the protons but with no clear relationship with the individual speeds (e.g., mass-per-charge dependency). With the recent release of HIS 1D radial heavy ion data products, Rivera et al., 2025 examined O^{6+} and proton differential streaming and found that they behave similarly to the alpha particles across varying distances from the Sun (e.g., relationship to alfvén velocity and bulk flow speed). The top left plot in Figure 5.9 shows their

results with the number number of measurements plotted with magnetic field orientation on the x-axis and the magnitude of O6+ to proton differential streaming along the y-axis. It is clear that the greatest separation in speeds are found when the magnitude field is pointed parallel or antiparallel to the radial direction from the Sun. Interestingly, the early Helios studies assumed that alpha to proton differential streaming is always radially aligned regardless of field orientation and can be distinguished during periods when the magnetic field alignment is non-radial. Most studies, however, have remain agnostic on this issue (e.g., (Ďurovcová et al., 2017; Mostafavi et al., 2022). Some recent approaches (e.g., L. Berger et al., 2011; Rivera et al., 2025) have changed this assumption and used the magnetic field angle to predict the increased magnitude of differential streaming from the measured values during large deviations with the radial axis; the presumption that we only see the projection of the differential streaming along the radial axis during periods of non-radial field alignment is bolstered by the fact that the greatest values of differential streaming occur when the magnetic field is radially aligned. In addition, Rivera et. al., 2025 found momentary periods of negative differential streaming with protons moving faster than O^{6+} that coincided with inversions in the magnetic field polarity (i.e., antiparallel to the radial direction). Importantly, Ďurovcová et al., 2017 analyzed changes in alpha to proton differential streaming over a solar cycle and found the existence of separate populations with positive vs negative differential streaming in slower wind that are easily distinguished from one another at solar minimum The bottom plot in Figure 5.9 shows histograms of proton-alpha differential streaming for three separate wind speed categories separated by solar minimum (blue) and solar maximum (pink). The bimodal positive and negative differential streaming can be found in the slow wind at on the right and is most easily distinguished at solar minimum. Additionally, they found that during solar maximum, a large plasma population with no differential speed appears that is associated with ICMEs indicating they inhibit the mechanisms that produce

Figure 5.9 Summary of Heavy Ion Differential Streaming

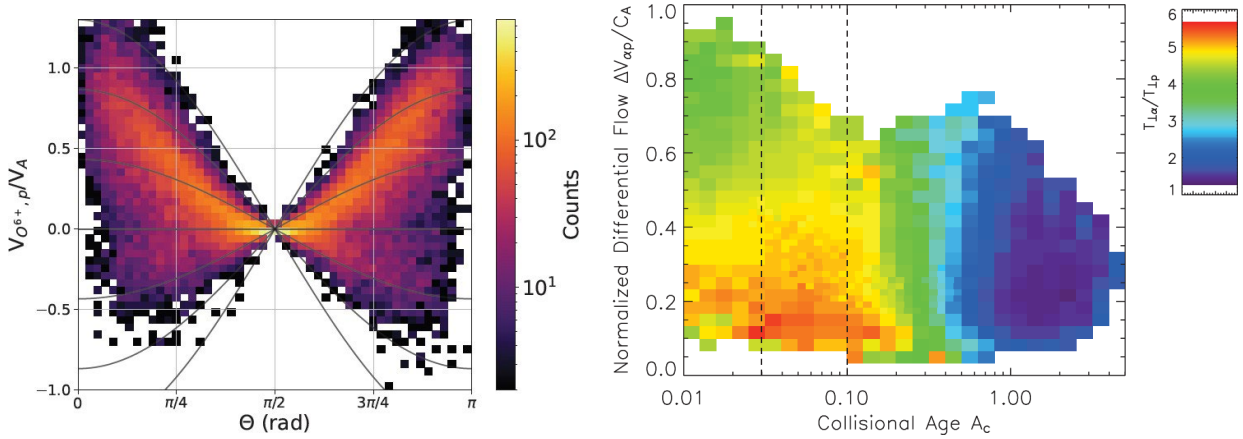

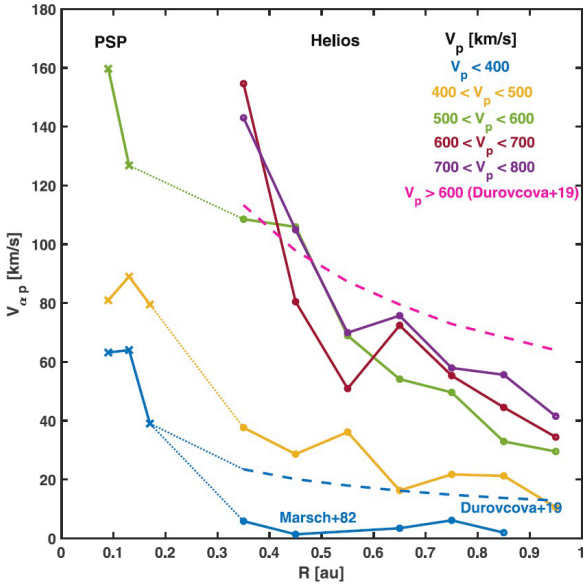

(**Top-Left**) Plot of O^{6+} to proton differential streaming as a function of magnetic field orientation. The greatest (negative and positive) differential streaming occurs when the field is radially aligned (0° and 180°)(Rivera et al. 2025). (**Top-Right**) Ratio of alpha to proton perpendicular temperature as a function of differential speed and collisional age. Heating is maximized when the ions flow together and as particles collide, they relax towards equilibrium (Kasper, et al., 2008). (**Middle-Left**) Differential speed as a function of proton velocity and distance from the Sun. Higher speed exhibits higher differential flow (Mostafavi et. al., 2022). (**Bottom**) Fast and slow wind contain different differential streaming populations. The slow wind contains two distributions that flow in positive (alphas faster) and negative (protons faster) differential flow. ICMEs during solar maximum produce plasma with no differential flow (Ďurovcová et al., 2025).

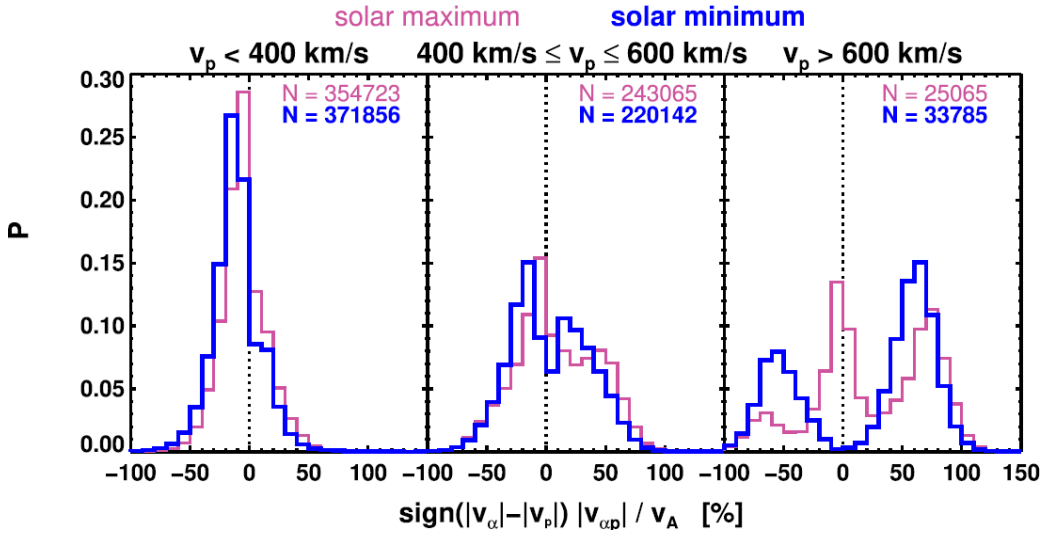

differential flow. Therefore, there is strong evidence linking ion differential flows with the ambient solar wind acceleration and determine the heating mechanisms that occur in interplanetary space.

It is important to extend studies of differential flow into the inner heliosphere and with heavier ions than alphas in order to search for any dependencies that may reveal source acceleration mechanisms. However, to date an in-depth analysis of the differences in velocity between alpha particles and O^{6+} i.e., without reference to the bulk proton flow has yet to be undertaken. The HIS instrument has produced reliable radial velocity distributions functions for both alpha particles and O^{6+} that enable a detailed comparison between the two at varying distances in the inner Heliosphere. Understanding when and how alpha and O^{6+} differential streaming occurs will assist in answering important science questions concerning the acceleration of ions as they leave the corona. In addition, determining the evolution of differential streaming will provide further insight into the heating process that occurs in the solar wind. While the 3D VDFs calibrations are still being developed it is nevertheless important to analyze the existing 1D data set for apparent trends. Hence, analysis of the new HIS data set provides an important opportunity to study solar wind energization and transport mechanisms.

The data used for 1-D differential streaming study was collected from January 2022 to May 2023.[74] The measurements were collected from three instruments: the Proton-Alpha Sensor (PAS), the Solar Orbiter Magnetometer (MAG), and the Heavy Ion Sensor (HIS) (Horbury et al., 2020; Owen et al., 2020). The MAG instrument provides three-dimensional vector data of the magnetic field to determine any impact from field strength and direction on differential speed, and likewise the PAS instrument provides proton data products (e.g., density, bulk flow velocity, temperature, etc.). The 1-D velocities of alpha and O^{6+} data products were provided by the HIS instrument and quantify the radial velocities only. The first step was to match the time cadences between the three instruments because the MAG (8 Hz or

[74] The HIS instrument experience a mishap at the end of April 2023 after which it was decommissioned once tests could determine the ultimate cause.

every 0.125 sec) and PAS (0.25 Hz or every 4 sec) instruments record measurements significantly faster than HIS (1.6 mHz or every 10 minutes). The MAG and PAS data were averaged over 10 minutes to match the HIS observation time resolution. The proton data used for the differential speed is the motion along the x-axis in the spacecraft coordinate reference frame to match the HIS alpha and O^{6+} observations. The x-coordinate in the spacecraft reference frame (SRF) is the pointing direction and nearly always pointed forward towards the Sun and therefore aligned with the backwards/antiparallel radial direction. The magnetic field angle is calculated using the positive SRF x-coordinate which roughly corresponds with the negative radial direction. Thus, 0° is backwards pointing and 180° points outwards. Since the off-axis motion is not measured the differential speed between the ions is a simple scalar subtraction. In addition, the alfvén speed, magnetic field angle, flow angle, and other characteristics of the solar wind were calculated to investigate for correlation with the differential speed. The definition of the scalar alfvén velocity is:

$$VV_{AA} = \frac{|BB|_{MMAAMM}}{\sqrt{\mu_0 mm_{pp} mm_{PPAAII}}}$$

Here V_A is the alfvén velocity, $|B|_{MAG}$ is the magnetic field strength recorded by MAG, μ_0 is the permeability of free space, m_p is the mass of a proton, and n_{pas} is the proton number density measured by PAS. Using these steps the data was prepared for the differential streaming study.

We first performed an analysis of the alpha to proton and O^{6+} to proton differential streaming individually to ensure consistency with the observations made in previous studies before analyzing the speed separation of the two species together. Our results show the behavior of alpha-proton and O^{6+}-proton differential streaming display similar properties to those previously recognized (Mostafavi et al., 2022; Rivera et al., 2025); the greatest differential streaming values occur more often during periods of close proximity to the Sun. This is evidenced in Figure 5.10 plot C that shows the greatest positive values of differential streaming (x-axis) are visible at the lowest distances (y-axis) in the bottom right corner.

Figure 5.10 Observations of Alpha-Proton Differential Streaming

Plots of the O^{6+}-proton and alpha-proton differential streaming results. Typically, O^{6+} and alpha particles differential stream together and exhibit similar properties. (Top-Left) The alpha-proton differential speed as a function of magnetic field angle and radial distance. Greater values correspond to radial and anti-radial alignment and closer distances to the Sun. (Bottom-Left) Alpha-proton differential speed in relation to distance from the Sun and proton velocity. The higher differentials correlate positively with bulk flow speed. (Top-Right) Impact of alfvén velocity on differential speed. Differential speeds are capable of achieving higher values with greater alfvén speed but rarely exceeds it. (Bottom-Right) O^{6+} differential speed plotted with magnetic field angle and strength. Higher O^{6+}-proton speeds occur during larger field strengths that occur closer to the Sun.

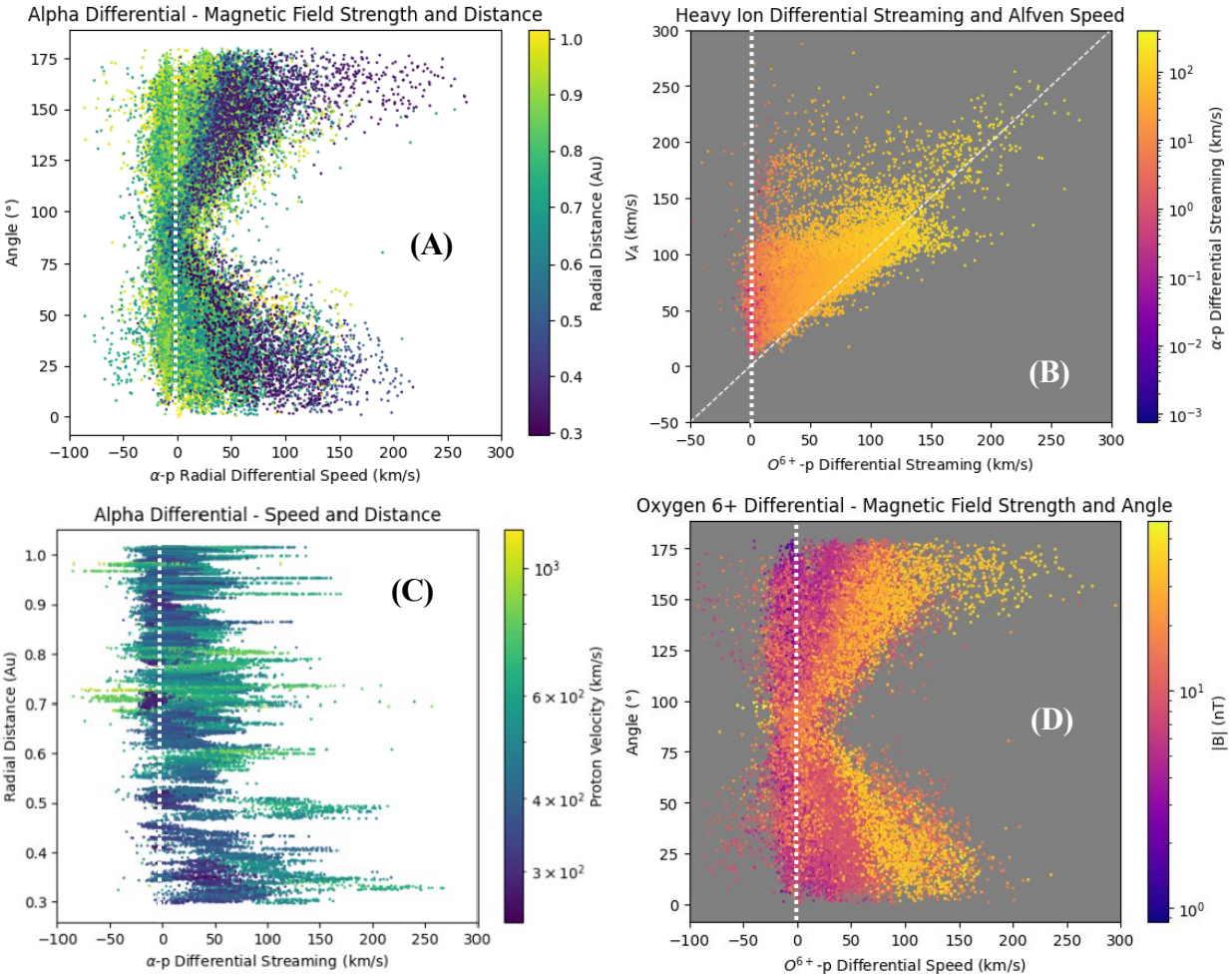

The data in plot C are color coded by proton velocity. It can be seen that slowest wind speeds (blue) are clustered around zero differential flow and that both the He^{2+} and O^{6+} ions differential streaming with respect to protons exhibit greater values (green and yellow) in fast wind streams. It is important to note that nearly all trends in differential streaming are with the maximum values only – low differential streaming appears during all solar wind classification schemes investigated by this study. The O^{6+}-proton differential speed and proton alfvén velocity are plotted in the plot B of Figure 5.10. There is a clear

linear trend between differential streaming and the lower bound of the alfvén velocity with the differential speed rarely exceeding its value. Furthermore, from Figure 5.10 plots A and D it can be seen that the highest alpha-proton and O^{6+}-proton differential streaming values occur when the magnetic field is aligned (parallel and antiparallel) with the radial direction. This is consistent with the assumption that the differential streaming is field aligned that is made by some contemporary studies (e.g., L. Berger et al., 2011; Rivera et al., 2025). In addition, the existence of negative differential streaming (protons moving faster than alphas, O^{6+}) is clearly visible in the data. This can be seen in the left-hand side of the white dotted line in all four plots. However, periods exist with negative differential speed i.e., the protons move faster than the heavy ions that correspond equally with a parallel (180°) and antiparallel (0°) magnetic field orientation (i.e., at the bottom and top of plots A and D in Figure 5.10). Correspondingly, the greatest positive alpha-proton and O^{6+}-proton differential streaming values occur during *both* positive and negative magnetic radial field polarity. Thus, from the first look at the data it does not appear the heavy ions differentially stream along the direction of the magnetic field line but rather in the absence of transverse fields that cause scattering (further discussion below). Rather, heavy ion differential speed exhibits a positive response with the total magnetic field strength which is likely due to the magnitude of both increasing closer to the Sun (seen in Figure 5.10 plot D). It will ultimately require the calibration of the HIS 3D VDFs to conclusively determine the directional properties of the differential streaming along axes perpendicular to the radial direction and to what degree they are linked with the direction of the magnetic field. Nonetheless, the data analysis of individual heavy ion differential motion proved consistent with the solar wind plasma behavior described in previous studies such as their relationships with solar distance, alfvén speed, bulk velocity, and magnetic field orientation (e.g., Ďurovcová et al., 2017; Mostafavi et al., 2022; Rivera et al., 2025).

After finding concurrence between the heavy ion to proton differential streaming with previous studies, we proceeded with analyzing the data for O^{6+}-alpha differential streaming. Under most circumstances in which differential streaming occurs the alpha-proton and O^{6+}-proton separations occur

together. This is shown in Plot A of Figure 5.12 where the alpha-proton and O^{6+}-proton differential streaming is plotted along the x- and y-axis, respectively, and color-coded by magnetic field angle. The clear linear trend demonstrates the positive relationship between the two. However, we found that many of the trends that are exhibited in the individual alpha and O^{6+} streaming with respect to protons do not appear in the O^{6+}- alpha differential streaming. To analyze the relationship between O^{6+} and alpha streaming with respect to other plasma parameters the Pearson coefficients were calculated to analyze the correlations and are listed in the table in Figure 5.11. There are moderate to strong positive relationships with O^{6+}-alpha streaming and proton density, field strength, and O^{6+}-proton differential streaming. In contrast, there are negative correlations with solar distance, alpha temperature, and all ion speeds. Interestingly, there is no relationship found between O^{6+}- alpha differential streaming and alpha-proton streaming, O^{6+} temperature, or alfvén speed when analyzed for the complete data set. The negative correlation between alpha temperature and O^{6+}-alpha streaming matches that between alpha temperature and alpha-proton streaming found by Kasper et al., 2008 i.e., as differential streaming increases the (possibly in situ) heating is reduced. The modest negative correlation between O^{6+}-alpha differential streaming and distance from the Sun is a result of higher magnitudes occurring at closer proximity and is further illustrated in plot B of Figure 5.12. The largest instances of differential streaming are more abundant at smaller distances near the bottom of the plot but with instances of equivalent magnitudes occurring further away. The relationship between distance and the variations in differential streaming was further explored in Figure 5.13 with the O^{6+}-alpha differential

Figure 5.11 O^{6+}-Alpha Differential Streaming Pearson Coefficients

Physical Parameter	Correlation
Solar Distance	-0.24
Proton Density	0.2
Proton Temperature	-0.3
He^{2+} Temperature	-0.17
O^{6+} Temperature	0.03
Proton Speed	-0.36
He^{2+} Speed	-0.33
O^{6+} Speed	-0.26
Alfvén Speed	0.07
Magnetic Field Strength	0.27
Magnetic Field Angle	0.08
O^{7+}/O^{6+}	0.09
O_{Avg}	0.14
O5+ Abundance	-0.03
O6+ Abundance	-0.13
O7+ Abundance	0.11
O8+ Abundance	0.13
He^{2+}-Proton Differential Streaming	-0.01
O^{6+}-Proton Differential Streaming	0.24

Figure 5.12 First Observations of Oxygen 6+ to Alpha Differential Streaming

Plots of the O^{6+}-alpha differential streaming results. (**Top-Left**) The correlation between O^{6+}-proton and alpha-proton differential streaming. They typically occur during the same instances with similar magnitudes, however, there is a clear preference for O^{6+} (positive) differential speed when the field is parallel aligned. (**Bottom-Left**) Alfvén velocity has similar correlation for O^{6+}-alpha differential streaming as others. The trend is linear, however, the O^{6+}-alpha rarely exceeds *half* the alfvén speed. (**Top-Right**) The lack of influence of distance on O^{6+}-alpha differential speed. The negative values clearly occur for higher values of bulk flow speed. (**Bottom-Right**) Differential speed with predicted non-radial values. There is similarly little relationship between O^{6+}-alpha differential streaming and the magnitude of O^{6+} or alpha to proton differentials. However, there is a distinct polarity in O^{6+}-alpha differential speed and magnetic field polarity for a smaller secondary population.

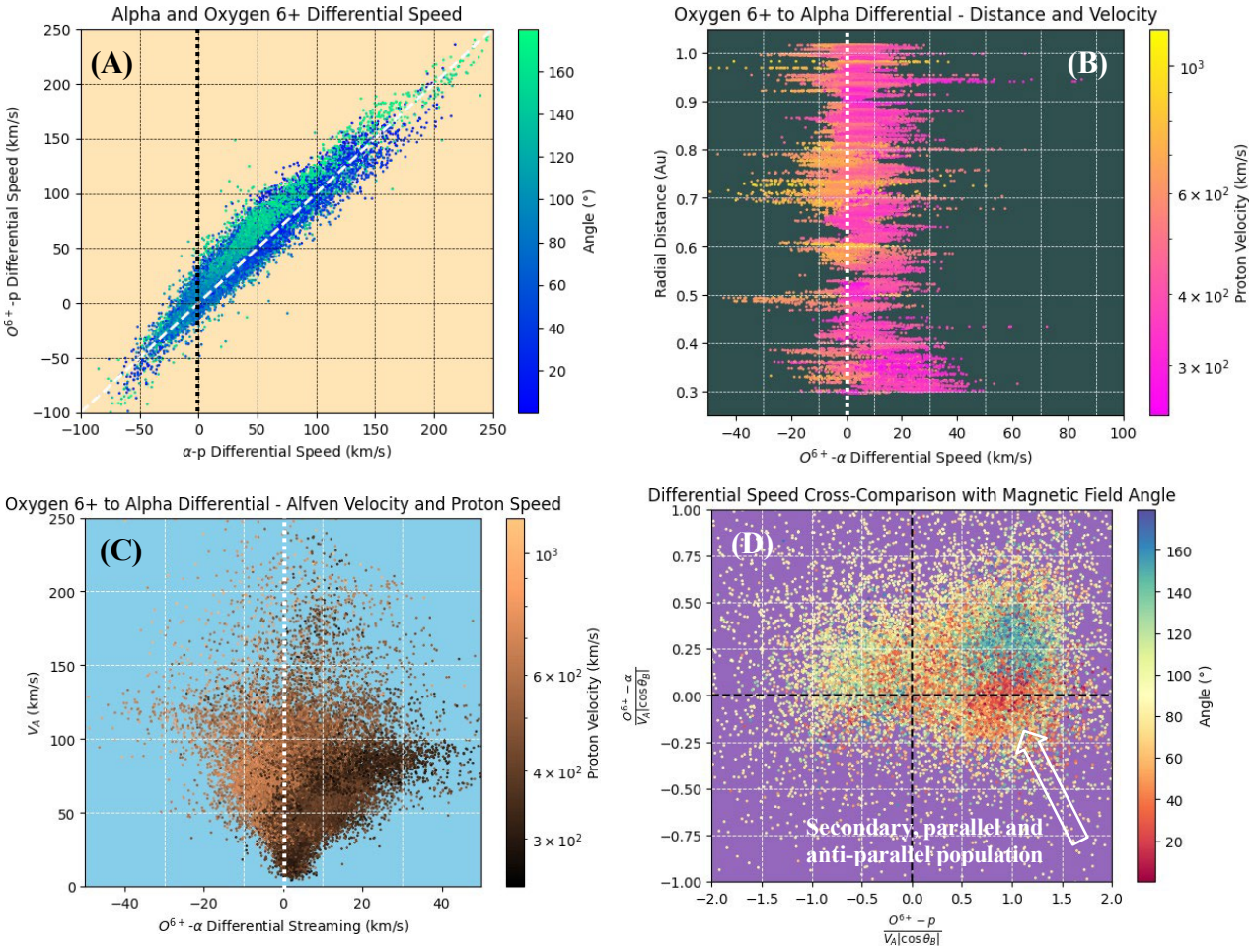

streaming observations (positive-orange/negative-blue) plotted as a time series over the duration of the period under study together with the proton-alpha differential streaming colored black in the background. The spacecraft radial distance is overlaid with a dotted red line. The closer proximities demonstrate clear increases in alpha-proton streaming magnitudes that are not as obvious in the O^{6+}-proton streaming data. Overall, it is more common to find positive (O^{6+} > alpha) than negative (O^{6+} < alpha) differential

streaming with a probability of 78.62% and 21.38%, respectively; this corresponds with the dominant positive streaming found between either ion and protons. While there is no correlation overall, as seen in plot C of Figure 5.12 the linear trend between alfvén velocity and the *peak* values of O^{6+}-alpha differential streaming continues similar to other ion differential streaming although it rarely exceeds *half* the magnitude whereas other streaming extends to the full. There is also a modest bimodal distribution appearing between positive streaming in slow wind and negative streaming appearing in fast wind. This can be seen by the separation between the color-coded wind speeds by the positive vs negative division denoted by a white dotted line in plots B and C of Figure 5.12. The separation between wind speeds corresponds with a negative correlation between O^{6+}-alpha streaming and proton temperature and velocity. Next, the positive relationship found in the Pearson coefficient between O^{6+}-alpha and O^{6+}-proton streaming was further investigated in plot D of Figure 5.12. Initial examination indicates that a clear relationship between the two parameters is not obvious by the relative scatter of the data. In plot D the differential streaming and magnetic field orientation shows a broad scatter of O^{6+}-alpha streaming while the magnetic field is perpendicular to the radial direction denoted by beige data points; under closer

Figure 5.13 O^{6+}-Alpha Differential Streaming Time Series

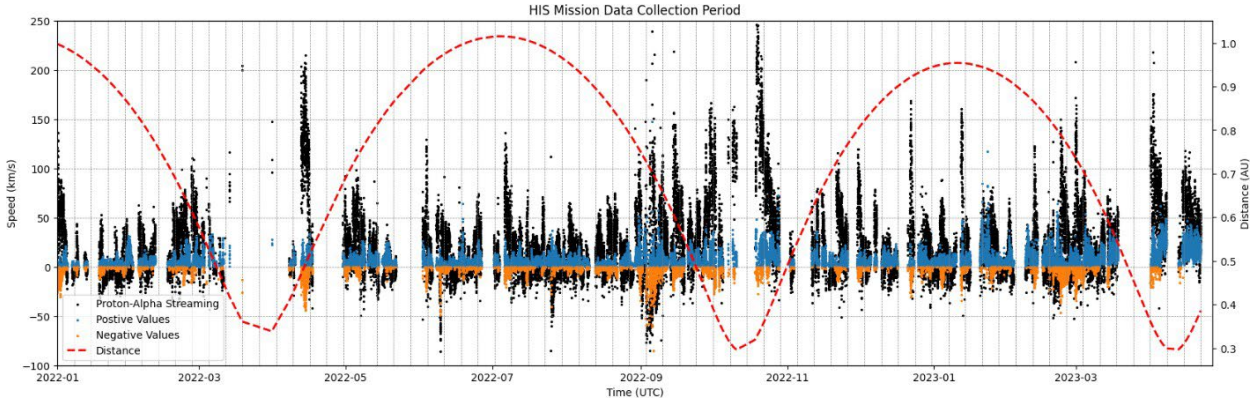

Figure 5.12: Time series plot of the positive (blue) and negative (orange) differential streaming for O^{6+} and alphas with the alpha-proton differential streaming (black) overlaid. In addition, spacecraft distance is plotted on the opposing y-axis. It is clear that alpha-proton differential streaming is greatest at perihelion but there is not a similar trend for O^{6+}-alpha differential streaming. Nevertheless, O^{6+}-alpha differential is typically present although it never approaches the same value as the heavy ion to proton differentials (max < $V_A/2$).

inspection, however, there is a smaller secondary population whose differential streaming direction correlates with the radial magnetic field polarity shown as red and blue data. The differential speed of the secondary populations displays a positive relationship between the parallel radial magnetic field direction and O^{6+} differentially streaming faster than alpha particles. In contrast, alpha particles in the smaller secondary population move faster during antiparallel radial magnetic polarity i.e., exhibit a negative differential speed (see further discussion below). This must be largely driven by the separation between O^{6+} and proton speed and thus produces the positive correlation between the two. Therefore, we have discovered some clear instances in which radial magnetic field polarity is indicative of differential streaming flow direction between O^{6+} and alphas.

After the discovery of the secondary population that contained field aligned O^{6+}-alpha speed separations the differences in positive and negative O^{6+}-alpha differential streaming were investigated further. The data were separated into positive and negative streaming distributions and illustrated in plots A-D in Figure 5.14. In the top left (plot A) the two separate distributions are plotted as a function of parallel (x-axis) and perpendicular (y-axis) temperatures. The top right (plot B) the data are plotted by proton velocity and density, by radial distance and field strength in the bottom left (plot C), and O^{6+} and alpha to proton differential streaming (plot D) in the bottom right. From the smaller regions of the blue negative distributions overlapping of the large positive regions colored white in all plots it is apparent that the positive differential streaming occurs more often and across all solar wind mode classification types. In addition, the majority of instances in which negative differential streaming occurs are found in solar wind plasma that is slower and dense (plot B) and heated to higher temperatures (plot A). In contrast, there is no clear trend between positive and negative O^{6+}-alpha differential speed and alfvén speed (plot C in in Figure 5.12), magnetic field strength and radial distance (plot C in Figure 5.14), or heavy ion to proton differential speed magnitude (plot D in Figure 5.14). Hence, it is clear that negative O^{6+}-alpha is more common in the slow wind mode in which temperature anisotropies are recorded as higher local temperatures. In addition, when combined with theprevious results the overlap in positive and negative

streaming distributions are indicative of a secondary particle population of the slow solar wind in which heavy ions are streaming and counter-streaming with respect to one another in relation to the magnetic field direction.

Figure 5.14 O^{6+}-Alpha Differential Streaming – Positive vs Negative Distributions

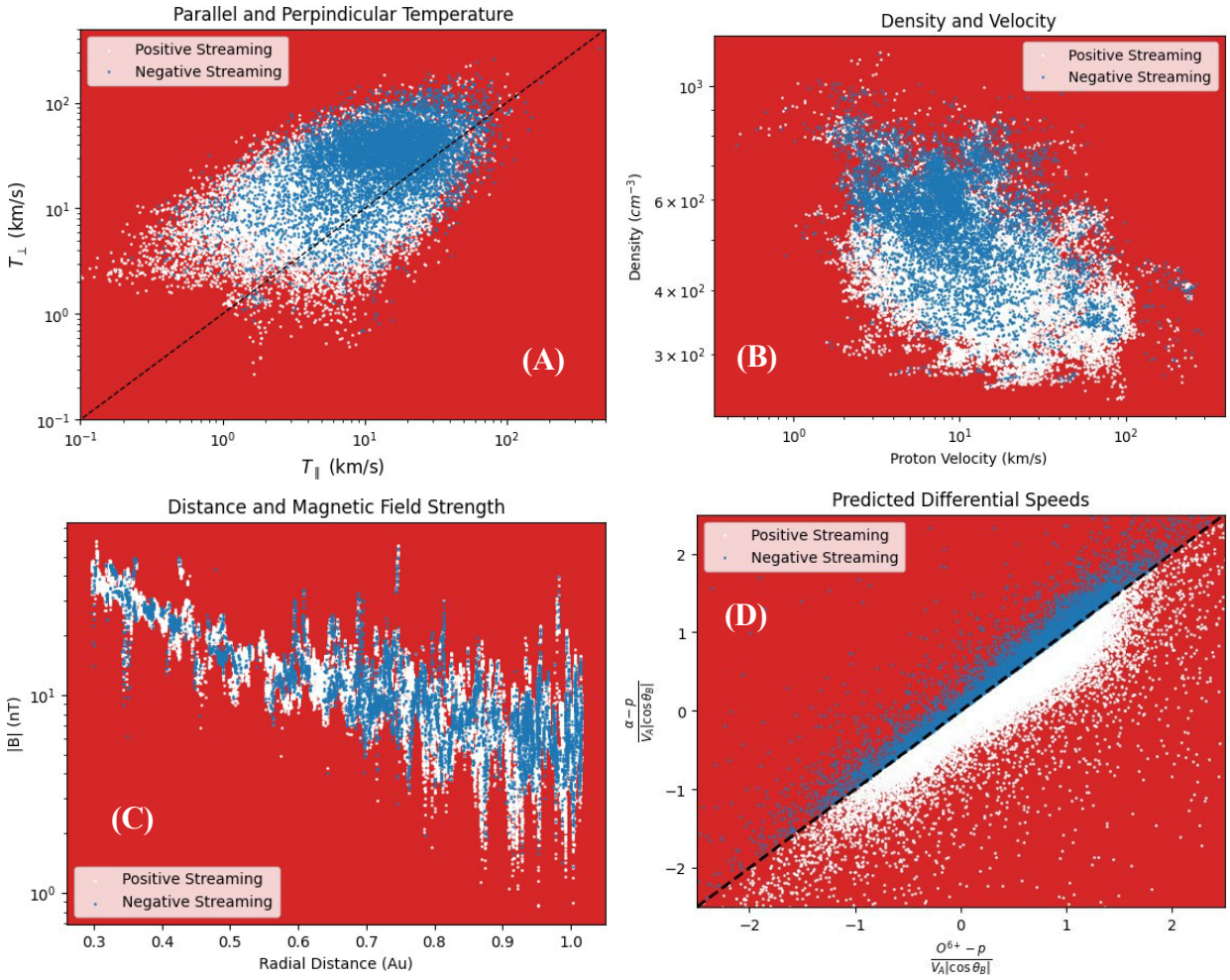

Plots exploring the positive and negative O^{6+}-alpha differential speed using the predicted values for measurements with off-angle magnetic field. (Top-Left) Negative differential streaming occurs at high temperatures (perpendicular and parallel). (Top-Right) Negative differential streaming appears in slower and more dense solar wind plasmas. (Bottom-Left) Radial distance and magnetic field strength do not appear to influence the polarity of O^{6+}-alpha differential speed. (Bottom-Right) Positive and negative O^{6+}-alpha differential speed occur for all magnitudes of heavy ion to proton differential speeds.

Finally, to further investigate the data it is possible to organize the differential streaming data using assumptions concerning the alfvén speed and magnetic field orientation in similar manner to that developed in previous studies (e.g., Rivera et. al., 2025, L. Berger et. al., 2011). First, the magnitude of the O^{6+}-alpha differential speed is divided by the proton alfvén velocity (defined above) since it often places a limit on the total achievable separation in speed. Second, if the differential motion is assumed to follow the magnetic field vector, then the radial differential velocity can be treated as a projection for periods when the field angle is non-radial. Thus, for instances with off-radial field orientations the differential speed can be predicted using,

$$\Delta \hat{?}_{ii-jj} = \frac{\Delta vv_{ii-j\ \ j}}{VV_{AA}|\cos\theta\theta_{BB}|}$$

In this equation Δvv_{ii-jj} is the measured differential speed between ions i and j, V_A is the alfvén velocity, θ_B is the angle the magnetic field makes with the radial direction, and $\Delta \hat{?}_{ii-jj}$ and is the predicted differential streaming. When the magnetic field is non-radial, the predicted value is increased by a factor proportional to the radial differential speed and the inverse of the absolute cosine of the field angle. The absolute value prevents a sign change in the measured differential speed when the angle is greater than 90°. Naturally, the certainty in these regions is reduced – the predictions often result in anomalously large values. Nevertheless, the majority of off-radial predictions exhibit values very similar to the radial-aligned values which may provide further evidence that the differential streaming is aligned with the magnetic field vector. The results are shown in the top two plots (A and B) in Figure 5.15. In both instances the magnitude of the differential streaming is plotted along the x-axis and the magnetic field orientation is plotted along the y-axis. The data is color coded by velocity (plot A) and density (plot B) From reviewing the shape of plots A and D using the predicted field aligned differential streaming values it is clear the strength of differential speed is slightly higher during intervals with transverse field alignment and tapers towards lower values for parallel and antiparallel radial alignments. This behavior is also exhibited in

studies of alpha-proton and O^{6+}-proton differential streaming that use the same assumptions concerning alfvén velocity and magnetic field orientation. The relationship between speed and density and positive and negative speed separation is further confirmed in plots A and D of Figure 5.15 as well. Under closer inspection there are two populations that occur at nearly all magnitudes and field orientations but are slightly shifted in average differential speed with respect to each other. The separate distributions are further demonstrated by the two populations that are found in histograms of the alpha-proton (plot C) and O^{6+}-proton (plot D) differential speed distributions in Figure 5.15. The two separate distributions are denoted at their peak abundances by orange and red dotted lines in both histograms. By combining the results from Figure 5.14and Figure 5.15, it is clear that the two distributions found in the histograms correspond with the primary (beig) and secondary populations (red and blue) seen in plot D of Figure 5.12 in which one population has larger spread in values and is generally more positive but does not align with the magnetic field and a second population that is equally positive and negative and aligns with the magnetic field. Specifically, in the smaller secondary population the positive, outward radial magnetic field corresponds with faster O^{6+} and the backwards field direction results in faster alpha differential streaming. This secondary population of roughly equal positive and negatively streaming particles in the slow wind was also described by Ďurovcová et al. 2017 (see bottom plot in Figure 5.9). One possible explanation is the secondary population exhibits behavior of particles that are trapped and bouncing back and forth while being carried by the magnetic field and are thus moving with the bulk flow and centered at zero differential speed. Another possible answer is that the particles in the secondary population are being accelerated into bimodal distributions by the orientation of waves contained within the magnetic field. The larger population uncorrelated with field orientation likely represents the nascent solar wind heavy ions that were emitted from the corona and have yet to be slowed or captured by the magnetic field carried by the protons, and therefore is out of resonance as it streams out ahead at faster positive differential streams. Further studies into the existence of the two populations will provide additional to context as to what physical mechanisms may cause them.

In this study we present the first detailed analysis of O^{6+} to alpha differential streaming in the solar wind. It is now understood that although the two species frequently stream together there are continuous periods during which they display relatively small variances establishing a near ubiquitous presence of differential flow. In many ways the O^{6+}-alpha differential streaming is different from either

Figure 5.15 O^{6+}-Alpha Differential Streaming – Field Angle and Secondary Population

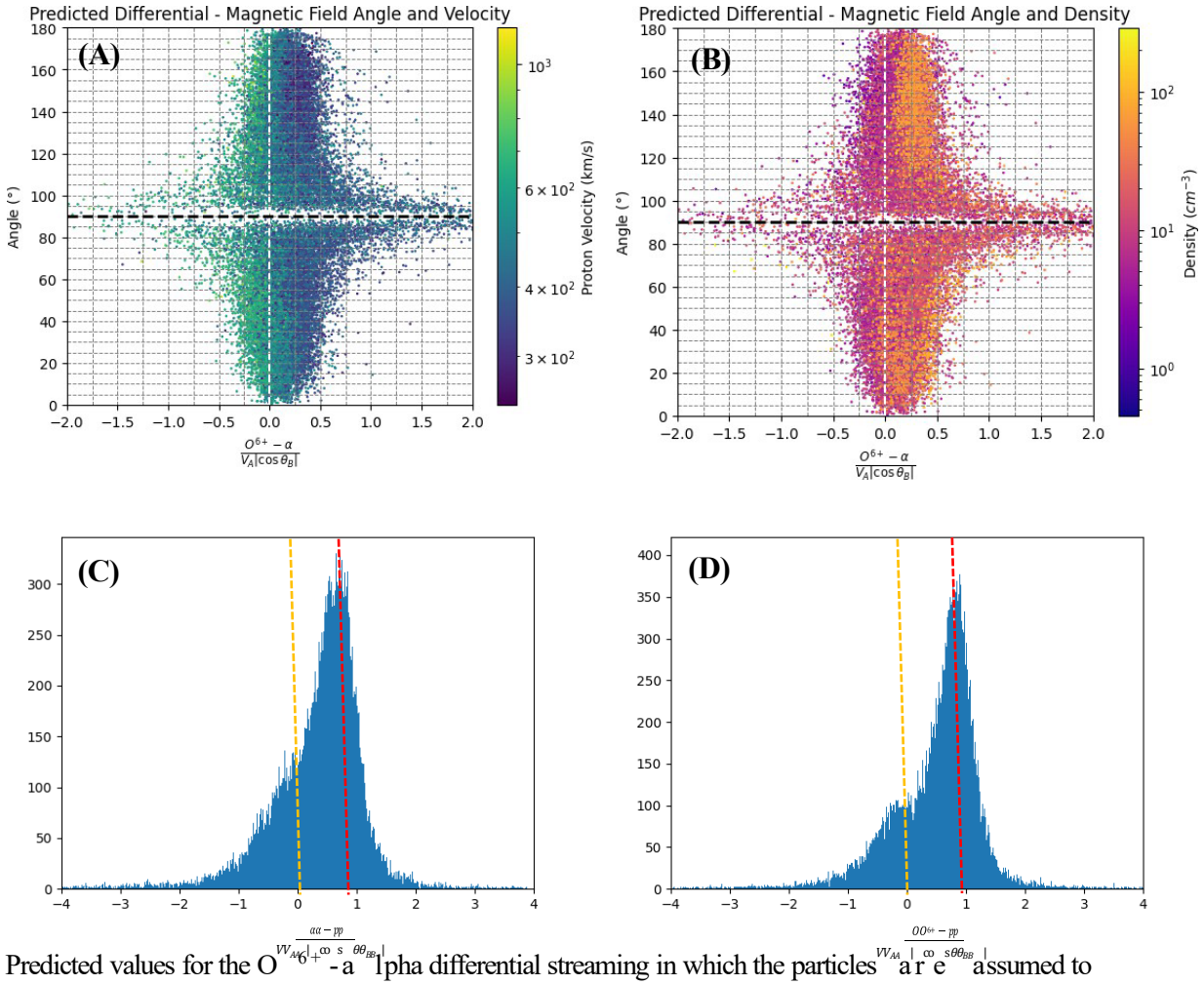

Predicted values for the O^{6+}-alpha differential streaming in which the particles are assumed to differentially stream along the magnetic field lines plotted with proton velocity (**Top-Left**) and density (**Top-Right**). As the field angle approach 90° the predicted streaming values become more uncertain. There is slightly more positive differential streaming than negative overall. The results from these plots appear to contradict results in Figure 5.13 by showing that slow, dense plasmas predominately stream positive. However, it is rather that both negative and positive distributions overlap and the positive values are simply more abundant. This can be explained by the histograms (**Bottom**) for the O^{6+}-proton and alpha-proton distributions in which there are clearly two overlapping populations (orange and red dotted lines). The secondary (orange) population centered on zero differential streaming has roughly equal positive and negative streaming but is dominated by the larger (red) positive-dominant streaming

heavy ion motion with respect to protons. There is not as clear a relation to radial distance, field strength, and no clear relationship to the alpha-proton differential streaming. Rather, the O^{6+}-alpha streaming appears to be guided by the O^{6+}-proton differential streaming and occurs in the presence of higher local temperatures of alphas. In addition, the proton velocity, density, and magnetic field direction are all plasma parameters that correlate with O^{6+} to alpha differential streaming. Potentially, the most interesting result is the presence of two distributions and what they may entail. In general, there is a larger, slightly more positive differential streaming population that corresponds with faster wind and no response to magnetic field orientation. Conversely, there is a secondary population that exhibits roughly equal positive and negative differential streaming that corresponds with magnetic field direction that exists in slow, dense, heating solar wind. Future studies may separate the two populations for additional insight through their individual analyses. An interesting line of inquiry that is within the performance capabilities of the HIS instrument is to determine if the differences in primary and secondary populations exhibit charge state dependencies. For example, this is a very small positive correlation between O^{6+}-alpha differential streaming and O^{7+}/O^{6+} values or higher Oxygen charge states. Furthermore, additional analysis using individual case studies of solar wind conditions may lead to methods for separating the two populations for individual analysis. The presence of alfvén waves, separate particle beams, or high temperature anisotropies are all good candidates for exploring the creation of the secondary field-aligned distribution. The results of this study further indicate that heavy ion differential streaming is an important tool for determining the causes of solar wind production. Indeed, the existence of two populations could potentially help designate different source regions and coronal conditions that produce acceleration. In addition, the discovery of trapped populations moving with positive and negative differential streaming that roughly center to zero indicates that some instances of differential streaming could be the result of transport effects. Ultimately, further calibration of HIS heavy ion 3D VDFs will enable tracking ion differential speeds above, below, and within the ecliptic plan and their relationship with the magnetic field and bulk flow velocity vectors. The results of this study and future work will continue to provide

important understanding of the heavy ion kinetics in the solar wind and what they may tell us about the yet unknown acceleration mechanisms within the solar corona.

Chapter 6

Conclusion

We are currently living through an important historical period in space physics and exploration. Over recent decades humanity has gone from virtually knowing nothing about the fundamental physical interactions happening just a few hundred miles above their head to sending orbiters to nearly every planet in the solar system. Throughout this evolution exciting breakthroughs have occurred that at first appear unique to other worlds and environs other than our own but inevitably result in greater knowledge of our own beginnings and the ongoing interactions with our local cosmos. Undoubtedly, new discoveries await as we continue this same exploratory process to visit new planets and follow in the footsteps of previous missions with greater technology and capabilities; for it is the advancement and innovation of technology that has enabled all these new and exciting scientific developments. Science and engineering are brought together to produce the technology necessary for progressing our understanding – by exceeding prior capabilities and our imagination for what can be achieved. This has manifested itself in our current period where for the first time commercial entities are able to achieve what only nation states could do before. A new era in space presents itself in which viable business opportunities have turned permanent human settlements from science fiction into technology demonstrations and mission proposals. Throughout it all has been and will always be a continuous need for sensors that define what we are able to perceive and therefore know. Whether it's for safety or for studies, space particle detectors will accompany all human and autonomous vehicles for every foreseeable future in which we have a continued presence in space. Our instruments' capabilities are the definition of what we can learn and

know, and their advancement is a vital component to properly conducting the scientific investigations and exploratory missions of the new era. Triple-coincidence time-of-flight spectrometers are a pinnacle of decades of space detector developments and finally provide the complete set of parameters available to analyze the particles within a plasma. While no sensor can provide a complete picture of its surrounding environment, the charge-resolving capabilities of time-of-flight detectors are unparalleled in their ability to discover new particle physics in space. They arrive after generations of the world's best scientists and engineers applied their trade towards experimental physics in space and are thus nontrivial in design and operation. Nonetheless, their demand for future mission is well-recognized and deserved for their ability to determine plasma source regions and mechanisms as well as in situ particle kinetics. They stand ready to make exciting new discoveries of our Sun, neighboring planetary bodies, and local interstellar neighborhood. To be sure, advanced capabilities in time-of-flight sensors are needed; but more so is their proliferation throughout space and for that reason SWaP-efficiency in the new age has become paramount.

The design of the T-FIPS spectrometer is idealized for the next age in space exploration and analysis within which we are currently living. It combines the charge-resolving powers provided through the advanced techniques of triple-coincidence time-of-flight technology with heritage design and modern engineering methods to provide the first of its kind in SWaP-efficiency. The conceptual development of the T-FIPS instrument has nearly been achieved. For the most part, all that remains is to advance the existing models by marrying them to hardware assembly and experimental results. With the development of its computer-aided designs (CADs) and ion optical simulations, the feasibility and scientific applicability of the T-FIPS instrument have been demonstrated. In addition to the ion optical simulations of the modified ToF chamber with a new energy detection system are the models of an electrostatic lens for a secondary option for ESA filter and modernized electroformed meshes. In addition, electromechanical analysis of the Fisheye ESA elucidates areas for future improvements in energy range. Furthermore, generalized principles of operation and techniques for manufacturing and assembly have

established broad rules that help theoretically understand the fundamental operation of the individual subcomponents that are necessary for optimization of current designs, and envisioning new instruments. Examples of these include the principles of photon occulting, MCP alignment, and using advancements in additive and subtractive manufacturing. In sum, the conceptual development of the T-FIPS spectrometer has been the primary purpose of this research and has been largely accomplished; the next step to bring it closer to delivery will take place through hardware developments and the evaluation of a prototype in the laboratory.

The next phase of T-FIPS development has already begun. With the advanced stage of the conceptual models in place the purchase and production of hardware components was made ready. Thanks to the heavily leveraged heritage from the FIPS mission most of the difficulty comes from implementing the new energy detector into a compact system while maintaining the high voltage capabilities of the electromechanical design; nonetheless, these consist of complex challenges that require important decisions necessary to continue the design towards a final prototype form. In addition, undertaking the experimental analysis of the instrument's operation and performance is critical for determining the individual subcomponents before bringing them together into a complete sensor. The tests already performed include operating the FIPS ToF chamber and testing the performance of the Fisheye ESA. While the tests on the FIPS ToF chamber ultimately proved unsuccessful, important insight was provided on how to operate a system similar to the T-FIPS prototype. Moreover, it resulted in the important decision to disassemble the components for use on the prototype chamber. Likewise, the ongoing tests using the Fisheye ESA are yielding critical understanding for how to operate the first subcomponent of the T-FIPS spectrometer while also generating experimentally determined performance characteristics. The analysis of the Fisheye ESA in the laboratory is an important first step in a chain of experimental tests that will include the Start and Stop MCPs, energy detector subsystem, the modified ToF chamber (with new electroformed grids), and finally the cumulative T-FIPS prototype. No doubt there are still many challenges that lie ahead; however, the conceptual background and the selection of

pivotal design choices have illuminated the pathway towards the final development. Once achieved, the performance analysis of the T-FIPS sensor will identify it as a SWaP-efficient, charge-resolving time-of-flight spectrometer ready for scientific discovery in the current modern period.

The truly final stage of an instrument's development is achieved through accomplishing its primary purpose: scientifically useful data products. The research performed through analysis of an instrument's data products is the engine by which knowledge and discovery in space occur. In this work we performed the first on-orbit calibrations of the ÉPÉÉ plasma spectrometer as it studied the ions in the topside ionosphere. The ionosphere is an essential component to understanding the impact of space weather on our planet due to its proximity and impact on society's technological infrastructure. Nonetheless, complete understanding of our closest space environment eludes space physicists due to the practical challenges that arise from deploying in situ monitors to LEO; therefore, the calibration of and first observations from the ÉPÉÉ instrument embody an important breakthrough in this stalemate. Continued operation of ionosphere spectrometers will provide long awaited knowledge of the topside regions that will characterize the constant diurnal behavior and transient storm time conditions that are needed or designing and implementing remedial actions.[75] Likewise, the advancement of deep space monitors are important for studying our Sun and the initiating mechanisms of the solar wind, its transients, and the space weather they create. The HIS instrument is the most powerful triple-coincidence time-of-flight mass spectrometer deployed to interplanetary space and the development and analysis of its data products has already resulted in important scientific breakthroughs. In particular, the calibration of the 3D VDFs of heavy ions will conclude decades of inquiry that began with the first VDFs of inner Heliosphere ions presented by the Helios mission in the 70's and 80's. Ultimately, the value of the HIS data products are derived from its unprecedented ability to measure heavy ions to identify the solar wind

[75] The opening of Very Low Earth Orbit (VLEO) via airbreathing satellites will ultimately close this observational hole in the ionosphere over the next few decades.

source locations on the Sun and resolve their in situ kinetics. The research performed in this study determined the first characteristics of O^{6+} to alpha differential streaming in the solar wind and the important kinetics that take place. We showed unique properties that exist separately for the differential streaming behavior of each individual heavy ion the context in which they occur. Furthermore, we showed the potential existence of two distinct populations that open a window into solar wind acceleration and transport. By continuing to deploy high quality sensors like HIS and other triple-coincidence mass spectrometers into the solar wind we will enable more fundamental studies of its plasma phenomena and ultimately determine the mechanisms that drive our Sun.

To conclude, humanity has always been subconsciously pushed towards discovery and adventure and for our moment in history that drive is manifesting itself in space exploration. Science will always lead discovery, and the application of commercial interests may accelerate change but will never replace the role of science. We are living through the Early Space Age which began through decades of novel challenges, technological development, and extreme accomplishments. What presents itself now is a well-honed machine that stands ready to embark on a new era in human history in which we will learn untold secrets of the local cosmos. Human civilization can exist beyond our planet if sufficient thought and resources are applied towards it. When done properly, space instrumentation will provide the information necessary to learn and manage the extreme environments beyond our protective atmosphere and magnetosphere. Thus, through the advancement of space technology, and particle sensors in particular, we advance our capability to harness new regions and unlock a new period in human existence.

References

Acton, C., Bachman, N., Semenov, B., & Wright, E. (2018). A look towards the future in the handling of space science mission geometry. *Planetary and Space Science*, *150*, 9–12. https://doi.org/10.1016/j.pss.2017.02.013

Acton, C. H. (1996). Ancillary data services of NASA's Navigation and Ancillary Information Facility. *Planetary and Space Science*, *44*(1), 65–70. https://doi.org/10.1016/0032-0633(95)00107-7

Alfven, H., & Lindblad, B. (1947). Granulation, Magneto-Hydrodynamic Waves, and the Heating of the Solar Corona. *Monthly Notices of the Royal Astronomical Society*, *107*(2), 211–219. https://doi.org/10.1093/mnras/107.2.211

Allegrini, F., Wimmer-Schweingruber, R. F., Wurz, P., & Bochsler, P. (2003). Determination of low-energy ion-induced electron yields from thin carbon foils. *Nuclear Instruments and Methods in Physics Research, Section B: Beam Interactions with Materials and Atoms*, *211*(4), 487–494. https://doi.org/10.1016/S0168-583X(03)01705-1

Allison, S. K., Frankel, S. P., Hall, T. A., Montague, J. H., Morrish, A. H., & Warshaw, S. D. (1949). Construction and calibration of a cylindrical electrostatic analyzer. *Review of Scientific Instruments*, *20*(10), 735–744. https://doi.org/10.1063/1.1741368

Alterman, B. L., Rivera, Y. J., Lepri, S. T., & Raines, J. M. (2025). The transition from slow to fast wind as observed in composition observations. *Astronomy and Astrophysics*, *694*. https://doi.org/10.1051/0004-6361/202451550

Andrews, G. B., Zurbuchen, T. H., Mauk, B. H., Malcom, H., Fisk, L. A., Gloeckler, G., Ho, G. C., Kelley, J. S., Koehn, P. L., Lefevere, T. W., Livi, S. S., Lundgren, R. A., & Raines, J. M. (2007). The energetic particle and plasma spectrometer instrument on the MESSENGER spacecraft. *Space Science Reviews*, *131*(1–4), 523–556. https://doi.org/10.1007/s11214-007-9272-5

Appleton, E. V. (1946). Two Anomalies in the Ionosphere. *Nature*, *157*(3995), 691–691. https://doi.org/10.1038/157691a0

Asplund, M., Amarsi, A. M., & Grevesse, N. (2021). The chemical make-up of the Sun: A 2020 vision. *Astronomy and Astrophysics*, *653*. https://doi.org/10.1051/0004-6361/202140445

Bader, M. (1962). Preliminary Explorer 12 data on protons below 20 kev. *Journal of Geophysical Research*, *67*(13), 5007–5011. https://doi.org/10.1029/jz067i013p05007

Bale, S. D., Drake, J. F., McManus, M. D., Desai, M. I., Badman, S. T., Larson, D. E., Swisdak, M., Horbury, T. S., Raouafi, N. E., Phan, T., Velli, M., McComas, D. J., Cohen, C. M. S., Mitchell, D., Panasenco, O., & Kasper, J. C. (2023). Interchange reconnection as the source of the fast solar wind within coronal holes. *Nature*, *618*(7964), 252–256. https://doi.org/10.1038/s41586-023-05955-3

Bame, S. J., Hundhausen, A. J., Asbridge, J. R., & Strong, I. B. (1968). Solar Wind Ion Composition. *Physical Review Letters*, *20*(8), 393–395. https://doi.org/10.1103/PhysRevLett.20.393

Barjatya, A., Swenson, C. M., Thompson, D. C., & Wright, K. H. (2009). Invited article: Data analysis of the floating potential measurement unit aboard the international space station. *Review of Scientific Instruments*, *80*(4). https://doi.org/10.1063/1.3116085

Benkhoff, J., van Casteren, J., Hayakawa, H., Fujimoto, M., Laakso, H., Novara, M., Ferri, P., Middleton, H. R., & Ziethe, R. (2010). BepiColombo-Comprehensive exploration of Mercury: Mission overview and science goals. *Planetary and Space Science*, *58*(1–2), 2–20. https://doi.org/10.1016/j.pss.2009.09.020

Berger, L., Wimmer-Schweingruber, R. F., & Gloeckler, G. (2011). Systematic measurements of ion-proton differential streaming in the solar wind. *Physical Review Letters*, *106*(15). https://doi.org/10.1103/PhysRevLett.106.151103

Berger, T. E., Dominique, M., Lucas, G., Pilinski, M., Ray, V., Sewell, R., Sutton, E. K., Thayer, J. P., & Thiemann, E. (2023). The Thermosphere Is a Drag: The 2022 Starlink Incident and the Threat of Geomagnetic Storms to Low Earth Orbit Space Operations. *Space Weather*, *21*(3). https://doi.org/10.1029/2022SW003330

Bilitza, D., Truhlik, V., Omura, Y., & Moldwin, M. B. (2024). Development and Improvement of the International Reference Ionosphere with special emphasis on the topside and extension to the plasmasphere. *Annals of Geophysics*, *67*(4). https://doi.org/10.4401/ag-9145

Bolton, S. J., Janssen, M., Thorne, R., Levin, S., Klein, M., Gulkis, S., Bastian, T., Sault, R., Elachi, C., Hofstadter, M., Bunker, A., Dulk, G., Gudim, E., Hamilton, G., Johnson, W. T. K., Leblanc, Y., Liepack, O., McLeod, R., Roller, J., … West, R. (2002). Ultra-relativistic electrons in Jupiter's radiation belts. *Nature*, *415*(6875), 987–991. https://doi.org/10.1038/415987a

Bridge, H. S., Dilworth, C., Rossi, B., Scherb, F., & Lyon, E. F. (1960). An instrument for the investigation of interplanetary plasma. *Journal of Geophysical Research*, *65*(10), 3053–3055. https://doi.org/10.1029/jz065i010p03053

Brooks, D. H., Ugarte-Urra, I., & Warren, H. P. (2015). Full-Sun observations for identifying the source of the slow solar wind. *Nature Communications*, *6*. https://doi.org/10.1038/ncomms6947

Brown, W. L. (1965). *Studies of Trapped Radiation by the Telstar I and Explorer XV Satellites* (pp. 189–211). https://doi.org/10.1007/978-94-011-7542-5_14

Brown, W. L., Buck, T. M., Medford, L. V., Thomas, E. W., Gummel, H. K., Miller, G. L., & Smits, F. M. (1963). The Spacecraft Radiation Experiments. *Bell System Technical Journal*, *42*(4), 899–941. https://doi.org/10.1002/j.1538-7305.1963.tb04023.x

Burch, J. L., Moore, T. E., Torbert, R. B., & Giles, B. L. (2016). Magnetospheric Multiscale Overview and Science Objectives. In *Space Science Reviews* (Vol. 199, Numbers 1–4, pp. 5–21). Springer Netherlands. https://doi.org/10.1007/s11214-015-0164-9

Cohen, I. J., Turner, D. L., Kollmann, P., Clark, G. B., Hill, M. E., Regoli, L. H., & Gershman, D. J. (2023). A Localized and Surprising Source of Energetic Ions in the Uranian Magnetosphere Between Miranda and Ariel. *Geophysical Research Letters*, *50*(8). https://doi.org/10.1029/2022GL101998

Colón-Rodríguez, S., Liemohn, M. W., Raines, J. M., & Lepri, S. T. (2025). Solar Wind Heavy Ions and Alpha Particles Within Earth's Magnetosphere and Their Variability With Upstream Conditions. *Journal of Geophysical Research: Space Physics*, *130*(8). https://doi.org/10.1029/2025JA033852

Crooker, N. U., Antiochos, S. K., Zhao, X., & Neugebauer, M. (2012). Global network of slow solar wind. *Journal of Geophysical Research: Space Physics*, *117*(4). https://doi.org/10.1029/2011JA017236

Daly, A., Li, W., Ma, Q., Shen, X. C., Yoon, P. H., Menietti, J. D., Kurth, W. S., Hospodarsky, G. B., Mauk, B. H., Clark, G., Allegrini, F., Connerney, J. E. P., & Bolton, S. J. (2023). Plasma Wave and Particle Dynamics During Interchange Events in the Jovian Magnetosphere Using Juno Observations. *Geophysical Research Letters*, *50*(23). https://doi.org/10.1029/2023GL103894

Del Zanna, L., & Velli, M. (2002). Coronal heating through Alfven waves. *Advances in Space Research*, *30*(3), 471–480. https://doi.org/10.1016/S0273-1177(02)00320-4

Desai, M. I., Drake, J. F., Phan, T., Yin, Z., Swisdak, M., McComas, D. J., Bale, S. D., Rahmati, A., Larson, D., Matthaeus, W. H., Dayeh, M. A., Starkey, M. J., Raouafi, N. E., Mitchell, D. G., Cohen, C. M. S., Szalay, J. R., Giacalone, J., Hill, M. E., Christian, E. R., … Kasper, J. C. (2025). Magnetic Reconnection–driven Energization of Protons up to ∼400 keV at the Near-Sun Heliospheric Current Sheet. *The Astrophysical Journal Letters*, *985*(2), L38. https://doi.org/10.3847/2041-8213/ada697

Desai, M. I., Drake, J. F., Swisdak, M., Fitzmaurice, A., McComas, D. J., Bale, S. D., Phan, T., Berland, G., Mitchell, D. G., Cohen, C. M. S., Hill, M. E., Christian, E. R., Schwadron, N. A., McNutt, R. L., Matthaeus, W. H., Rahmati, A., Whittlesey, P., Livi, R., & Larson, D. (2026). Proton and Heavy Ion Acceleration by Magnetic Reconnection at the Near-Sun Heliospheric Current Sheet. *The Astrophysical Journal*, *1000*(2), 300. https://doi.org/10.3847/1538-4357/ae48f2

Dewey, R. M., Raines, J. M., Sun, W., Slavin, J. A., & Poh, G. (2018). MESSENGER Observations of Fast Plasma Flows in Mercury's Magnetotail. *Geophysical Research Letters*, *45*(19), 10,110-10,118. https://doi.org/10.1029/2018GL079056

Dougherty, M. K., Khurana, K. K., Neubauer, F. M., Russell, C. T., Saur, J., Leisner, J. S., & Burton, M. E. (2006). Identification of a Dynamic Atmosphere at Enceladus with the Cassini Magnetometer. In *New Series* (Vol. 311, Number 5766).

Drake, J. F., Bale, S. D., Swisdak, M., Raouafi, N. E., & Velli, M. (2023). *Development of a structured, turbulent solar wind as a result of interchange reconnection*. http://arxiv.org/abs/2306.03425

Ďurovcová, T., Šafránková, J., Němeček, Z., & Richardson, J. D. (2017). Evolution of Proton and Alpha Particle Velocities through the Solar Cycle. *The Astrophysical Journal*, *850*(2), 164. https://doi.org/10.3847/1538-4357/aa9618

Emmert, J. T. (2015). Thermospheric mass density: A review. In *Advances in Space Research* (Vol. 56, Number 5, pp. 773–824). Elsevier Ltd. https://doi.org/10.1016/j.asr.2015.05.038

Evans, D. S. (1965). Low energy charged-particle detection using the continuous-channel electron multiplier. *Review of Scientific Instruments*, *36*(3), 375–382. https://doi.org/10.1063/1.1719576

Ewald, H., & Liebl, H. (1955). Der Astigmatismus des Toroidkondensators. *Zeitschrift Für Naturforschung A*, *10*(11), 872–876. https://doi.org/10.1515/zna-1955-1114

Fan, C. Y., Gloeckler, G., & Simpson, J. A. (1965). Cosmic radiation helium spectrum below 90 Mev per nucleon measured on Imp 1 satellite. *Journal of Geophysical Research*, *70*(15), 3515–3527. https://doi.org/10.1029/jz070i015p03515

Feldman, U., Landi, E., & Schwadron, N. A. (2005). On the sources of fast and slow solar wind. *Journal of Geophysical Research: Space Physics*, *110*(A7). https://doi.org/10.1029/2004JA010918

Fisk, L. A. (1996). Motion of the footpoints of heliospheric magnetic field lines at the Sun: Implications for recurrent energetic particle events at high heliographic latitudes. *Journal of Geophysical Research: Space Physics*, *101*(A7), 15547–15553. https://doi.org/10.1029/96ja01005

Fisk, L. A., & Schwadron, N. A. (2001). The Behavior of the Open Magnetic Field of the Sun. *The Astrophysical Journal*, *560*(1), 425–438. https://doi.org/10.1086/322503

Fisk, L. A., Zurbuchen, T. H., & Schwadron, N. A. (1999). On the Coronal Magnetic Field: Consequences of Large-Scale Motions. *The Astrophysical Journal*, *521*(2), 868–877. https://doi.org/10.1086/307556

Geiss, J., Eberhardt, P., Bühler, F., Meister, J., & Signer, P. (1970). Apollo 11 and 12 solar wind composition experiments: Fluxes of He and Ne isotopes. *Journal of Geophysical Research*, *75*(31), 5972–5979. https://doi.org/10.1029/JA075i031p05972

Gershman, D. J., & Zurbuchen, T. H. (2010). Modeling extreme ultraviolet suppression of electrostatic analyzers. *Review of Scientific Instruments*, *81*(4). https://doi.org/10.1063/1.3378685

Gilbert, J. A., Gershman, D. J., Gloeckler, G., Lundgren, R. A., Zurbuchen, T. H., Orlando, T. M., McLain, J., & von Steiger, R. (2014). Invited Article: Characterization of background sources in space-based time-of-flight mass spectrometers. *Review of Scientific Instruments*, *85*(9). https://doi.org/10.1063/1.4894694

Gilly, C. R., & Cranmer, S. R. (2020). The Effect of Solar Wind Expansion and Nonequilibrium Ionization on the Broadening of Coronal Emission Lines. *The Astrophysical Journal*, *901*(2), 150. https://doi.org/10.3847/1538-4357/abb1ad

Gloeckler, G. (1990). Ion composition measurement techniques for space plasmas. *Review of Scientific Instruments*, *61*(11), 3613–3620. https://doi.org/10.1063/1.1141581

Gloeckler, G., Balsiger, H., B�rgi, A., Bochsler, P., Fisk, L. A., Galvin, A. B., Geiss, J., Gliem, F., Hamilton, D. C., Holzer, T. E., Hovestadt, D., Ipavich, F. M., Kirsch, E., Lundgren, R. A., Ogilvie, K. W., Sheldon, R. B., & Wilken, B. (1995). The solar WIND and suprathermal ion composition investigation on the WIND spacecraft. *Space Science Reviews*, *71*(1–4), 79–124. https://doi.org/10.1007/BF00751327

Gloeckler, G., Cain, J., Ipavich, F. M., Tums, E. O., Bedini, P., Fisk, L. A., Zurbuchen, T. H., Bochsler, P., Fischer, J., Wimmer-Schweingruber, R. F., Geiss, J., & Kallenbach, R. (1998). Investigation of the composition of solar and interstellar matter using solar wind and pickup ion measurements with SWICS and SWIMS on the ACE spacecraft. *Space Science Reviews*, *86*(1–4), 497–539. https://doi.org/10.1023/A:1005036131689

Gloeckler, G., Ipavich, F., Studemann, W., Wilken, B., Hamilton, D., Kremser, G., Hovestadt, D., Gliem, F., Lundgren, R., Rieck, W., Tums, E., Cain, J., Masung, L., Weiss, W., & Winterhof, P. (1985). The Charge-Energy-Mass Spectrometer for 0.3-300 keV/e Ions on the AMPTE CCE. *IEEE Transactions on Geoscience and Remote Sensing*, *GE-23*(3), 234–240. https://doi.org/10.1109/TGRS.1985.289519

Gloeckler, J. G., Geiss, H. J., Balsiger, H., Bedini, P., & Cain, J. C. (1992). The Solar Wind Ion Composition Spectrometer. *Astronomy and Astrophysics*, *92*, 267–289.

Gonin, M., Kallenbach, R., Bochsler, P., & Biirgi, A. (1995a). Charge exchange of low energy particles passing through thin carbon foils: Dependence on foil thickness and charge state yields of Mg, Ca, Ti, Cr and Ni. In *Nuclear Instruments and Methods in Physics Research B* (Vol. 101).

Gonin, M., Kallenbach, R., Bochsler, P., & Biirgi, A. (1995b). Charge exchange of low energy particles passing through thin carbon foils: Dependence on foil thickness and charge state yields of Mg, Ca, Ti, Cr and Ni. In *Nuclear Instruments and Methods in Physics Research B* (Vol. 101).

Grant, S. D. T., Jess, D. B., Zaqarashvili, T. V., Beck, C., Socas-Navarro, H., Aschwanden, M. J., Keys, P. H., Christian, D. J., Houston, S. J., & Hewitt, R. L. (2018). Alfvén wave dissipation in the solar chromosphere. *Nature Physics*, *14*(5), 480–483. https://doi.org/10.1038/s41567-018-0058-3

Gringauz, K. I. (1963). The structure of the ionized gas envelope of earth from direct measurements in the U.S.S.R. of local charged particle concentrations. *Planetary and Space Science*, *11*(3), 281–296. https://doi.org/10.1016/0032-0633(63)90030-8

Gurnett, D. A., & Bhattacharjee, A. (2017). *Introduction to Plasma Physics*. Cambridge University Press. https://doi.org/10.1017/9781139226059

Hanson, W. B., & Moffett, R. J. (1966). lonization transport effects in the equatorial F region . *Journal of Geophysical Research*, *71*(23), 5559–5572. https://doi.org/10.1029/jz071i023p05559

Herrero, F. A. (1992). Light-trap design using multiple reflections and solid-angle attenuation: application to a spaceborne electron spectrometer. *Applied Optics*, *31*(25), 5331. https://doi.org/10.1364/AO.31.005331

Hoffman, J. H. (1967). Composition measurements of the topside ionosphere. *Science*, *155*(3760), 324–325. https://doi.org/10.1126/science.155.3760.322

Hoffman, J. H., Dodson, W. H., Lippincott, C. R., & Hammack, H. D. (1974). Initial ion composition results from the Isis 2 satellite. *Journal of Geophysical Research*, *79*(28), 4246–4251. https://doi.org/10.1029/ja079i028p04246

Hooks, D. E., Carpenter, B., Hickethier, M., Clark, C., Brown, N., McBride, M., Loza-Hernandez, I., Stull, J. A., & Maldonado, C. A. (2024). Ultra-black coatings for space instruments: A comparison of traditional Ebonol C processes and a method for future repeatability. *Journal of Manufacturing Processes*, *113*, 230–237. https://doi.org/10.1016/j.jmapro.2024.01.057

Horbury, T. S., O'Brien, H., Carrasco Blazquez, I., Bendyk, M., Brown, P., Hudson, R., Evans, V., Oddy, T. M., Carr, C. M., Beek, T. J., Cupido, E., Bhattacharya, S., Dominguez, J. A., Matthews, L., Myklebust, V. R., Whiteside, B., Bale, S. D., Baumjohann, W., Burgess, D., … Walsh, A. P. (2020). The Solar Orbiter magnetometer. *Astronomy and Astrophysics*, *642*. https://doi.org/10.1051/0004-6361/201937257

Huang, C. S. (2023). Identification of Penetration and Disturbance Dynamo Electric Fields and Their Effects on the Generation of Equatorial Plasma Bubbles. *Journal of Geophysical Research: Space Physics*, *128*(11). https://doi.org/10.1029/2023JA031766

Huang, J., Kasper, J. C., Vech, D., Klein, K. G., Stevens, M., Martinović, M. M., Alterman, B. L., Ďurovcová, T., Paulson, K., Maruca, B. A., Qudsi, R. A., Case, A. W., Korreck, K. E., Jian, L. K., Velli, M., Lavraud, B., Hegedus, A., Bert, C. M., Holmes, J., … de Wit, T. D. (2020). Proton Temperature Anisotropy Variations in Inner Heliosphere Estimated with the First Parker Solar Probe Observations. *The Astrophysical Journal Supplement Series*, *246*(2), 70. https://doi.org/10.3847/1538-4365/ab74e0

Hundhausen, A. J., Gilbert, H. E., & Bame, S. J. (1968). THE STATE OF IONIZATION OF OXYGEN IN THE SOLAR WIND. In *The Astrophysical Journal* (Vol. 152).

Ipavich, F. M., Lundgren, R. A., Lambird, B. A., & Gloeckler, G. (1978). Measurements of pulse-height defect in Au□Si detectors for H, He, C, N, O, Ne, Ar, Kr from ≈2 to ≈ 400 keV/nucleon. *Nuclear Instruments and Methods*, *154*(2), 291–294. https://doi.org/10.1016/0029-554X(78)90412-3

Jakosky, B. M., Slipski, M., Benna, M., Mahaffy, P., Elrod, M., Yelle, R., Stone, S., & Alsaeed, N. (2017). *Mars' atmospheric history derived from upper-atmosphere measurements of 38 Ar/ 36 Ar*. *355*(6332), 1408–1410. https://doi.org/10.2307/24918119

Kallenbach, R., Gonin, M., Bochsler, P., & Bürgi, A. (1995). Charge exchange of B, C, O, Al, Si, S, F and Cl passing through thin carbon foils at low energies: Formation of negative ions. *Nuclear Instruments and Methods in Physics Research Section B: Beam Interactions with Materials and Atoms*, *103*(2), 111–116. https://doi.org/10.1016/0168-583X(95)00646-X

Kasper, J. C., Bale, S. D., Belcher, J. W., Berthomier, M., Case, A. W., Chandran, B. D. G., Curtis, D. W., Gallagher, D., Gary, S. P., Golub, L., Halekas, J. S., Ho, G. C., Horbury, T. S., Hu, Q., Huang, J., Klein, K. G., Korreck, K. E., Larson, D. E., Livi, R., … Schwadron, N. A. (2019). Alfvénic velocity spikes and rotational flows in the near-Sun solar wind. *Nature*, *576*(7786), 228–231. https://doi.org/10.1038/s41586-019-1813-z

Kasper, J. C., Lazarus, A. J., & Gary, S. P. (2008). Hot solar-wind helium: Direct evidence for local heating by alfvén-cyclotron dissipation. *Physical Review Letters*, *101*(26). https://doi.org/10.1103/PhysRevLett.101.261103

Klein, K. G., Spence, H., Alexandrova, O., Argall, M., Arzamasskiy, L., Bookbinder, J., Broeren, T., Caprioli, D., Case, A., Chandran, B., Chen, L. J., Dors, I., Eastwood, J., Forsyth, C., Galvin, A., Genot, V., Halekas, J., Hesse, M., Hine, B., … Zweibel, E. (2023). HelioSwarm: A Multipoint, Multiscale Mission to Characterize Turbulence. *Space Science Reviews*, *219*(8). https://doi.org/10.1007/s11214-023-01019-0

Knoll, G. F. (2010). *Radiation Detection and Measurement* (J. Welter & D. Matteson, Eds.; 4th ed.). John Wiley and Sons, Inc.

Kohlhase, C. E., & Penzo, P. A. (1977). Voyager mission description. *Space Science Reviews*, *21*(2). https://doi.org/10.1007/BF00200846

Krieger, A. S., Timothy, A. F., & Roelof, E. C. (1973). A coronal hole and its identification as the source of a high velocity solar wind stream. *Solar Physics*, *29*(2), 505–525. https://doi.org/10.1007/BF00150828

Krimigis, S. M., Armstrong, T. P., Axford, W. I., Bostrom, C. O., Fan, C. Y., Gloeckler, G., & Lanzerotti, L. J. (1977). The Low Energy Charged Particle (LECP) experiment on the Voyager spacecraft. *Space Science Reviews*, *21*(3). https://doi.org/10.1007/BF00211545

Krimigis, S. M., Haerendel, G., McEntire, R. W., Paschmann, G., & Bryant, D. A. (1982). The active magnetospheric particle tracer explorers (AMPTE) program. *Eos, Transactions American Geophysical Union*, *63*(45), 843–850. https://doi.org/10.1029/EO063i045p00843

Landi, E., Alexander, R. L., Gruesbeck, J. R., Gilbert, J. A., Lepri, S. T., Manchester, W. B., & Zurbuchen, T. H. (2012). Carbon ionization stages as a diagnostic of the solar wind. *Astrophysical Journal*, *744*(2). https://doi.org/10.1088/0004-637X/744/2/100

Lepri, S. T., Landi, E., & Zurbuchen, T. H. (2013). Solar wind heavy ions over solar cycle 23: Ace/swics measurements. *Astrophysical Journal*, *768*(1). https://doi.org/10.1088/0004-637X/768/1/94

Lepri, S. T., & Rivera, Y. J. (2021). Elemental Abundances of Prominence Material inside ICMEs. *The Astrophysical Journal*, *912*(1), 51. https://doi.org/10.3847/1538-4357/abea9f

Lepri, S. T., & Zurbuchen, T. H. (2010). Direct observational evidence of filament material within interplanetary coronal mass ejections. *Astrophysical Journal Letters*, *723*(1 PART 2). https://doi.org/10.1088/2041-8205/723/1/L22

Lin, M. Y., & Ilie, R. (2022). A Review of Observations of Molecular Ions in the Earth's Magnetosphere-Ionosphere System. In *Frontiers in Astronomy and Space Sciences* (Vol. 8). Frontiers Media S.A. https://doi.org/10.3389/fspas.2021.745357

Livi, S., Lepri, S. T., Raines, J. M., Dewey, R. M., Galvin, A. B., Louarn, P., Collier, M. R., Allegrini, F., Alterman, B. L., Bert, C. M., Bruno, R., Chornay, D. J., D'Amicis, R., Eddy, T. J., Ellis, L., Fauchon-Jones, E., Fedorov, A., Gershkovich, I., Holmes, J., … Wurz, P. (2023). First results from the Solar Orbiter Heavy Ion Sensor. *Astronomy and Astrophysics*, *676*. https://doi.org/10.1051/0004-6361/202346304

Ludwig, G. H. (1959). Cosmic-ray instrumentation in the first U. S. earth satellite. *Review of Scientific Instruments*, *30*(4), 223–229. https://doi.org/10.1063/1.1716522

Maldonado, C. A., Eddy, T. J. A., Fernandes, P. A., Kim, K. H., Derr, J. R., Barjatya, A., Debchoudhury, S., Wilson, G. R., Rogers, A. J., Dunn, M. S., Klem, S. M., Weaver, B. P., Ulrich, R. A., Potter, K. D., Moran, K. R., Castro, L. A., McGlown, J. M., Williams, D. J., Neal, P., & Stauffer, J. (2025). *Initial On-Orbit Cross-Calibration of the Electric Propulsion Electrostatic Analyzer Experiment (ÉPÉÉ)*.

Marsch, E. (2006). Kinetic Physics of the Solar Corona and Solar Wind Living Reviews in Solar Physics. *Living Rev. Solar Phys*, *3*, 1. http://www.livingreviews.org/lrsp-2006-1http://www.mps.mpg.de/

Marsch, E. (2012). Helios: Evolution of distribution functions 0.3-1 AU. *Space Science Reviews*, *172*(1–4), 23–39. https://doi.org/10.1007/s11214-010-9734-z

Marsch, E., Mühlhäuser, K. -H., Schwenn, R., Rosenbauer, H., Pilipp, W., & Neubauer, F. M. (1982). Solar wind protons: Three-dimensional velocity distributions and derived plasma parameters measured between 0.3 and 1 AU. *Journal of Geophysical Research: Space Physics*, *87*(A1), 52–72. https://doi.org/10.1029/ja087ia01p00052

Marsch, E., Yao, S., & Tu, C. (2009). Proton beam velocity distributions in an interplanetary coronal mass ejection. In *Annales Geophysicae* (Vol. 27, Number 2). Gale Academic OneFile. http://www.ann-

Martyn, D. F. (1954). Theory of Height and Ionization Density Changes at the Maximum of a Chapman-like Region, taking account of Ion Production, Decay, Diffusion and Tidal Drift. *Physics of the Ionosphere, Report of the Conference Held at the Cavendish Laboratory*, 254.

Mason, G. M., Gold, R. E., Krimigis, S. M., Mazur, J. E., Andrews, G. B., Daley, K. A., Dwyer, J. R., Heuerman, K. F., James, T. L., Kennedy, M. J., LeFevere, T., Malcolm, H., Tossman, B., & Walpole, P. H. (1998). The Ultra-Low-Energy Isotope Spectrometer (ULEIS) for the ACE spacecraft. *Space Science Reviews*, *86*(1–4), 409–448. https://doi.org/10.1023/A:1005079930780

McComas, D. J., Allegrini, F., Pollock, C. J., Funsten, H. O., Ritzau, S., & Gloeckler, G. (2004). Ultrathin (∼10 nm) carbon foils in space instrumentation. *Review of Scientific Instruments*, *75*(11), 4863–4870. https://doi.org/10.1063/1.1809265

Mcentire, R. W., Keath, E. P., Fort, D. E., Lui, A. T. Y., & Krimigis, S. M. (1985). The Medium-Energy Particle Analyzer (MEPA) on the AMPTE CCE Spacecraft. In *IEEE TRANSACTIONS ON GEOSCIENCE AND REMOTE SENSING* (Number 3).

McIlwain, C. E. (1960). Direct measurement of particles producing visible auroras. *Journal of Geophysical Research*, *65*(9), 2727–2747. https://doi.org/10.1029/jz065i009p02727

Mitra, S. K. (1946). Geomagnetic Control of Region F2 of the Ionosphere. *Nature*, *158*(4019), 668–669. https://doi.org/10.1038/158668a0

Morel, X., Berthomier, M., Berthelier, J.-J., Morel, X., Berthomier, M., & Berthelier, J.-J. (2017). Electrostatic analyzer with a 3-D instantaneous field of view for fast measurements of plasma distribution functions in space Electrostatic analyzer with a 3-D in-stantaneous field of view for fast measurements of plasma distribution functions in space Electrostatic analyzer with a 3-D instantaneous field of view for fast measurements of plasma distribution functions in space. *Journal of Geophysical Research Space Physics*, *122*(3). https://doi.org/10.1002/2016JA023596ï

Mostafavi, P., Allen, R. C., McManus, M. D., Ho, G. C., Raouafi, N. E., Larson, D. E., Kasper, J. C., & Bale, S. D. (2022). Alpha–Proton Differential Flow of the Young Solar Wind: Parker Solar Probe Observations. *The Astrophysical Journal Letters*, *926*(2), L38. https://doi.org/10.3847/2041-8213/ac51e1

Namba, S., & Maeda, K. I. (1939). *Radio Wave Propagation*. Corona.

NASA Science Editorial Team. (2026, April 17). *NASA Shuts Off Instrument on Voyager 1 to Keep Spacecraft Operating*. NASA. https://science.nasa.gov/blogs/voyager/2026/04/17/nasa-shuts-off-instrument-on-voyager-1-to-keep-spacecraft-operating/

Nénon, Q., Laffitau, U., & Rabia, J. (2025). Injections of Multi-MeV Electrons in the Magnetosphere of Jupiter. *Journal of Geophysical Research: Space Physics*, *130*(9). https://doi.org/10.1029/2025JA034199

Neugebauer, M., & Snyder, C. W. (1962). The Mission of Mariner II: Preliminary Observations Profile of Events. *Science*, *138*(3545), 1095–1095. https://doi.org/10.1126/science.138.3545.1095

Nolte, J. T., Krieger, A. S., Timothy, A. F., Gold, R. E., Roelof, E. C., Vaiana, G., Lazarus, A. J., Sullivan, J. D., & McIntosh, P. S. (1976). Coronal holes as sources of solar wind. *Solar Physics*, *46*(2), 303–322. https://doi.org/10.1007/BF00149859

Nwankwo, O. G., & Ridley, A. J. (2025). Viscosity-Driven Dynamics of the Midnight Temperature Maximum in the Low-Latitude Thermosphere. *Journal of Geophysical Research: Space Physics*, *130*(12). https://doi.org/10.1029/2025JA034011

O'Brien, B. J., Laughlin, C. D., & Gurnett, D. A. (1964). High-latitude geophysical studies with satellite Injun 3: 1. Description of the satellite. *Journal of Geophysical Research*, *69*(1), 1–12. https://doi.org/10.1029/jz069i001p00001

Ogasawara, K., Allegrini, F., Desai, M. I., Livi, S., & McComas, D. J. (2012). A linear mode avalanche photodiode for ion detection in the energy range 5-250 keV. *IEEE Transactions on Nuclear Science*, *59*(5 PART 3), 2601–2607. https://doi.org/10.1109/TNS.2012.2210244

Ogasawara, K., Livi, S. A., Allegrini, F., Broiles, T. W., Dayeh, M. A., Desai, M. I., Ebert, R. W., Llera, K., Vines, S. K., & McComas, D. J. (2016). Next-generation solid-state detectors for charged particle spectroscopy. *Journal of Geophysical Research: Space Physics*, *121*(7), 6075–6091. https://doi.org/10.1002/2016JA022559

Osterbrock, D. E. (1961). The Heating of the Solar Chromosphere, Plages, and Corona by Magnetohydrodynamic Waves. *The Astrophysical Journal*, *134*, 347. https://doi.org/10.1086/147165

Owen, C. J., Bruno, R., Livi, S., Louarn, P., Al Janabi, K., Allegrini, F., Amoros, C., Baruah, R., Barthe, A., Berthomier, M., Bordon, S., Brockley-Blatt, C., Brysbaert, C., Capuano, G., Collier, M.,

Demarco, R., Fedorov, A., Ford, J., Fortunato, V., … Zouganelis, I. (2020). The Solar Orbiter Solar Wind Analyser (SWA) suite. *Astronomy and Astrophysics*, *642*. https://doi.org/10.1051/0004-6361/201937259

Parker, E. N. (1958). Dynamics of the Interplanetary Gas and Magnetic Fields. *The Astrophysical Journal*, *128*, 664. https://doi.org/10.1086/146579

Parkinson, R. (n.d.). *Properties and applications of electroless nickel Nickel Development Institute Properties and applications of electroless nickel*.

Persson, M., Futaana, Y., Ramstad, R., Masunaga, K., Nilsson, H., Hamrin, M., Fedorov, A., & Barabash, S. (2020). The Venusian Atmospheric Oxygen Ion Escape: Extrapolation to the Early Solar System. *Journal of Geophysical Research: Planets*, *125*(3). https://doi.org/10.1029/2019JE006336

Poletto, G. (2015). Solar coronal plumes. *Living Reviews in Solar Physics*, *12*(1). https://doi.org/10.1007/lrsp-2015-7

Popecki, M. A., Adams, B., Craven, C. A., Cremer, T., Foley, M. R., Lyashenko, A., O'Mahony, A., Minot, M. J., Aviles, M., Bond, J. L., Stochaj, M. E., Worstell, W., Elam, J. W., Mane, A. U., Siegmund, O. H. W., Ertley, C., Kistler, L. M., & Granoff, M. S. (2016). Microchannel plate fabrication using glass capillary arrays with Atomic Layer Deposition films for resistance and gain. In *Journal of Geophysical Research: Space Physics* (Vol. 121, Number 8, pp. 7449–7460). https://doi.org/10.1002/2016JA022580

Porco, C. C., Helfenstein, P., Thomas, P. C., Ingersoll, A. P., Wisdom, J., West, R., Neukum, G., Denk, T., Wagner, R., Roatsch, T., Kieffer, S., Turtle, E., Mcewen, A., Johnson, T. V, Rathbun, J., Veverka, J., Wilson, D., Perry, J., Spitale, J., … Squyres, S. (2006). Cassini Observes the Active South Pole of Enceladus. In *New Series* (Vol. 311, Number 5766).

Raines, J. M., DiBraccio, G. A., Cassidy, T. A., Delcourt, D. C., Fujimoto, M., Jia, X., Mangano, V., Milillo, A., Sarantos, M., Slavin, J. A., & Wurz, P. (2015). Plasma Sources in Planetary Magnetospheres: Mercury. In *Space Science Reviews* (Vol. 192, Numbers 1–4, pp. 91–144). Kluwer Academic Publishers. https://doi.org/10.1007/s11214-015-0193-4

Raines, J. M., Gershman, D. J., Slavin, J. A., Zurbuchen, T. H., Korth, H., Anderson, B. J., & Solomon, S. C. (2014). Structure and dynamics of Mercury's magnetospheric cusp: MESSENGER measurements of protons and planetary ions. *Journal of Geophysical Research: Space Physics*, *119*(8), 6587–6602. https://doi.org/10.1002/2014ja020120

Raines, J. M., Gershman, D. J., Zurbuchen, T. H., Sarantos, M., Slavin, J. A., Gilbert, J. A., Korth, H., Anderson, B. J., Gloeckler, G., Krimigis, S. M., Baker, D. N., McNutt, R. L., & Solomon, S. C. (2013). Distribution and compositional variations of plasma ions in Mercury's space environment: The first three Mercury years of MESSENGER observations. *Journal of Geophysical Research: Space Physics*, *118*(4), 1604–1619. https://doi.org/10.1029/2012JA018073

Raptis, S., Turner, D. L., Caprioli, D., Szalay, J. R., Clark, G., & Haggerty, C. C. (2026). Relativistic electron acceleration at the bow shock of Jupiter and beyond. *Nature*, *654*(8117), 47–51. https://doi.org/10.1038/s41586-026-10473-z

Rivera, Y. J., Klein, K. G., Wang, J. H., Matteini, L., Verscharen, D., Coburn, J. T., Badman, S. T., Lepri, S. T., Dewey, R. M., Raines, J. M., Alterman, B. L., Stubbs, T. J., Delano, K. C., Livi, R., Livi, S. A., Galvin, A. B., Owen, C. J., & Stevens, M. L. (2025). Observational Constraints on the Radial Evolution of O 6+ Temperature and Differential Flow in the Inner Heliosphere . *The Astrophysical Journal Letters*, *990*(2), L60. https://doi.org/10.3847/2041-8213/adfa97

Rodríguez-Pacheco, J., Wimmer-Schweingruber, R. F., Mason, G. M., Ho, G. C., Sánchez-Prieto, S., Prieto, M., Martín, C., Seifert, H., Andrews, G. B., Kulkarni, S. R., Panitzsch, L., Boden, S., Böttcher, S. I., Cernuda, I., Elftmann, R., Espinosa Lara, F., Gómez-Herrero, R., Terasa, C., Almena, J., … Zong, Q. (2020a). The Energetic Particle Detector: Energetic particle instrument suite for the Solar Orbiter mission. *Astronomy and Astrophysics*, *642*. https://doi.org/10.1051/0004-6361/201935287

Rodríguez-Pacheco, J., Wimmer-Schweingruber, R. F., Mason, G. M., Ho, G. C., Sánchez-Prieto, S., Prieto, M., Martín, C., Seifert, H., Andrews, G. B., Kulkarni, S. R., Panitzsch, L., Boden, S., Böttcher, S. I., Cernuda, I., Elftmann, R., Espinosa Lara, F., Gómez-Herrero, R., Terasa, C., Almena, J., … Zong, Q. (2020b). The Energetic Particle Detector: Energetic particle instrument suite for the Solar Orbiter mission. *Astronomy and Astrophysics*, *642*. https://doi.org/10.1051/0004-6361/201935287

Rosen, A., & Farley, T. A. (1961). Characteristics of the Van Allen radiation zones as measured by the scintillation counter on Explorer VI. *Journal of Geophysical Research*, *66*(7), 2013–2028. https://doi.org/10.1029/jz066i007p02013

Rubin, M., Altwegg, K., Balsiger, H., Berthelier, J. J., Combi, M. R., de Keyser, J., Drozdovskaya, M., Fiethe, B., Fuselier, S. A., Gasc, S., Gombosi, T. I., Hänni, N., Hansen, K. C., Mall, U., Rème, H., Schroeder, I. R. H. G., Schuhmann, M., Sémon, T., Waite, J. H., … Wurz, P. (2019). Elemental and molecular abundances in comet 67P/Churyumov-Gerasimenko. *Monthly Notices of the Royal Astronomical Society*, *489*(1), 594–607. https://doi.org/10.1093/mnras/stz2086

Schwadron, N. A., Allegrini, F., Bzowski, M., Christian, E. R., Dayeh, M. A., Desai, M. I., Fairchild, K., Frisch, P. C., Funsten, H. O., Fuselier, S. A., Galli, A., Janzen, P., Kubiak, M. A., McComas, D. J., Moebius, E., Reisenfeld, D. B., Sokół, J. M., Swaczyna, P., Szalay, J. R., … Zirnstein, E. J. (2018). Time Dependence of the IBEX Ribbon and the Globally Distributed Energetic Neutral Atom Flux Using the First 9 Years of Observations. *The Astrophysical Journal Supplement Series*, *239*(1), 1. https://doi.org/10.3847/1538-4365/aae48e

Slavin, J. A., Acuña, M. H., Anderson, B. J., Baker, D. N., Benna, M., Boardsen, S. A., Gloeckler, G., Gold, R. E., Ho, G. C., Korth, H., Krimigis, S. M., McNutt, R. L., Raines, J. M., Sarantos, M., Schriver, D., Solomon, S. C., Trávníček, P., & Zurbuchen, T. H. (2009). MESSENGER Observations of Magnetic Reconnection in Mercury's Magnetosphere. *Science*, *324*(5927), 606–610. https://doi.org/10.1126/science.1172011

Solomon, S. C., McNutt, R. L., Gold, R. E., & Domingue, D. L. (2007). MESSENGER mission overview. In *Space Science Reviews* (Vol. 131, Numbers 1–4, pp. 3–39). https://doi.org/10.1007/s11214-007-9247-6

Swaczyna, P., McComas, D. J., Zirnstein, E. J., Sokół, J. M., Elliott, H. A., Bzowski, M., Kubiak, M. A., Richardson, J. D., Kowalska-Leszczynska, I., Stern, S. A., Weaver, H. A., Olkin, C. B., Singer, K. N., & Spencer, J. R. (2020). Density of Neutral Hydrogen in the Sun's Interstellar Neighborhood. *The Astrophysical Journal*, *903*(1), 48. https://doi.org/10.3847/1538-4357/abb80a

Szabo, P. S., Poppe, A. R., Mutzke, A., Fatemi, S., Vorburger, A., & Wurz, P. (2023). Energetic Neutral Atom (ENA) Emission Characteristics at the Moon and Mercury From 3D Regolith Simulations of Solar Wind Reflection. *Journal of Geophysical Research: Planets*, *128*(9). https://doi.org/10.1029/2023JE007911

Szalay, J. R., Allegrini, F., Bagenal, F., Bolton, S. J., Clark, G., Connerney, J. E. P., Ebert, R. W., Ergun, R. E., Mauk, B., McComas, D. J., Valek, P., & Wilson, R. J. (2021). Proton Outflow Associated With Jupiter's Auroral Processes. *Geophysical Research Letters*, *48*(1). https://doi.org/10.1029/2020GL091627

Tu, C. Y., Marsch, E., & Qin, Z. R. (2004). Dependence of the proton beam drift velocity on the proton core plasma beta in the solar wind. *Journal of Geophysical Research: Space Physics*, *109*(A5). https://doi.org/10.1029/2004JA010391

Van Allen, J. A., Ludwig, G. H., Ray, E. C., & McIlwain, C. E. (1958). Observation of High Intensity Radiation by Satellites 1958 Alpha and Gamma. *Journal of Jet Propulsion*, *28*(9), 588–592. https://doi.org/10.2514/8.7396

Van Allen, J. A., McIlwain, C. E., & Ludwig, G. H. (1958). *Radiation Measurements from Explorer IV*. https://digital.lib.uiowa.edu/node/439847

Verniero, J. L., Chandran, B. D. G., Larson, D. E., Paulson, K., Alterman, B. L., Badman, S., Bale, S. D., Bonnell, J. W., Bowen, T. A., de Wit, T. D., Kasper, J. C., Klein, K. G., Lichko, E., Livi, R., McManus, M. D., Rahmati, A., Verscharen, D., Walters, J., & Whittlesey, P. L. (2022). Strong Perpendicular Velocity-space Diffusion in Proton Beams Observed by Parker Solar Probe. *The Astrophysical Journal*, *924*(2), 112. https://doi.org/10.3847/1538-4357/ac36d5

Vorburger, A., Wurz, P., Barabash, S., Wieser, M., Futaana, Y., Lue, C., Holmström, M., Bhardwaj, A., Dhanya, M. B., & Asamura, K. (2013). Energetic neutral atom imaging of the lunar surface. *Journal of Geophysical Research: Space Physics*, *118*(7), 3937–3945. https://doi.org/10.1002/jgra.50337

Waite, J. H., Combi, M. R., Ip, W.-H., Cravens, T. E., McNutt, R. L., Kasprzak, W., Yelle, R., Luhmann, J., Niemann, H., Gell, D., Magee, B., Fletcher, G., Lunine, J., & Tseng, W.-L. (2006). Cassini Ion and Neutral Mass Spectrometer: Enceladus Plume Composition and Structure. *Science*, *311*(5766), 1419–1422. https://doi.org/10.1126/science.1121290

Waite Jr, J. H., Combi, M. R., Ip, W.-H., Cravens, T. E., McNutt Jr, R. L., Kasprzak, W., Yelle, R., Luhmann, J., Niemann, H., Gell, D., Magee, B., Fletcher, G., Lunine, J., & Tseng, W.-L. (2006). Cassini Ion and Neutral Mass Spectrometer: Enceladus Plume Composition and Structure. In *New Series* (Vol. 311, Number 5766).

Weberg, M. J., Zurbuchen, T. H., & Lepri, S. T. (2012). ACE/swics observations of heavy ion dropouts within the solar wind. *Astrophysical Journal*, *760*(1). https://doi.org/10.1088/0004-637X/760/1/30

Wilken, B., & Stüdemann, W. (1984). A compact time-of-flight mass-spectrometer with electrostatic mirrors. *Nuclear Instruments and Methods in Physics Research*, *222*(3), 587–600. https://doi.org/10.1016/0167-5087(84)90391-0

Wolfe, J. H., Silva, R. W., McKibbin, D. D., & Mason, R. H. (1966). The compositional, anisotropic, and nonradial flow characteristics of the solar wind. *Journal of Geophysical Research*, *71*(13), 3329–3335. https://doi.org/10.1029/jz071i013p03329

Wright, K. H., Swenson, C. M., Thompson, D. C., Barjatya, A., Koontz, S. L., Schneider, T. A., Vaughn, J. A., Minow, J. I., Craven, P. D., Coffey, V. N., Parker, L. N., & Bui, T. H. (2008). Charging of the International Space Station as observed by the floating potential measurement unit: Initial results. *IEEE Transactions on Plasma Science*, *36*(5 PART 2), 2280–2293. https://doi.org/10.1109/TPS.2008.2003257

Xiong, C., & Lühr, H. (2023). Field-aligned scale length of depleted structures associated with post-sunset equatorial plasma bubbles. *Journal of Space Weather and Space Climate*, *13*(4). https://doi.org/10.1051/swsc/2023002

Young, D. T., Bame, S. J., Thomsen, M. F., Martin, R. H., Burch, J. L., Marshall, J. A., & Reinhard, B. (1988). 2π-radian field-of-view toroidal electrostatic analyzer. *Review of Scientific Instruments*, *59*(5), 743–751. https://doi.org/10.1063/1.1139821

Young, D. T., Berthelier, J. J., Blanc, M., Burch, J. L., Coates, A. J., Goldstein, R., Grande, M., Hill, T. W., Johnson, R. E., Kelha, V., Mccomas, D. J., Sittler, E. C., Svenes, K. R., Szegö, K., Tanskanen, P., Ahola, K., Anderson, D., Bakshi, S., Baragiola, R. A., … Zinsmeyer, C. (2004). Cassini Plasma Spectrometer Investigation. *Space Science Reviews*, *114*(1–4), 1–112. https://doi.org/10.1007/s11214-004-1406-4

Young, D. T., Ghielmetti, A. G., Shelley, E. G., Marshall, J. A., Burch, J. L., & Booker, T. L. (1987). Experimental tests of a toroidal electrostatic analyzer. *Review of Scientific Instruments*, *58*(4), 501–508. https://doi.org/10.1063/1.1139260

Zhao, L., Landi, E., Lepri, S. T., & Carpenter, D. (2022). Depletion of Heavy Ion Abundances in Slow Solar Wind and Its Association with Quiet Sun Regions. *Universe*, *8*(8). https://doi.org/10.3390/universe8080393

Ziegler, J. F., Ziegler, M. D., & Biersack, J. P. (2010). SRIM - The stopping and range of ions in matter (2010). *Nuclear Instruments and Methods in Physics Research, Section B: Beam Interactions with Materials and Atoms*, *268*(11–12), 1818–1823. https://doi.org/10.1016/j.nimb.2010.02.091

Zou, S., Lyons, L. R., Wang, C. P., Boudouridis, A., Ruohoniemi, J. M., Anderson, P. C., Dyson, P. L., & Devlin, J. C. (2009). On the coupling between the Harang reversal evolution and substorm dynamics: A synthesis of SuperDARN, DMSP, and IMAGE observations. *Journal of Geophysical Research: Space Physics*, *114*(1). https://doi.org/10.1029/2008JA013449

Zurbuchen, T. H., Raines, J. M., Gloeckler, G., Krimigis, S. M., Slavin, J. A., Koehn, P. L., Killen, R. M., Sprague, A. L., Mcnutt, R. L., & Solomon, S. C. (2008). MESSENGER Observations of the Composition of Mercury's Ionized Exosphere and Plasma. In *New Series* (Vol. 321, Number 5885).

Zurbuchen, T. H., Weberg, M., von Steiger, R., Mewaldt, R. A., Lepri, S. T., & Antiochos, S. K. (2016). COMPOSITION OF CORONAL MASS EJECTIONS. *The Astrophysical Journal*, *826*(1), 10. https://doi.org/10.3847/0004-637X/826/1/10